JUSTUS-LIEBIG-UNIVERSITÄT GIESSEN Philipps Universität Marburg THM TECHNISCHE HOCHSCHULE MITTELHESSEN

FORSCHUNGSCAMPUS MITTELHESSEN

Investigation of hot plume impact on space launch vehicle aft-body flows

Dissertation

Zur

Erlangung des akademischen Grades des Doktors der Ingenieurwissenschaften (Dr.-Ing.)

Dem Promotionszentrum für Ingenieurwissenschaften

am Forschungscampus Mittelhessen

vorgelegt von

Jan-Erik Schumann

Aus Hachenburg

Gießen, 26. Oktober 2022

Begutachtet durch:

Prof. Peter Klar und Prof. Uwe Probst und Prof. Andreas Dillmann

Acknowledgement

Several persons have tremendeously supported me during the process of research and writing this dissertation. First and foremost, I would like to thank my main supervisor for the majority of the research process, the late Prof. Dr. Klaus Hannemann, who offered me the opportunity to work on this topic in his department at DLR. He always pushed me to take the next step in my research and his broad experience provided the guidance for the overall path of this dissertation. On the other hand, he allowed the freedom to pursue the directions I thought most promising, allowing me to build up my own experience. Even when weakened by his disease he tried his best to push the process forward, and I am deeply saddened by his early passing. I also thank my subject-specific supervisor Dr. Volker Hannemann who was always available to discuss detailed problems or concerns with and gave helpful insights into the numerical algorithms. Further thanks are due to my supervisor Prof. Dr. Chris Volkmar and reviewer of my dissertation Prof. Dr. Uwe Probst for their availability in the PhD process I also thank Prof. Dr. Peter Klar and Prof. Andreas Dillmann for their willingness to act as supervisor and reviewers short notice.

Special thanks goes to all the colleagues inside and outside of DLR that I had the honor of working with over the years. This includes everyone in the Spacecraft Department, in particular the numerics group, who made the work place so very welcoming and comfortable. Further I would like to thank Axel Probst for his time and patience discussing the ins and outs of the LES/DES implementation in TAU. I also thank Prof. Johan Larsson for his willingness to invite me to Maryland and for drastically improving my understanding of LES modeling and turbulence in general. I also gratefully acknowledge the Gauss Centre for Supercomputing e.V. (www.gauss-centre.eu) for funding this project this research was conducted in by providing computing time on the GCS Supercomputer SuperMUC-NG at Leibniz Supercomputing Centre (www.lrz.de). Special thanks are extended to the Sonderforschungsbereich Transregio 40 (SFB TRR40) of the Deutsche Forschungs Gesellschaft DFG for providing an excellent framework in which to conduct this research and funding my position at DLR.

Finally, I would like to thank my family, in particular my parents who gave me the freedom to choose what I want to do and supported me up until and throughout my university years. I also thank Noah, for making the last year of my PhD so much more enjoyable, providing so many small but welcome distractions, as well as Felix who arrived just before the submission of the thesis. The biggest thanks, however, is to the love of my life, Genevieve, for supporting me in pursuing this project and even moving halfway around the world for it. She motivated me to keep going when I felt stuck and made sure I had the right balance between work and free time. I could not have done this without her.

Abstract

The transonic flow around generic space launch vehicle aft-body geometries is investigated numerically using hybrid RANS-LES methods. A sensitivity study shows that the qualitative results are mostly insensitive to changes in grid resolution and numerical settings, but certain aspects such as circumferential grid resolution and LES filter length definition can affect the obtained quantitative results. It is further found that the presence of a plume leads to the appearance of an additional spectral contribution in the flow. The main investigations showed that changing the plume properties leads to a downstream shift of the reattachment location due to the stronger acceleration of the external flow. An increased wall temperature leads to a similar shift that is attributed to the slower development of turbulent structures in higher temperature shear layers. As a consequence the pressure fluctuations and the nozzle forces are reduced as well. However, the underlying flow phenomena are unaffected by the plume properties and wall temperature, with the exception of an additional spectral feature in the pressure fluctuations due to the interaction of shear layer movement and nozzle flow plume separation once the reattachment occurs mostly beyond the nozzle lip. A shorter nozzle strongly affects the recirculation region shape, pressure fluctuations and nozzle forces and does not show the observed flow phenomena observed for the longer nozzle configuration.

Zusammenfassung

Die transonische Strömung um generische Trägerraketengeometrien wird numerisch mit hybriden RANS-LES Methoden untersucht. Eine Sensitiviätsstudie zeigt, dass die qualitativen Ergebnisse größtenteils unabhängig von Netzauflösung und numerischen Einstellungen sind, aber dass bestimme Aspekte wie Umfangsauflösung und Filterlängendefinition die quantitativen Ergebnisse beeinflussen können. Des weiteren zeigt sich, dass die Präsenz eines Abgasstrahls einen zusätzlichen spektralen Beitrag erzeugt. Eine Änderung der Strahl-Eigenschaften führt zu einer Verschiebung der Wiederanlegeposition stromab, erzeugt durch die stärkere Beschleunigung der externen Strömung. Die Erhöhung der Wandtemperaturen führt zu einer ähnlichen Verschiebung, die auf die langsamere Entwicklung der turbulenten Strukturen in der heißeren Scherschicht zurückgeführt wird. Dies führt zu einer Reduktion der Druckfluktuationen and Düsenkräfte. Die zugrunde liegenden Stömungsphänomene zeigen sich allerdings unabhängig von Strahleigenschaften und Wandtemperaturen, mit der Ausnahme eines zusätzlichen spektralen Beitrags durch die Interaktion von Scherschichtbewegung und Strömungsablösung in der Düse sobald die Wiederanlegeposition stromab der Düsenlippe liegt. Eine kürzere Düse verändert die Form der Rezirkulationzone, die Druckfluktuationen und Düsenkräfte stark und zeigt die bei der Konfiguration mit langer Düse beobachteten Strömungsphänomene nicht.

Table of Contents

Nomenclature

Vectors are denoted by an underline such as $\underline{u}$. Matrices/tensors are denoted in bold such as $\boldsymbol{I}$. For quantities with diverse units (e.g. state vectors) the unit column is left blank.

Latin Symbols

Symbol	Description	Units
A	Area	m^2
A_r, b_r, k_r, K_r	Reaction coefficients	—
c	Speed of sounds	m/s
	Concentration	$mole/m^3$
c_p	Heat capacity at constant pressure	J/(kg·K)
	Pressure coefficient	—
c_v	Heat capacity at constant volume	J/(kg·K)
C	Coherence	—
	Sutherland temperature	K
d	Distance	m
D	Diameter	m
$\underline{D}$	Matrix dissipation term	
$\mathcal{D}$	Diffusion coefficient	m^2/s
e	Specific internal energy	J/kg
E	Specific total energy	J/kg
f	Force	N
	Frequency	1/s
	Model function	—
F	Blending function	—
$\boldsymbol{F}$	Flux	
G	Power Spectral Density	Pa/Hz
h	Specific enthalpy	J/kg
H	Specific total enthalpy	J/kg
$\underline{H}$	Convective flux approximation	
$\boldsymbol{I}$	Identity	—
J	Diffusion mass flux	$kg/(s{\cdot}m^2)$
k	Wave number	1/m
	Specific turbulent kinetic energy	J/kg
K_{rot}	Symmetry factor	—

continued on next page

Latin Symbols

Symbol	Description	Units
l, L	Length	m
$\dot{m}$	Mass flux (per unit area)	kg/(m^2·s)
M	Mach number	—
$\mathcal{M}$	Molar mass	kg/mol
$\underline{n}$	Normal vector	m^2
N	Number of	—
p	Thermodynamic pressure	Pa
Pr	Prandtl number	—
q	Heat flux	kW/m^2
$\underline{Q}$	Source term vector	
$\underline{R}$	Residual	
$\mathcal{R}$	Specific gas constant	J/(kg·K)
Re	Reynolds number	—
S	Grid sensor	—
$\boldsymbol{S}$	Strain rate tensor	1/s
Sc	Schmidt number	—
Sr	Strouhal number	—
t	Time	s
T	Temperature	K
u	Velocity in axial or x-coordinate direction	m/s
$\underline{u}$	Velocity vector	m/s
$\underline{U}$	Vector of conservative variables	
v	Velocity in circumferential or y-coordinate direction	m/s
v_n	Normal velocity	m/s
V	Volume	m^3
w	Velocity in radial or z-coordinate direction	m/s
x, y, z	Coordinate direction	m
Y	Mass fraction	—

Greek Symbols

Symbol	Description	Units
α, β	Coefficient	—
$\boldsymbol{\alpha}$	Matrix dissipation operator	
γ	Ratio of heat capacities	—
δ_{99}	Boundary layer thickness	m
δ_{ij}	Kronecker delta	—
Δ	Filter length	m
ϵ	small number	—

continued on next page

Greek Symbols

Symbol	Description	Units
ε, Φ	Dissipation source term	
η	Kolmogorov length scale	m
θ	Characteristic temperature	K
Θ	Vorticity thickness	m
κ	Thermal conductivity	W/(m·K)
λ	Characteristics length	m
	Frequency	1/s
μ	Dynamic Viscosity	Pa·s
ν	Kinematic viscosity	m^2/s
ρ	Density	kg/m^3
σ^2	PSD integral	
$\boldsymbol{\sigma}$	Shear stress tensor	Pa
τ	Time scale	s
$\boldsymbol{\tau}$	Turbulent stress tensor	Pa
Ψ	Pressure sensor	—
ω	Chemical source term	$kg/(m^3 \cdot s)$
	Inverse turbulent time scale	1/s
∇	Nabla-operator	—

Subscripts

Symbol	Description
0	stagnation
ax	axial
$circ$	circumferential
D	Diameter
f	face
hyb	hybrid
i	coordinate direction
	inner
I	Point index
j	coordinate direction
m	mode
o	outer
r	real
	reactions
	reattachment
rad	radial
ref	reference

continued on next page

Subscripts

Symbol	Description
s	species
t	turbulent
tot	total
∞	free stream

Superscripts

Symbol	Description
$+$	Non-dimensional
$*$	Pseudo
0	Formation
DTS	Dual time stepping
el	Electronic
Eu	Euler
eq	equilibrium
int	internal
l, L	Left
kin	kinetic
n	step
NS	Navier-Stokes
rot	Rotational
r, R	Right
$trans$	Translational
vib	Vibrational

Abbreviations

Symbol	Description
CFD	Computational fluid dynamics
CSD	Cross Spectral Density
DLR	Deutsches Zentrum für Luft- und Raumfahrt e.V.
DMD	Dynamic Mode Decomposition
(ID)DES	(Improved Detached) Delayed Eddy Simulation
LES	Large Eddy Simulation
(sp)PSD	(scaled premultiplied) Power Spectral Density
RANS	Reynolds-Averaged Navier-Stokes
TAU	Flow solver at DLR

List of Figures

List of Tables

1 Introduction

1.1 Motivation

During the ascent through the atmosphere space launch vehicles experience significant aerodynamic and aerothermodynamic loads. A particularly affected area is the region at the bottom of the vehicle. At the end of the main body the sudden change in diameter leads to flow separation and a recirculation region forms as shown schematically in Fig. 1.1. The pressure distribution on the nozzle surface as well as the overall size of the recirculation region is highly unsteady, as are the associated mechanical loads. A particular phenomenon is the so-called "base buffeting" that describes the appearance of radial forces on the nozzle structure with a pronounced frequency [16]. At least one mission failure was attributed to these loads and their "non-exhaustive definition" [11]. The observed mechanical loads depend strongly on the vehicle design in the base region, in particular on the nozzle length since this geometrical pa-

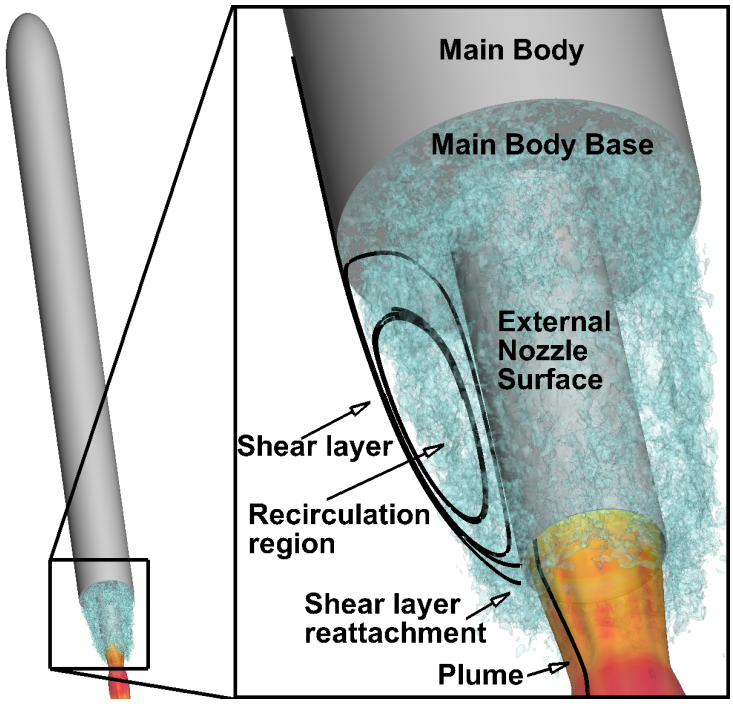

Figure 1.1: Schematic depiction of the flow field at the base of a space launch vehicle.

rameter determines where the turbulent shear layer reattaches at the respective free stream conditions, and hence at which point during the mission the most critical loads appear. For the European ARIANE 5 vehicle it was found that this is the case in transonic flight with Mach number $M \approx 0.8$. As a result, this phenomenon was the focus of both experimental and numerical aerodynamics research on reduced scale models (e.g. [8, 9, 16]). It was also the focus of branch B of the Sonderforschungsbereich Transregio 40, funded by the German Research Foundation (DFG) [1]. This research initiative focused on the fundamental flow physics of the phenomena by investigating simplified geometries with similar geometrical proportions as full scale launch vehicles. Sub-project B5 investigated in particular the impact of realistic plumes and heated walls on these phenomena using numerical simulations. The present thesis focuses on the investigations conducted in this project.

Numerical simulations of these phenomena need to resolve the unsteady spatial and temporal scales in the flow to allow an evaluation of the unsteady features and mechanical loads. Methods that have these capabilities, e.g. Large Eddy Simulations (LES) or Detached Eddy Simulation (DES), require significantly more computational resources than simpler approaches such as Reynolds-Averaged Navier-Stokes (RANS) simulations, but provide the detailed view of the flow that is required to investigate fundamental flow physics. Additionally, mean quantities obtained with these high fidelity methods can be compared to those obtained with lower cost methods. This helps to judge the feasiblity of applying these lower cost methods for future applications. Furthermore, the demonstration of the required numerical capabilities on representative generic test cases allows to confidently apply the high-fidelity methods for critical load points in the design phase of vehicle development processes as well.

The present work focuses on the impact of hot plumes on the base flow region characteristics of generic space launch vehicle configurations at transonic flow conditions. In particular, the effect of substituting an air plume - which is usually used in the literature (e.g. [8, 9, 61]) - with a hot propulsive plume is investigated. Additionally, the effect of hot nozzle walls on the recirculation region is investigated which, to the authors knowledge, has never been considered in previous research. This is important since the base region of the launch vehicle is affected by direct heating from the hot propulsive plume as well as from the hot nozzle structure. Finally, the effect of a shorter nozzle length that is more representative of next generation vehicles such as ARIANE 6 is explored. As flow solver the DLR TAU-Code with an implemented hybrid RANS-LES method is used to investigate these issues numerically.

In the following a short overview of previous investigations of the phenomena as available in the open literature is given. Subsequently, the underlying theoretical principles and mathematical equations defining the investigated flow physics are presented in Chapter 2, followed in Chapter 3 by the numerical methods used to solve these equations. A sensitivity study utiliz-

ing generic test cases from the literature is conducted in Chapter 4 to find optimal numerical parameter settings, investigate the sensitivity of the results and demonstrate the agreement of the computed results with available experimental and numerical data. The investigation of configurations with hot plumes and hot walls is presented in Chapter 5. Finally, the conclusions of the investigation as well as interesting avenues of research for further exploration are presented in Chapter 6.

1.2 Previous investigations and state of the art

Aft-body flows of space launch vehicles are dominated by the presence of a turbulent shear layer that separates from the main body as sketched in Fig. 1.1. Hence, the most fundamental geometrical approximation to better understand the flow field is that of a cylindrical blunt based body with diameter D aligned with the free stream. This configuration was, among others, investigated experimentally by Merz et al. [39] for different subsonic Mach numbers. They found that the pressure coefficient on the base is independent of the radial position and independent of the Mach number for $M \leq 0.8$. Further, their investigation showed that the size of the recirculation region at the base of the cylinder grows with increasing Mach number and that the centerline velocity distribution exhibits a strong similarity for all investigated free stream Mach numbers. Merz [38] also showed that the pressure fluctuations on the base surface increase with Mach number while the approximated dominant frequency of the pressure fluctuations decreases. At $M = 0.8$ the non-dimensional frequency (Strouhal number $\mathrm{Sr}_D = \frac{fD}{U_\infty}$ with frequency f and free stream velocity U_∞) was approximated to be around 0.1.
However, for the analysis of expected loads on a space launch vehicle the blunt based cylinder has the disadvantage that pressure loads are only available on the base surface, whereas for actual vehicles the external nozzle surface pressure distribution is most critical. A configuration that resembles actual launch vehicles much closer was investigated experimentally by Deprés et al. [9]. They studied a geometry consisting of two cylinders: a larger diameter cylinder acting as the main body of the vehicle and a smaller cylinder (diameter D_2 and length L) protruding from its base representing the nozzle extension. Their findings confirmed the dominant frequency of $\mathrm{Sr}_D \approx 0.1$ for a blunt based cylinder, but also showed that even the short cylindrical rear body ($L/D = 0.6$) with smaller diameter ($D_2/D = 0.4$) protruding from the base affects the observed flow field and pressure spectra. More specifically, in their investigation the dominant frequency of the base pressure fluctuations shifts towards $\mathrm{Sr}_D \approx 0.2$, which also dominates the pressure fluctuations on the rear body surface and was attributed to vortex shedding of large-scale turbulent structures. If the rear body length is increased to allow a mean reattachment position of the shear layer on the rear body ($L/D = 1.2$, corresponding to the geometrical relations on an ARIANE 5 launch vehicle) they found that the dominant

frequency is only visible in the center of the recirculation region whereas near the base a lower frequency of $\mathrm{Sr}_D \approx 0.1$ and near the reattachment location a higher broadband frequency of $\mathrm{Sr}_D \approx 0.6$ dominates. The former was attributed to a periodic growing of the recirculation region whereas the latter to impingement of shear layer vortices in the recirculation region. The effect of a cold air jet originating from the rear body was also investigated with the conclusion that for a shorter rear body the jet interacts directly with the recirculation region and changes the observed quantities whereas for a longer rear body no significant effect can be observed.

The configuration with a jet and $L/D = 1.2$ was also investigated numerically by Deck and Thorigny [8] who showed that the dominant lateral forces on the rear body also exhibit fluctuations with $\mathrm{Sr}_D \approx 0.2$ and that they originate from an anti-symmetric pressure mode. Weiss et al. [73] further elaborated on this anti-symmetric mode and found that it corresponds to a helical absolute instability in the center of the reattachment region. Several other investigations were concerned with certain aspects of the flow around generic launch vehicles such as the effects of boosters [33, 41], wake control [72] and wind tunnel walls [71]. Hannemann et al. [16] and Lüdeke et al. [30] investigated the flow around a 1/60-scale model of the actual ARIANE 5 launch vehicle - instead of a generic approximation - without plume both experimentally and numerically.Their investigations showed that also for a more complex geometry hybrid RANS-LES approaches yield good agreement with experimental measurements.

Recently, Statnikov et al. [61] further extended the understanding of the underlying flow phenomena for generic configurations with the mentioned geometric relations at the dominant frequencies of $\mathrm{Sr}_D \approx 0.1$, $\mathrm{Sr}_D \approx 0.2$ and $\mathrm{Sr}_D \approx 0.35$ using Dynamic Mode Decomposition (DMD). They showed that the smallest frequency is associated with a "longitudinal cross-pumping" of the recirculation region, which grows and shrinks the entire recirculation region leading to an axisymmetric pressure footprint on the nozzle structure. In contrast, the most dominant frequency $\mathrm{Sr}_D \approx 0.2$ is associated with a "cross-flapping" of the turbulent shear layer leading to vortex shedding and an antisymmetric pressure footprint. Pain et al. [42] elaborated on this using 3D Fourier Analysis to show that the cross-flapping exhibits a helical pressure mode, leading to the pronounced buffeting force at this frequency. The $\mathrm{Sr}_D \approx 0.35$ frequency was found to be related to the swinging of the shear layer, which also shows an antisymmetric pressure footprint and hence contributes to the buffeting loads as well [61].

However, all of these investigations featured either no plume or a plume resulting from expanding compressed air. The plume on actual launch vehicles typically consists of fluids with higher speeds of sound, leading to exit velocities that are larger by a factor of around 5. Stephan and Radespiel [62] investigated the effects of an underexpanded helium jet on the supersonic flow field around a generic launch vehicles geometry and found an impact on both mean and fluctuating pressure measurements. This indicates that the plume conditions, in particular

the ratio between plume exit velocity and external flow free stream velocity, have a significant impact on the flow field and mechanical loads.

Furthermore, in realistic launch vehicles the plume is the result of a combustion and thus is significantly hotter than a plume of compressed air or (cold) helium. This hot plume not only interacts with the external flow, but can also heat up the nozzle structure, especially if part or all of the nozzle cooling is achieved by radiative cooling. To the author's knowledge, neither the impact of a hot plume nor of hot walls on the aft-body flow field of generic space launch vehicles has been fundamentally investigated using high-fidelity numerical simulations.

2 Theoretical principles

This chapter details the basic equations that describe the investigated flow phenomena.

2.1 Conservation Equations

The system of equations of motion, often referred to as the Navier-Stokes-Equations, for a compressible fluid consisting of N_s species consists of $N_s + 5$ equations. Using tensor notation it reads

$$\frac{\partial \rho}{\partial t} + \frac{\partial}{\partial xj}(\rho u_j) = 0 \tag{2.1}$$

$$\frac{\partial}{\partial t}(\rho Y_s) + \frac{\partial}{\partial x_j}(\rho u_j Y_s) = -\frac{\partial J_{s,j}}{\partial x_j} + \omega_s \tag{2.2}$$

$$\frac{\partial}{\partial t}(\rho u_i) + \frac{\partial}{\partial x_j}(\rho u_i u_j) + \frac{\partial p}{\partial x_i} = \frac{\partial \sigma_{ij}}{\partial x_j} + \rho f_i \tag{2.3}$$

$$\frac{\partial}{\partial t}(\rho E) + \frac{\partial}{\partial x_j}(\rho H u_j) = -\frac{\partial q_j}{\partial x_j} + \frac{\partial}{\partial x_j}(u_i \sigma_{ij}) + \rho u_i f_i \tag{2.4}$$

where either the equation for conservation of mass (equation (2.1)) or one of the species mass conservation equations (equations (2.2)) can be omitted since the system is overspecified due to $\sum_{s=1}^{N_s} Y_s = 1$, and hence a system of $N_s + 4$ equations has to be solved. For $N_s = 1$ equation (2.1) is equal to equations (2.2) and the equations for a single species are recovered.

In these equations ρ is the fluid density, u_i are the components of the velocity vector $\underline{u} = (u, v, w)^T$, Y_s is the mass fraction of species s, p is the thermodynamic pressure and E and H are mass specific total energy and total enthalpy of the fluid, respectively. ω_s is a mass source term for the partial densities $\rho_s = \rho Y_s$ due to reactions (see Sec. 2.3) and f_i are external forces that might act on the fluid.

In addition to equations (2.1) to (2.4) an equation of state is required. In the present thesis only thermally perfect fluids are considered, i.e. the ideal gas law

$$p = \rho \mathcal{R} T = \rho \frac{\mathcal{R}_u}{\mathcal{M}} T \tag{2.5}$$

with the universal gas constant $\mathcal{R}_u = 8.314$ J/(mol·K), mixture-specific gas constant $\mathcal{R}$ and temperature T is valid. The mixture molar mass $\mathcal{M}$ is computed from the species molar masses

according to

$$\frac{1}{\mathcal{M}} = \sum_{s=1}^{N_s} \frac{Y_s}{\mathcal{M}_s} \tag{2.6}$$

.

The specific total enthalpy is defined as

$$H = h + \frac{1}{2}\underline{u}^T\underline{u} = E + \frac{p}{\rho} = e + \frac{1}{2}\underline{u}^T\underline{u} + \frac{p}{\rho} \tag{2.7}$$

where e is the specific internal energy and h is the specific enthalpy. The specific internal energy and enthalpy are obtained as mass fraction weighted averages of the species specific internal energy e_s and enthalpy h_s, respectively, as

$$\Phi = \sum_{s=1}^{N_s} Y_s \Phi_s. \tag{2.8}$$

where Φ is the quantity to be averaged.

The species specific energies and enthalpies are split into contributions from translation, rotation, vibration, electronic excitation and formation which leads to

$$\begin{aligned} e_s &= e_s^{trans} + e_s^{rot} + e_s^{vib} + + e_s^{el} + e_s^0 \\ &= \frac{3}{2}\mathcal{R}_s T + K_{rot}\mathcal{R}_s T + \sum_v^{n_v} \frac{\mathcal{R}_s \theta_s^{vib,v}}{\exp\left(\theta_s^{vib,v}/T\right) - 1} + \mathcal{R}_s \frac{\sum_e^{n_e} g_s^{el,e}\theta_s^{el,e}\exp\left(-\theta_s^{el,e}/T\right)}{\sum_e^{n_e} g_s^{el,e}\exp\left(-\theta_s^{el,e}/T\right)} + e_s^0 \end{aligned} \tag{2.9}$$

with

$$e_s^0 = \mathcal{R}_s \theta_s^0 \tag{2.10}$$

Here $\mathcal{R}_s = \frac{\mathcal{R}_u}{\mathcal{M}_s}$ is the gas constant of the species, T is the macroscopic fluid temperature, K_{rot} is 1 for linear molecules and 1.5 for nonlinear ones, n_v and n_e are the number of vibrational and electronic states of excitation, respectively, g is the degeneracy of an electronic state and θ^{vib}, θ^{el} and θ^0 are the characteristic temperatures of vibrational and electronic excitation and formation, respectively.

Additionally, the heat capacity at constant volume is $c_{v,s} = \frac{de_s}{dT}$ and thus can also be computed based on equation (2.9). The heat capacity at constant pressure is $c_{p,s} = c_{v,s} + \mathcal{R}_s$. The species internal energies and heat capacities can be tabulated over temperature at the start of a simulation and then be accessed when needed.

The (frozen) speed of sound and Mach number are

$$c = \sqrt{\gamma \frac{p}{\rho}} \qquad \text{and} \qquad M = \frac{\sqrt{\underline{u}^T\underline{u}}}{c} \tag{2.11}$$

with heat capacity ratio $\gamma = \frac{c_p}{c_v}$ where c_p and c_v are the mass fraction weighted averages of the species heat capacities.

If one calorically perfect gas is considered the computations are simplified since the specific heat capacities are constant and thus

$$h = c_p T \qquad \text{and} \qquad e = c_v T \tag{2.12}$$

with

$$c_v = \frac{\mathcal{R}}{\gamma - 1} \tag{2.13}$$

with gas specific, but constant, heat capacity ratio γ.

The diffusion mass flux in the conservation equations is a function of the spatial gradients of all mass fractions (and less pronounced of pressure and temperature gradients) [19], but can be approximated using Fick's law as

$$J_{s,j} = -\rho \mathcal{D}_s \frac{\partial Y_s}{\partial x_j} = -\rho \mathcal{D} \frac{\partial Y_s}{\partial x_j} \tag{2.14}$$

neglecting differential diffusion (i.e. the species diffusion coefficients are replaced by one mixture diffusion coefficient).

The shear stress tensor for a Newtonian fluid is defined as

$$\sigma_{ij} = 2\mu \left(S_{ij} - \frac{\delta_{ij}}{3} \frac{\partial u_k}{\partial x_k} \right) \quad \text{with } S_{ij} = \frac{1}{2} \left(\frac{\partial u_i}{\partial x_j} + \frac{\partial u_j}{\partial x_i} \right) \tag{2.15}$$

where μ is the dynamic viscosity, $\boldsymbol{S}$ is the strain rate tensor and Stokes' hypothesis is applied.

The energy flux consists of heat transport described by Fourier's law and diffusion heat flux called Dufour's effect [13]. Thus

$$q_j = -\kappa \frac{\partial T}{\partial x_j} + \sum h_s J_{s,j} = -\kappa \frac{\partial T}{\partial x_j} - \frac{\mu}{Sc} \sum h_s \frac{\partial Y_s}{\partial x_j} \tag{2.16}$$

where κ is the mixture thermal conductivity and the Schmidt number Sc= $\frac{\mu}{\rho \mathcal{D}}$ is introduced.

2.2 Transport coefficients

For one calorically perfect gas the viscosity can often be sufficiently calculated from Sutherland's law [65] as

$$\mu = \mu_{ref} \left(\frac{T}{T_{ref}} \right)^{1.5} \frac{T + C}{T_{ref} + C} \tag{2.17}$$

where μ_{ref}, T_{ref} and C have gas dependent values. Furthermore, in this case the thermal conductivity κ can be expressed as a function of (constant) Prandtl number Pr = $\frac{\mu c_p}{\kappa}$. However,

for very high or very low temperatures, certain gases and/or higher accuracy more elaborate methods to compute the transport coefficients can be used.

One possibility is to fit the viscosity to existing data bases (e.g. Gurvich et al. [14]) and subsequently compute the thermal conductivity via a modified Eucken equation [18]. Alternatively, the transport coefficients can be computed based on collision integrals (e.g. Hirschfelder et al. [19]). In the present thesis the latter approach is chosen, as it provides the most accurate description of the transport coefficients over a wide range of temperatures. Particularly for polar species like water vapor (H_2O) the collision integrals improve the accuracy of the transport coefficients notably. However, instead of computing the collision integrals in each point for each iteration based on the individual mixture composition, the transport coefficients are pre-computed for each species over the whole temperature range. The obtained transport coefficients for the different species are summarized in appendix C. The mixture transport coefficients for a certain composition are then computed according to the mixture rules of Wilke [74] for the viscosity and of Herning and Zipperer [17] for the thermal conductivity:

$$\mu = \sum_{S=0}^{N_s} \frac{c_S \mu_S}{\sum_{s=0}^{N_s} c_s \Phi_{S,s}} \qquad \text{with} \quad \Phi_{S,s} = \frac{1}{\sqrt{8}} \left(1 + \frac{\mathcal{M}_S}{\mathcal{M}_s}\right)^{-\frac{1}{2}} \left[1 + \left(\frac{\mu_S}{\mu_s}\right)^{\frac{1}{2}} \left(\frac{\mathcal{M}_s}{\mathcal{M}_S}\right)^{\frac{1}{4}}\right]^2 \tag{2.18}$$

$$\kappa = \sum_{S=0}^{N_s} \frac{c_S \kappa_S}{\Phi_S} \qquad \text{with} \quad \Phi_S = \sum_{s=0}^{N_s} c_s \sqrt{\frac{\mathcal{M}_s}{\mathcal{M}_S}} \tag{2.19}$$

with species concentration $c_s = \frac{\rho_s}{\mathcal{M}_s}$. This avoids the time-consuming computation of the collision integrals during the simulations while still maintaining accurate descriptions of the transport properties for each species.

2.3 Chemical reactions

The chemical source term ω_s in equation (2.2) describes the rate of production or destruction for each species due to chemical reactions whereas the reaction heat is indirectly incorporated by including the formation energy in equation (2.9). It is the consequence of a set of chemical reactions, where each reaction r is associated with stoichiometric coefficients α^r and β^r for forward and backward reaction, respectively. This can be described by a chemical equation that symbolically represents the specific reaction as

$$\sum_{s=1}^{N_s} \alpha_s^r X_s \longleftrightarrow \sum_{s=1}^{N_s} \beta_s^r X_s \tag{2.20}$$

where X_s are the different species molceules (i.e. O_2, O, H_2O, etc.). For the considered reactions the number of involved species is either two or three and all stoichiometric coefficients of non-

involved species are zero.

The chemical source term for species X_s can be calculated from the law of mass action as the sum over all reactions N_r:

$$\omega_s = \mathcal{M}_s \sum_{r=1}^{N_r} (\beta_s^r - \alpha_s^r) \left[k_r^f \prod_{S=1}^{N_s} (c_S)^{\alpha_S^r} - k_r^b \prod_{S=1}^{N_s} (c_S)^{\beta_S^r} \right]. \tag{2.21}$$

Using the modified Arrhenius equation the forward and backward reaction rates are

$$k_r^f = A_r T^{b_r} \exp\left(\frac{-E_r}{T}\right) \qquad k_r^b = \frac{k_r^f}{K_r^{eq}} \tag{2.22}$$

where A_r, b_r, E_r and K_r^{eq} are reaction dependent coefficients. Third body efficiencies are included in the coefficient A_r by multiplying it with the respective third body efficiency of the different passive species.

The reaction mechanism used in Chapter 5 is detailed in appendix C. For further details the reader is referred to the literature (e.g. Gerlinger [13]).

2.4 Turbulence

To quantify the ratio between inertial and viscous forces in the flow the dimensionless Reynolds number is introduced as

$$\mathrm{Re} = \frac{\rho U L}{\mu} \tag{2.23}$$

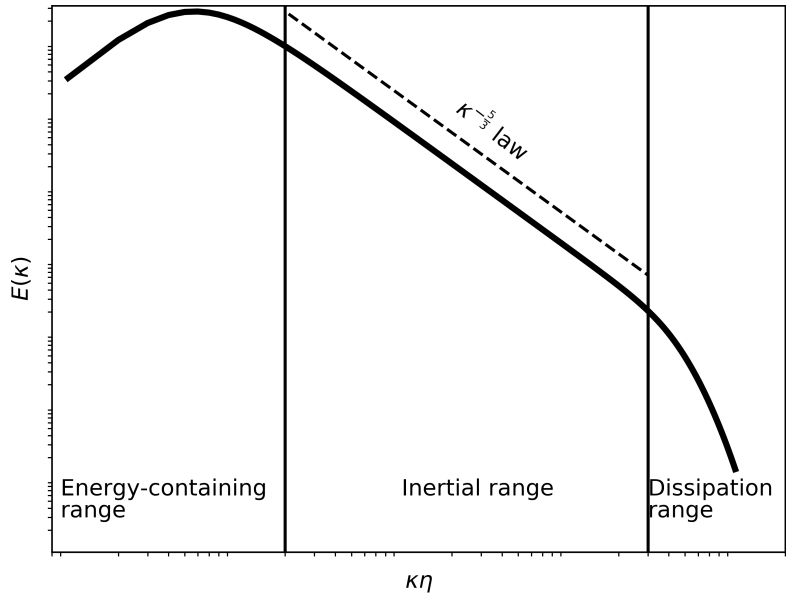

Figure 2.1: Isotropic turbulence energy spectrum.

with a characteristic length scale L and characteristic velocity U. For low Reynolds numbers the flow is typically laminar ("layered") with layers of different velocities flowing parallel and without much interaction between each other. If the Reynolds number is increased the non-linear terms in the Navier-Stokes equations gain importance and perturbations to the layered flow can be observed. An increase in Reynolds number beyond a certain flow dependent threshold moves the flow into the turbulent regime where the laminar layers are destroyed by chaotic fluctuations in the flow that also lead to additional mass, momentum and heat transport in the direction of mean velocity gradients [43].

The turbulent fluctuations are random and chaotic in nature and cover a wide range of scales. For isotropic flows in turbulent equilibrium the distribution of turbulent fluctuations of different scales can be described by an energy spectrum as seen in Fig. 2.1. The wave number is defined as $k = \frac{2\pi}{\lambda}$ where λ is the characteristic size of the turbulent structure. Turbulent structures, also referred to as eddies, are typically created at large scales in the order of the geometry of the considered flow problem and receive their energy from the mean flow by turbulence production processes. Through (mostly inviscid) interactions with other eddies an energy transfer to smaller and smaller scales occurs and the initially high anisotropy of eddies is reduced. The smaller the eddies become the more they are affected by viscous effects and consequently more turbulent energy is dissipated into heat at smaller scales. This process is called the Turbulent Energy Cascade [43]. The different regions of the spectrum in Fig. 2.1 are typically described as the Energy-containing range - containing the largest, often anisotropic, and most energetic eddies -, the inertial range - in which interactions between eddies lead to smaller and smaller scales - and the dissipation range - in which eddies become small enough to be significantly affected by viscous effects and dissipate kinetic to thermal energy. The size of the inertial subrange, and thus the distance in terms of wave number between the energy containing and the dissipation range, increases with the Reynolds number. Furthermore, in the inertial subrange the energy follows the $k^{-\frac{5}{3}}$-law [43].

In accordance with this, Kolomogorov's equilibrium theory assumes that for high enough Reynolds numbers the transfer from large to small scales occurs only due to inviscid effects and energy dissipation mainly affects the smallest scales. In this case the energy dissipation rate at the smallest scales has to be equal to the rate of energy supply of the medium scales as well as to turbulent production rate at the largest scales.

Then the Kolmogorov length, velocity and time scale of the smallest scales can be determined purely as a function of kinematic viscosity $\nu = \frac{\mu}{\rho}$ and dissipation rate ε as [43]

$$\eta = \left(\frac{\nu^3}{\varepsilon}\right)^{\frac{1}{4}} \qquad u_\nu = (\varepsilon\nu)^{\frac{1}{4}} \qquad \tau_\nu = \left(\frac{\nu}{\varepsilon}\right)^{\frac{1}{2}}. \tag{2.24}$$

To completely describe a turbulent flow all scales have to be resolved down to the Kolomogorov

scale. If all scales of the flow are captured in a numerical computation this method is called Direct Numerical Simulation (DNS). However, the computational effort strongly increases if flows at high Reynolds number and/or complex geometries are considered since the number of numerical grid points required to resolve all scales increases as approximately $N \sim \mathrm{Re}^{37/14}$ for wall bounded flows [5]. Hence, currently DNS can only be applied to limited Reynolds number ranges and/or relatively small domain sizes - unless large amounts of computational resources are available.

Alternatively, all or part of the turbulent contributions can be modelled, leading to less strict requirements on the grid resolution. If the whole turbulent spectrum is modelled and only the mean flow is resolved, this method is called Reynolds-Averaged Navier-Stokes (RANS) simulation. The RANS equations will be derived below and the used RANS turbulence models are detailed in Sec. 3.4.

As described above, the largest eddies are both the most anisotropic, and thus flow dependent, and contain the most energy. This makes them on the one hand the most difficult to model and on the other the most important to capture correctly. In Large Eddy Simulations (LES) the largest eddies are resolved by the grid and numerical scheme and only the smaller - more isotropic and less flow dependent - eddies require modelling. This increases the accuracy of the results and also allows for e.g. an analysis of the unsteady turbulent features of the flow, but obviously also increases the required computational resources in comparison to RANS simulations. This is especially true in the boundary layer region near the wall, where the finest grid resolution is required. Depending on the approach used in the boundary layer a further distinction exists between wall-resolved and wall-modelled LES. The former resolves the largest eddies down to the wall of a turbulent boundary layer and the latter uses some kind of model near the wall to reduce resolution requirements. These models can, for example, consist of traditional wall models or RANS turbulence models that are activated near the wall [43].

There also exist methods combining RANS and LES approaches in which parts of the flow domain that are less important or feature less complex flow phenomena are handled with RANS and regions with large flow separation or in which detailed spectral information is required by LES. These methods are commonly referred to as Hybrid RANS-LES Methods (HRLM). Several different approaches to hybrid RANS-LES modelling with their respective advantages and disadvantages exist and the one used in the present thesis is presented in Sec. 3.4.

In the following the RANS and the filtered Navier-Stokes equations (that are the basis for RANS simulations and LES, respectively) are derived.

2.4.1 Reynolds-Averaging and Filtering

Using Reynolds-averages any flow quantity can be decomposed into a mean and a fluctuating part as $\Phi = \overline{\Phi} + \Phi'$ using

$$\overline{\Phi}(x,t) = \lim_{\Delta t \to \infty} \frac{1}{\Delta t} \int_t^{t+\Delta t} \Phi(x,t')dt'. \tag{2.25}$$

Even though $\overline{\Phi}$ is technically independent of time, it can be used for unsteady flows - sometimes denoted as Unsteady RANS or URANS - as well if there is a spectral gap, i.e. the smallest time scale of global unsteady motions $\Delta_{unsteady}$ is much larger than the largest time scale of turbulent fluctuations $\Delta_{fluctuations}$. Then it is possible to find an averaging period Δt so that

$$\Delta_{fluctuations} << \Delta t << \Delta_{unsteady}. \tag{2.26}$$

Averaged quantities possess the following properties:

$$\overline{\Phi'} = 0 \qquad \overline{\overline{\Phi}} = \overline{\Phi} \qquad \overline{\frac{\partial \Phi}{\partial x_j}} = \frac{\partial \overline{\Phi}}{\partial x_j} \qquad \overline{\frac{\partial \Phi}{\partial t}} = \frac{\partial \overline{\Phi}}{\partial t} \qquad \overline{\Phi_1 \Phi_2} = \overline{\Phi}_1 \overline{\Phi}_2 + \overline{\Phi'_1 \Phi'_2}. \tag{2.27}$$

For flows with constant density this is sufficient. However, in order to avoid additional unclosed terms arising from fluctuating quantities in compressible flows density-weighted averages, or Favre-averages, are introduced. With these a flow quantity can be decomposed as $\Phi = \widetilde{\Phi} + \Phi''$ using

$$\widetilde{\Phi} = \frac{\overline{\rho \Phi}}{\overline{\rho}}. \tag{2.28}$$

The following properties apply to Favre-averaged quantities:

$$\begin{array}{lllll} \widetilde{\Phi''} = 0 & \widetilde{\widetilde{\Phi}} = \widetilde{\Phi} & \widetilde{\frac{\partial \Phi}{\partial x_j}} = \frac{\partial \widetilde{\Phi}}{\partial x_j} & \widetilde{\frac{\partial \Phi}{\partial t}} = \frac{\partial \widetilde{\Phi}}{\partial t} & \widetilde{\Phi_1 \Phi_2} = \widetilde{\Phi}_1 \widetilde{\Phi}_2 + \widetilde{\Phi''_1 \Phi''_2} \\ \overline{\rho \Phi''} = 0 & \overline{\Phi''} = -\frac{\overline{\rho' \Phi'}}{\overline{\rho}} & \overline{\widetilde{\Phi}} = \widetilde{\Phi} & \overline{\rho \Phi} = \overline{\rho} \widetilde{\Phi} & \overline{\rho \Phi_1 \Phi_2} = \overline{\rho} \widetilde{\Phi}_1 \widetilde{\Phi}_2 + \overline{\rho \Phi''_1 \Phi''_2} \end{array}. \tag{2.29}$$

Averaging the equations of motion and using the above properties the RANS equations can be derived as (see appendix A for details)

$$\frac{\partial \overline{\rho}}{\partial t} + \frac{\partial}{\partial xj}(\overline{\rho} \widetilde{u}_j) = 0 \tag{2.30}$$

$$\frac{\partial}{\partial t}(\overline{\rho} \widetilde{Y}_s) + \frac{\partial}{\partial x_j}(\overline{\rho} \widetilde{u}_j \widetilde{Y}_s) = -\frac{\partial}{\partial x_j}(\overline{\rho u_j Y_s} - \overline{\rho} \widetilde{u}_j \widetilde{Y}_s) - \frac{\partial \overline{J}_{s,j}}{\partial x_j} + \overline{\omega}_s \tag{2.31}$$

$$\frac{\partial}{\partial t}(\overline{\rho} \widetilde{u}_i) + \frac{\partial}{\partial x_j}(\overline{\rho} \widetilde{u}_i \widetilde{u}_j) + \frac{\partial \overline{p}}{\partial x_i} = \frac{\partial \overline{\sigma}_{ij}}{\partial x_j} - \frac{\partial \tau_{ij}}{\partial x_j} + \overline{\rho f_i} \tag{2.32}$$

$$\begin{aligned} \frac{\partial}{\partial t}(\overline{\rho} \widetilde{E}) + \frac{\partial}{\partial x_j}(\overline{\rho} \widetilde{H} \widetilde{u}_j) = &-\frac{\partial \overline{q}_j}{\partial x_j} + \frac{\partial}{\partial x_j}(\widetilde{u}_i \overline{\sigma}_{ij} + \overline{u''_i \sigma_{ij}}) \\ &- \frac{\partial}{\partial x_j}(\overline{\rho u_i u_i u_j} - \overline{\rho u_i u_i} \widetilde{u}_j) - \frac{\partial}{\partial x_j}\left(\overline{\rho h u_j} - \overline{\rho} \widetilde{h} \widetilde{u}_j\right) + \overline{\rho u_i f_i}. \end{aligned} \tag{2.33}$$

These equations look very similar to the instantaneous equations (2.1) to (2.4), but introduce new terms that appear due to interactions of fluctuating quantities. To close the equations the additional terms need to be modelled. The first of these terms occurs in the mass fraction equation and describes the additional mass fraction transport due to turbulent fluctuations. This term is usually modelled using a gradient diffusion approach analogous to the molecular diffusive transport as

$$\overline{\rho u_j Y_s} - \overline{\rho}\widetilde{u}_j\widetilde{Y}_s = \overline{\rho u_j'' Y_s''} \approx -\overline{\rho}\mathcal{D}_t\frac{\partial\widetilde{Y}_s}{\partial x_j} = -\frac{\mu_t}{Sc_t}\frac{\partial\widetilde{Y}_s}{\partial x_j} \tag{2.34}$$

with turbulent diffusivity $\mathcal{D}_t$, turbulent Schmidt number $\mathrm{Sc}_t = \frac{\mu_t}{\rho\mathcal{D}_t}$ in which the turbulent viscosity μ_t appears that is computed as part of the turbulence model in Sec. 3.4. Similarly a turbulent Prandtl number $\mathrm{Pr}_t = \frac{\mu_t c_p}{\kappa_t}$ can be defined. Typically Pr_t and Sc_t are assumed to be constant and between 0.5 and 1, depending on the considered flow topology and species involved.

The other term in the mass fraction equation is the average of the molecular diffusion mass flux $\overline{J}_{s,j}$. For this term it is assumed that it is well represented by the molecular diffusion flux calculated from the (Favre-)averaged density and mass fraction as

$$\overline{J}_{s,j} \approx -\overline{\rho}\mathcal{D}\frac{\partial\widetilde{Y}_s}{\partial x_j}. \tag{2.35}$$

Additionally, the average mass source term due to reactions needs to be defined. For complex chemical reaction schemes that are highly dependent on turbulent interactions, models are available that try to capture this behaviour (e.g. using probability density functions) [13]. In the current thesis the term is modelled as a function of the (Favre-)averaged quantities and the effect of fluctuations is neglected. Hence

$$\overline{\omega}_s \approx \omega_s\left(\overline{\rho}, \widetilde{Y}_s, \widetilde{T}\right). \tag{2.36}$$

The momentum equations yield two new unknowns: the averaged viscous stress tensor $\overline{\sigma_{ij}}$ and the Reynold stress tensor $\tau_{ij}^{RANS} = \overline{\rho u_i'' u_j''}$. The former is usually approximated by neglecting fluctuations in viscosity and replacing Reynolds-averages by Favre-averages as

$$\overline{\sigma_{ij}} \approx 2\mu\left(\widetilde{S}_{ij} - \frac{\delta_{ij}}{3}\frac{\partial\widetilde{u}_k}{\partial x_k}\right). \tag{2.37}$$

The latter describes the effect of velocity fluctuations on the mean flow and can be interpreted as an additional stress term, hence the name Reynolds stresses or turbulent stresses. Details about the modelling will be given in Sec. 3.4.

The averaged heat flux $\overline{q}_j$ in the energy equation is approximated analogously to the viscous stresses (i.e. neglecting fluctuations and replacing Reynolds- with Favre-averages) as

$$\overline{q}_j \approx -c_p \frac{\mu}{Pr} \frac{\partial \widetilde{T}}{\partial x_j} - \frac{\mu}{Sc} \sum \widetilde{h}_s \frac{\partial \widetilde{Y}_s}{\partial x_j}. \tag{2.38}$$

The term originating from the kinetic energy can be written as

$$\overline{\rho u_i u_i u_j} - \overline{\rho u_i u_i} \widetilde{u}_j = \widetilde{u}_i \overline{\rho u_i'' u_j''} + \frac{1}{2} \overline{\rho u_i'' u_i'' u_j''} = \widetilde{u}_i \tau_{ij}^{RANS} + \frac{1}{2} \overline{\rho u_i'' u_i'' u_j''}. \tag{2.39}$$

The first term in this expression that contains the Reynolds stress tensor can be computed using the turbulence models described in Sec. 3.4. The second term describes molecular diffusion of turbulent kinetic energy and can be modelled together with the turbulent transport of turbulent kinetic energy using a gradient diffusion approach leading to

$$\frac{1}{2} \overline{\rho u_i'' u_i'' u_j''} - \overline{u_i'' \sigma_{ij}} \approx - \left(\mu + \frac{\mu_t}{\sigma_k} \right) \frac{\partial \widetilde{k}}{\partial x_j} \tag{2.40}$$

where σ_k is a dimensionless model constant and $\widetilde{k} = \frac{1}{2} \frac{\tau_{ii}}{\overline{\rho}}$ is the turbulent kinetic energy. The last term that requires modelling is the heat transport due to turbulent fluctuations which is modelled as

$$\overline{\rho h u_j} - \overline{\rho} \widetilde{h} \widetilde{u}_j = \overline{\rho h'' u_j''} \approx -c_p \frac{\mu_t}{Pr_t} \frac{\partial \widetilde{T}}{\partial x_j} - \frac{\mu_t}{Sc_t} \sum h_s \frac{\partial \widetilde{Y}_s}{\partial x_j}. \tag{2.41}$$

As mentioned above, in RANS simulations all turbulent scales are modelled, but in LES the largest turbulent scales are resolved and only the smaller scales are modelled. With a similar notation to the RANS approach, in LES the flow field is decomposed into resolved and unresolved contributions. Mathematically, this is done by filtering the equations of motion and decomposing quantities into spatially low-pass filtered and high-pass filtered parts as

$$\Phi = \overline{\Phi} + \Phi' \quad \text{and} \quad \Phi = \widetilde{\Phi} + \Phi'' \tag{2.42}$$

where the low-pass filtered field can be described by a convolution integral

$$\overline{\Phi}(x,t) = \int_\Omega G(x - x') \Phi(x,t) dx' \qquad \text{with} \int_\Omega G(x - x') dx' = 1 \tag{2.43}$$

and Favre-filtered quantities are again described by equation (2.28), with the overbar indicating filtering instead of averaging now. Instead of an explicit filter implicit filtering by means of the spatial discretization is used since in a finite-volume approach

$$\Phi(x,t) = \frac{1}{|V|} \int_V \Phi(x',t) dx' \qquad \text{with } |V| = \int_V dx' = 1. \tag{2.44}$$

with cell volume V. This corresponds to a filter as in equation (2.43) that vanishes outside of V [46].

Unlike in RANS, the properties for consecutive filtering of quantities do not apply in general (i.e. for a general filter $\overline{\overline{\Phi}} \neq \overline{\Phi}$ and $\overline{\Phi'} \neq 0$). This leads to additional contributions in terms featuring multiplication of two quantities as can be seen by a comparison of averaged and filtered quantities:

$$\overline{\rho\Phi_1\Phi_2}^{RANS} = \overline{\rho}\widetilde{\Phi_1}\widetilde{\Phi_2} + \overline{\rho\Phi_1''\Phi_2''} \qquad \overline{\rho\Phi_1\Phi_2}^{LES} = \overline{\rho\widetilde{\Phi_1}\widetilde{\Phi_2}} + \overline{\rho\widetilde{\Phi_1}\Phi_2''} + \overline{\rho\Phi_1''\widetilde{\Phi_2}} + \overline{\rho\Phi_1''\Phi_2''} \quad (2.45)$$

However, the equations of motion (equations (2.30) to (2.33)) remain unchanged by replacing the RANS Reynolds stresses by their LES counterparts

$$\begin{aligned} \tau_{ij}^{LES} &= \overline{\rho\widetilde{u}_i\widetilde{u}_j} + \overline{\rho\widetilde{u}_i u_j''} + \overline{\rho u_i''\widetilde{u}_j} + \overline{\rho u_i'' u_j''} - \overline{\rho}\widetilde{u}_i\widetilde{u}_j \\ &= \underbrace{\overline{\rho\widetilde{u}_i\widetilde{u}_j} - \overline{\rho}\widetilde{u}_i\widetilde{u}_j}_{L_{ij}} + \underbrace{\overline{\rho\widetilde{u}_i u_j''} + \overline{\rho u_i''\widetilde{u}_j}}_{C_{ij}} + \underbrace{\overline{\rho u_i'' u_j''}}_{R_{ij}}. \end{aligned} \quad (2.46)$$

Here $\boldsymbol{L}$ is called the Leonard term that is associated with the resolved scale interactions, $\boldsymbol{C}$ the cross term that represents interactions between resolved and non-resolved scales and $\boldsymbol{R}$ the Reynolds term which, as in RANS, describes the interactions between non-resolved scales [43]. Even though the simplifications in equations (2.34), (2.39) and (2.41) are technically only valid for the averaged equations, the respective modelling of these terms can be applied to the filtered equations as well and is assumed in the scope of the hybrid RANS/LES model presented in Sec. 3.4.

2.5 Integral form of the conservation equations

The resulting system of equations can also be written in integral form which leads to a more concise formulation and derivation of the used numerical algorithm in Chapter 3.

Applying Gauss' theorem to the integral over a control volume V one obtains

$$\int_V (\nabla \boldsymbol{F})\, dV = \int_{\partial V} (\boldsymbol{F}\underline{n})\, dS \quad (2.47)$$

where $S = \partial V$ is the boundary of the control volume and $\underline{n}$ is the outward-pointing unit normal vector of ∂V.

Using this the following notation for equations (2.30) to (2.33) can be used:

$$\frac{\partial}{\partial t}\int_V \underline{U}\, dV = -\int_{\partial V} \boldsymbol{F}^{tot}\underline{n}\, dS + \int_V \underline{Q} dV = -\int_{\partial V} \boldsymbol{F}^{Eu}\underline{n} + \boldsymbol{F}^{NS}\underline{n}\, dS + \int_V \underline{Q} dV \quad (2.48)$$

with $\underline{U} = \left(\overline{\rho}\widetilde{Y}_s, \overline{\rho}\widetilde{\underline{u}}, \overline{\rho}\widetilde{E}\right)^T$, i.e. the mass conservation equation (2.30) is dropped, but all species conservation equations are used.

The inviscid fluxes $\boldsymbol{F}^{Eu}$ and the viscous fluxes $\boldsymbol{F}^{NS}$ are defined as

$$\boldsymbol{F}^{Eu} = \begin{pmatrix} \overline{\rho}\widetilde{Y}_s\widetilde{\underline{u}}^T \\ \overline{\rho}\widetilde{\underline{u}}\,\widetilde{\underline{u}}^T + \overline{p}\boldsymbol{I} \\ \overline{\rho}\widetilde{H}\widetilde{\underline{u}}^T \end{pmatrix} \tag{2.49}$$

$$\boldsymbol{F}^{NS} = \begin{pmatrix} \mathcal{D}_{tot}\nabla\widetilde{Y}_s \\ \overline{\boldsymbol{\sigma}} - \boldsymbol{\tau} \\ \kappa_{tot}\nabla\widetilde{T} + \mathcal{D}_{tot}\sum_{s=0}^{n}\widetilde{h}_s\nabla\widetilde{Y}_s + \mu_k\nabla\widetilde{k} + \left(\left(\overline{\boldsymbol{\sigma}} - \boldsymbol{\tau}\right)\widetilde{\underline{u}}\right)^T \end{pmatrix} \tag{2.50}$$

with $\kappa_{tot} = \kappa + \kappa_t = \frac{\mu}{\mathrm{Pr}} + \frac{\mu_t}{\mathrm{Pr}_t}$, $\mathcal{D}_{tot} = \mathcal{D} + \mathcal{D}_t = \frac{\mu}{\mathrm{Sc}} + \frac{\mu_t}{\mathrm{Sc}_t}$ and $\mu_k = \mu + \frac{\mu_t}{\sigma_k}$ for a more concise notation.

The source term vector follows as $\underline{Q} = \left(\overline{\omega_s}, \overline{\rho\underline{f}}, \overline{\rho\underline{u}^T\underline{f}}\right)^T$.

Since in the rest of this thesis only the averaged/ filtered variables are considered the notation for the instantaneous variables will be used for averaged and filtered variables for better readability (i.e. overbars and tildes are dropped) unless specifically stated otherwise.

3 Numerical Methods

This chapter describes the numerical methods that are used in the computations. All Computations employ the DLR TAU-Code (TAU) [15]. TAU is a second-order finite volume solver developed at the German Aerospace Center (DLR) and is used in flow regimes from subsonic to hypersonic flows in research, aircraft design and other industry applications. In the following the description of how equation (2.48) is discretized and solved numerically in TAU is presented. At the end of the chapter a short description of the tools used to analyse the obtained unsteady flow field data is presented as well.

3.1 Domain discretization

The computational domain is discretized using a primary grid that can consist of hexahedra, tetrahedra, pyramids and prisms. In a preprocessing step a dual grid is generated from the primary grid that introduces control volumes around each point P_I of the primary grid, allowing for each control volume to be uniquely referred to by P_I. For the construction of the dual grid cells the center of the edge between two primary grid points is required as well as the centers of the primary grid cells connected to that edge. For each primary grid cell two triangular boundaries associated with the two grid points can be constructed using the edge center, the cell center and the two respective primary grid face center points. Subsequently all boundaries between two points are merged together to one face for which a normal vector $\underline{n}$ is defined by the sum of the normal vectors of the merged boundaries. To avoid sharp angles the calculation of the centres of the primary grid edges, faces and and cells is optimised by different point weights. Details about this procedure can be found in the literature (e.g. [24, 46]).

Considering one of the resulting dual grid volume elements with volume V_I, equation (2.48) can be discretized as

$$\frac{\partial \underline{U}_I}{\partial t} = -\frac{1}{V_I}\sum_{f=1}^{N_f} \boldsymbol{F}_f^{tot}\underline{n}_f = -\frac{1}{V_I}\sum_{f=1}^{N_f} A_f \boldsymbol{F}_f^{tot}\underline{\hat{n}}_f \tag{3.1}$$

where N_f is the number of faces of the volume element, A_f is the area of face f and $\underline{\hat{n}}_f$ is the unit normal vector of face f.

3.2 Temporal discretization

In order to discretize the left hand side of equation (3.1) a time stepping scheme has to be employed. To simplify the following notation, the equation can also be written as

$$\frac{\partial \underline{U}_I}{\partial t} = -\underline{R}(\underline{U}) \tag{3.2}$$

where $\underline{R}(\underline{U})$ is called the residual and consists of all spatially discretized terms on the right hand side of equation (3.1).

For all computations in the present thesis a dual time stepping scheme is used that employs a backward difference formula (BDF) for the discretization of the time derivative. The second-order BDF formula leads to the following expression:

$$\frac{3}{2\Delta t}\underline{U}^{n+1} - \frac{2}{\Delta t}\underline{U}^{n} + \frac{1}{2\Delta t}\underline{U}^{n-1} = -\underline{R}(\underline{U}^{n+1}) \tag{3.3}$$

where Δt is the time step size and superscript n denotes the current time step. Rewriting this equation under introduction of a pseudo time t^* a steady-state problem of the form

$$\frac{d\underline{U}^{n+1}}{dt^*} = -\left(\underline{R}(\underline{U}^{n+1}) + \frac{3}{2\Delta t}\underline{U}^{n+1} - \frac{2}{\Delta t}\underline{U}^{n} + \frac{1}{2\Delta t}\underline{U}^{n-1}\right) = -R^{DTS}(\underline{U}^{n+1}) \tag{3.4}$$

can be obtained. This equation can be solved using techniques for steady-state systems including local time stepping, residual smoothing and preconditioning techniques [22, 27, 45]. For the convergence of the steady state problem a Lower-Upper Symmetric Gauss-Seidel (LU-SGS) scheme [10] or a three-stage explicit Runge-Kutta scheme is used. One iteration of the respective scheme is referred to as an inner iteration in the following.

Ideally the dual time stepping residual R^{DTS} would approach zero for the inner iterations to be considered converged. In practice, iterations are usually stopped once $R^{DTS} < \epsilon$ where ϵ is a user defined small number. For simple cases ϵ can be chosen very small, optimally in the order of the machine precision, to judge proper convergence. However, for more complex flows this procedure is overly conservative and instead the convergence can be judged using a Cauchy criterion to test whether significant flow variables are converged. In TAU the convergence of a variable Φ at inner iteration i over the last N_{cauchy} inner iterations can be tested as

$$\frac{|\Phi^{(i)} - \Phi^{(i-k)}|}{|\Phi|} < \epsilon_{cauchy} \qquad \forall k = 1, ..., (N_{cauchy}) \tag{3.5}$$

where ϵ_{cauchy} is a user-defined threshold. Using a higher number N_{cauchy} and a lower threshold ϵ_{cauchy} the convergence criterion can be tuned to be more conservative. In the present thesis several variables are tested for convergence and convergence has to be reached for all tested variables for the inner iterations to be considered converged, with typical values being

$N_{cauchy} = 10 \dots 20$ and $\epsilon_{cauchy} = 10^{-6} \dots 10^{-5}$. The used variables are global values like the drag coefficient, the mean resolved kinetic energy, vorticity magnitude and velocity skewness as well as local values like the maximum eddy viscosity and the maximum non-dimensional first wall distance.

3.3 Spatial discretization

Since the flow variables in a finite volume approach are constant within each volume element there may be a discontinuity at the faces between two cells. Consequently, the flux vector $\boldsymbol{F}_f^{tot}\underline{\hat{n}}_f$ over face f cannot be computed directly, but has to be spatially discretized and must be computed from the states on one or both sides of the face. In the current thesis the inviscid fluxes $\boldsymbol{F}_f^{Eu}\underline{\hat{n}}_f$ are computed using a central scheme with matrix dissipation, the viscous fluxes $\boldsymbol{F}_f^{NS}\underline{\hat{n}}_f$ are computed using a gradient reconstruction described below and the turbulent fluxes are computed using Roe's scheme [48].

3.3.1 Central scheme with matrix dissipation

Due to their good dissipation properties central schemes are very suitable for the use in scale resolving simulations. With a central scheme the flux through a face can be described as

$$\boldsymbol{F}_f^{Eu}\underline{\hat{n}}_f = \underline{H}_f^{conv} - \underline{D}_f \tag{3.6}$$

where $\underline{H}_f^{conf}$ is the convective flux approximation and $\underline{D}_f$ is a matrix dissipation term used to stabilize the computation.

The used convective flux approximation is a skew-symmetric scheme developed by Kok [26] with Low-Dissipation Low-Dispersion settings [29]. With this the computation of the convective flux reads

$$\underline{H}_f^{conv} = \begin{pmatrix} \dot{m}_s \\ \dot{m}\frac{1}{2}(\underline{u}^L + \underline{u}^R) + \frac{1}{2}(p^L + p^R)\underline{\hat{n}} \\ \dot{m}(e_f^{kin} + e_f^{int}) + \sum_{s=1}^{N_s} \dot{m}_s e_s^0 + \frac{1}{2}(v_n^L p^R + v_n^R p^L) \end{pmatrix} \tag{3.7}$$

with the mass fluxes

$$\dot{m}_s = \frac{1}{2}(\rho_s^L v_n^L + \rho_s^R v_n^R) \qquad \text{and} \qquad \dot{m} = \sum_{s=1}^{N_s} \dot{m}_s \tag{3.8}$$

with the face normal velocity $v_n = \underline{u}\,\underline{\hat{n}}$ and superscripts L and R denoting the left and right state, respectively. This formulation ensures local and global conservation of kinetic energy and pressure [26] by splitting the transported energy into internal and kinetic energy and using

geometric means for the computation of the face values. In the original literature [26, 29] this concept is only applied to single-species flows without reactions, for which the internal energy does not contain the formation enthalpy. For multi-species flows the mass flux can straightforwardly be extended to incorporate contributions from all species as in equation (3.8). However, if a species has a non-zero enthalpy of formation, this enthalpy has to be subtracted from the internal energy and be added separately to ensure that the transported enthalpy of formation correctly corresponds to the transported species mass fluxes and only the sensible internal energy is averaged at the face. Using this the definition of internal and kinetic energy at the face follows as

$$e_f^{kin} = \frac{1}{2}\left(\underline{u}^L \underline{u}^R\right) \tag{3.9}$$

$$e_f^{int} = \sqrt{\left(e^L - \sum_{s=1}^{N_s} Y_s^L e_s^0\right)\left(e^R - \sum_{s=1}^{N_s} Y_s^R e_s^0\right)}. \tag{3.10}$$

To improve the dispersive properties of the scheme the velocities and pressure are extrapolated before using them in equation (3.7) as

$$\Phi^L = \Phi^l + \alpha_\Phi \nabla\Phi^l d \tag{3.11}$$

$$\Phi^R = \Phi^r + \alpha_\Phi \nabla\Phi^r d \tag{3.12}$$

where Φ^l and Φ^r are the non-extrapolated values at the left and right of the face, respectively, and d is the distance between both involved cell centers. For $\alpha = 0.36$ optimal dispersion properties are obtained. Note that neither density nor speed of sound are extrapolated [29].

The matrix dissipation contribution [22, 31] for face f is computed as

$$\underline{D}_f = \boldsymbol{\alpha}\left(\Psi\left(\underline{U}^l - \underline{U}^r\right) + k^{(4)} sc_4 \left(\Psi - 1\right)\left(1 + \frac{2\Phi_f^l \Phi_f^r}{\Phi_f^l + \Phi_f^r}\right)\left(\nabla^2\underline{U}^l - \nabla^2\underline{U}^r\right)\right) \tag{3.13}$$

where $\boldsymbol{\alpha}$ is the matrix dissipation operator, Ψ a pressure sensor, $k^{(4)}$ a dissipation coefficient, sc_4 a scaling factor for the number of cell faces, Φ_f is a cell stretching indicator and $\nabla^2\underline{U}$ is the Laplacian of the conservative variables. Note that for all terms in the computation of the artificial dissipation the non-extrapolated values (i.e. before application of equations (3.11)

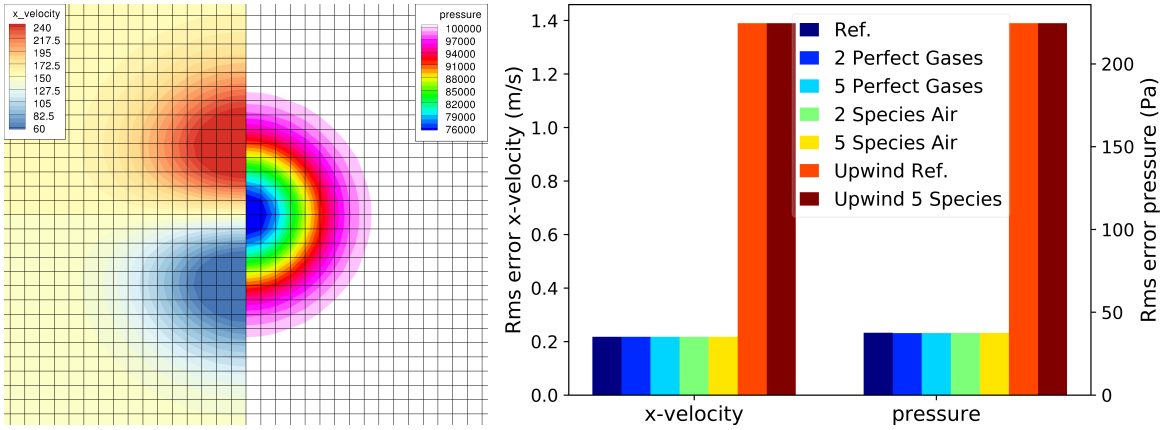

Figure 3.1: Initial solution of horizontal velocity and pressure (left) and comparison of errors between different schemes (right) for the vortex transport test case.

and (3.12)) are used. The individual terms are computed as

$$\Psi = \min(\varepsilon_\Psi \cdot \max(\Psi^l, \Psi^r), 1) \qquad \text{with} \qquad \Psi^i = \left| \frac{\sum_{k=1}^{N_{neigh}} (p^i - p^k)}{\sum_{k=1}^{N_{neigh}} (p^i + p^k)} \right| \tag{3.14}$$

$$sc_4 = \frac{9}{N^l_{neigh}(1 + N^l_{neigh})} + \frac{9}{N^r_{neigh}(1 + N^r_{neigh})} \tag{3.15}$$

$$\Phi_f^{l/r} = 0.5 \cdot \max\left(0, \frac{\lambda_c^{l/r} - \lambda_c^f}{\lambda_c^f}\right) \tag{3.16}$$

where λ_c are the maximum eigenvalues of the flux Jacobian and N_{neigh} is the number of neighboring points. The pressure sensor Ψ leads to a formulation that mimics a first order Roe scheme in the vicinity of shocks and thus reduces unphysical oscillations in these regions. The behaviour can be tuned with the parameter ε_Ψ where a lower value leads to lower dissipation, but less stable behaviour. The scaling factor sc_4 scales the dissipation with the number of faces to ensure that the same amount of dissipation is added in structured and unstructured grids. The term Φ_f scales the dissipation as a function of the cell aspect ratio to increase stability in regions with high aspect ratio cells.

The matrix dissipation operator $\boldsymbol{\alpha}$ is the derivative of the convective flux with respect to the conservative variables and also includes a preconditioning matrix that improves the accuracy of the added artificial dissipation in the limit of $M \to 0$. Details about the matrix dissipation operator and the preconditioning procedure, including the extension for multi-species mixtures and general equations of state, are detailed in appendix D.

Figure 3.1 shows the results of the implementation of the extended central flux and precon-

ditioning scheme for different chemistry schemes for the convective vortex transport test case [29]. In this 2D test case a vortex is inviscidly convected through the computational domain which allows to determine an analytical solution for a given time difference. On the left of the figure the initial field for horizontal velocity and pressure is displayed and on the right the errors from the analytical solution in both variables after the vortex has been transported are visible. The reference is the previous implementation using just one perfect gas which was validated by Löwe et al. [29]. Next the results for 2 and 5 equal perfect gases, respectively, with uniform decomposition and without formation energy are shown and the difference is essentially indistinguishable. The next two cases are realistic air as described in appendix C, considering 2 species (N_2, O_2) and 5 species (N_2, O_2, N, O, NO), respectively, with a realistic decomposition (i.e. $Y_{N_2} = 0.76$, $Y_{O_2} = 0.24$ and trace amount of N, O, NO), but without reactions. The agreement is again very good. The remaining small deviations can be attributed to slightly different gas properties and differences in the exact numerical operations. The latter are introduced by e.g. summation errors or different derivative computations for more complex fluid models. For comparison the errors using the upwind scheme AUSMDV [69] are included as well. It is visible that the errors are significantly larger, showing the superiority of the used central scheme and the retained qualities with the multispecies implementation.

Probst et al. [44] also propose a hybrid blending of certain parameters that increase stability in the RANS regions, but allow for high accuracy and low dissipation in the LES regions. The hybrid blending function is applied to the parameters listed in Table 3.1. The parameter "Low dispersion" indicates whether equations (3.11) and (3.12) are used and the last parameter indicates the threshold for an entropy fix that is used to correct the eigenvalues.

3.3.2 Approximation of viscous fluxes

The terms in the viscous fluxes (equation (2.50)) that have to be discretized are functions of the gradients of velocity, temperature, partial densities or kinetic turbulent energy. The gradients of quantity Φ in cell I can be computed using the Green-Gauss divergence theorem as

$$\nabla\Phi = (\Phi_x, \Phi_y, \Phi_z) = \frac{1}{V_I} \sum_{j=1}^{N_f} A_f \frac{1}{2} (\Phi_j + \Phi_I)\, \underline{\hat{n}} \tag{3.17}$$

Parameter	$k^{(4)}$	ε_Ψ	Low Dispersion	Entropy fix threshold
RANS value	$\frac{1}{64}$	8	No	0.2
LES value	$\frac{1}{1024}$	1	Yes	0.05

Table 3.1: Parameters used in hybrid blending formulation

where f is the face between cells I and j.

To improve the gradient computation a correction step is applied to compute the gradients at the face from the cell center gradients [24]. Subsequently other necessary variables at the face (e.g. viscosity, diffusivity or velocity) are computed from the arithmetic mean of both cells adjacent to the face and the viscous flux vector is computed from those mean values and the corrected gradients at the face.

3.4 Turbulence modelling

As established in section 2.4 turbulence consists of structures with different length scales down to the Kologorov length. Based on the RANS equations derived in mentioned subsection, turbulence models aim to model the effects of turbulence in the flow without the need to resolve those turbulent scales. For this the Reynolds stresses

$$\tau_{ij}^{RANS} = \overline{\rho u_i'' u_j''} \tag{3.18}$$

need to be modelled.

The most common turbulence models can be divided into two classes: Reynolds stress models (RSM) and eddy viscosity models. The former are based on transport equations that can be derived for each entry in the Reynolds stress tensor. The latter model the turbulent stresses in analogy to the viscous stresses by introducing an eddy viscosity μ_t (in analogy to the molecular viscosity μ) and are based on the Boussinesq hypothesis that

$$\tau_{ij}^{RANS} = -2\mu_t S_{ij} + \frac{2}{3}\rho k \delta_{ij} \tag{3.19}$$

with the Kronecker delta δ_{ij}.

In the present thesis the $k-\omega$ Shear-Stress-Transport (SST) eddy viscosity model developed by Menter [35] is used. This model introduces two additional transport equations for the specific turbulent kinetic energy k and the specific dissipation rate ω

$$\frac{\partial \rho k}{\partial t} + \frac{\partial}{\partial x_k}\left(\rho k u_k\right) = \rho P^{(k)} - \rho \varepsilon^{(k)} + \rho D^{(k)} \tag{3.20}$$

$$\frac{\partial \rho \omega}{\partial t} + \frac{\partial}{\partial x_k}\left(\rho \omega u_k\right) = \rho P^{(\omega)} - \rho \Phi^{(\omega)} + \rho C_D^{(\omega)} + \rho D^{(\omega)} \tag{3.21}$$

with production terms P, dissipation terms ε and Φ, diffusion terms D and cross-diffusion term C_D. The eddy viscosity is computed as

$$\mu_t = \frac{\rho k}{\omega} \frac{1}{\max\left(1, \frac{\Omega F_2}{\omega a_1}\right)} \tag{3.22}$$

The values of model constants and definitions of the different terms are detailed in appendix B.

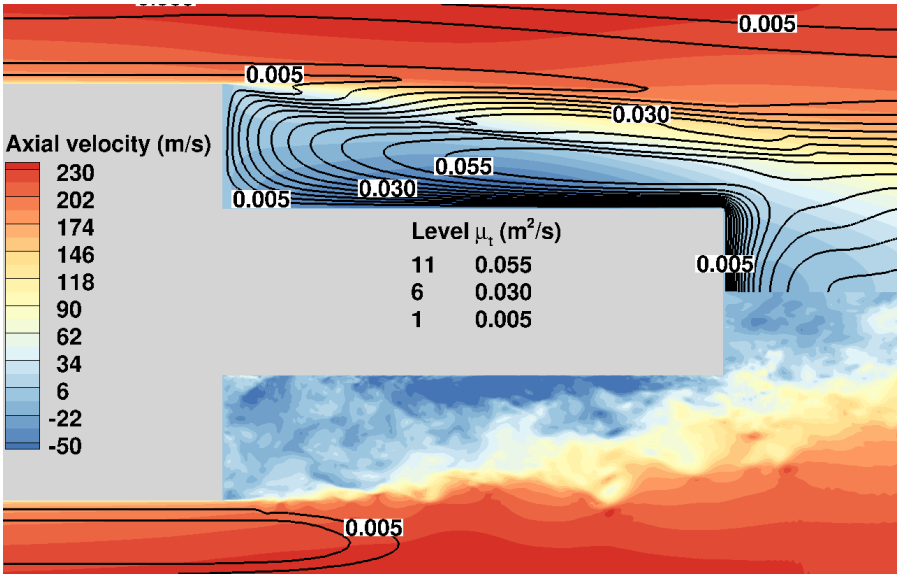

Figure 3.2: Example of an instantaneous flow field computed with RANS (top) and DES (bottom). Color contours show the axial velocity and contour lines display eddy viscosity levels.

3.4.1 Hybrid RANS-LES formulation

As mentioned in section 2.4, LES and hybrid RANS-LES reduce the modelled turbulent contributions by resolving the largest eddies and modelling only the smaller ones. A particular hybrid RANS-LES method is Detached Eddy Simulation (DES) [58]. DES is based on the similarity between the RANS and filtered Navier-Stokes equations (equations (2.30) to (2.33)). Assuming that the same modelling approaches apply to the filtered equations as to the RANS equations the sets of equations can be considered formally equal and a unified hybrid turbulence model can be applied. This hybrid model then models both RANS and LES regions with the same underlying equations and the interpretation of filtered or averaged values depends on the active mode. Additionally, the RANS model acts as the subgrid scale and wall model for the LES.

DES intrinsically provides the ability of switching between RANS and LES mode and is based on existing RANS turbulence models. Thus DES is relatively easy to implement into a code already capable of computing turbulent flows in RANS mode. Essentially only one change to the RANS turbulence model exists to switch from RANS to LES behaviour. This change is the length scale used for computing the dissipation of turbulent kinetic energy $\varepsilon^{(k)}$ (equation (B.2)) so that for application of DES with the $k-\omega$ SST model [64]

$$\varepsilon_{DES}^{(k)} = \frac{k^{3/2}}{l_{DES}} \qquad \text{with} \quad l_{DES} = \min\left(l_{RANS}, l_{LES}\right) \tag{3.23}$$

with

$$l_{LES} = C^{DES}\Delta \qquad \text{and} \quad l_{RANS} = \frac{\sqrt{k}}{\beta^{(k)}\omega} \tag{3.24}$$

where Δ is the filter length (see below) and

$$C^{DES} = (1-F)C_o^{DES} + FC_i^{DES} \quad \text{with} \quad C_i^{DES} = 0.78 \quad \text{and} \quad C_o^{DES} = 0.61 \tag{3.25}$$

a model constant that is blended with Menter's blending function from equation (B.10).

With this model construction the model switches to LES mode if the grid resolution is finer than the RANS length scale l_{RANS}, hence increases the dissipation term for the kinetic turbulent energy and consequently reduces the turbulent viscosity since less turbulence has to be modelled. This allows the solution to develop more resolved turbulent structures, as is displayed for an exemplary axisymmetric flow field in Fig. 3.2. The reduction of eddy viscosity is visible by the absence of black isolines in the recirculation region and the resulting higher unsteadiness can be observed in the less smooth velocity isocontours.

As an improvement to the original DES formulation that showed a strong grid dependence under certain conditions [36], shielding functions were developed that prevent this so-called grid induced stress depletion (Delayed Detached Eddy Simulation, DDES [60]) and also allow for a wall-modelled LES behaviour and decrease log-layer mismatch (Improved Delayed Detached Eddy Simulation, IDDES [56, 67]). In the present thesis the IDDES formulation is used for which the length scale in equation (3.23) is defined as

$$l_{IDDES} = \min(l_{RANS}, l_{hyb}) \tag{3.26}$$

$$l_{hyb} = \widetilde{f}_d(1-f_e)l_{RANS} + (1-\widetilde{f}_d)l_{LES} \tag{3.27}$$

where the functions $\widetilde{f}_d$ and f_e are shielding functions to prevent premature switching into LES mode and log-layer mismatch, respectively. The formulation of the functions can be found in appendix B.

Filter length definition

On isotropic grids the filter length Δ due to the discretization can be straightforwardly defined as the length of the cell edges. However, if the grid cells are anisotropic, i.e. the cell dimensions in different directions are not the same, this is no longer the case and the filter length becomes ambiguous. For simplicity a cartesian grid is assumed in the following, i.e. each cell is a cuboid aligned with the coordinate directions and has dimensions Δ_x, Δ_y and Δ_z.

In many standard LES solvers the definition based on the cell volume is used that reads

$$\Delta_{vol} = \sqrt[3]{\Delta_x\Delta_y\Delta_z}. \tag{3.28}$$

With this definition problems occur if one or two cell dimensions are excessively refined since e.g.

$$\Delta_x \to 0 \Rightarrow \Delta_{vol} \to 0 \tag{3.29}$$

and thus the turbulent viscosity approaches zero even though the larger cell dimensions are not able to resolve all scales. When presenting the original DES formulation Spalart [58] proposed to use a definition based on the maximum edge length instead

$$\Delta_{max} = \max(\Delta_x, \Delta_y, \Delta_z) \tag{3.30}$$

which does not yield problems of vanishing turbulent viscosity for highly anisotropic cells. However, it is too conservative since a slight refinement in one direction will actually resolve smaller scales in that direction, especially if the turbulent structures are anisotropic as well, but this change is not reflected in the filter length. To circumvent this problem several flow-dependent filter length definitions were developed, but in the present thesis only the following developed by Chauvet et al. [4]

$$\Delta_\omega = \frac{1}{|\underline{\omega}|}\sqrt{\omega_x^2\Delta_y\Delta_z + \omega_y^2\Delta_x\Delta_z + \omega_z^2\Delta_x\Delta_y} \tag{3.31}$$

and Mockett et al. [40]

$$\widetilde{\Delta}_\omega = \frac{1}{\sqrt{3}|\underline{\omega}|}\max_{n,m}|(\underline{l}_n - \underline{l}_m)| \qquad \text{with} \quad \underline{l}_n = \underline{\omega} \times (\underline{r}_n - \underline{r}) \tag{3.32}$$

are used. Here $\underline{r}$ is the coordinate vector of the cell center and $\underline{r}_n$ is the coordinate vector of cell corner point n. Both definitions are based on the vorticity vector $\underline{\omega} = (\omega_x, \omega_y, \omega_z)^T$ and make the definition less sensitive to the resolution in the main vorticity direction in order to accelerate transition from 2D to 3D turbulence. However, the Δ_ω definition features the same problem as Δ_{vol} of approaching zero under certain conditions.

In TAU a slightly different definition of $\widetilde{\Delta}_\omega$ is used since the positions of cell corners are not defined and thus the distances cannot be computed. Instead positions of neighbouring cell centers $\underline{x}_n$ are considered so that

$$\widetilde{\Delta}_\omega^{TAU} = \frac{1}{2|\underline{\omega}|}\max_{n,m}|(l_n - l_m)| \qquad l_n = \underline{\omega} \times (x_n - x) \tag{3.33}$$

This essentially replaces the evaluation of the cell size as the diagonals of the cell by an evaluation as the distance to neighbouring cells. A fundamental comparison of the different filter length definitions and their respective behaviour in generic test cases can be found in Schumann et al. [53].

To be valid also on non-cartesian and unstructured grids, some definitions are slightly modified from the above descriptions by directly using the known cell volume for Δ_{vol}, the maximum

cell dimension independent of coordinate direction for Δ_{max} and using the face area vectors for the computation of Δ_ω [7].

The investigations in Chapter 4 are conducted with the Δ_ω definition and in this chapter the effect of switching to the improved definition $\widetilde{\Delta}_\omega$ is evaluated as well. For the simulations with hot plumes in Chapter 5 the improved definition $\widetilde{\Delta}_\omega$ is used.

3.5 Chemistry modelling

The chemical source terms ω_s in equation (2.30) are included in a point implicit manner using a source term jacobian to decrease the stiffness of the equations. Further details on the numerical handling of the chemistry modelling can be found in Karl [24].

3.6 Boundary conditions

Boundary conditions have to be applied at the border of the computational domain to allow for a solution of the conservation equations. Several different boundary conditions exist in TAU and only those used in the present thesis will concisely be presented here.

- ▷ **Viscous wall:** This condition is applied where a no-slip condition is required. It is enforced by assuming a zero velocity on the boundary and then computing the remaining fluxes without the momentum fluxes. The option between adiabatic and isothermal heat transfer exists with the former setting the heat transfer through the wall to zero and the latter assuming a given temperature at the wall and computing the remaining fluxes without the energy flux.
- ▷ **Farfield:** Using the local characteristics this boundary conditions sets values for certain variables in ghost cells next to the boundary. Subsequently, the flux from those ghost cells into the boundary cells is computed and added to fluxes in the boundary cells.
- ▷ **Dirichlet:** At this boundary condition the values are simply set at the boundary points.
- ▷ **Exit pressure outflow:** This boundary sets a given pressure in combination with extrapolated values and calculates the fluxes towards this state.

3.7 Spectral and modal analysis

To analyse the unsteady behavior of the flow several methods can be employed. Traditional spectral analysis of a time signal $x(t)$ uses a Fourier Transformation to obtain the signal in frequency space $X(f)$ [63]. From the Fourier transformed signal the Power Spectral Density (PSD) $G(f)$ of the signal at each (sampled) frequency f can be derived to analyse which

harmonic frequencies the time signal is composed of. In the present thesis Fast-Fourier Transformation (FFT), and more specifically Welch's method [63], is used for this purpose. The data is typically displayed in the form of a (scaled) premultiplied PSD (e.g. [8])

$$\text{spPSD} = \frac{\text{pPSD}}{\sigma^2} = \frac{fG(f)}{\sigma^2} \qquad \text{with} \qquad \sigma^2 = \int_0^\infty G(f)df. \tag{3.34}$$

The premultiplication with the frequency simplifies the identification of peaks in the spectrum when the frequency is displayed on a logarithmic axis and the premultiplied PSD on a linear axis. Scaling the spectra with the integral of the PSD over the whole frequency range σ^2 removes the effect of the total energy of the fluctuations and thus enables a better comparison of frequency amplitudes between cases with slightly different levels of fluctuations.

To analyse two signals with respect to each other the cross correlation function, and its Fourier Transformation, the cross spectral density (CSD) function, can be employed [63]. The cross correlation between two signals is equal to unity if the signals correlate perfectly and is typically plotted over the time lag, i.e. how much the second signal has to be shifted in time to reach a certain level of cross correlation. The CSD function is a complex-valued function of the frequency and from it the coherence function [73] can be computed as

$$C = \frac{\text{CSD}_{12}}{\sqrt{\text{CSD}_{11}\text{CSD}_{22}}} \tag{3.35}$$

where index 1 and 2 represent the two evaluated locations. This definition leads to $|C(f)| \leq 1$, with an absolute value of unity indicating a complete correlation of two signal at the given frequency. Additionally, the phase of the coherence function represents the phase relationship between the two signals at a given frequency and hence can be used to determine the leading and trailing signal (at the respective frequency).

Used on a series of sensors with the same axial and radial but different circumferential positions, the coherence function for axisymmetric geometries is real-valued due to the (stochastic) isotropy of the flow as well as 2π periodic. Thus the real part of the coherence function can be decomposed into different circumferential modes m (see left of Fig. 3.3) via

$$C_r = \sum_{m=0}^{\infty} C_{r,m} \cos(m\Delta\phi) \tag{3.36}$$

where $\Delta\phi$ is the angle between the evaluated positions. The coefficients $C_{r,m}$ then allow to investigate the dominance of different pressure modes at the evaluated location. Particularly $C_{r,1}$ is of interest in this evaluation as this mode exhibits an overall force in one direction and thus is directly related to the buffeting loads. An example of $C_{r,0}$, $C_{r,1}$ and $C_{r,2}$ plotted over the frequency is shown on the right of Fig. 3.3. Visible is a peak for $C_{r,1}$ at $\text{Sr}_D \approx 0.2$ and

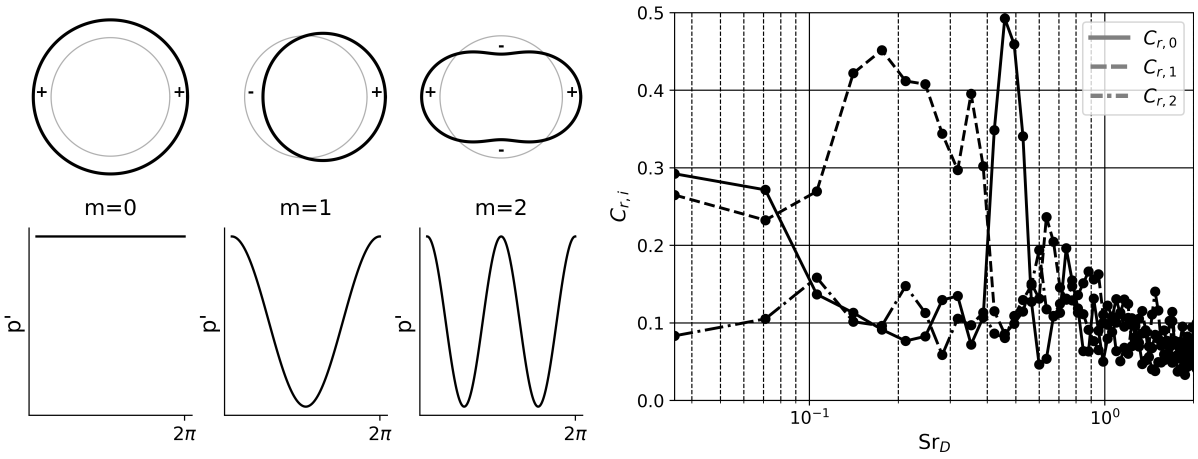

Figure 3.3: Schematic visualization of the different pressure modes (left) and exemplary amplitude of the coherence modes (right).

$\mathrm{Sr}_D \approx 0.35$ indicating the antisymmetric modes responsible for the buffeting loads and a peak for $C_{r,0}$ at $\mathrm{Sr}_D \approx 0.5$ that indicates a symmetric mode. For the higher modes $C_{r,2}$ and higher no significant amplitudes are visible.

The mentioned methods based on Fourier Transformations have the disadvantage, however, that the relationship between time signals at different locations is lost or only two signals can be analysed with respect to their relationship. Alternatively, or in conjunction, modal decomposition techniques like Dynamic Mode Decomposition (DMD) [51] can be employed. This method takes into account the whole unsteady flow field $\underline{U}(x, y, z, t)$ over N snapshots

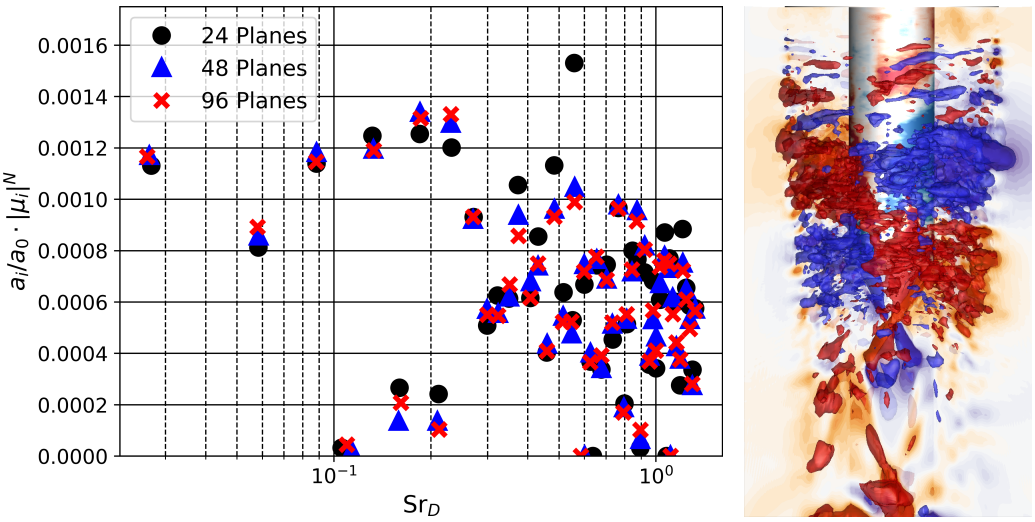

Figure 3.4: Example of the mode amplitudes (left) and of the shape of a pressure mode (right).

and decomposes it as

$$\underline{U}(x,y,z,t) = \sum_{n=1}^{N} a_n \exp(\lambda_n t)\underline{\phi}(x,y,z) \tag{3.37}$$

with amplitudes $a_n \in \mathbb{C}$, frequencies $\lambda \in \mathbb{C}$ and spatial modes $\underline{\phi}_n \in \mathbb{C}^3$. The spatial modes can help to identify the physical processes responsible for different frequency contributions. To reduce the required computational resources - in particular random access memory (RAM) - the evaluated part of the computational domain is limited to regions of interest in the following. Additionally, the number of circumferential planes is reduced to 48 planes, i.e. a resolution of 7.5° for the investigations in Chapter 5. The obtained mode frequencies are unaffected by this reduction in circumferential resolution as is shown on the left of Fig. 3.4 where each marker represents one obtained mode, and the amplitude, in particular of the dominant modes, is not affected significantly either. An example of an obtained pressure mode is shown on the right of Fig. 3.4. The shown case is a mode responsible for the buffeting loads at $\mathrm{Sr}_D \approx 0.2$ for which the strong antisymmetric pressure distribution - with regions of decreased pressure in blue and those with increased pressure in red - can be observed. Further information on the details of the employed DMD algorithm and the theoretical principles can be found in Schmid [51] and Jovanović et al. [23].

4 Sensitivity Study

In this chapter the sensitivity of the numerical results to several parameter changes is investigated based on a configuration with available literature data. Additionally, the investigation is used to determine optimal settings for the simulations in Chapter 5.

In the following the investigated geometry and the numerical setup will be described first in Sec. 4.1 and 4.2 before the results of the simulations are presented. The sensitivity study itself is split into two parts: Sensitivity towards grid resolution and topology [52] in Sec. 4.3 and towards parameter settings [55] in Sec. 4.4.

4.1 Investigated geometry and reference data

The model geometry considered in this chapter was first investigated experimentally by Deprés et al. [9] and is shown in Fig. 4.1. It consists of a cylinder with diameter $D = 0.1$ m followed by a second cylinder with diameter $D_2 = 0.4D$ and length $L = 1.2D$, resembling a generic space

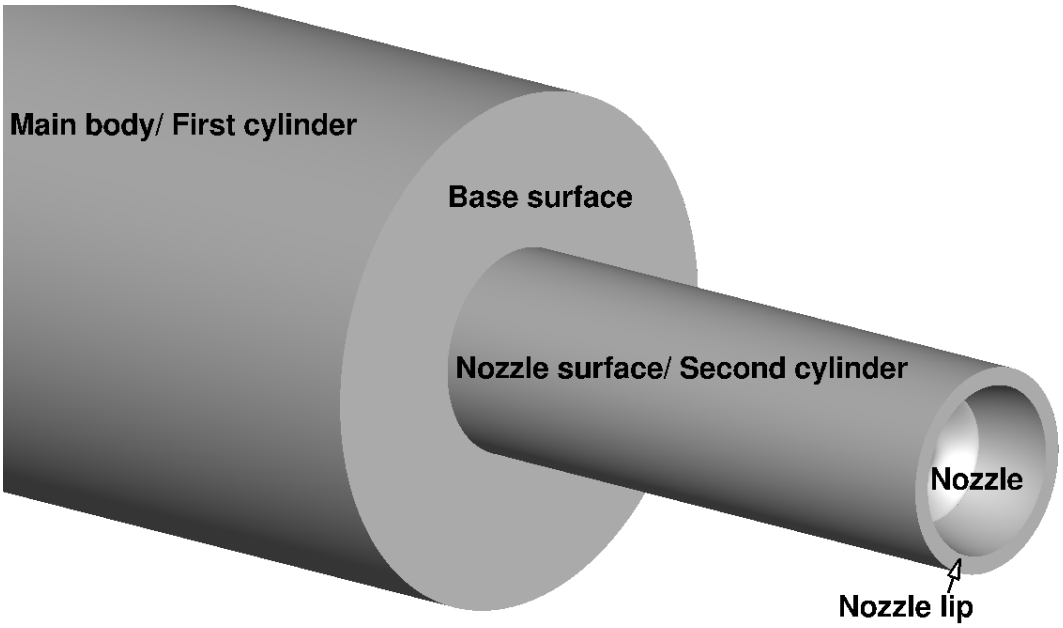

Figure 4.1: Investigated model geometry.

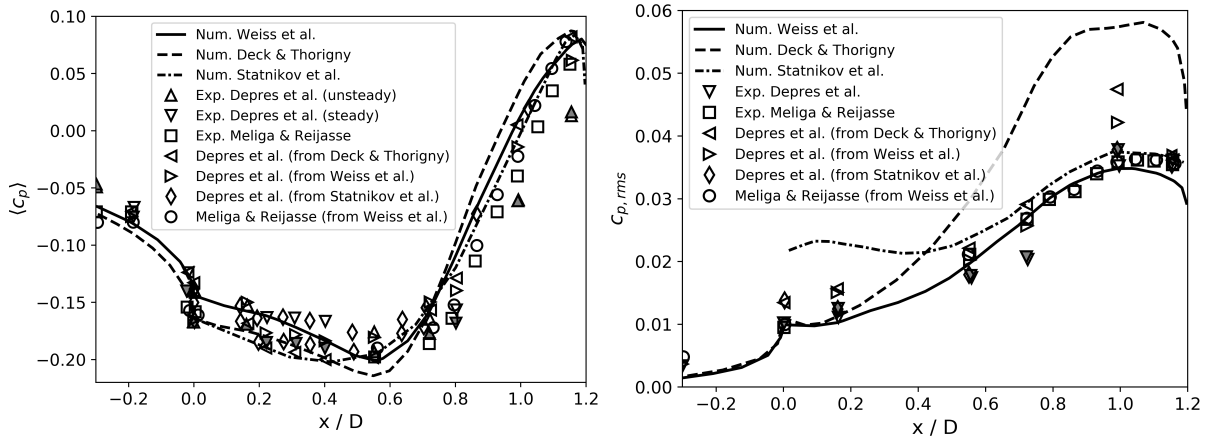

Figure 4.2: Mean wall pressure coefficient and rms wall pressure coefficient in the literature: Deprés et al. [9], Deck and Thorigny [8], Meliga and Reijasse [33], Weiss et al. [73], Statnikov et al. [61].

launch vehicle. The second cylinder is either closed or contains a supersonic nozzle contour connected to a high pressure air supply. A coordinate system with origin on the symmetry axis and at the junction of the two cylinders is used in the following to describe positions. The free stream is at transonic conditions which are summarized together with the conditions in the nozzle in Table 4.1. A detailed description of the model geometry and experimental considerations can be found in Deprés et al. [9].

From the experimental investigations mean and root-mean-square (rms) surface wall pressure

$$\langle c_p \rangle = \left\langle \frac{p - p_\infty}{\frac{\rho_\infty}{2} U_\infty^2} \right\rangle \qquad c_{p,rms} = \sqrt{\left\langle \left(\frac{p - \langle p \rangle}{\frac{\rho_\infty}{2} U_\infty^2} \right)^2 \right\rangle} \tag{4.1}$$

at several axial locations are available. Here $\langle\rangle$ denote temporal means and p_∞, ρ_∞ and U_∞ are the free stream pressure, density and velocity, respectively. Steady and unsteady pressure sensors were used in Deprés et al. [9] and the pressure distribution with and without an active plume was investigated. A similar experimental data set is available in Meliga and Reijasse [33], but only for the case without an active plume. Numerical comparison data can be found in Deck and Thorigny [8] (with active plume), Weiss et al. [73] (without active plume) and Statnikov et al. [61] (with active plume). The reference data as obtained from the different publications is shown in Fig. 4.2.

U_∞	M_∞	p_∞	T_∞	$p_{0,nozzle}$	$T_{0,nozzle}$	$\frac{\delta_{99}}{D}\|_{x=-2.45D}$
235.767 m/s	0.7	72813 Pa	282.332 K	2.45 MPa	300 K	0.2

Table 4.1: Flow conditions for sensitivity study

Displayed are the numerical data sets in solid, dashed and dash-dotted lines, respectively. The experimental data points reported in Deprés et al. [9] are shown as upwards (unsteady sensors) or downwards (steady sensors) pointing triangles; empty symbols are used for the case without an active plume whereas filled symbols indicate the case with an active plume. Left pointing triangles indicate the experimental values attributed to Deprés et al. [9] as reported by Deck and Thorigny [8], right pointing triangles indicate them as reported by Weiss et al. [73] and diamonds indicate them as reported by Statnikov et al. [61]. It is visible that there are certain discrepancies for $x/D > 0$ between the experimental values reported in the different publications that are beyond the read-off accuracy of data extraction. For $x/D < 0.6$ the values reported by Deck and Thorigny [8] and Weiss et al. [73] agree with those reported by Deprés et al. [9]. However, the values reported by Weiss et al. [73] for $0.2 < x/D < 0.5$ appear to be those with plume whereas the remaining values are those without plume (the numerical investigation is without plume as well). For $x/D > 0.6$ larger discrepancies are visible, with both numerical investigations reporting higher pressure coefficients at the sensor locations than reported by Deprés et al. [9]. The values reported by Statnikov et al. [61] appear to be shifted upstream from those reported by Deprés et al. [9], with a stronger shift for values further downstream (e.g. the last sensor location is at $x/D \approx 1.02$ whereas it is at $x/D = 1.15$ for all other publications). The experimental data reported by Meliga and Reijasse [33] is only reproduced by Weiss et al. [73] and these two publications agree much better, but there is still a small deviation especially for locations closer to the nozzle lip.

For the rms pressure coefficients Deck and Thorigny [8] and Weiss et al. [73] report higher values than the original publication by Deprés et al. [9]. The values reported by Statnikov et al. [61] correspond to those reported by Deprés et al. [9] and those reported by Meliga and Reijasse [33] and Weiss et al. [73] agree as well.

In the following, the pressure distributions reported by Weiss et al. [73] are considered for comparison to the newly obtained data. Several arguments can be found for these values being the most reasonable/ trustworthy:

- ▷ The deviations to the values reported by Meliga and Reijasse [33] are small (mean) or close to zero (rms) and can be explained by read-off/ extraction inaccuracies.
- ▷ The authors are from the same group as Deprés et al. [9] and hence possible post-processing errors in Deprés et al. [9] might be corrected, providing an explanation for the differences.
- ▷ The publication is more recent than Deck and Thorigny [8].
- ▷ The sensor locations agree with those by Deprés et al. [9] whereas the sensor locations differ in Statnikov et al. [61].

Additionally, Weiss et al. [73] provide data points from both experimental investigations,

whereas the other numerical investigations only provide those by Deprés et al. [9]. Hence, the choice of Weiss et al. [73] allows to refer to one publication and provides some consistency between the different data sets. It also allows to compare the two experimental data sets directly, which shows that there are some appreciable differences between the two experimental investigations. This provides an estimation of the error bars in the experiments and/or shows the sensitivity of the obtained pressure distributions to small experimental differences.

All publications also feature a spectral analysis of the wall pressure data. However, the obtained spectral content is not always evaluated at the same locations or based on the same quantities. Deprés et al. [9] show pressure spectra at six axial locations $x/D \in [0, 0.16, 0.55, 0.72, 0.99, 1.15]$, whereas Meliga and Reijasse [33] only show five of those ($x/D \in [0, 0.55, 0.72, 0.99, 1.15]$), Deck and Thorigny [8] show four ($x/D \in [0, 0.16, 0.55, 0.72, 1.15]$), Weiss et al. [73] one ($x/D = 0.99$) and Statnikov et al. [61] show two ($x/D \in [0.6, 1.15]$).

In Deprés et al. [9] only the location $x/D = 0.72$ shows a clear peak at $Sr_D \approx 0.2$, whereas in Meliga and Reijasse [33] it is visible as the main peak for $x/D = 0.55$ and $x/D = 0.72$ and is also visible as a minor peak accompanying a broadband peak around $Sr_D \approx 0.6$ for $x/D = 0.99$ and $x/D = 1.15$. For the last location a very minor peak is also visible in Deprés et al. [9]. Both publications show the broadband peak for the last two locations. In Deprés et al. [9] a small and not very distinct peak at $\mathrm{Sr}_D \approx 0.1$ for all locations exists with varying intensity whereas this feature does not appear in Meliga and Reijasse [33]. Overall, the spectra in Deprés et al. [9] are significantly more affected by noise and show fewer distinct features than those reported by Meliga and Reijasse [33]. The spectra in Deck and Thorigny [8] are also more noisy, with a peak at $\mathrm{Sr}_D \approx 0.2$ only visible at $x/D = 0.16$ and $x/D = 0.55$ whereas at the other two locations the first peak appears at $\mathrm{Sr}_D \approx 0.3$. Additionally, the first location shows a very distinct peak at $\mathrm{Sr}_D \approx 0.1$. At all locations except the first a broadband contribution around $\mathrm{Sr}_D \approx 0.6$ appears. Weiss et al. [73] only show a spectrum at one location, which features peaks at $\mathrm{Sr}_D \approx 0.1, 0.2, 0.25, 0.35$ as well as a strong broadband contribution around $\mathrm{Sr}_D \approx 0.6$. They also show that the peak at $\mathrm{Sr}_D \approx 0.2$ is most strongly visible for $0.35 < x/D < 0.8$. In Statnikov et al. [61] peaks at $\mathrm{Sr}_D \approx 0.1$, $\mathrm{Sr}_D \approx 0.2$ and $\mathrm{Sr}_D \approx 0.35$ appear for both considered locations. Due to the non-premultiplied presentation of the spectra a broadband contribution is not clearly distinguishable here.

Taking into account these significant differences between the different sets of experimental and numerical reference data, a consistent quantitative comparison regarding the spectral content of the wall pressure is challenging. The most dominant qualitative spectral features for comparison that can be concluded from the reference data are:

- ▷ A broadband peak centered around $\mathrm{Sr}_D \approx 0.6$ appears for $x/D > 0.9$ [8, 9, 33, 73].
- ▷ A peak at $\mathrm{Sr}_D \approx 0.2$ appears for $0.35 < x/D < 0.8$. It might remain as a (smaller) peak

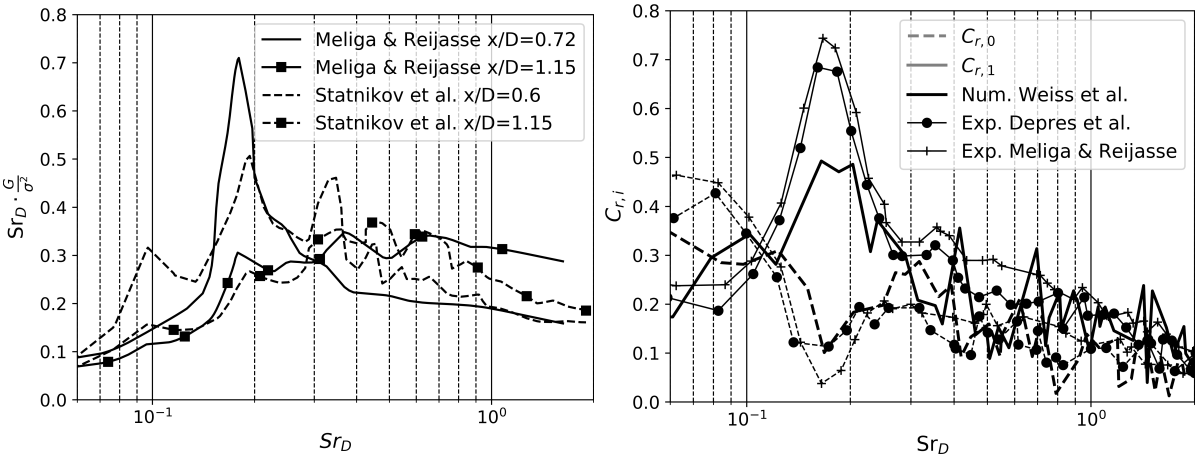

Figure 4.3: Wall pressure spectra (left) and coherence modes (right) in different publications: Deprés et al. [9],Meliga and Reijasse [33],Weiss et al. [73],Statnikov et al. [61]

for locations further downstream [33, 61, 73].

- ▷ A minor peak at $\mathrm{Sr}_D \approx 0.1$ can be visible [8, 9, 61, 73].
- ▷ A minor peak at $\mathrm{Sr}_D \approx 0.3 \ldots 0.4$ can be visible [61, 73].

Since the spectra in Deprés et al. [9] and Deck and Thorigny [8] are particularly noisy and contain fewer dominant features and Weiss et al. [73] only provide quantitative spectra for one location, only those reported by Meliga and Reijasse [33] and Statnikov et al. [61] are displayed on the left of Fig. 4.3. Both the spectra at a location in the center of the recirculation region and near the nozzle lip are shown. Note that since the spectra are extracted from the respective publication they appear considerably smoother than the original data.

An additional quantity for comparison is the spectral analysis of the circumferential coherence modes based on the wall pressure (cf. Section 3.7). The first four modes at $x/D = 0.72$ are reported by Weiss et al. [73] both for their own numerical investigation as well as for the experimental data by Deprés et al. [9] and Meliga and Reijasse [33]. Since $C_{r,2}$ and $C_{r,3}$ show very small amplitudes over all frequencies, only the symmetric mode $C_{r,0}$ and the antisymmetric mode $C_{r,1}$ are displayed on the right of Fig. 4.3. The dominant features in these distributions are a peak at $\mathrm{Sr}_D \approx 0.1$ for the symmetric mode and one at $\mathrm{Sr}_D \approx 0.2$ for the antisymmetric mode.

A final quantity to compare are the spectra based on the radial forces on the surface of the second cylinder as reported by Statnikov et al. [61]. Both the scaled premultiplied PSD of the forces in the individual directions as well as the average of both uni-directional spectra are displayed in Fig. 4.4 . The spectra show two very distinct peaks in the buffeting forces at $\mathrm{Sr}_D \approx 0.2$ and $\mathrm{Sr}_D \approx 0.35$.

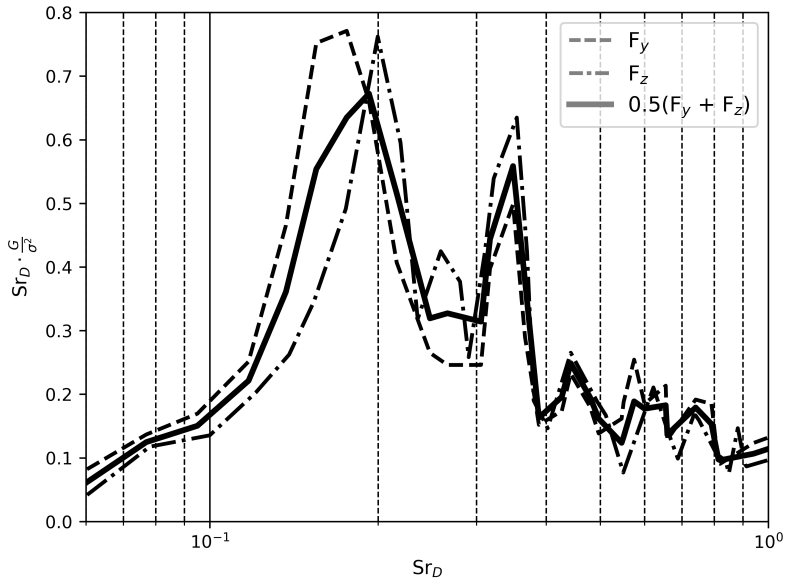

Figure 4.4: Nozzle force spectra as reported by Statnikov et al. [61]

Due to the large discrepancies between the different data sets regarding wall pressure coefficients and spectra and the availability of coherence modes and force spectra in only one publication, the focus of the sensitivity study is not the quantitative comparison with the literature data. Rather, the study focuses on the changes introduced to the obtained data by changing grid features and parameter settings, and the literature data is used predominantly to evaluate a general agreement with the most dominant features reported by other authors.

4.2 Numerical setup

All model walls are modelled as viscous and adiabatic walls. As an inflow condition at $x = -1.2D$ a farfield condition with values prescribed from a precursor RANS simulation is used that captures the experimentally found boundary layer thickness at $x = -2.45D$. At the top the domain is bounded at $r = 7.5D$ by a farfield condition with free stream values and an exit-pressure outflow condition with a constant pressure of p_∞ is used at $x = 10D$. The plume, if active, is introduced by a dirichlet boundary condition in the supersonic part of the nozzle based on a precursor RANS simulation of the whole nozzle.

$\mathcal{R}_{air}$	γ_{air}	Pr_{air}	$\frac{\mathrm{Pr}_{air}}{\mathrm{Pr}_t}$	$\mu_{ref,air}$	C_{air}	$T_{ref,air}$
287 J/(kg·K)	1.4	0.72	0.8	$1.716 \cdot 10^{-5}$ kg/(m·s)	110.4 K	273.15 K

Table 4.2: Gas specific constants for air

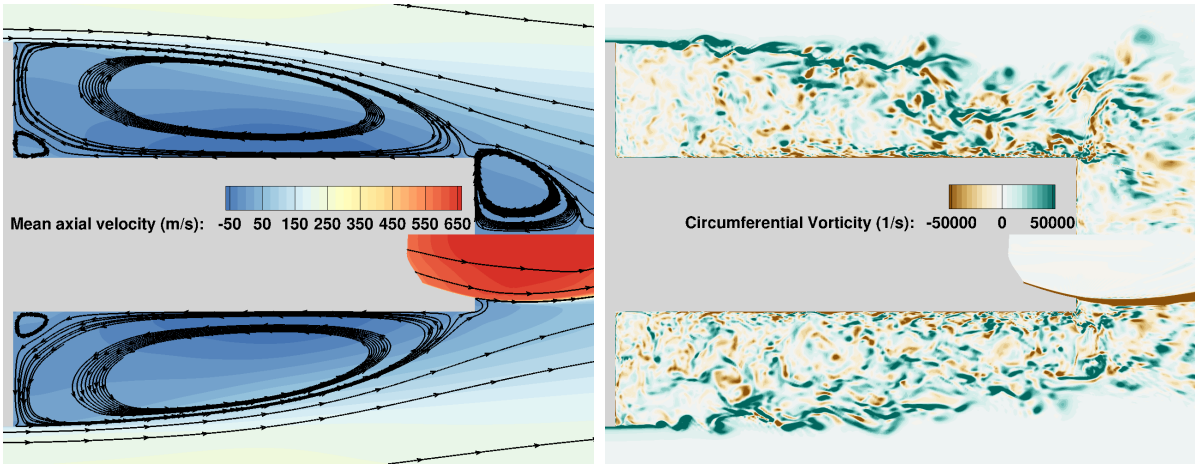

Figure 4.5: Representative flow field in an axial-radial plane. Mean streamlines and axial velocity contours (left) and instantaneous circumferential vorticity (right). Inactive (top) and active (bottom) plume case.

The gas is modelled as a calorically perfect gas with constant $\mathcal{R}_{air}$, γ_{air}, Pr_{air} and Pr_t and Sutherland's law is used to compute transport coefficients. Table 4.2 summarizes the values used.

An IDDES approach based on the SST $k-\omega$ model as described in Sec. 3.4 is used. The LES region is determined by the model, but for $x > 2D$ the model is forced into RANS mode in order to damp fluctuations towards the outflow boundary. The numerical settings described in Chapter 3 are applied. Based on the grid resolution in the reattachment zone and the free stream velocity the time step is chosen as $\Delta t = 10^{-6}$ s which corresponds to half of that used by Deck and Thorigny [8].

The initial solution for each case is interpolated from a previous investigation on a coarser grid that was left to naturally develop from a URANS solution. To ensure a statistical steady-state, data collection is only started after global variables such as drag coefficient, skewness of the velocity field and total turbulent kinetic energy in the domain do not show a significant transient behaviour any more. Data collection is then continued for about 38 convective time units (CTUs), which allows a spectral resolution of $\Delta \mathrm{Sr}_D \approx 0.05$ using Welch's method with 3 segments [63]. Here one CTU is defined as the ratio between model diameter D and free stream velocity U_∞. The mean and rms wall pressure data as well as wall pressure spectra are averaged in the circumferential direction since the geometry is completely axisymmetric.

It should be noted that some deviations, especially in the amplitudes of the spectral analysis, are expected due the relatively short data collection period. A longer data collection period would possibly increase stochastic significance of the results and will be evaluated in section

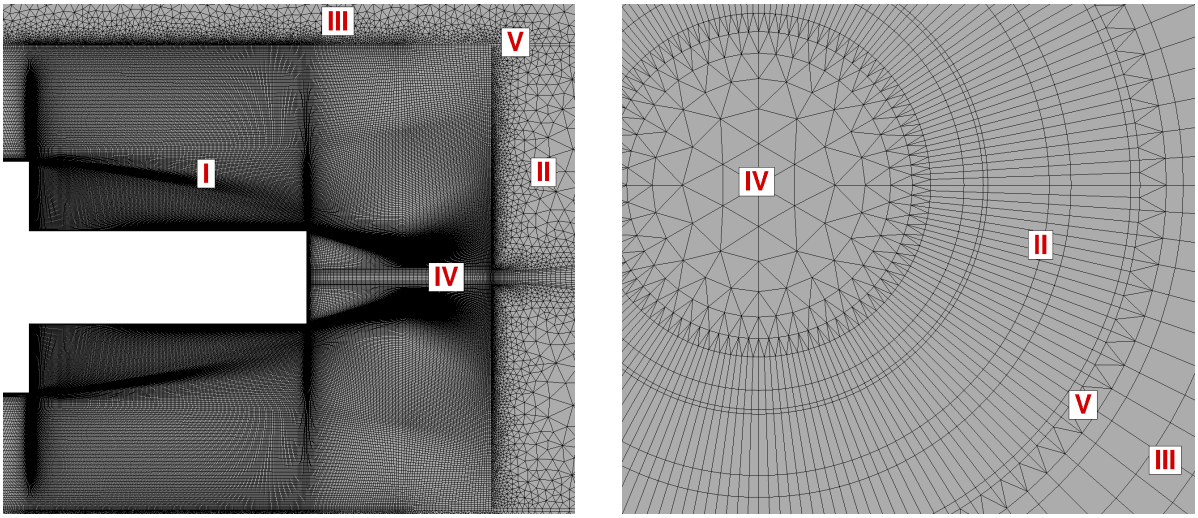

Figure 4.6: Grid topology with different grid regions marked with Roman numerals. Cut through the axis (left) and at a constant axial position (right).

4.4. However, the cost of extending the data collection period by a factor of two for just one case equals the same computational cost as investigating a different grid or parameter variation. It is hence deemed most practical and economical to allow for some quantitative discrepancies in order to evaluate a larger variety of different sensitivities.

The general flow topology around the model geometry with and without an active plume can be seen in Fig. 4.5: Upon reaching the end of the first cylinder the turbulent boundary layer separates and the resulting main shear layer grows, developing larger turbulent shear layer structures and increasing velocity and pressure fluctuations. Near the end of the second cylinder the shear layer reattaches and thus creates the main recirculation region that is bounded by the base of the first cylinder, the nozzle surface and the shear layer. The turbulent structures from the shear layer are partially transported upstream in the recirculation region and hence are able to interact with the main shear layer. In the base corner a small secondary vortex is visible. Without an active plume, a second shear layer is created downstream of the model that forms a second recirculation region in the wake of the second cylinder. With an active plume this recirculation region does not exist and instead the turbulent structures are transported downstream and a shear layer between supersonic plume and transonic external flow is visible.

4.3 Grid study

In this section the configuration without an active plume is considered for its supposed simplicity and since comparison data by Weiss et al. [73] also does not feature a plume. The

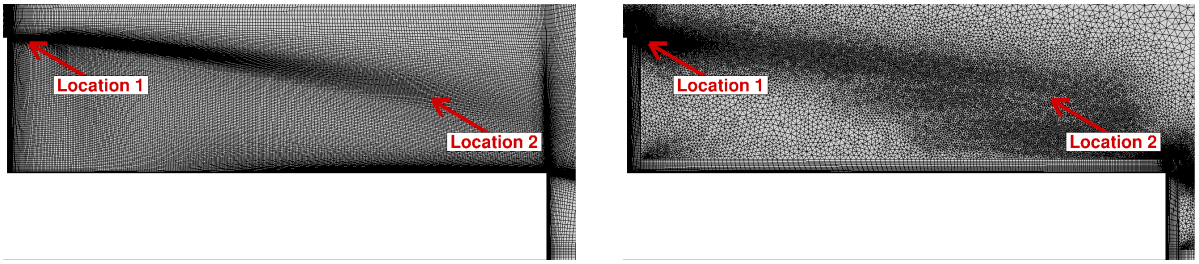

Figure 4.7: Detailed view of the grid topology in the focus region. Grid G1 with hexahedral elements (left) and grid G4 with prismatic elements (right).

employed grid topology is based on the following considerations:

- ▷ It should be possible to use a structured grid (for low dissipation) in the region where most turbulent structures appear (region of interest/ focus region).
- ▷ Towards the boundaries the resolution should be reduced to reduce the total number of grid points, stabilize the simulation and reduce the effects of boundary conditions.
- ▷ The grid should be axisymmetric to mirror the axisymmetry of the model geometry and allow averaging in the circumferential direction.
- ▷ For stability, accuracy and computational effort the number of cell faces at the axis should be in the same order of magnitude as for other cells in the domain.

The resulting grid topology is shown in Fig. 4.6. It consists of 5 different grid regions. Region I is the region of interest which employs a fine resolution with hexahedral elements and thus is completely structured (i.e. in axial, radial and circumferential direction). Alternatively, this region can also be populated with prismatic elements that are unstructured in-plane, but still allow axisymmetry, as shown on the right of Fig. 4.7. Regions II and III in Fig. 4.6 consist of prismatic elements that allow for a coarsening towards the outflow and the top of the domain, but are fully axisymmetric. Region V connects regions I and II with region III. Using prismatic elements the circumferential resolution in region III can be reduced by a factor of 2 (or 4, if two of these connector regions are used) from that in region I and II. Region IV, also consisting of prisms, is the region near the axis, where the circumferential resolution is reduced to prevent an excessive number of faces in cells at the axis. Additionally, this reduction of circumferential planes also leads to a more uniform circumferential resolution since this resolution naturally increases with decreasing radius, i.e. the closer the cells are to the axis the smaller the circumferential distances between the cells.

In total 7 grids are initially investigated in this section, of which 5 (G0 to G4) share the same circumferential resolution of 1.875°. The initial grid G0 is based on experiences from previous investigations and on grid designs in the literature [8, 61, 73]. A first non-dimensional wall

distance of $\Delta y^+ = \Delta y \sqrt{\frac{\rho}{\mu}\left(\frac{\partial u}{\partial y}\right)_{wall}} < 1$ is satisfied on all walls and the cell growth ratio is kept below 1.15 near walls and below 1.5 in all other parts of the domain. Over 99 % of the grid features cell growth ratios of below 1.1. Cell aspect ratios away from walls are kept as small as possible, but due to the fine resolution near walls aspect ratios of up to about 100 can appear in the initial parts of the shear layers just downstream of the first and second cylinder.

Grids G0 to G4 are summarized in Table 4.3 which also shows the axial and radial non-dimensional grid spacings at two representative locations for each grid. Location 1 is at $x = 0.03D$, $r = 0.5D$, i.e. in the initial part of the shear layer, and location 2 at $x = 0.95D$, $r = 0.37D$, i.e. in the region above the reattachment location - both locations are also marked in Fig. 4.7. The locations have been chosen such that the resolution changes between the different grids are reflected in Table 4.3. Location 1 is also located at the interface between the structured wall layer and the unstructured region for grid G4. The difference in resolution is also displayed in Fig. 4.8 which shows the relative difference in cell volume compared to grid G1 for the respective grids.

Compared to the initial grid, 0.3 Mio. points are added in the medium grid G1 in the region $0 < x < 0.15D$ to increase the axial resolution, which is also visible by the brown coloured regions behind the base in the figure; the radial and circumferential resolution remain the same. On the fine grid G2 another 1 Mio. points are added in the region of the main shear layer to increase the radial resolution as indicated by the green areas in the figure. Following indications from grid sensors for grid G1 (discussed in subsection 4.3.1) the coarse grid G3 contains about 2.4 Mio points less than grid G1. The removed points reduce the radial resolution predominantly in the region $0.25D < r < 0.4D$ and the axial resolution in the region $0.8D < x < 0.12D$. Finally, a grid with an unstructured region of interest (G4) is investigated for which the cell sizes are chosen such that they represent the distribution and computational effort comparable to G1. For this grid less information can be obtained from the cell volume comparison in the figure because of the very different cell volumes between isotropic triangles and anisotropic quadrilaterals (or prisms and hexahedra) in the other grids. The lower number of grid points

Grid	Initial (G0)	Medium (G1)	Fine (G2)	Coarse (G3)	Prism (G4)
Points (Mio)	15.5	15.8	16.8	13.4	11.0
Δ^+_{ax}, Δ^+_{rad} | Loc. 1	105, 1	90, 1	90, 1	90, 1	10, 5
Δ^+_{ax}, Δ^+_{rad} | Loc. 2	230, 110	230, 110	230, 95	320, 135	135, 135
x_r/D	1.174	1.176	1.179	1.180	1.180

Table 4.3: Summary of investigated grids with circumferential resolution 1.875°. x_r indicates the reattachment location.

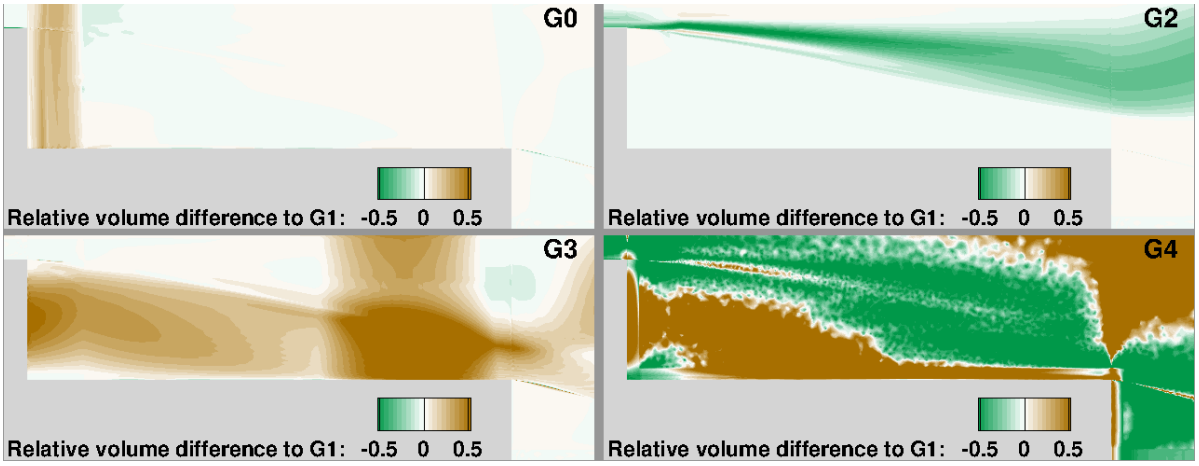

Figure 4.8: Resolution differences between the investigated grids. Displayed is the relative cell volume difference in comparison to grid G1.

for this grid can be explained by the larger number of faces each grid points possesses[1]. Near solid walls this grid features layers of hexahedral elements to avoid an excessive amounts of points to achieve a sufficiently small first wall distance.

The last two initial grids share the in-plane (axial and radial) resolution with grid G2, but feature a finer circumferential resolution of 1.406° (G5) and 0.938° (G6), respectively. This allows to separate the effects of in-plane refinement from those of circumferential refinement. These grids with changing circumferential resolution are summarized in Table 4.4 and further information on grids G2b and G6b are discussed in subsection 4.3.5.

[1] On average, an unstructured cell is connected to 5 other cells in-plane whereas a structured cell is connected to 4 other cells.

Grid	1.875° (G2)	1.406° (G5)	0.938° (G6)	1.875° (G2b)	0.938° (G6b)
Plume	Off	Off	Off	On	On
Points (Mio)	16.8	22.4	33.5	15.8	31.7
Δ^+_{circ} | Loc. 1	660	495	330	660	330
Δ^+_{circ} | Loc. 2	230	170	115	230	115
x_r/D	1.179	1.179	1.179	1.172	1.187

Table 4.4: Summary of investigated grids with constant in-plane resolution. x_r indicates the reattachment location.

4.3.1 Grid sensor evaluation

Two grid sensors are used to judge the resolution in the domain and detect areas that require a finer resolution. The first grid sensor is an absolute grid sensor by Reuß et al. [47] that computes the ratio of resolved to total turbulent kinetic energy at each point as

$$S_{abs} = \frac{k_{res}}{k_{res} + k_{sgs}} \qquad \text{with} \quad k_{res} = \frac{1}{2}\langle(\underline{u} - \langle\underline{u}\rangle)^2\rangle \quad \text{and} \quad k_{sgs} = \frac{1}{2}\langle(\underline{u} - \langle\overline{\underline{u}}\rangle)^2\rangle \tag{4.2}$$

where $\overline{\underline{u}}$ is the space filtered velocity field. As proposed by Reuß et al. [47] a support of $N = 4$ neighbours is used for the filtering procedure, i.e. the spatial filter is applied consecutively four times (cf. Reuß et al. [47] for further details). Optimally, $S_{abs} > 0.8$ should be satisfied in the whole region of interest.

Since S_{abs} only determines whether or not to refine a grid region, a second - directional - approach by Toosi and Larsson [66] is used in combination with it. This approach is based on energy in the barely resolved small-scale field in different directions and two sensors can be defined as the ratios between the resolved energy in the different directions as

$$S_{ax-rad} = \frac{A_{rad}}{A_{ax}} \qquad \text{and} \qquad S_{ax-circ} = \frac{A_{circ}}{A_{ax}} \tag{4.3}$$

$$A_n = \langle \underline{u}^{*,n} \cdot \underline{u}^{*,n} \rangle \quad with \quad \underline{u}^{*,n} = -\frac{\Delta_n^2}{4} \underline{n}^T \left(\nabla\nabla^T \underline{u}\right) \underline{n} \tag{4.4}$$

where n is the direction the sensor is evaluated in. These sensors indicate an under-resolution in the axial direction for values larger than unity and in the second (radial or circumferential, respectively) direction for values smaller than unity. However, they do not give an indication whether the grid is fine enough as it is and thus could as well be interpreted as suggesting a coarsening in the axial directions for values smaller than unity and coarsening in the second direction for values larger than unity. In combination, sensor S_{abs} detects regions that could most likely profit from refinement and sensors S_{ax-rad} and $S_{ax-circ}$ determine the kind of refinement necessary.

In Fig. 4.9 the grid sensor output for the different grids without plume (G0 to G6) is visualized. The left column displays S_{abs}, the center column S_{ax-rad} and the right column $S_{ax-circ}$.

S_{abs} shows that the resolved turbulence is above 80% in nearly the whole LES region even on the coarsest grid G0. However, regions where the sensor shows underresolution exist in the initial part of the shear layer with values as low as $S_{abs} \approx 0.6$ as well as near the symmetry axis in the second recirculation region. The axial refinement near the base wall clearly improves the resolved turbulence on grid G1, showing a substantially smaller region where $S_{abs} < 0.7$, especially very close to the separation location. This is improved further on grid G2, for which the lowest readings are a small region with $S_{abs} > 0.73$. The deterioration of grid resolution

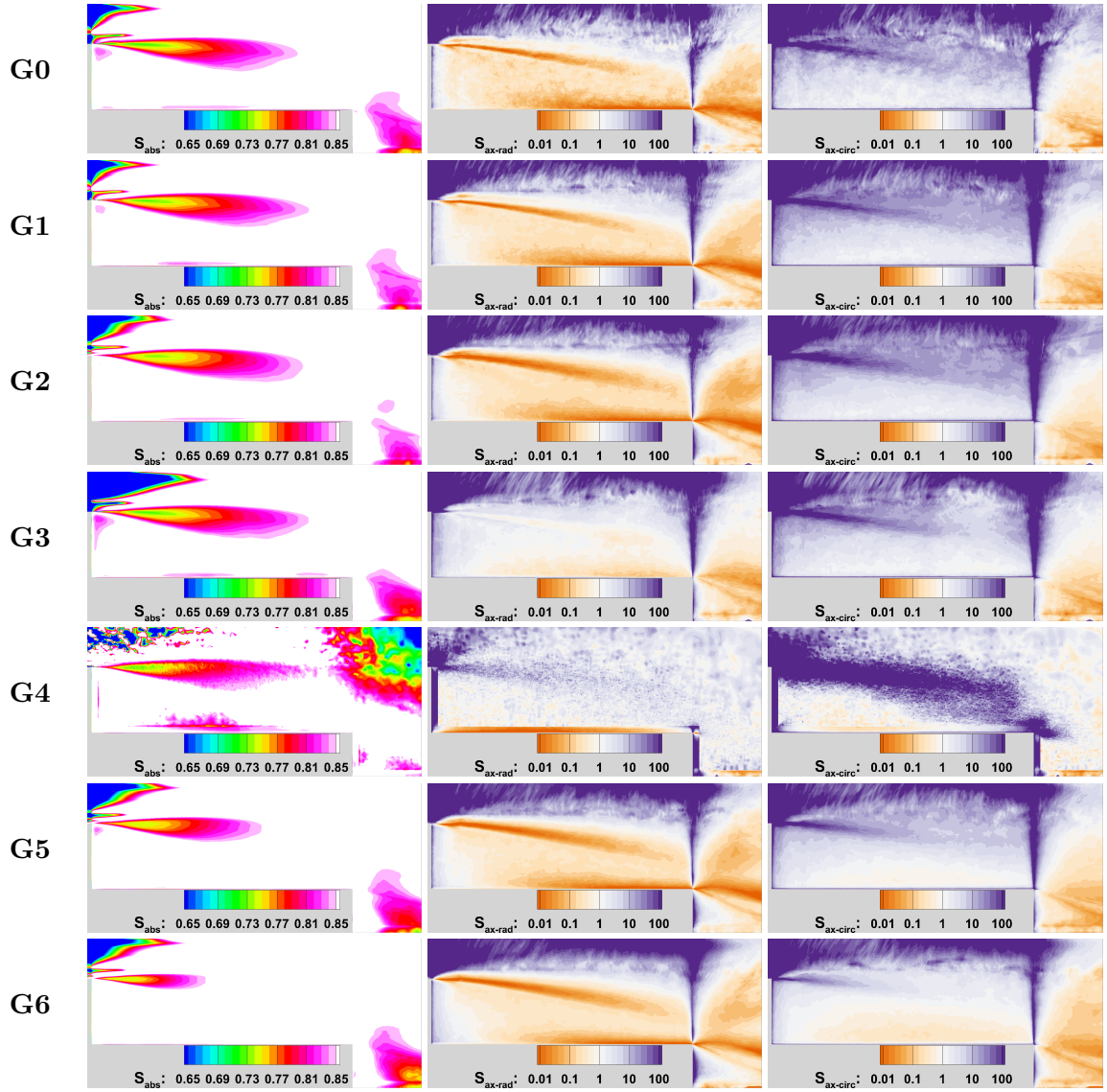

Figure 4.9: Grid sensor readings S_{abs} (left), S_{ax-rad} (center) and $S_{ax-circ}$ (right) for grids G0 to G6 (from top to bottom).

and resolved turbulence due to the coarser resolution for grid G3 compared to G1 is also present, with values slightly reduced from G1, but better than for G0. This is the case even though the resolution in the shear layer was not significantly reduced, but only that slightly below the shear layer, i.e. in a region where $S_{abs} > 0.8$ on grid G1. This shows that the grid sensor depends not purely on the resolution in the evaluated area, but also on the resolution in nearby regions. For the grid with unstructured elements G4 S_{abs} shows very similar values to G1 directly after separation since in this region the structured wall layer with similar resolution

to G1 is present. At the interface to unstructured elements the resolved turbulence is suddenly improved above $S_{abs} > 0.8$ due to the much smaller cell sizes in the axial direction. As the cell sizes increase further downstream the resolved turbulence reduces again towards similar values as for G1 with $S_{abs} > 0.73$. The strong coarsening in this grid away from the recirculation region is also visible by the strong decrease of S_{abs} in the top right corner of the visualization. For increased circumferential resolution S_{abs} shows a clear improvement from grid G2 to G5 and G6, with a much smaller region of $S_{abs} < 0.8$ in the shear layer. In fact, for grid G6 only a very small region remains where $0.75 < S_{abs} < 0.8$. Interestingly, S_{abs} actually deteriorates in the region behind the second cylinder even though the resolution is increased. This is an indication that this region is not adequately resolved since it deteriorates upon refinement.

The directional sensor S_{ax-rad} on grid G0 indicates that in most regions the radial direction is over-resolved, particularly in the shear layers and near the wall of the second cylinder. This is to be expected since in these regions the radial resolution is determined by the wall spacing which has to be in the order of $\Delta y_w^+ < 1$ and cannot be radically increased without creating very skewed grid cells. An axial over-resolution is only indicated towards larger radii where the radial resolution is reduced while the axial resolution is not. Another region of axial over-resolution is visible above the end of the second cylinder, which is due to the axial resolution required to achieve a unity non-dimensional wall spacing at the base wall of the second cylinder.

The distribution of this sensor does not change significantly on grid G1 with the exception of the region near the main base wall where the radial over-resolution is reduced. This shows that the grid sensor properly picks up the resolution changes since this was the only region of changed resolution between grids G0 and G1. For grid G2 the only change is visible in the shear layer where the sensor indicates that the radial over-resolution is increased which matches the refinement executed.

On grid G3 S_{ax-rad} shows values around unity in the whole recirculation region due to the coarsening approach being applied according the sensor readings on grid G1. This shows that the general principle of coarsening to achieve better grid sensor readings works, but in combination with S_{abs} (discussed above) it also shows that the coarsening should be less aggressive. A possibly better approach would be to apply a slight coarsening in combination with refining of the other direction, e.g coarsen the radial resolution below the shear layer less aggressively and in addition refine the axial resolution for $0.1 < x/D < 0.6$. This might achieve both $S_{ax-rad} \approx 1$ and $S_{abs} > 0.8$.

The results on the unstructured grid G4 show a similar distribution to G3, with values around unity in most of the recirculation region. A slight over-resolution in the axial direction is visible in the shear layer. This indicates that the shear layer requires cells that are slightly finer in the radial than the axial direction, as expected.

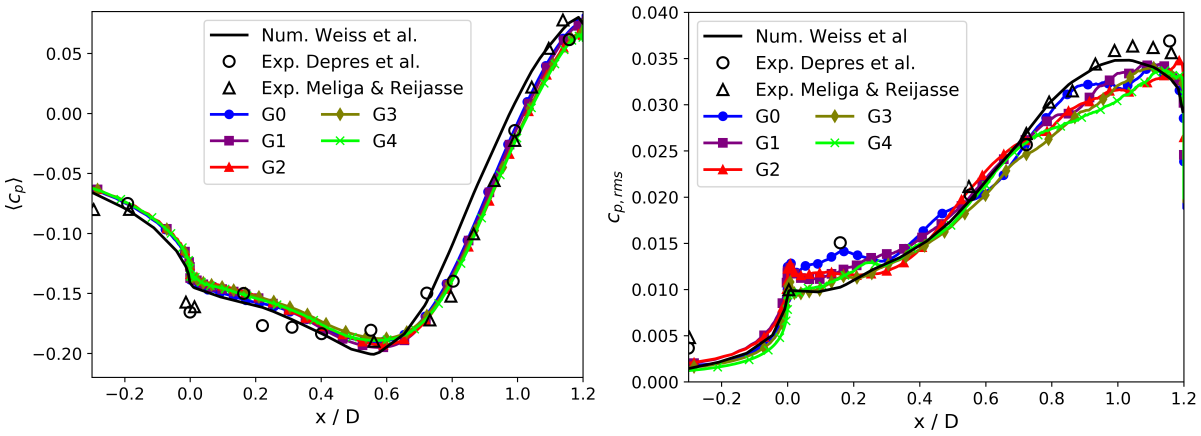

Figure 4.10: Mean (left) and rms (right) wall pressure for grids G0 to G4.

For the grids with different circumferential resolution (G2, G5, G6) the directional sensor for the in-plane resolution S_{ax-rad} shows expectedly very similar distributions, but the sensor shows values slightly closer to unity for the refined resolution. This indicates that this sensor is also not completely independent of the resolution in the non-considered direction.

The other directional sensor $S_{ax-circ}$ shows very similar distributions for grids G0 to G3 indicating an over-resolution in the axial direction over the circumferential direction, particularly for larger radii. The similar behavior on these grids is to be expected due to the similar axial resolutions and the unchanged circumferential resolution between these grids. Small changes are visible for grid G3 in the area above the reattachment region where an axial coarsening is applied and hence the sensor is closer to unity. For the unstructured grid G4 the over-resolution in the axial direction is even more pronounced, albeit only in the shear layer since the resolution is decreased away from this region. Clear differences are also observable for grids G5 and G6 for which the strong axial over-resolution disappears more and more with refined circumferential resolution. In turn, the circumferential over-resolution at lower radii (behind the second cylinder and directly above the second cylinder) increases.

4.3.2 Results for in-plane grid refinement and topology change

The qualitative flow fields on grids G0 to G4 are nearly indistinguishable and the representative flow field for grid G2 is shown in Fig. 4.5. Figure 4.10 shows a comparison of the axial distribution of the mean and rms wall pressure coefficients along with numerical and experimental data from Weiss et al. [73]. It is visible that results for the mean pressure on all grids agree well with the literature data and differ only minimally between grids. Slightly larger differences are visible for the pressure fluctuations, but no clear trend can be observed. Compared to the

experimental and numerical reference data, on all grids the minimum in mean wall pressure and maxima in rms wall pressure are shifted slightly downstream, indicating a slightly later reattachment position in the current investigation than in the experimental setup. The mean reattachment location x_r, defined as the location where the mean axial velocity gradient at the wall approaches zero, is shown in Tables 4.3 and 4.4. It is visible that the reattachment location only differs marginally, varying between $1.174D$ on the initial grid G0 and $1.180D$ (+0.5%) on grids G3 and G4.

The left column of Fig. 4.11 shows a spectral analysis of the wall pressure data. Displayed is the scaled premultiplied Power Spectral Density (cf. Section 3.7) as color contours over axial position and (logarithmic) Strouhal number $\mathrm{Sr}_D = \frac{f \cdot D}{U}$. The overall appearance is very similar for all grids, with a shift from lower frequency contributions at upstream positions towards higher frequencies near the end of the second cylinder. On all grids broadband content centered around $\mathrm{Sr}_D \approx 0.6$ towards the end of the second cylinder, i.e. for $x/D > 0.9$, is visible that was also visible in all reference data sets. All spectra also show an increased amplitude near the base ($x/D < 0.2$) at frequencies around $\mathrm{Sr}_D \approx 0.1$. The dominant spectral feature, the peak at $\mathrm{Sr}_D \approx 0.2$ in the region $0.4 < x/D < 0.8$, is clearly visible on all grids except for the initial grid G0 where it is very faint and shifted upstream. This is noteworthy since the number of grid points between G0 and G1 differs only by about 2% and those points were exclusively used to increase the axial resolution directly behind the step. The extent and strength of the peak between the remaining cases also differs slightly, with amplitude increasing from G3 to G1 to G2 to G4.

A quantitative comparison of the spectra at a location in the center of the recirculation region and in the reattachment region is shown in Fig. 4.12. This shows that the peak height also compares well with the experimental data from literature [33]. At the first evaluated location in the center of the recirculation region ($x/D = 0.6$) grids G1, G2 and G4 show very similar distributions that agree to within 10% with the experimentally observed amplitude. On grid G0 the amplitude is drastically lower and on grid G3 the amplitude is also reduced compared to G1, G2 and G4. However, the exact amplitude differs between axial locations as is visible in Fig. 4.11 and at a slightly further downstream location $x/D = 0.7$ the amplitudes for G1, G2 and G3 are actually very similar. Moreover, as detailed in Sec. 4.1, the exact observed peak amplitudes differ between publications and also depend on spectral content at other frequencies due to the scaling process. This is also visible in the numerical data [61] that is plotted in the figure which shows a much lower main peak amplitude, but shows additional peaks.

At the end of the second cylinder ($x/D = 1.15$) all spectra show broadband spectral content around $\mathrm{Sr}_D \approx 0.6$ with large deviations in the individual spectra peaks. One detail that is visible is that for grids G1 to G4 a peak of varying intensity at $\mathrm{Sr}_D \approx 0.2$ is visible whereas on

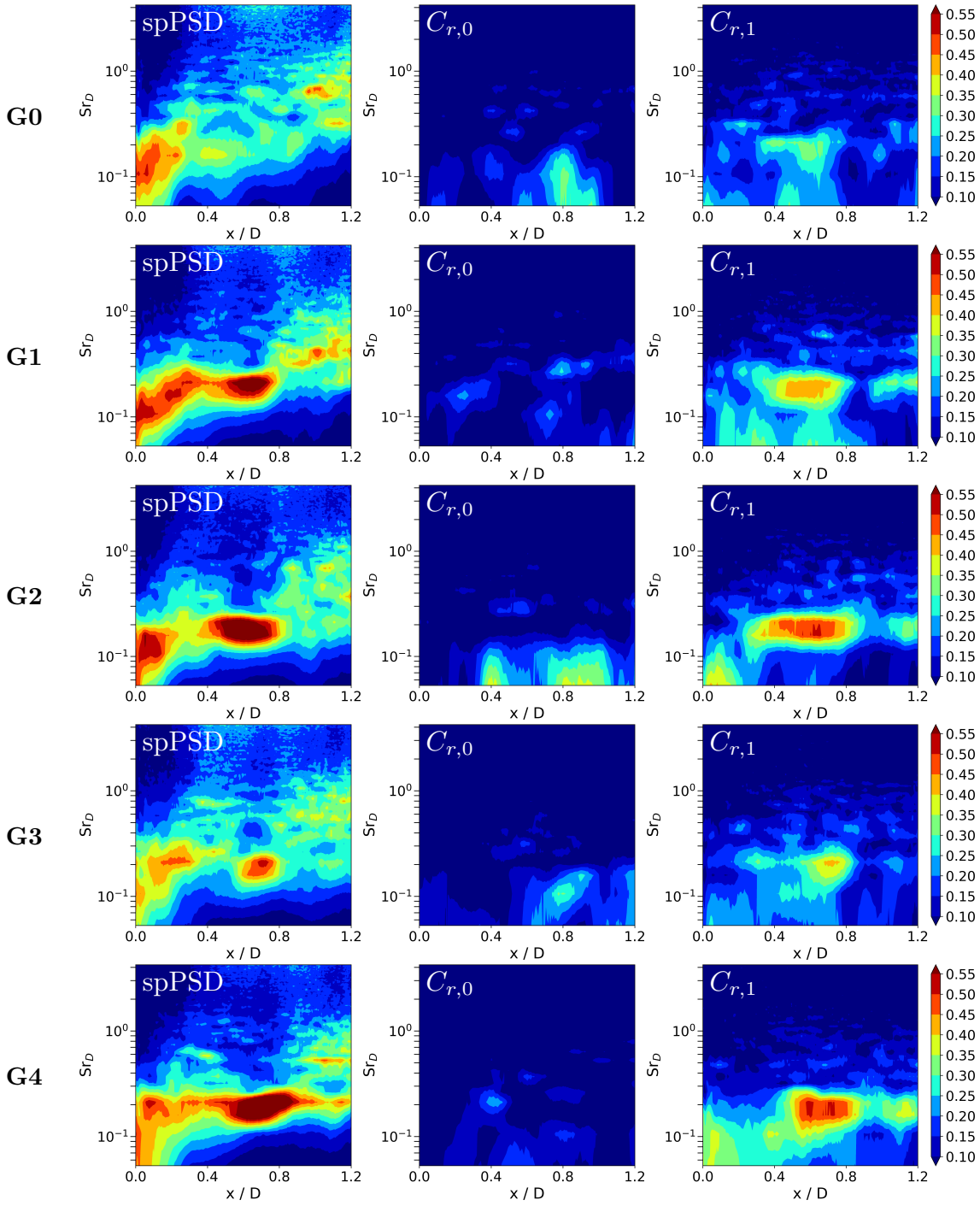

Figure 4.11: Wall pressure spectral content and circumferential coherence modes of the external nozzle surface wall pressure for grids G0 to G4 (from top to bottom).

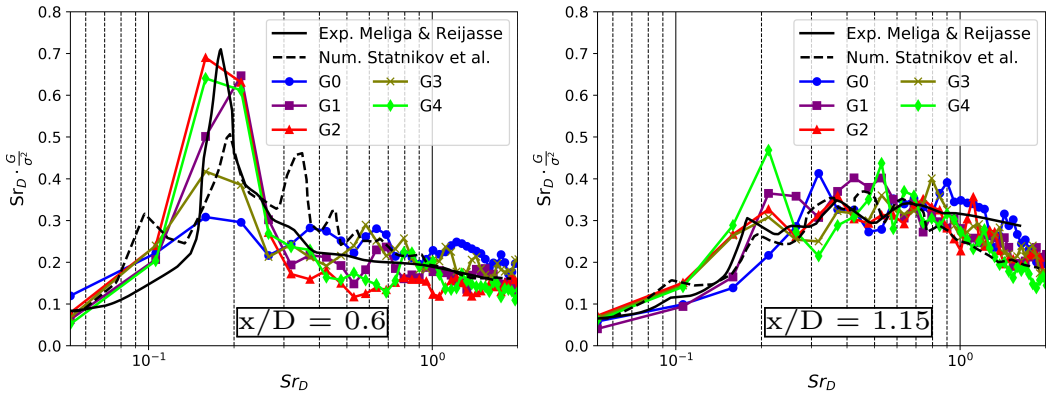

Figure 4.12: Wall pressure spectra at two locations for grids G0 to G4. Exp.: [33], Num.: [61].

grid G0 this does not appear.

The center and right column of Fig. 4.11 show a visualization of the circumferential coherence modes $C_{r,0}$ and $C_{r,1}$, in a similar fashion to the spectral content in the left column. It is visible that the amplitude of the symmetric mode $C_{r,0}$ is very small, except for small frequencies $\mathrm{Sr}_D \leq 0.1$ in the center of the recirculation region for some cases. However, no clear pattern emerges, possibly since this is very close to the minimum resolvable frequency. For the antisymmetric mode $C_{r,1}$ all grids show an increased amplitude in the center of the recirculation region for $\mathrm{Sr}_D \approx 0.2$. The strength of this feature corresponds closely to the overall spectral content at this frequency for the respective grid, i.e. grids G2 and G4 show the highest amplitudes ($C_{r,1,max} \approx 0.6$). With a lower intensity some content at lower frequencies $\mathrm{Sr}_D \leq 0.1$ is also visible, for most cases towards upstream axial locations $x/D < 0.2$.

The resulting buffeting force spectra are shown in Fig. 4.13 as scaled premultiplied PSD. On all grids the peak in the buffeting loads around $\mathrm{Sr}_D \approx 0.2$ is visible, but the initial grid G0 clearly deviates and shows a lower amplitude as well as a shift towards slightly higher frequencies. Grid G1 shows a second peak around $\mathrm{Sr}_D \approx 0.43$ that is not visible on any other grid and on grid G3 there are slightly increased levels for $\mathrm{Sr}_D > 0.5$, but less pronounced than on grid G0. The spectra for G2 and G4 are very similar, showing only very small deviations from each other and no other clear peaks aside from the main peak.

4.3.3 Results for circumferential grid refinement

In the following the effect of circumferential resolution on the results is investigated by comparing results on grids G2, G5 and G6 (cf. table 4.4). In contrast to the resolution changes in axial or radial direction discussed above, the effect of changes in circumferential resolution is much more pronounced and changes even the mean flow field.

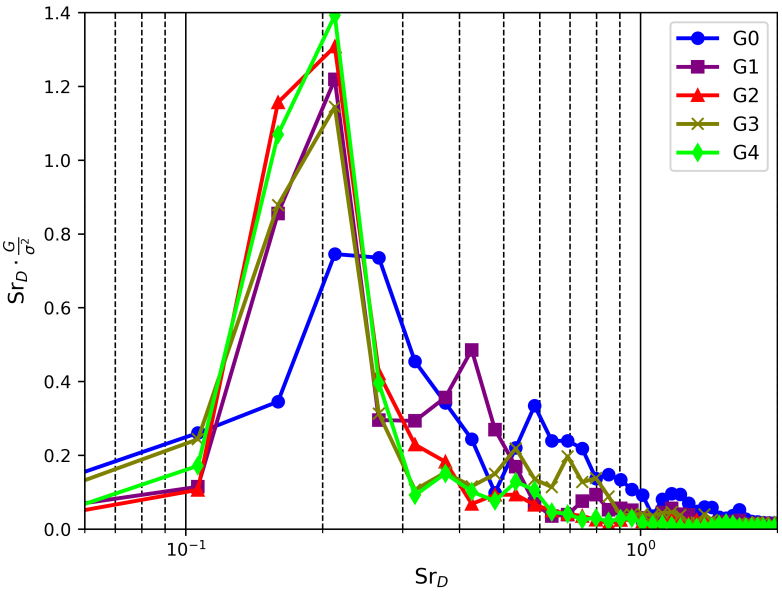

Figure 4.13: Force spectra for grids G0 to G4.

This is visible in Fig. 4.14 which shows streamlines based on mean velocity and the mean axial velocity as a color contour near the end of the second cylinder. Whereas a clear reattachment on the second cylinder is visible for results on grid G2, results on grid G6 show a flow field in which the recirculation regions above and behind the second cylinder merge and no reattachment is visible any more. The second recirculation region also grows, both in axial and radial direction, for the finer grids with the end of the recirculation being at $x/D \approx 1.45$ for G2 and $x/D \approx 1.6$ for G6. The radial growth in combination with higher velocities in the second recirculation region prevents a reattachment close to the nozzle lip and leads to a vortex appearing at the end of the second cylinder. The results on grid G5 still show a reattachment, but also feature the vortex - if smaller - as well. They can thus be interpreted as an intermediate state between G2 and G6. In the following results are mainly compared on grids G2 and G6.

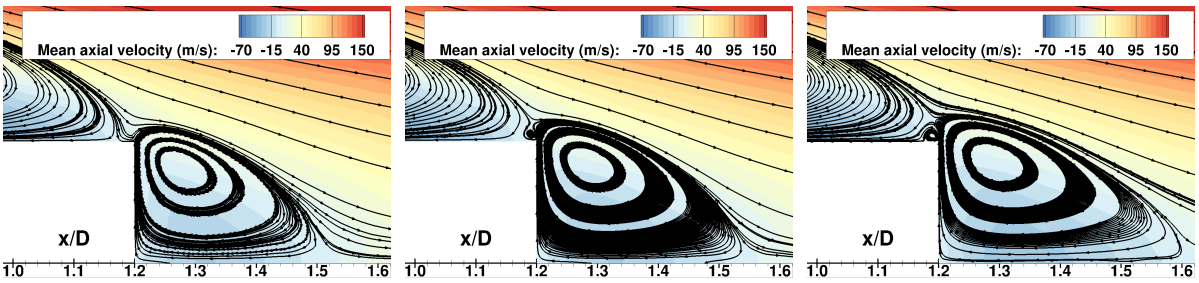

Figure 4.14: Averaged flow field at the end of the recirculation region for grids G2 (left), G5 (middle) and G6 (right).

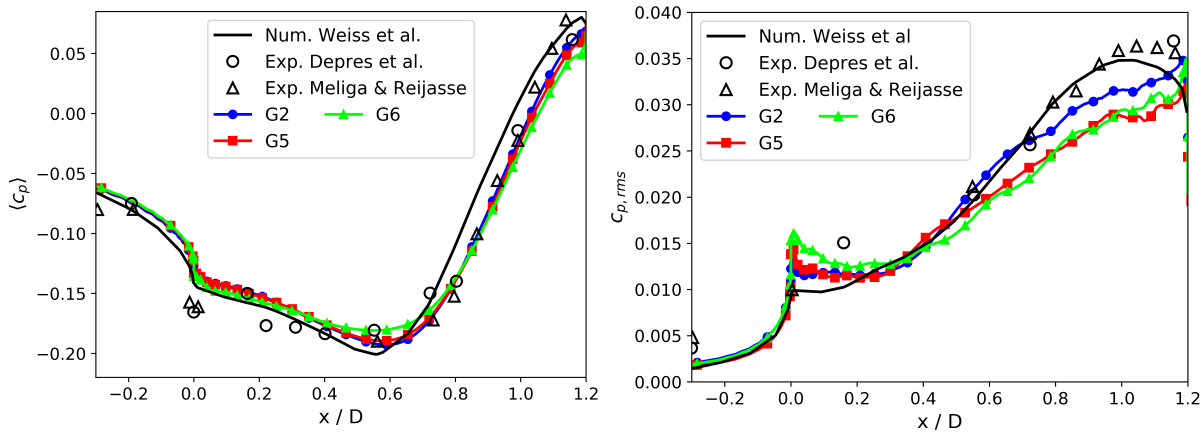

Figure 4.15: Mean and rms wall pressure coefficients for grids with changing circumferential resolution.

The change in flow topology is also visible in mean and rms wall pressure coefficients in Fig. 4.15. Whereas the mean pressure on grids G2 and G5 shows very similar behaviour, it differs on grid G6. G6 shows a lower pressure gradient than G2 in the first part of the main recirculation region with a lower pressure in the base corner ($x/D = 0$) and a higher minimum pressure ($x/D \approx 0.55$). Additionally, the pressure at the end of the second cylinder is lower than on grid G2, leading to a lower pressure gradient in the second half of the recirculation region as well. The rms pressure distribution indicates more pressure fluctuations near the base wall for G6, but clearly reduced rms values for $x/D > 0.4$ on grids G5 and G6. Even though the mean reattachment location shown in Table 4.4 is the same on all grids, from the stream lines in Fig. 4.14 it is apparent that for grid G6 $\frac{\partial u}{\partial r}_{wall} = 0$ (i.e. the condition used to determine flow reattachment) does not actually represent the shear layer reattachment location - which does not exist - but instead the upstream end of the vortex at the nozzle lip.

The differences between grids G2 and G6 are also clearly visible in contours of the scaled premultiplied Power Spectral Density of the wall pressure which is shown in Fig. 4.16. For all grids the peak at $Sr_D \approx 0.2$ is visible, but this peak is shifted further downstream to $0.55 < x/D < 0.9$ (G2: $0.4 < x/D < 0.8$) and is less pronounced for grid G6. Instead, an additional strong peak is visible at $Sr_D \approx 0.4 \ldots 0.5$ in the region between $1.0 < x/D < 1.2$ that is related to the new vortex seen in the mean flow field. From individual snapshots it becomes clear that this vortex moves - and sometimes disappears - over time, leading to the strong peak in the spectrum. Smaller peaks with this frequency appear further upstream as well and the broadband frequency content around $\mathrm{Sr}_D \approx 0.6$ for $x/D > 0.9$ is completely dominated by this new strong peak.

The circumferential coherence modes displayed in Fig. 4.16 differ less clearly from those on the

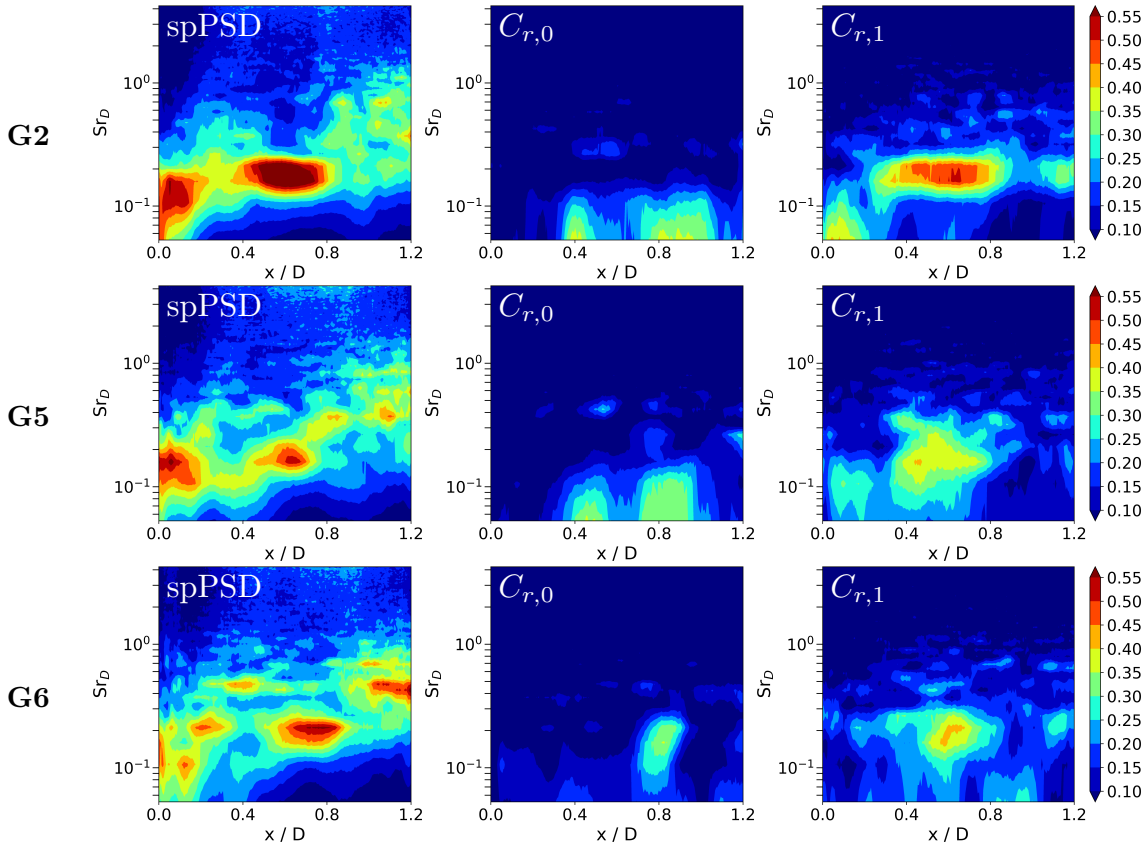

Figure 4.16: Wall pressure spectral content and circumferential coherence modes on the external nozzle surface for grids G5 (top) and G6 (bottom).

coarse grid G2. However, it is visible that the peak for $C_{r,1}$ is less distinct and more smeared across different frequencies. Similarly, the buffeting force spectra in Fig. 4.17 only show small differences, with a slightly reduced peak amplitude for the finer grids as well as a slightly increased spectral content for $0.3 < \mathrm{Sr}_D < 0.5$.

4.3.4 Discussion of grid sensitivities

The results show that the sensitivity of the mean flow field and reattachment length as well as spectral content of pressure and force history is very insensitive to in-plane refinement, with the exception of the axial spacing in the initial part of the shear layer (G0 to G1). In contrast, the circumferential resolution has a significantly bigger impact on mean flow field and pressure spectra, whereas force spectra remain similar.

Evaluating the grid sensors one can state see that they are able to capture the changes in grid resolution and the grid sensor output confirms the changes in the obtained solutions: The

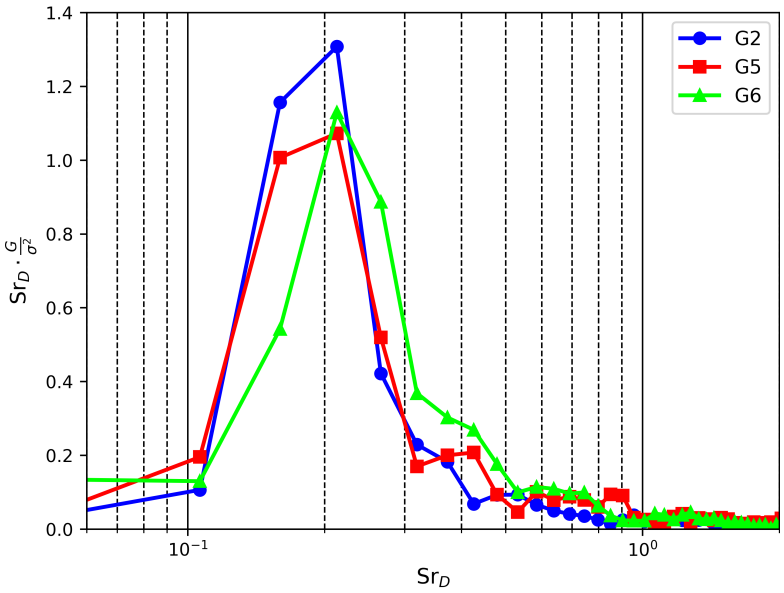

Figure 4.17: Force spectra for grids with changing circumferential resolution.

improvement in the spectral content and buffeting loads from G0 to G1, the further slight improvement from G1 to G2, the slight deterioration from G1 to G3 and the similar quality of results on the unstructured grid G4 to grids G1 and G2 being reflected in the grid sensors readings are all reflected in S_{abs}. Additionally, the differences between grids G2, G5 and G6 are also reflected. Furthermore, the combination of S_{abs}, S_{ax-rad} and $S_{ax-circ}$ allows to pinpoint areas and direction of refinement. However, it was shown that the sensors are also slightly affected by changes in resolution that they are not supposed to be evaluating, e.g. S_{abs} decreases in the shear layer even though resolution was only decreased in adjacent grid regions and the in-plane resolution sensor S_{ax-rad} shows small differences for different circumferential resolutions. Hence, the sensors are a very useful tool to evaluate sufficient resolution and possible avenues of grid improvement, but still require some trial and error procedure to find optimal grid designs. It should also be noted, however, that the grid sensor show converged results after significantly less time steps than what is necessary for meaningful spectral analysis [66]. Thus, the trial and error procedure is still much faster than when not using grid sensors.

The drastic differences - not just in the quantitative analysis, but in the qualitative mean flow field - for the grids with changed circumferential resolution are surprising. Even more so, since neither the vortex at the end of the second cylinder nor a merged recirculation region were observed in the previous experimental [9] or numerical investigations [71, 73]. It is counter-intuitive to assume that a refinement of grid resolution - and thus reduction of numerical errors - should negatively affect the accuracy of the solution. Thus other possible explanations are

investigated.

One hypothesis for the drastic changes is that they originate from the reattachment location being predicted slightly too far downstream on all grids. This is supported by the fact that on all investigated grids the resulting wall pressure data shows the minimum mean wall pressure always slightly further downstream and does not show the distinct peak in rms pressure that is visible in the experimental or numerical literature data [73]. The reason for this difference is not clear, but could be related to slightly different free stream conditions. Uncertainties in the inflow conditions stem from the low amount of data available on the boundary layer conditions aside from the boundary layer thickness. Additionally, effects from the wind tunnel layout cannot be ruled out either.

The late reattachment of the shear layer just before the end of the second cylinder then makes the whole flow field more susceptible to effects from changes in the second recirculation region as well as small changes in the computed reattachment length, than a reattachment further upstream would. When the second recirculation region grows, both in axial and in radial direction as is the case for grid G6, two separate recirculation regions cannot be maintained and thus they merge, preventing reattachment of the shear layer and changing the qualitative flow field.

Following this hypothesis the main effect of circumferential grid refinement is on the secondary recirculation region and the changes in this region are affecting the remainder of the flow field. Since structures that interacted in the main shear layer and impinged on the surface are transported into the secondary shear layer it does seem likely that the proper resolution of the structures behind the model requires a finer resolution. Hence, the circumferential refinement has a larger impact in this region due to the smaller structures than on the larger structures in the main shear layer.

One possibility to confirm this hypothesis would be to modify the inflow conditions such that the reattachment is shifted further upstream and recompute the solution on grids G2 and G6. Another possibility is to remove the second recirculation region and thus prevent it from affecting the main recirculation region, which can be achieved by a plume exiting the second cylinder. In either case, no impact of circumferential grid refinement should be visible and results on grids G2 and G6 should not differ significantly.

Since the target geometry, i.e. a generic space launch vehicle with hot plume, features a plume[2], the latter option is chosen and investigated in subsection 4.3.5. An additional advantage of this choice is that experiences for this type of flow can be obtained that might be helpful for the investigations in chapter 5.

[2]The geometry without plume in the current investigation was merely chosen for - supposed - simplicity.

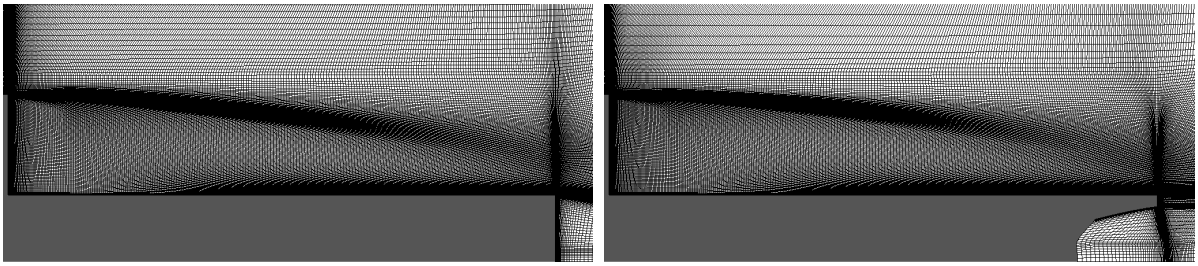

Figure 4.18: In-plane grids without plume (for grids G2 and G6,left) and with plume (for grids G2b and G6b, right).

4.3.5 Results with active air plume

Two additional grids G2b and G6b for the geometry with an active air plume are investigated. Both grids feature the same circumferential resolution and essentially the same in-plane resolution in the majority of the domain as grids G2 and G6, respectively. Small differences appear due to the nozzle in the second cylinder for grids G2b and G6b, which is discretized using a hexahedral grid, except near the axis, where prismatic elements are used again as described at the start of the section (Sec. 4.3). Additionally, the grid towards the boundaries is slightly coarser to compensate for the additional grid points in the nozzle. A comparison of the respective in-plane grids is shown in Fig. 4.18.

Due to deterioration of numerical stability once an active plume is added, the relaxation solver used to progress the inner iterations has to be changed from Backward Euler to a 3-stage Runge-Kutta scheme. However, the changes to the flow field introduced by this modification are expected to be minor since this change should predominantly affect the convergence of the inner iterations and only marginally the final converged state.

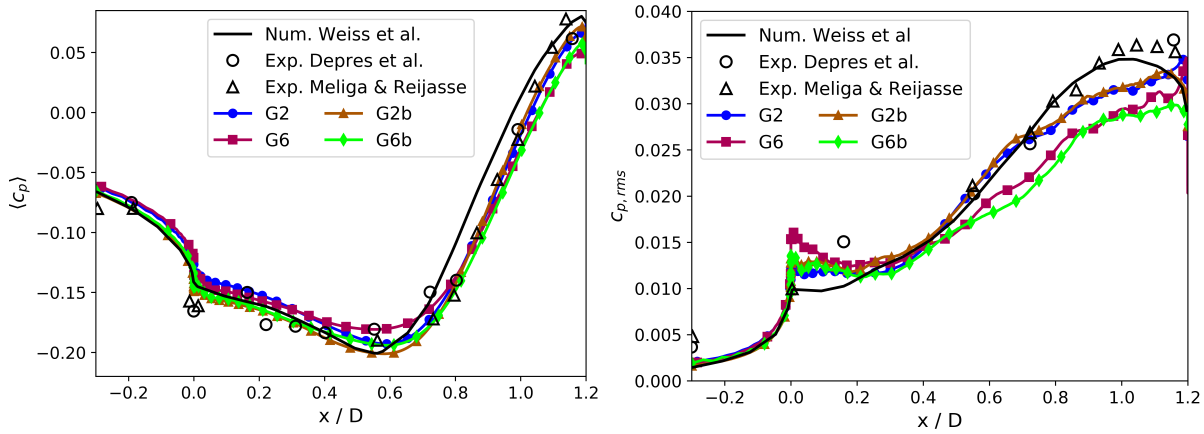

Figure 4.19: Mean and rms wall pressure with and without active plume.

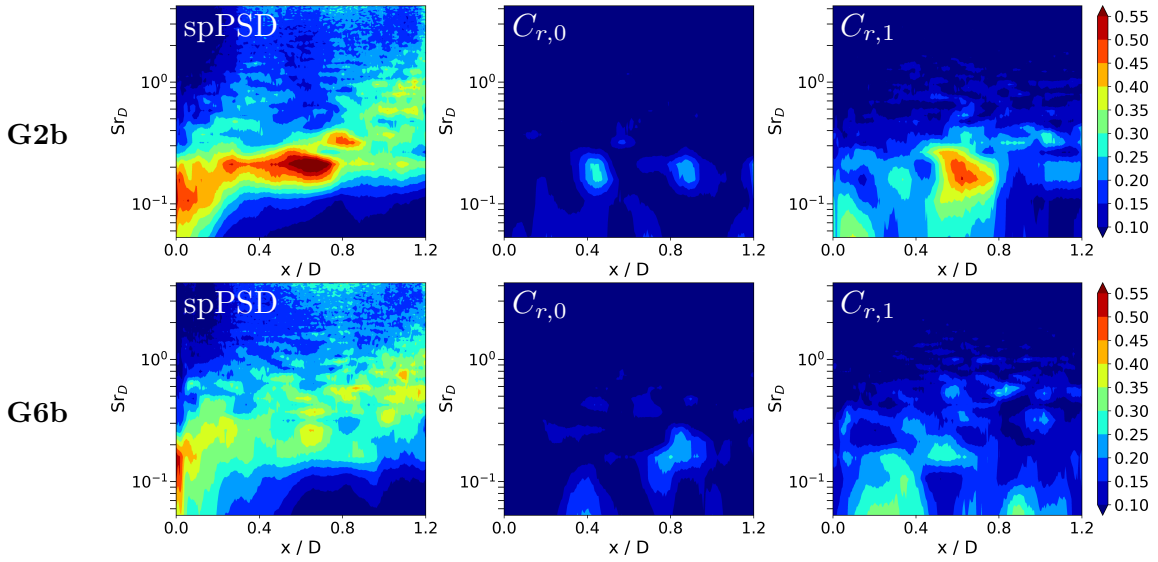

Figure 4.20: Wall pressure spectral content and circumferential coherence modes on the external nozzle surface with active plume.

The mean flow fields for grids G2b and G6b show no significant differences; a representative flow field is shown in Fig. 4.5. This confirms that the effect of circumferential resolution on the qualitative flow field shown in Fig. 4.14 was predominantly due to its impact on the second recirculation region. Hence, no critical influence of grid resolution on the qualitative mean flow field is expected for geometries with an active plume. However, quantitative differences in the mean wall pressure are visible as shown on the left of Fig. 4.19 where the results with the coarse and fine circumferential resolution with and without plume, respectively, are shown.

The mean pressure level in the upstream part of the recirculation region $0.0 < x/D < 0.4$ is clearly decreased by the presence of a plume, independent of circumferential grid resolution. This also matches the experimental observations by Deprés et al. [9]. On the other hand, the axial pressure gradient is mainly affected by the circumferential resolution, and only weakly by the presence of a plume: Both results on coarser grids (G2 and G2b) show a steeper pressure gradient in the upstream part of recirculation region and thus also a stronger minimum than the finer grids (G6 and G6b). Further differences with increased circumferential resolution are visible in the region $0.8 < x/D < 1.2$ where the coarser grids show again a slightly steeper pressure gradient. When comparing with the experimental reference data, the fine grid appears to capture the negative pressure gradient in the upstream part of the recirculation region better, whereas the positive pressure gradient in the downstream part is even stronger than that predicted on the coarse grid.

An interesting difference between the cases with and without plume can also be found in the

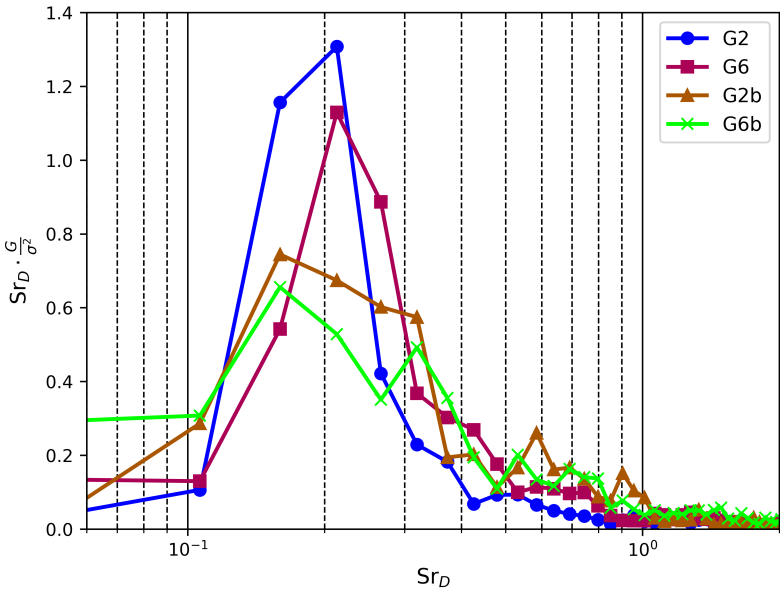

Figure 4.21: Force spectra with and without active plume.

distribution of pressure fluctuations on the right of Fig. 4.19. That is, the cases with an active plume show a peak in rms pressure coefficient around $x/D \approx 1.15$ that cannot be observed for the cases without plume. For the latter the pressure fluctuations continue to increase until the end of the second cylinder. This indicates a more stable reattachment for the cases with active plume as the peak in fluctuations is associated with the reattachment process [9]. Aside from this, the rms pressure distribution for the finer grids G6 and G6b agree reasonably well, as do results for the coarser grids G2 and G2b. Hence, only a small influence of the plume is found on the pressure fluctuations in the recirculation region, except near the mean reattachment position. An additional observation is that both with and without plume a circumferential refinement leads to a slight reduction in pressure fluctuations, particularly for $x/D > 0.5$.

The reattachment locations in Table 4.4 show that on the coarse grid, the presence of a plume shifts the reattachment location further upstream from $x/D = 0.179$ for grid G2 to $x/D = 0.172$ for grid G2b. However, the circumferential grid refinement shifts the reattachment location further downstream to $x/D = 0.187$ for grid G6b. This is likely a main factor for the strong change in the flow field for grid G6 compared to G2 (i.e. circumferential refinement without plume).

The spectral content of the wall pressure signal for the cases with active plume is visible in Fig. 4.20. The broadband turbulence around $\mathrm{Sr}_D \approx 0.6$ is clearly present for both cases. However, on the coarse grid the dominant peak $\mathrm{Sr}_D \approx 0.2$ appears for a much wider range of axial locations. as well as with clearly larger amplitudes. Additionally, on the finer grid

the peak is shifted towards slightly higher frequencies of about $\mathrm{Sr}_D \approx 0.24$. The decrease in amplitude appears to be caused by an increase in additional spectral content for frequencies within $0.4 < \mathrm{Sr}_D < 0.9$ as well as $\mathrm{Sr}_D > 2$. The peak at $\mathrm{Sr}_D \approx 0.2$ in the coherence mode $C_{r,1}$ also is drastically reduced for the fine grid, with the peak amplitude for $\mathrm{Sr}_D \approx 0.2$ only around 0.25 whereas it is 0.5 on the coarse grid.

Compared to the case without plume the results in spectral content and circumferential coherence appear fairly similar for the coarse grids (G2 and G2b). One interesting observation is that for both cases with active plume the spectra show a small peak at $\mathrm{Sr}_D \approx 0.3..0.35$ that was not visible in the spectra for the cases without plume in Fig. 4.16.

This feature is also visible in the force spectra displayed in Fig. 4.21. Both spectra with active plume feature an increased content at $\mathrm{Sr}_D \approx 0.35$, more clearly visible on the finer grid G6b. This additional peak in the spectra was also observed by Statnikov et al. [61] who also investigated a configuration with an active plume. This indicates that this feature might be due to an interaction between the external flow and the plume. In comparison to the cases without plume, the peak height of the main peak is in turn reduced. Additionally, the frequency of the main peak appears slightly reduced towards just below $\mathrm{Sr}_D \approx 0.2$ rather than above.

TODO Summary

4.4 Parameter study

In addition to the sensitivity to grid resolution in the following the sensitivity to changes in numerical parameters is investigated. This includes changes to the time step size, the used turbulence model, the fluid model, the applied filter length definition and in the data collection period. The time step size, turbulence model and fluid model variation are investigated on the coarse grid G2b, whereas the effect of filter length definition is investigated on the fine grid. The effect of the data collection period is investigated for the previous settings (cf. 4.2) on the coarse grid as well as for the settings with changed filter length definition on the fine grid. This is achieved by increasing the data collection period by a factor of two, i.e. data is collected for 76 CTUs instead of 38 CTUs. These cases are indicated with the suffix "Long". The solution with the previous settings on grids G2b acts as the reference solution for this investigation.

Ref.	Ref. Long	Δt_1	Δt_2	Turb. model	Fluid model	$\widetilde{\Delta}_\omega$	$\widetilde{\Delta}_\omega$ Long
1.172	1.170	1.170	1.177	1.176	1.185	1.169	1.170

Table 4.5: Mean reattachment location x_r/D for all investigated parameter variations.

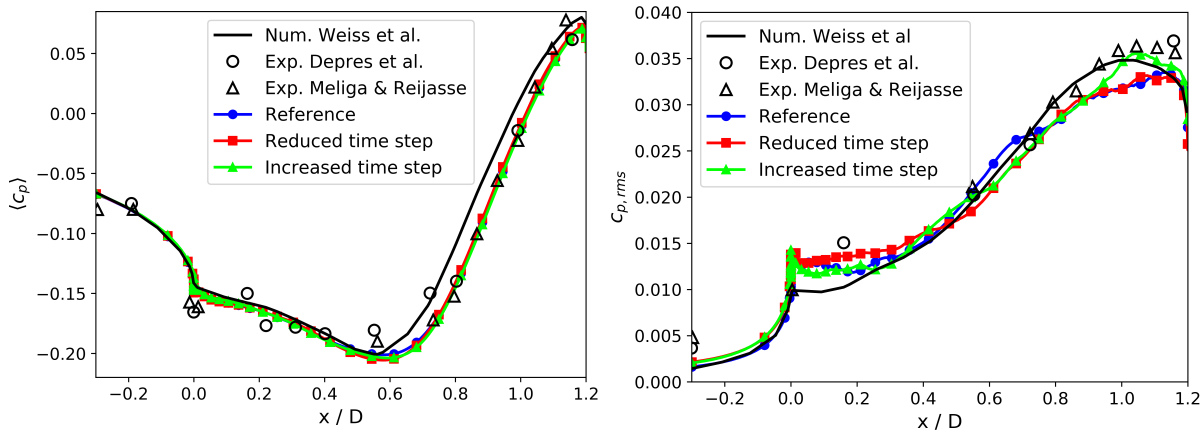

Figure 4.22: Mean and rms wall pressure coefficients for different time step sizes.

4.4.1 Mean flow field

The qualitative mean flow field does not change visibly between the different parameter settings and corresponds to that shown in Fig. 4.5. Quantitative changes in the mean flow are discussed in the following based on the reattachment locations shown in Table 4.5 as well as the pressure distributions in Figs. 4.22, 4.23 and 4.24.

Time step size

Since a dual time stepping scheme is used (see Sec. 3.2), no direct limitation of the chosen time step size Δt exists. A generally accepted approach to determine the time step for DES was proposed by Spalart [59] that determines the time step size as the ratio between the target grid spacing and the maximum velocity in the focus region (typically the free stream velocity), leading to an expression inspired by the Courant-Friedrichs-Lewy (CFL) number. This is equivalent to choosing the time step size such that the convection of the smallest resolvable structures can be captured. Using this approach with a target grid spacing equal to the axial resolution in the middle of the shear layer (i.e. at $x/D \approx 0.3$) and the velocity as the free stream velocity, a time step of $\Delta t_0 \approx 1 \cdot 10^{-6}$ s can be determined as was mentioned in Sec. 4.2.

However, it is also stated that this value can differ substantially between numerical schemes and is only an approximation [59]. Furthermore, the location of maximum velocity is not always the limiting one and the target grid spacing depends on the selected location, adding uncertainty in this regard as well. To check the sensitivity to the choice of the time step, two variations are tested, i.e. $\Delta t_1 = 0.5\Delta t_0$ and $\Delta t_2 = 2\Delta t_0$. This investigation uses the coarser grid G2b because the time step is determined by the axial and radial resolution since the velocity in circumferential direction is significantly lower and thus the temporal convection

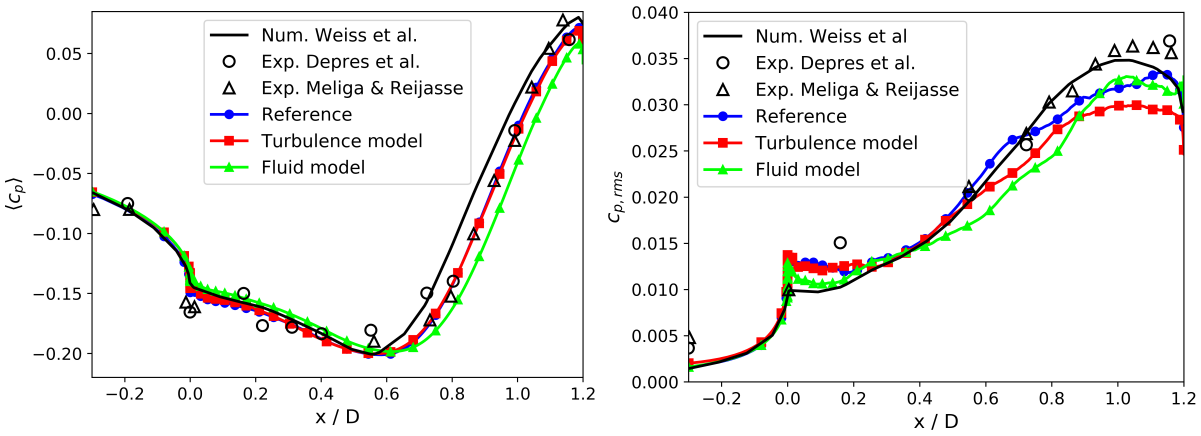

Figure 4.23: Mean and rms wall pressure coefficients for different modelling approaches.

of structures in this direction should not be limiting the time step size.

The mean reattachment location for both the reduced and the increased time step size agrees to within 0.4% with the reference solution (Δt_1: $x_r/D = 1.170$, Δt_2: $x_r/D = 1.177$). The obtained mean pressure distributions shown in Fig. 4.22 are nearly indistinguishable. The pressure fluctuations illustrated by the rms value of the pressure differ slightly more, in particular for the increased time step size, with the largest differences of about 11% appearing in the reattachment region.

Turbulence model

An IDDES approach based on the Spalart-Allmaras (SA) turbulence model [60] in its SA-negative formulation [2, 50] is employed to test the sensitivity of the results to the turbulence model. Aside from gaining an interesting insight into the behavior of different turbulence modeling approaches, this also provides an alternative in case the 2-equation approach encounters stability issues[3]. Additionally, since the SA model is a one-equation model, the computational resources are reduced by about 10% compared to computations with the k-ω SST model.

Similarly to the changed time step sizes, the reattachment location and mean pressure distribution in Fig. 4.23 remain essentially unchanged from the reference solution. The pressure fluctuations show small differences, again particularly in the reattachment region, with the SA model showing a slightly lower overall level of pressure fluctuations that also deviates further from the experimental data. The maximum deviations are again about 10%.

The small differences between the two turbulence models are surprising, considering that for

[3]The k-ω SST turbulence model was observed to be less stable than e.g. the SA model due to high gradients of ω near the model walls.

RANS computations the two models show significant quantitative differences in the computed flow field. For example, the reattachment location in axisymmetric RANS computations for the SA model is at $x/D = 1.028$, whereas the k-ω model predicts a reattachment at $x/D = 1.188$, leading to corresponding differences in the pressure distributions. An explanation for the reduced impact with IDDES settings is that in the IDDES approach the majority of turbulent fluctuations is resolved and only the smallest scales and regions with attached flow are dominated by the turbulence model. Both the small scales (due to their isotropy) as well as the near wall region (since turbulence models are often developed and tuned for attached flows) are modelled well by both 1-equation and 2-equation models. Hence, if the resolution is sufficient, it seems plausible for both turbulence model approaches to yield similar results with IDDES settings.

Fluid modeling

As was shown in Sec. 3.3.1, for simple test cases single and multi-species approximations of a gas agree well, with the remaining differences attributed to small differences in species properties and to differences in the detailed numerical algorithms. In order to further investigate the behavior the described aft-body flow computation is repeated, but instead of using a single perfect gas, realistic air consisting of five species (74% N_2, 26% O_2 and trace amounts of N, O and NO, details in appendix C) is used. For this investigation the grid G2b is used to conserve computational effort.

The fact that the qualitative mean and instantaneous flow fields do not differ significantly confirms the retained low dissipative properties for the multi-species implementation. However, upon closer investigation a downstream shift of the mean reattachment location by about $\Delta x_r/D \approx 0.013$ is visible for the multi-species approach. This is confirmed by the pressure distribution displayed in Fig. 4.23 which is shifted downstream compared to the reference settings. However, the pressure fluctuations between the two cases agree well and only show a small decrease in pressure fluctuations in the center of the recirculation region whereas the pressure fluctuations in the remaining recirculation region are very similar.

The differences can partially be attributed to small changes in the fluid properties due to the different fluid modelling resulting e.g. in different transport coefficients. However, the viscosity, for example, only differs by less than 0.3%. Hence, even though both approaches should yield identical solutions at the considered conditions, numerical changes in the algorithms due to the expanded modeling capabilities are the most likely reason for the observed quantitative differences, particularly in the computation of the internal energy at the face (equation (3.7)) and in the preconditioning (see appendix D).

The pressure distributions for both the reference case and that with changed fluid model still

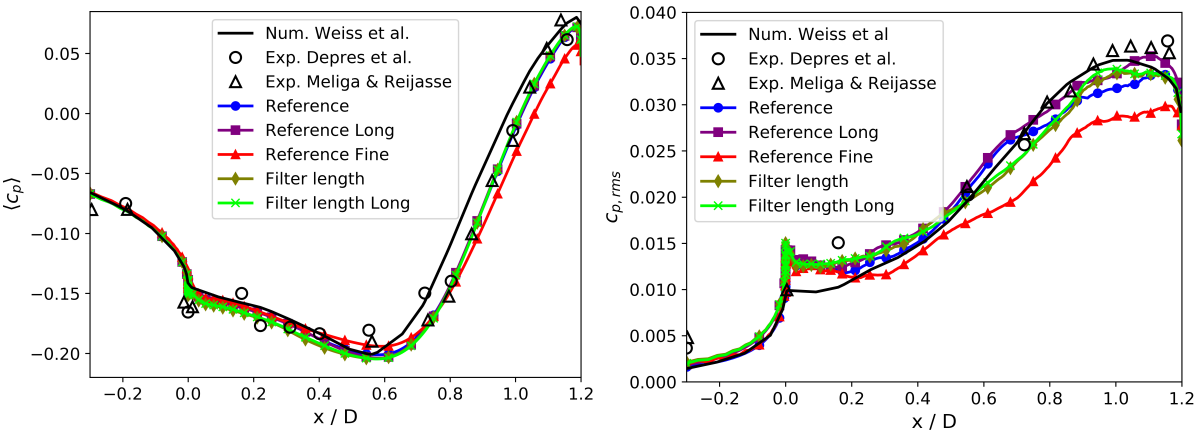

Figure 4.24: Mean and rms wall pressure coefficients for different filter length definitions and data collection periods.

agree reasonably with the experimental data. The average and maximum deviation in mean pressure coefficient between the reference settings and the more complex fluid model are only around 0.01 and 0.03 (relative pressure difference 0.4% and 1%), respectively. In terms of pressure fluctuations the difference in rms pressure coefficient from the reference solution is on average 0.0017 (8%) with a maximum deviation of 0.005 (21.5%).

Filter length definition

Since the general superiority of the $\widetilde{\Delta}_\omega$ definition over the Δ_ω definition is easily shown theoretically [40, 53], this investigation uses the fine grid G6b. This is to allow not only an estimation of the sensitivity of the solution to the changed filter length definition, but to also evaluate the general achievable accuracy with optimal settings (i.e. combination of best filter length definition and finest investigated grid).

Interestingly, with the improved filter length on the fine grid the reattachment location and pressure distributions in Fig. 4.24 are very similar to those obtained for the reference settings, i.e. on the coarser grid G2b with the suboptimal length scale definition Δ_ω, but differ considerably from the results on the finer grid G6b in subsection 4.3.3. Compared to the latter, the reattachment occurs significantly further upstream and the pressure distribution is shifted accordingly.

A possible explanation for this behavior can be found with the improved filter length on the fine grid the overall dissipation with the different settings. On the one hand, a finer circumferential resolution reduces the numerical dissipation due to the improved resolution. It is visible that this reduced dissipation leads to a downstream shift of the pressure distribution (G2b vs G6b), which appears logical since the momentum of the shear layer is dissipated less quickly. On the

other hand, the improved filter length definition prevents the filter length from approaching very small values for pencil shaped cells and hence increases the eddy viscosity in these cells, leading to higher dissipation from the turbulence model. Consequently, an upstream shift is observed with the optimized filter length which can be attributed to this increase in model dissipation since neither numerical settings nor the grid are changed. Comparing the solutions on the fine grid shows that the optimized filter length indeed increases the average eddy viscosity in the recirculation region by about 10%.

This also means that the objectively *better* solution on the coarse grid G2b compared to that on G6b is most likely due to a correct total dissipation for the wrong reasons: The excess numerical dissipation due to the coarse grid makes up for the lack in turbulent dissipation, leading to an approximation of the total dissipation on the coarse grid which otherwise can only be obtained with a more sophisticated filter length definition on the fine grid.

Data collection period

As described at the beginning of the chapter, the relatively short data collection period of 38 CTUs is chosen since with the available computational resources it is the only way to investigate a sufficient variety of different parameter influences. To investigate the effect of this choice, the data collection period is increased to 76 CTUs for two cases, namely the reference settings and the case with changed filter length definition (since it has objectively the best parameter settings).

The reattachment location (cf. Table 4.5) between the shorter and longer data collection period differs only marginally, as do the mean pressure coefficient distributions in Fig. 4.24. Slightly larger differences are visible in the rms pressure distributions, especially in the region $x/D > 0.8$, i.e. in the reattachment region, with differences of about 10% for the case with reference settings. For the case on the fine grid and the changed filter length definition the differences are even smaller.

4.4.2 Unsteady flow field

The scaled premultiplied PSD as well as the first two circumferential modes of the coherence function based on the wall pressure on the external nozzle surface for all considered parameter variations are displayed in Fig. 4.25. The corresponding visualizations with the reference settings on the coarse and fine grid are included as well.

For all considered cases a generally similar distribution of the spectral content is visible. However, differences in amplitude and axial extend of certain features are visible as well. Both cases with changed time step size show a more limited axial extend of the $\mathrm{Sr}_D \approx 0.2$ peak, and

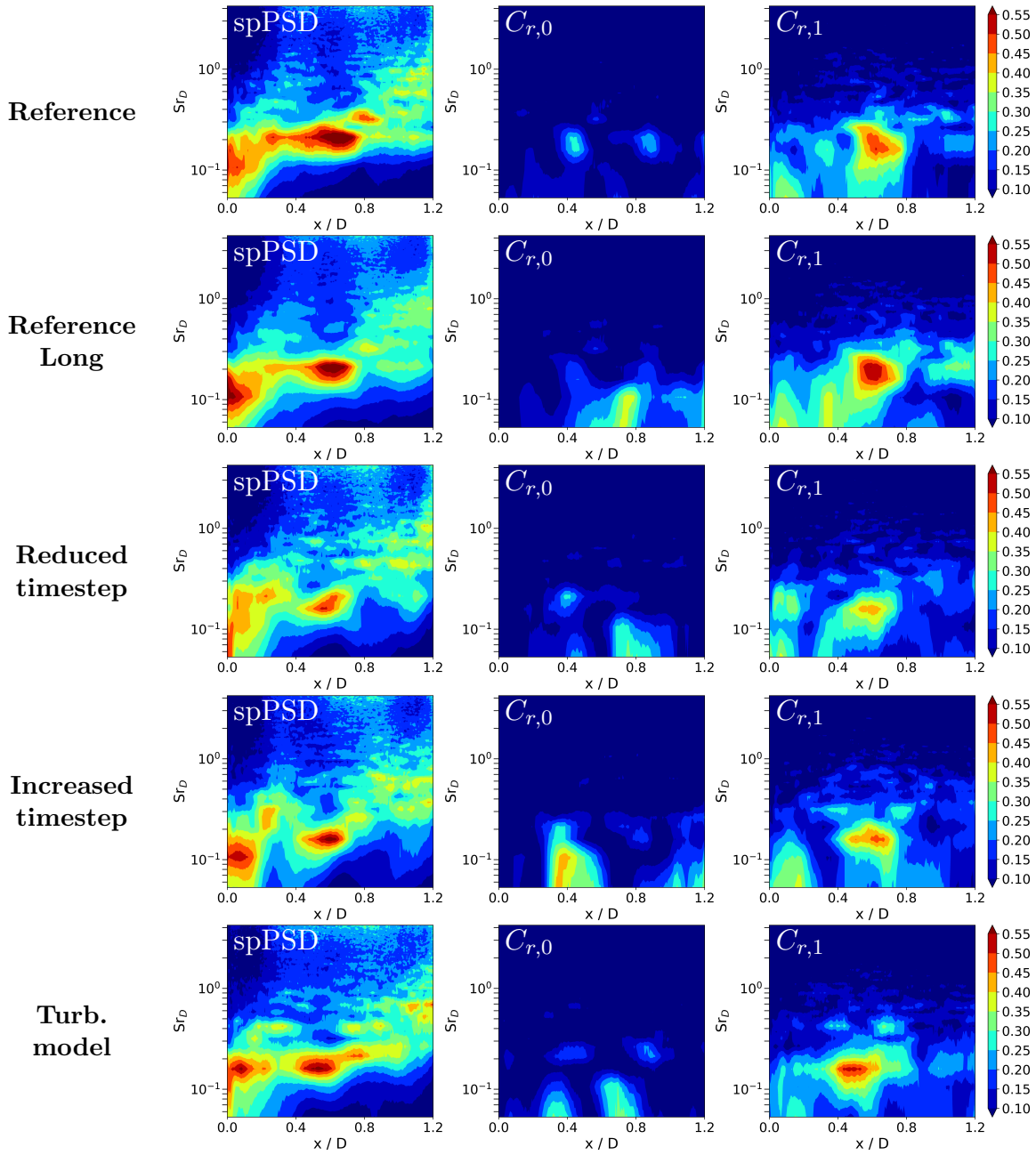

Figure 4.25: Wall pressure spectral content and circumferential coherence modes of the external nozzle surface wall pressure for parameter variations.

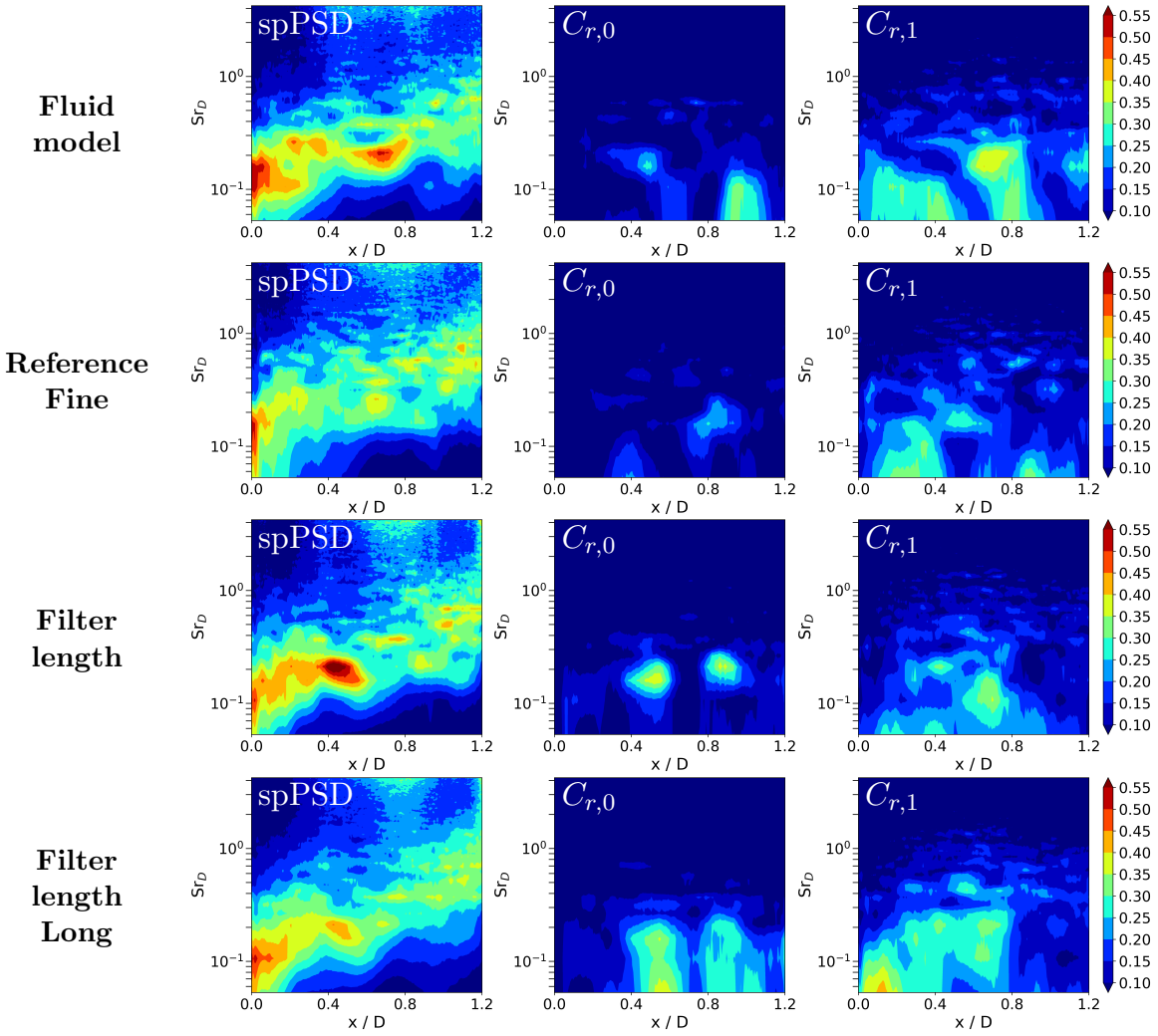

Figure 4.25: Wall pressure spectral content and circumferential coherence modes of the external nozzle surface wall pressure for parameter variations (ctd).

do not show the peak at $\mathrm{Sr}_D \approx 0.35$ as clearly. For the reduced time step size, the amplitude of the former peak is also reduced compared to the reference solution. With a change in turbulence model contributions around $\mathrm{Sr}_D \approx 0.2$ show an axial extend similar to the reference solution, with some contributions appearing even close to the base and as far downstream as $x/D \approx 1.0$. The changed fluid model shows the main peak with a slightly reduced amplitude, partially due to a larger axial extend of the peak at $\mathrm{Sr}_D \approx 0.35$. Additionally, in the region $0.2 < x/D < 0.4$ contributions with a slightly higher frequency than $\mathrm{Sr}_D \approx 0.2$ appear. For the case with the changed filter length a peak also appears at $\mathrm{Sr}_D \approx 0.2$, but is located further upstream around $0.3 < x/D < 0.6$, whereas for $0.6 < x/D < 0.8$ only a peak at $\mathrm{Sr}_D \approx 0.35$ is visible. With lower amplitude a contribution at $\mathrm{Sr}_D \approx 0.2$ is also visible for $0.2 < x/D < 0.4$

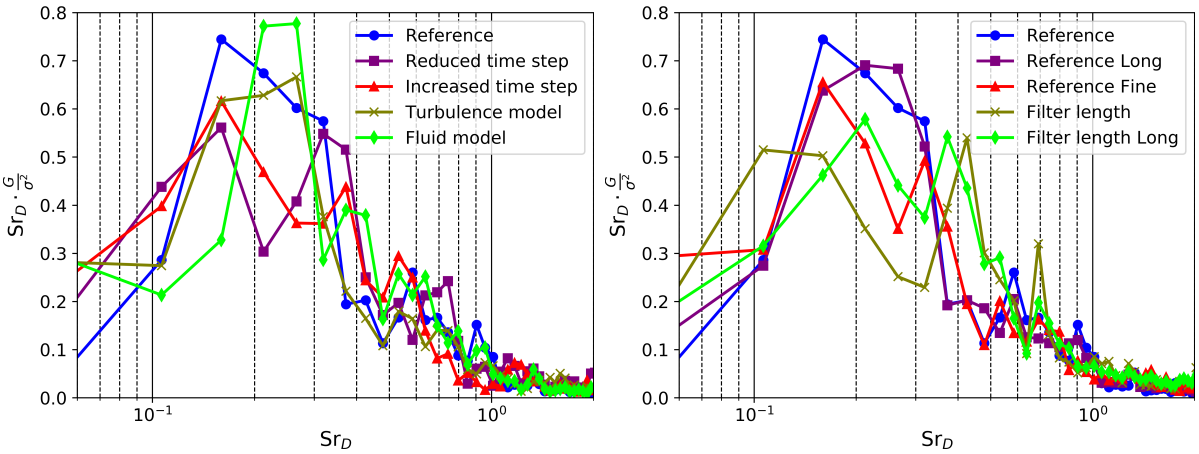

Figure 4.26: Force spectra for different parameter variations.

and for $0.8 < x/D < 1.0$. The differences to the case with reference settings on the fine grid and better agreement with that on the coarse grid are likely also related to the underestimation of the eddy viscosity with Δ_ω (as discussed above).

The increased data collection period has very little impact on the spectra for the reference settings. The contribution at $\mathrm{Sr}_D \approx 0.1$ is slightly stronger and the peaks around $\mathrm{Sr}_D \approx 0.2$ and $\mathrm{Sr}_D \approx 0.35$ are slightly reduced in strength. However, for the case on the fine grid (with the changed filter length definition) larger differences are visible. The amplitude of the upstream ($0.3 < x/D < 0.6$) and downstream ($x/D > 0.8$) part of the peak around $\mathrm{Sr}_D \approx 0.2$ is reduced and for $0.6 < x/D < 0.8$ the amplitude is increased. Additionally, the strength of the peak around $\mathrm{Sr}_D \approx 0.35$ is slightly reduced. This leads to a better agreement with the results with the reference settings. In general, the contours with the extended data collection period appear smoother and the noise levels are reduced. This is particularly visible for the broadband peak near the nozzle lip, where for the shorter data collection period random peaks are visible whereas for the longer period a more uniform amplitude distribution can be seen.

Regarding the circumferential modes of the coherence function, the results behave similarly to the pressure spectra with all cases showing a contribution in the center of the recirculation region for $C_{r,1}$. However, particularly for the case with reduced time step size, changed fluid model and changed filter length definition the amplitude is reduced. For the latter the frequency of the contribution is also shifted towards lower frequencies around $\mathrm{Sr}_D \approx 0.1 \ldots 0.15$. For $C_{r,0}$ most cases show some contribution for $\mathrm{Sr}_D < 0.1$, but with no clear agreement on the axial location. As mentioned in Section 4.3 the minimum resolvable frequency is likely too low for a reliable evaluation of this contribution. For the case with changed filter length definition two distinct peaks appear for $C_{r,0}$ around $\mathrm{Sr}_D \approx 0.2$ at $x/D \approx 0.5$ and $x/D \approx 0.9$ that are also

observable with reduced amplitude for the reference case. Similarly to the pressure spectra, the cases with increased data collection period also show smoother distributions for the coherence modes. For both longer data collection cases the peak for $C_{r,1}$ around $\mathrm{Sr}_D \approx 0.2$ appears slightly stronger and the contribution for $\mathrm{Sr}_D < 0.1$ increases for both $C_{r,0}$ and $C_{r,1}$.

Finally, the scaled premultiplied spectra of the buffeting loads are displayed in Fig. 4.26. It is visible that a peak around $\mathrm{Sr}_D \approx 0.2$ is visible for all cases except for that with the changed filter length, for which it is located around $\mathrm{Sr}_D \approx 0.1 \ldots 0.15$. This case also shows a secondary peak located around $\mathrm{Sr}_D \approx 0.42$. However, also the amplitude and exact distribution of the spectra for the other cases differ: Some cases (reduced time step, increased time step, fluid model) show a clear peak around $\mathrm{Sr}_D \approx 0.35$ whereas others do not. Similarly, the main peak frequency is shifted towards $\mathrm{Sr}_D \approx 0.25$ for some cases (turbulence model, fluid model). This behavior indicates that the spectra of the buffeting loads are very sensitive to the parameter changes and/or that the data collection period for a quantitative evaluation of this quantity is insufficient. The later argument is reinforced by the observable difference when increasing the data collection period for the case with changed filter length definition. With this, a main peak around $\mathrm{Sr}_D \approx 0.2$ and a secondary peak around $\mathrm{Sr}_D \approx 0.35$ is visible, leading to better agreement both with the reference solutions and the literature data.

4.5 Discussion and summary of sensitivities

Overall, the flow field is largely unaffected by changes in grid resolution and numerical parameters, but quantitative differences occur. The sensitivities in terms of several important quantities are summarized in Table 4.6. For the mean flow these include the differences in reattachment location x_r[4] as well as mean and rms pressure distribution. The sensitivity in terms of spectral content is more difficult to evaluate. A possible quantity is the relative difference of the maximum amplitude of the scaled premultiplied Power Spectral Density in the range $0.16 < \mathrm{Sr}_D < 0.22$ in the region $0.4 < x/D < 0.8$. This quantity is chosen since for most cases the peak at $\mathrm{Sr}_D \approx 0.2$ is the most dominant feature in the spectral content and is located between these axial positions. Additionally, the literature data also showed this approximate region for this dominant feature (cf. Section 4.1). However, this value obviously is still not fully representative of the overall spectral content for the different cases.

The considered sensitivities for the grid study are that to axial refinement (grid G0 vs. G1), radial refinement (grids G2 vs. G1), grid element type (grids G4 vs. G1) and circumferential refinement (grids G2b vs. G6b). Additionally, the sensitivity of the quantities to the presence of an air plume (grids G2b vs. G2) is displayed. The sensitivity to numerical changes is evaluated

[4] $\Delta x_r = x_r - x_{r,ref}$ with $x_{r,ref} = 1.172D$

with respect to the time step size (i.e. Δt_1 and Δt_2 vs. Δt_0), turbulence model (SA vs. k-ω SST), fluid model (multi-species vs. single species), filter length definition (Δ_ω vs. $\widetilde{\Delta}_\omega$) and data collection period (76 CTUs vs. 38 CTUs).

The table shows that the reattachment location varies only by less than 0.5% for most cases, but filter length definition, circumferential resolution and fluid model have a larger impact of about 1.5%. The mean pressure coefficient is also very insensitive for most cases, with average and maximum $\Delta \langle c_p \rangle$ around 0.003 and 0.007, respectively. About three times larger deviations are visible when adding a plume or changing fluid model or filter length definition. The rms pressure distribution shows average and maximum deviations of about 5% and 15%, respectively, for most cases, but average deviations of up to 11% appear for the changed filter length and maximum deviations of up to 47% for the added plume are visible. Note that the large value for the maximum deviation in the rms pressure can be misleading; for the plume sensitivity it is due to the different behavior near the nozzle lip where the rms pressure decreases for the case with plume whereas it continues to increase for the case without plume, as discussed in subsection 4.3.5. Hence, even though the distribution looks very similar, these large deviations occur due to very local differences.

The differences in the spectra peak amplitude differ widely, with largest deviations for the axial resolution (peak not visible on grid G0), circumferential resolution (peak barely visible for the finer resolution) and filter length definition (peak amplitude similar to that on the coarse grid). The deviation for the last two cases is related, however, due to a possible too strong reduction in dissipation for the fine grid with Δ_ω (as discussed above). The majority of the remaining cases shows deviations around 15% to 30%, with only two cases showing very small deviations.

This summary shows that the obtained solutions are generally insensitive to differences in the in-plane grid resolution (with the exception of the axial resolution immediately behind the step), time step size, turbulence model and data collection period. For the latter differences

	$\Delta x_r/D$	$\Delta \langle c_p \rangle$	$\frac{\Delta c_{p,rms}}{c_{p,rms}}$ [%]	$\frac{\Delta spPSD\|_{\mathrm{Sr}_D \approx 0.2}}{spPSD\|_{\mathrm{Sr}_D \approx 0.2}}$
Axial res.	0.002	Mean: 0.003, Max: 0.005	Mean: 5.4, Max: 17.9	46.5 %
Radial res.	0.003	Mean: 0.004, Max: 0.008	Mean: 4.6, Max: 14.2	0.7 %
Circ. res.	0.015	Mean: 0.007, Max: 0.023	Mean: 8.8, Max: 25.7	43.5 %
Element type	0.004	Mean: 0.005, Max: 0.009	Mean: 7.6, Max: 28.9	18.7 %
Plume	0.008	Mean: 0.010, Max: 0.028	Mean: 8.5, Max: 46.9	2.9 %
Time step size	0.005	Mean: 0.002, Max: 0.005	Mean: 5.1, Max: 15.1	23.3 %
Turb. model	0.004	Mean: 0.002, Max: 0.004	Mean: 5.5, Max: 13.9	15.9 %
Fluid model	0.013	Mean: 0.012, Max: 0.031	Mean: 8.4, Max: 21.5	22.2 %
Filter length	0.018	Mean: 0.010, Max: 0.026	Mean: 11.4, Max: 22.4	40.6 %
Data period	0.002	Mean: 0.001, Max: 0.003	Mean: 5.1, Max: 10.3	30.5 %

Table 4.6: Summary of the investigated sensitivities.

appear, however, in the spectral content of the flow and more pronounced for the buffeting force spectra, indicating that data collection periods of likely more than 76 CTUs are necessary to obtain reliable quantitative results from a spectral analysis.

Higher sensitivities are observed with respect to the fluid model, the circumferential grid resolution and the filter length definition. Hence, in Chapter 5 the investigations will be conducted with a fine circumferential resolution of 0.938° and the filter length definition $\widetilde{\Delta}_\omega$ will be used. The uncertainties due to the fluid model have to be accepted and taken into account, since for the investigations with hot plumes several species have to be considered. As will be seen however, the impact of hot plumes on the flow field is much larger than the changes observed in this chapter, and thus these small uncertainties do not significantly impact the interpretation of the results.

5 Aft-body flows with hot plumes

In this chapter the results obtained from simulations of aft-body flows in the presence of a hot plume are presented. The investigation includes two configurations that differ both in nozzle length and plume conditions and are hereafter referred to as the "Long nozzle" and "short nozzle" configuration. An experimental investigation of the same configurations was planned to allow comparison of the results. However, the results of these experimental investigations were not available at the time the numerical research was completed, and hence no direct comparison is included, but might be available at a future time.

First the common numerical setup and the model geometry are described in section 5.1. Subsequently the results for the long nozzle configuration are discussed in section 5.2 before the results for the short nozzle configuration are presented in section 5.3.

5.1 Numerical setup

The model geometry is similar to the one investigated in Chapter 4 since it also represents a generic space launch vehicle geometry. It consists of one large cylinder, representing the main body of the vehicle, with a diameter of $D = 0.0667$ m. This cylinder is followed by a nozzle structure for which the external surface is another cylinder with diameter $D_2 = 0.2D$. The downstream end of the large cylinder, also referred to as the base, is located at $x/D = 0$. The coordinate system origin is on the symmetry axis. For the long nozzle configuration the nozzle exit is located at $x/D = 1.2$ whereas for the short nozzle configuration it is located at $x/D = 0.4$. The nozzle itself is a conical nozzle with throat diameter $0.165D$, exit diameter $0.196D$ and nozzle exit half angle of 5°. To allow for optimal comparison between numerical and possible experimental data, the wind tunnel walls with a diameter of $D_{tunnel} = 5.1D$ are included in the simulation as well. The exit plane of the wind tunnel walls is located at $x/D = -0.16$ for the long nozzle configuration and at $x/D = -0.96D$ for the short nozzle configuration[1]. Figure 5.1 shows a detailed view of the model geometry for the long nozzle configuration. The injector and combustion chamber are only included in precursor RANS simulations that are required to obtain the correct conditions at the nozzle inlet and the correct wall temperatures on the model walls.

[1] The difference is due to experimental considerations for which the reduced nozzle length is achieved by extending the main body.

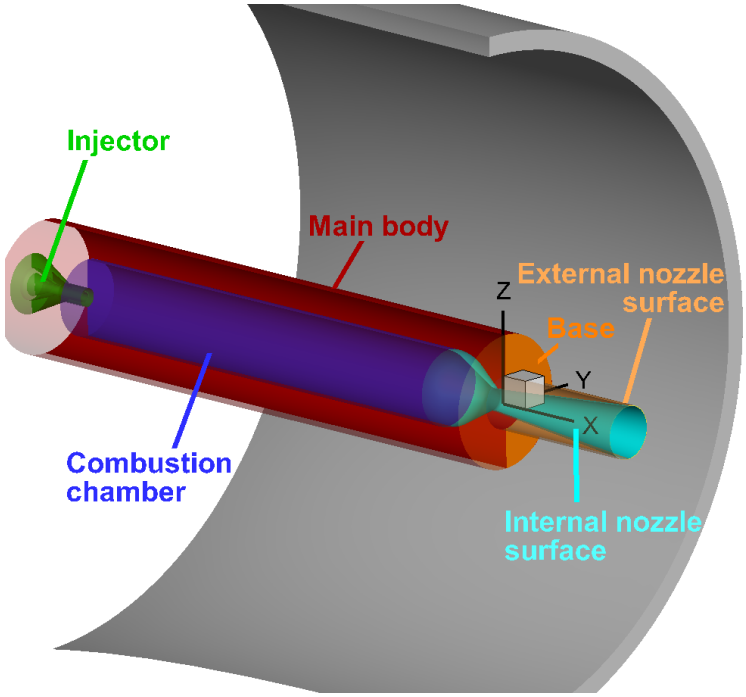

Figure 5.1: Model geometry for the investigations with hot plumes in the long nozzle configuration.

The external flow is created by a blow-down wind tunnel with a free jet test section [25] and creates a transonic flow with a Reynolds number of $\mathrm{Re}_D \approx 1.5 \cdot 10^6$. Free stream conditions are computed at a location one main body diameter upstream of the wind tunnel exit plane and are summarized in table 5.1. The computational domain does not include the full wind tunnel and model length, but the inflow into the computational domain is located about $1.8D$ upstream of the wind tunnel exit plane and includes a fully turbulent boundary layer on the model that is obtained by a separate precursor RANS simulation. The outflow is located at $x/D = 30$ and the radial boundary is located at $r/D = 7.5$. At both of these boundaries a farfield boundary condition with velocity $U_{farfield} = 10$ m/s, $T_{farfield} = 275$ K and $p_{farfield} = p_\infty$ is prescribed. All walls are modelled as viscous wall boundary conditions, except for the outside of the wind tunnel wall that is treated as a slip wall to improve the numerical behavior.

The grids used are created based on the results from Sec. 4.3 and are summarized in Table 5.2 as well as visualized in Fig. 5.2. Both grids feature a circumferential resolution of 0.938° and

U_∞	M_∞	p_∞	T_∞	$\frac{\delta_{99}}{D}$
252 m/s	0.799	100530 Pa	247.7 K	0.22

Table 5.1: Free stream conditions for investigations with hot plumes

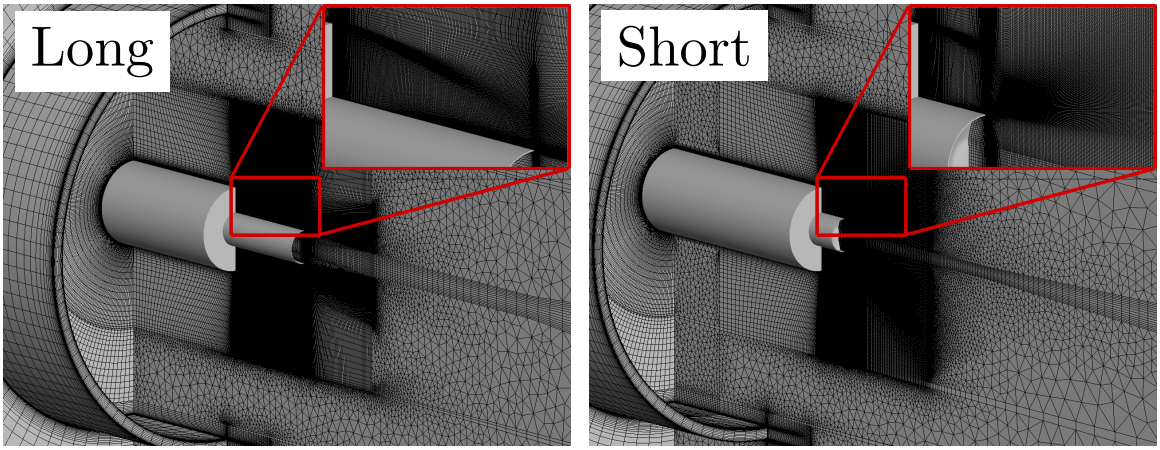

Figure 5.2: Grids used for the long nozzle configuration (left) and short nozzle configuration (right).

at all model walls a first wall distance of $\Delta_y^+ < 1$ is maintained; non-dimensional spacings at selected other locations are also summarized in Table 5.2. Note that these spacings are non-dimensionalized using the wall shear stress in the attached boundary just before separation in the cold wall case. For the short nozzle configuration slightly larger non-dimensional spacings are visible since the boundary layer develops for a longer distance and hence the wall shear stress at the separation location is increased. This is most clearly visible when comparing Δ_{circ}^+ since the dimensional circumferential resolution is equal for both grids at equal locations. Additionally, at locations 3 and 4 the spacing is increased for the short nozzle configuration since the shear layer reattaches further upstream and hence the resolution requirements in these downstream regions are less restrictive. Further, for the hot wall cases the actual non-dimensional spacings are reduced by about a factor 3 (long nozzle) or 2 (short nozzle) from those displayed in the table due to the reduced wall shear stress at the reference location as a consequence of the higher flow temperature.

For the investigation an $k-\omega$ SST IDDES model with the filter length definition $\Delta = \widetilde{\Delta}_\omega$ is used (see Sec. 3.4). The model is forced into RANS mode for $x/D > 2.24$, $x/D < 0.01$ and in the plume core, with the respective numerical settings described in chapter 3 applied in RANS

x/D, r/D	Points	Δ^+ Loc 1 0.12, 0.5	Δ^+ Loc 2 0.3,0.3	Δ^+ Loc 3 0.75,0.4	Δ^+ Loc 4 1.15, 0.3
Long nozzle	31.6 Mio.	135,15,330	210,150,195	255,65,255	165,90,195
Short nozzle	31.1 Mio.	135,15,350	235,220,205	365,90,270	450,130,205

Table 5.2: Summary of grids used to investigate aft-body flows with hot plumes. Δ^+ indicates Δ_{ax}^+, Δ_{rad}^+, Δ_{circ}^+.

and LES regions. Due to decreased stability with the stronger interaction between plume and external flow for the short nozzle configuration, for these simulations the whole plume is forced into RANS mode and the values for ε_Ψ and the entropy fix threshold in the RANS regions are increased from their default values described in Section 3.3 to 1024 and 1, respectively.

The time step is chosen as the ratio between free stream velocity and target grid spacing in the recirculation region [59] as $\Delta t = 2 \cdot 10^{-6}$ s, allowing to resolve each CTU with 130 time steps. The solution is left to develop for about 110 CTUs until a statistically steady state is reached. Subsequently, data collection for averages and spectra is continued for about another 110 CTUs. For the spectral analysis a frequency resolution of $\Delta Sr_D \approx 0.035$ is applied that allows to use Welch's method with 50% overlap and a total of 7 segments (cf. Sec. 3.7). Mean flow fields and point spectra are additionally averaged in the circumferential direction.

The combustion chamber conditions for the two hot plume configurations as well as for an air plume configuration are summarized in Table 5.3. The nozzle inflow conditions for the hot plumes are obtained from axisymmetric RANS simulations that are thermally coupled to a structure solver [54].

Only the downstream section of the divergent part of the nozzle is included in the IDDES investigations and a dirichlet boundary condition with values obtained from a RANS solution of the complete nozzle is used. Since the flow at this location is supersonic no differences between inclusion of the whole nozzle and just the supersonic part are visible in precursor RANS simulations. Additionally, this approach allows to reduce the required number of grid points slightly and improves stability.

5.2 Long nozzle configuration

The wall temperatures for the long nozzle hot wall case are shown on the left of Fig. 5.3. It is visible that the high temperatures in the combustion chamber and nozzle located inside the model heat up the walls of the main body as well as the base and the external nozzle surface. At the end of the main body wall temperatures of about 710 K are reached and the highest temperatures are visible in the base corner with around 720 K. Towards the nozzle lip the temperatures decrease to levels around 580 K. It is also visible that the temperature difference

Configuration	T_0	p_0
Air	300 K	2.15 MPa
Long	1000 K	2.15 MPa
Short	3000 K	2.21 MPa

Table 5.3: Combustion chamber conditions

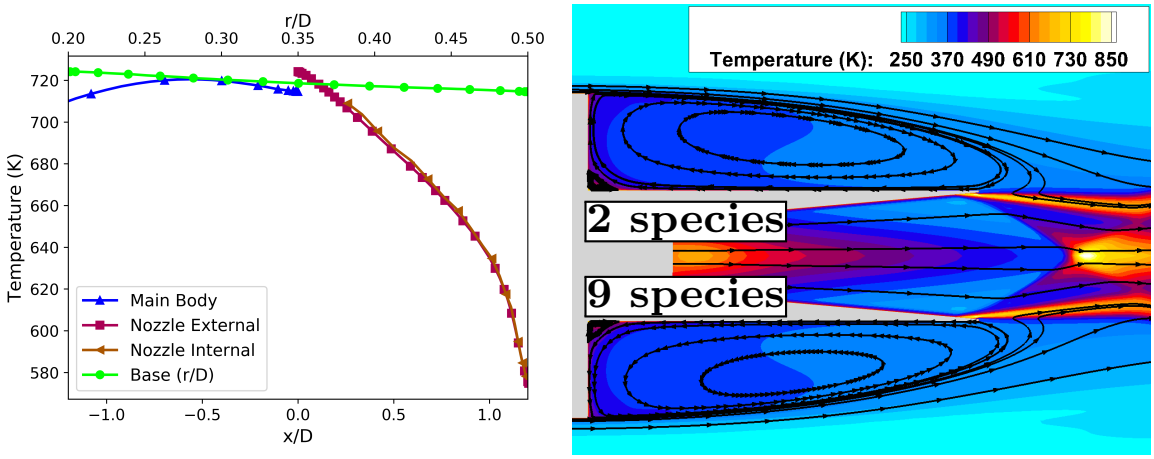

Figure 5.3: Wall temperatures (left) and RANS flow field (right) for the hot wall case of the long nozzle configuration.

between the internal and external nozzle walls is only minimal (about 10 K), which is due to the high thermal conductivity and small wall thickness of the nozzle material.

The resulting flow field of a RANS computation is displayed with streamlines and color contours of the temperature on the right of Fig. 5.3. It also features a comparison between an approach using 9 species and an active reaction scheme and one using only two species for external air flow and nozzle plume, respectively, and no chemical reactions. Both schemes are summarized in appendix C. It is visible that only minor differences between the two solutions appear. In particular, no post-combustion in the region of the nozzle lip is visible with activated chemical reactions. This confirms that an approach without chemical reactions and a reduced number of species is sufficient. Hence, for the IDDES computations the plume is treated as one component and the external air flow as a second. The two gas mixtures are allowed to mix, but no reactions are taken into account, i.e. the chemical reaction source term $\underline{\omega}$ in equation (2.30) is set to zero. Mixture properties and transport coefficients are given in appendix C.

Three different cases are investigated for this configuration. As a reference solution for comparison, the first case ("Air", "Air plume case") features a plume that results from expansion of compressed air. For the second case ("Cold", "Cold wall case") the plume is replaced by one that originates from an H_2-O_2 combustion with O/F=0.7, i.e. $Y_{H_2} \approx 0.54$ and $Y_{H_2O} \approx 0.46$. Chamber conditions for both plume conditions are summarized in Table 5.3. The external wall temperatures for these two cases are kept at ambient conditions of $T_{w,cold} = 300$ K. For the third case ("Hot", "Hot wall case") the wall temperatures are set to the values from the coupled simulations that are shown in Fig. 5.3.

5.2.1 Mean flow fields

The flow fields for the different cases are shown in Fig. 5.4. In the presence of an air plume the stream lines clearly show a mean reattachment location of the shear layer on the external nozzle surface just before the nozzle lip around $x_r/D = 1.191$ with maximum recirculation velocities of around 95.5 m/s at $x/D \approx 0.61$. The nozzle flow shows velocities of about 700 m/s in the core and flow separation from the nozzle walls approximately $0.075D$ upstream of the nozzle lip.

If the plume instead originates from an H_2-O_2 combustion, the core velocity is significantly increased to around 3600 m/s. Since the nozzle dimensions as well as the chamber pressure do not differ between the cases, the Mach number and pressure in the plume are comparable for both plume conditions, being only slightly influenced by different species properties. Since the external free stream conditions are also equivalent, the observed changes to the external flow field are purely due to differences in plume properties (i.e. velocity, temperature, density and fluid properties). The major difference in the external mean flow field is the growth of the recirculation region that shifts the mean reattachment location downstream and thus beyond the nozzle lip onto the plume. Due to the downward angle of the plume shear layer a mean reattachment location for this condition is not as clearly defined as it is for the solid reattachment ($\frac{\partial u}{\partial r}_w = 0$, i.e. the location where the axial velocity gradient in the wall normal direction is zero). A definition consistent with that for solid reattachment is to define it as the location where the axial velocity gradient in the radial direction is zero at the radius of the external nozzle surface (i.e. $\frac{\partial u}{\partial r}_{r=0.5D_2} = 0$). Using this definition the reattachment location shifts to $x_r/D = 1.324$, i.e. about $0.133D$ further downstream. The maximum backflow velocity of around 94.7 m/s occurs at $x/D \approx 0.64$.

For the hot wall case, the recirculation region grows even further with a mean reattachment location of $x_r/D = 1.454$, i.e. $0.130D$ further downstream than for the cold wall case. In this case the maximum backflow velocity is reduced to around 93.0 m/s and occurs at $x/D \approx 0.69$.

The superiority of the scale resolving simulations over RANS simulations for the prediction of the mean flow field is visible in Table 5.4 where the mean reattachment location is summarized for all three cases with both RANS and IDDES approach. The RANS approach overpredicts the recirculation region size for the first two cases, most dramatically for the air plume case with

	Air plume	Hot plume, cold walls	Hot plume, hot walls
IDDES	$1.191D$	$1.324D$	$1.454D$
RANS	$1.270D$	$1.366D$	$1.447D$

Table 5.4: Reattachment locations for different cases of the long nozzle configuration.

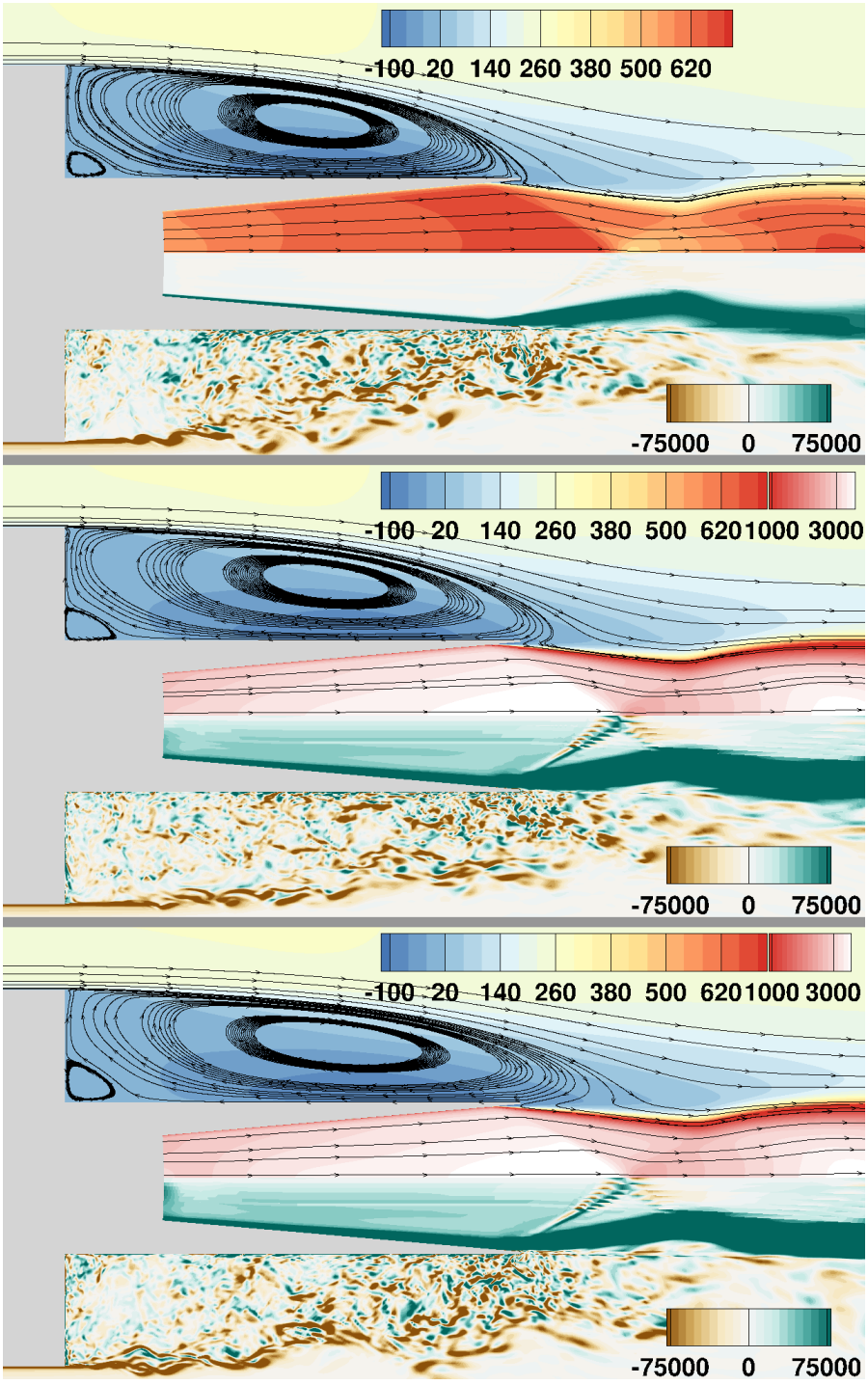

Figure 5.4: Mean and instantaneous flow fields for the cases with air plume (top), hot plume with cold walls (middle) and hot plume with hot walls (bottom). Mean axial velocity (top) in m/s and instantaneous circumferential vorticity (bottom) in 1/s.

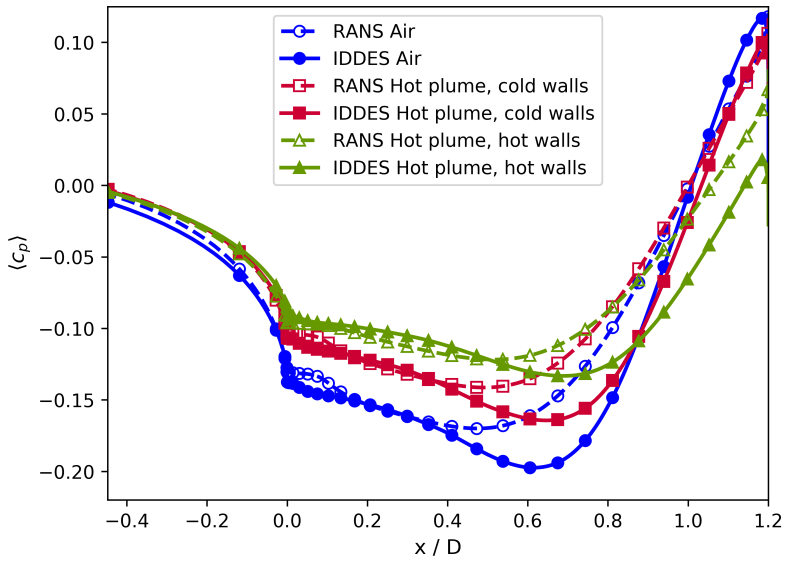

Figure 5.5: Mean pressure coefficient distribution for the long nozzle configuration.

a difference of about 0.08D (7%) that shifts the reattachment location from the nozzle surface onto the plume. For the hot wall case the RANS prediction is very close to that of the IDDES, however. Note that the RANS simulations are computed on an axisymmetric grid with the same in-plane resolution as the IDDES and use the same numerical settings (turbulence model, time step size, etc.) with the only difference being the substitution of the IDDES length scale in the turbulence equations. A RANS simulation on a full 360° grid was also conducted and showed negligible differences to the axisymmetric simulation. Hence, the differences can only be due to an improved capturing of the turbulent shear layer behaviour with scale resolving simulations that cannot be adequately modeled with the investigated RANS models.

However, the RANS solutions are able to capture the qualitative changes between the different cases, i.e. the trend of an increase of the recirculation region size between case 1 and case 2 and between case 2 and case 3. Furthermore, the further downstream the reattachment occurs, the closer the RANS results agree with the IDDES mean flow field.

This trend is also visible in the mean pressure distributions that are shown in Fig. 5.5. All cases show a decreasing pressure coefficient on the main body towards the separation location, but even this region is already affected by the further downstream flow field, with an earlier reattachment location associated with a stronger pressure decrease. At the separation location the pressure decreases along the base and a further decrease is visible on the external nozzle surface. In both RANS and IDDES the more upstream the reattachment location the stronger and further upstream is the pressure minimum on the external nozzle surface: Whereas the pressure minimum is located around $x/D = 0.6$ at $c_p = -0.2$ for the air plume case, it shifts

to $x/D = 0.7$ and $c_p = -0.13$ for the hot wall case. It is also visible that the stronger the pressure minimum, the larger the discrepancy in its prediction between RANS and IDDES, correlating with the larger discrepancies visible in the mean reattachment location. Another feature that is visible is that the pressure increase towards the nozzle lip also correlates with the strength of the pressure minimum, hence leading to a higher pressure at the nozzle lip for a smaller recirculation region. In combination, these features lead to the observation that the further upstream the reattachment occurs, the stronger the pressure varies between different axial positions.

The most plausible explanation for the growth of the recirculation region from case 1 to case 2 is the increased plume velocity. While the plume temperature is about three times higher for the H_2-H_2O plume than for the air plume, a direct effect of an increased plume temperature on the behaviour of the main shear layer could not be identified, particularly since the temperature in the recirculation region does not increase. Another considered effect is that of a higher plume momentum (and hence a contribution of the density difference) leading to a stronger impact on the recirculation region. However, the density of the hot plume is smaller by a factor of about 30 (whereas the velocity is only larger by a factor of about 5) and hence the smaller density and momentum shows the stronger impact. The only remaining quantity explaining the effect is thus the plume velocity. The impact of the plume velocity can be explained by a suction effect of the plume created by the acceleration of the external flow in the plume shear layer downstream of the nozzle lip. Consequently, a higher plume velocity creates a stronger suction effect and hence "pulls" the reattachment location further downstream.

The growth of the recirculation region from case 2 to case 3 can only be due to the increased external wall temperatures since the internal nozzle wall temperatures as well as plume inflow and free stream conditions for these two cases are equivalent. However, one can distinguish between the effect of the heated incoming boundary layer and that of the heated recirculation region. For this purpose two additional RANS simulation are conducted, for which either only the temperature of incoming boundary layer walls or that of the recirculation region (i.e. base and external nozzle surface) walls are increased whereas the respective other walls are set to an ambient temperature of 300 K. Even though it was shown above that the quantitative predictions with RANS modelling are not as accurate as those with IDDES, it was also shown that the qualitative comparison between different conditions was captured well. Hence, these simulation allow to quickly assess these two contributions (heated boundary layer vs. heated recirculation region) qualitatively.

The resulting flow fields are shown in Fig. 5.6. It is visible that the effect of the heated boundary layer is larger than that of the heated recirculation region. The former shifts the reattachment location by about $0.059D$ whereas the latter only by $0.025D$ compared to the cold wall RANS

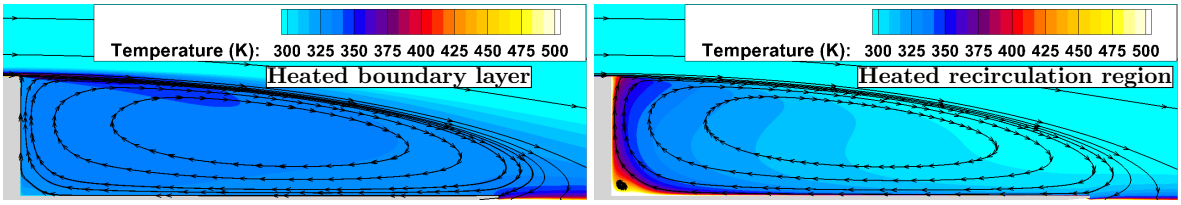

Figure 5.6: RANS flow field for the cases with heated boundary layer (left) and heated recirculation region surface (right).

solution. Interestingly, the overall effect appears as a superposition of the individual effects, i.e. the sum of the two individual changes matches the shift in reattachment location for the case with all heated walls reasonably well ($0.084D$ vs. $0.081D$). The distinction between the two different contributions is particularly of interest when applying the current findings to full scale space launch vehicles because for these the wall temperature of the main body will not be affected by the engine[2] and only the external nozzle surface and the base might experience a temperature increase.

For the heated recirculation region case only the fluid in the vicinity of the walls is heated up as is visible in Fig. 5.6. In comparison, the heated boundary layer case shows a much more uniform temperature distribution in as well as a stronger impact on the downstream part of the recirculation region. The left of Fig. 5.7 shows the axial temperature distribution at a constant radial location $r/D = 0.22$ (i.e. $0.02D$ above the external nozzle wall). This figure shows that in fact only for $x/D < 0.4$ the heated recirculation region walls lead to a higher temperature

[2]This is true at the considered transonic conditions during ascent. In retro-propulsive flight or at high altitudes an impingement of hot plume gases on the main body, and thus increased wall temperatures, can appear, however.

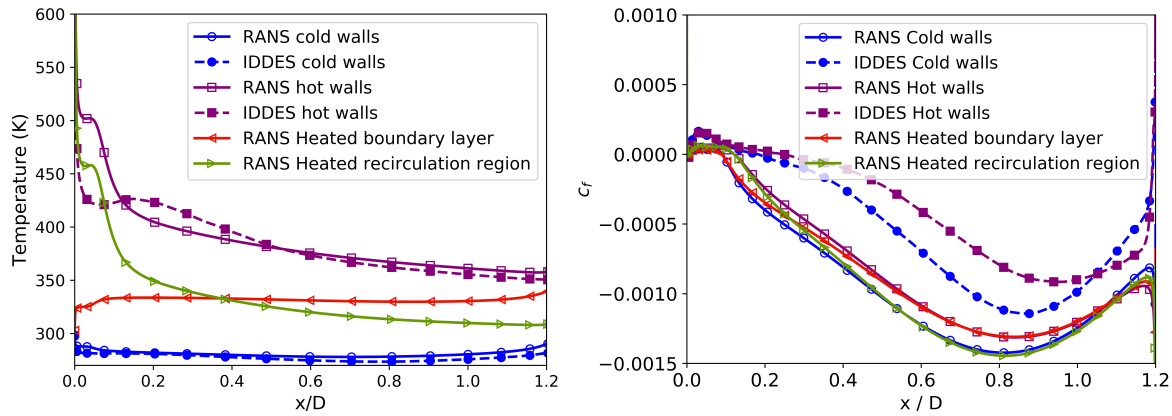

Figure 5.7: RANS temperature distribution at $r/D = 0.22$ (left) and wall friction coefficient distribution (right) for different wall temperatures.

this close to the wall, whereas for further downstream locations the heated boundary layer leads to a stronger impact on the fluid temperature. Towards the nozzle lip the latter case is only slightly colder than the hot wall case (350 K vs. 370 K).

The mean temperature from the IDDES simulations is displayed in the graph as well, showing a very similar distribution as the RANS results for the cold wall case. For the hot wall case the differences between RANS and IDDES are larger, especially near the base wall. This indicates differences in the wall heat transfer which will be analysed in more detail in subsection 5.2.2.

The differences for the partially heated wall computations are also reflected in the friction coefficient distribution on the right of Fig. 5.7. For $x/D < 0.2$ the friction coefficient c_f for the heated recirculation region case follows that of the hot wall case whereas the heated boundary layer case agrees with the cold wall case. This trend reverses between $0.2 < x/D < 0.4$ and the opposite correlation is the case for $x/D > 0.4$. This confirms that the influence of the recirculation region wall temperature is limited to the base region, except in close vicinity to the base wall. The figure also clearly shows the size of the corner vortex, which is larger by $\Delta x \approx 0.03D$ if base and external nozzle wall are heated, visible by the larger region with positive friction coefficient near the base. It seems possible that a larger corner vortex might also affect the size of the entire recirculation region. However, it seems more likely that the shifted reattachment location and the corner vortex size are independently caused by the increased wall temperature.

The downstream shift of the reattachment location with a heated boundary layer matches the general tendency of boundary layers with increased wall temperatures to separate earlier [21]. Further, Wu et al. [75] showed that in for laminar boundary layers a cooled wall decreases the separation bubble height and moves the reattachment location further upstream which is attributed to an accelerated turbulent transition process of the separated shear layer. By extension, heated walls lead to a slower transition process and a downstream shift of the reattachment location due to a slower build up of shear layer instabilities. Since similar processes, e.g. vortex roll up, K-H-like instabilities and hairpin vortices, appear in the early part of the turbulent shear layer in the current setup, it is plausible that similar correlations between shear layer growth and wall temperature are applicable. However, to the author's knowledge the connection, causality and fundamental interactions between wall temperature and shear layer growth for turbulent shear layers have not been the focus of a detailed investigation yet.

One way the shear layer development can be evaluated is the vorticity thickness

$$\Theta = \frac{U_\infty - \min\limits_r(u)}{\max\limits_r\left(\frac{\partial u}{\partial r}\right)} \tag{5.1}$$

which is shown in Fig. 5.8 for the IDDES computations. The vorticity thickness evolution for

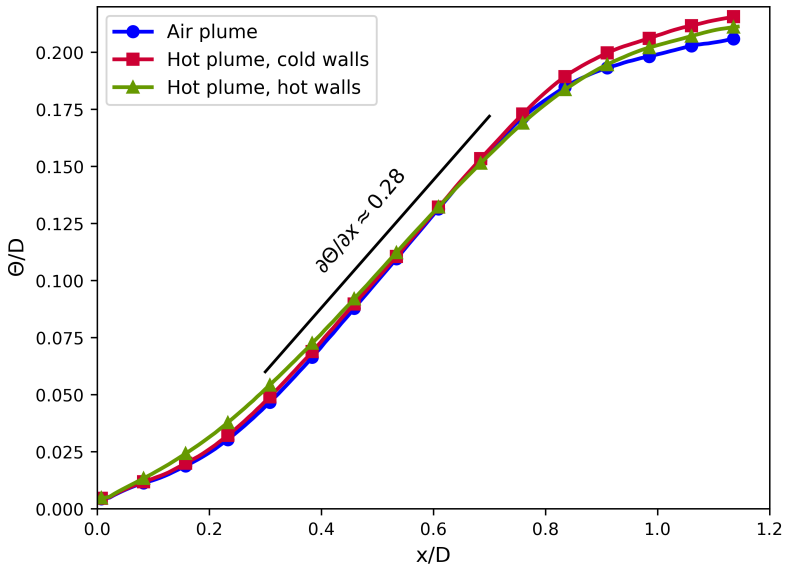

Figure 5.8: Vorticity thickness evolution for the long nozzle configuration.

the cases with cold walls is nearly indistinguishable for $x/D < 0.7$, i.e. independent of the plume conditions. In this region the flow behaves as for a free shear layer, whereas further downstream the effect of the reattachment process becomes dominant [8]. For the cases with cold walls the growth of the vorticity thickness in the linear region is about $\frac{\partial \Theta}{\partial x} \approx 0.28$ which agrees well with the value of $\frac{\partial \Theta}{\partial x} \approx 0.27$ observed by Statnikov et al. [61]. For the hot wall case, the vorticity thickness growth shows small differences, exhibiting a faster initial growth, but a slightly shallower slope in the linear region of about $\frac{\partial \Theta}{\partial x} \approx 0.26$. This is an additional indication of the slower instability processes in the shear layer.

5.2.2 Mean heat fluxes

While not of particular interest for the cases with cold walls, the heat flux from the walls to the recirculation region flow can be analysed for the hot wall case. The wall heat flux distribution along the axial direction on the external nozzle surface and along the radial direction on the base surface is displayed in Fig. 5.9. In the axial distribution the low heat flux in the base corner can be observed, followed by a local maximum that is caused by the increased heat transfer due to the corner vortex. The heat flux then slowly increases in the downstream direction due to the thinner penetration of the wall temperatures and thus higher temperature gradients near the nozzle lip as well as the larger amount of velocity fluctuations from impinging shear layer structures. At the nozzle lip the heat flux increases dramatically due to the highly unsteady flow field and the associated faster exchange of heated fluid. The radial distribution on the base surface also shows a local maximum at small radii that appears mostly related to

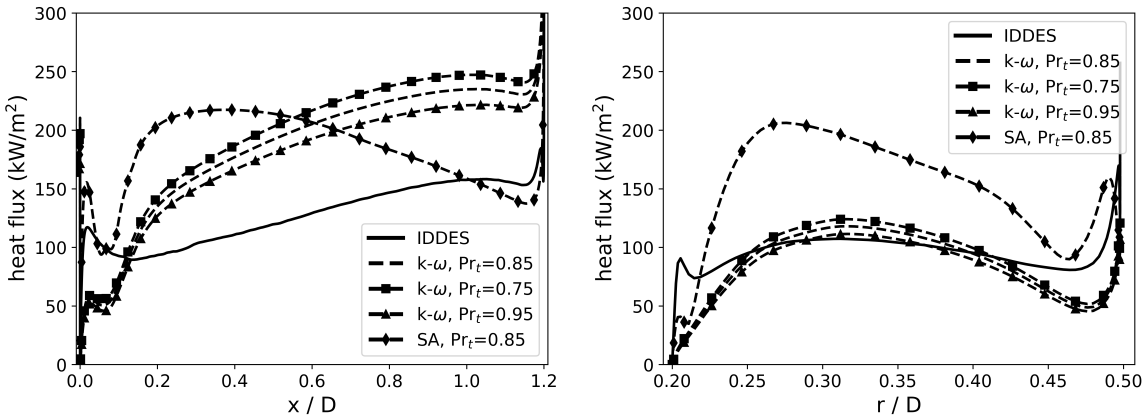

Figure 5.9: Mean heat flux distribution along the external nozzle surface (left) and the base surface (right).

the high temperatures in the base corner. A shallow maximum is visible around $r/D = 0.32$, which coincides with the top end of the corner vortex. This appears to be due to colder fluid being transported towards the base wall at this point whereas for smaller radii the (heated) fluid from the hot corner is present. Near the edge of the main body the heat flux increases again drastically which is related to the high velocities and corresponding high heat transfer associated with the boundary and shear layer.

The figure also shows the resulting heat fluxes from RANS computations with different settings. The heat fluxes from two different turbulence models differ drastically, with both predicting significantly different heat flux distributions than the scale resolving simulation. On the external nozzle surface the SA model [57] predicts a very strong increase of the heat flux due to the corner vortex as well as a strong peak in heat flux around $x/D \approx 0.3$ with a decrease further downstream. The k-ω SST model predicts a less distinct corner vortex influence, but a strong increase in the heat flux towards the end of the nozzle. It is also visible that changing the turbulent Prandtl number by $\Delta \mathrm{Pr}_t = 0.1$ impacts the quantitative heat fluxes by up to 8%, but does not change the qualitative behaviour.

The qualitative behaviour for the k-ω model is more alike to that obtained with the scale resolving simulation, but still predicts a heat flux that is about 50% higher. With the SA model the heat flux prediction differs even up to about 100% from the scale resolving simulation and shows a qualitatively different behaviour. In comparison, the heat fluxes on the base between the k-ω RANS and the IDDES agree relatively well with slightly larger differences occuring in the region of the corner vortex and near the top of the base where the RANS model predicts a lower heat flux. The turbulent Prandtl number has an even lower influence on the heat fluxes in this region. With the SA turbulence model the predicted heat fluxes are significantly higher

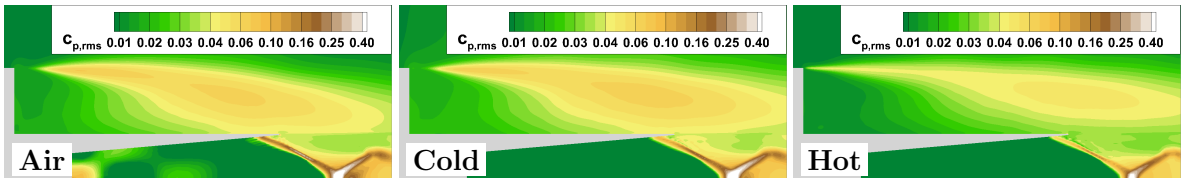

Figure 5.10: Rms pressure coefficient in the field for the long nozzle configuration.

than in the IDDES - again up to 100% - and the local maximum of the heat flux is shifted towards slightly lower radii.

An explanation for the observed differences in heat flux between the solutions are significant changes in the flow field. While for both the IDDES simulation and the RANS computation with k-ω model the reattachment occurs on the plume, the RANS computation with SA model predicts a reattachment just before the nozzle lip. Additionally, the separation location in the nozzle is located further downstream which affects the plume shape and possibly indirectly the recirculation region. Another difference is the strength of the corner vortex that features axial velocities of up to $0.1u_\infty$ for the SA model and only around $0.02u_\infty$ for the k-ω model. The mean axial velocities in the corner vortex region for the IDDES are between those two values at around $0.06u_\infty$. These relations match the observed differences in heat flux amplitude near the base on the external nozzle surface, reinforcing the connection of the local maximum to the corner vortex.

Based on the results from section 4.4, it can be expected that the IDDES results would be less sensitive to a change in turbulence model, as the differences between the flow fields were significantly reduced with IDDES than with RANS settings. However, the heat flux might also be influenced by the underlying turbulence for the scale resolving simulation since the heat flux is evaluated at the wall where the IDDES switches to RANS mode.

5.2.3 Unsteady flow fields

Apart from the higher accuracy in the prediction of mean flow features, the other huge advantage of scale resolving simulations over RANS simulations is the availability of time resolved flow field data. The analysis concerning this data is discussed in the following.

Pressure fluctuations and buffeting loads

Fig. 5.10 shows the rms pressure coefficient in the field for the three cases. It is clearly visible that the cases with cold walls feature higher maximum pressure fluctuations in the recirculation region of $c_{p,rms} \approx 0.067$ and $c_{p,rms} \approx 0.069$ for the case with air plume and

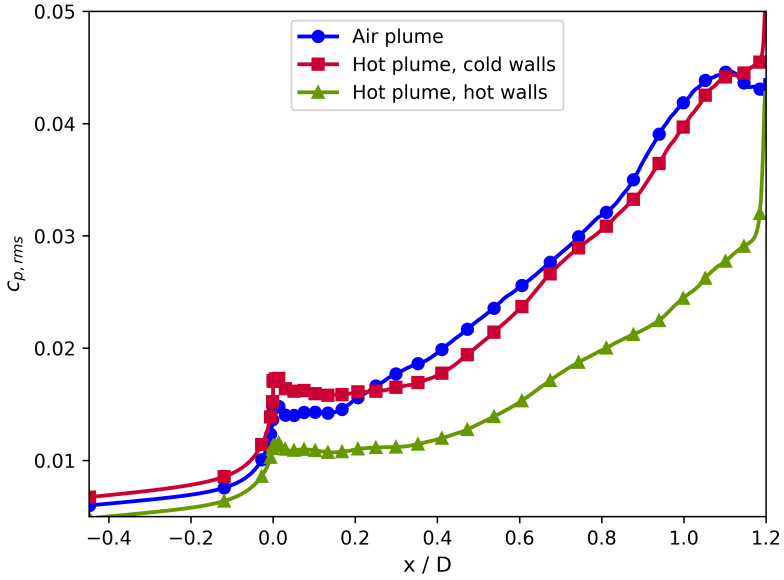

Figure 5.11: Rms wall pressure coefficient distribution for the long nozzle configuration.

hot plume, respectively. For the hot wall case the maximum is $c_{p,rms} \approx 0.052$. Additionally, the location of the maximum is also correlated to the reattachment location, i.e. further downstream for a further downstream mean reattachment. Another interesting observation is the thinner region of increased pressure fluctuations in the early shear layer for the hot wall case that is an additional indication of a slower shear layer development and growth due to the decelerated instability processes. The highest pressure fluctuations in the field can be observed in the vicinity of the separation shock in the plume, even though this region is not treated in LES but in (U)RANS mode.

A quantitative comparison of the axial distribution of the pressure fluctuations on the external walls is shown in Fig. 5.11. In contrast to the mean pressure distributions in Fig. 5.5, the pressure fluctuations for the cases with cold walls show very similar behaviours, as could already be seen from the pressure fluctuations in the field (cf. Fig. 5.10). For both cases there is a steady increase in pressure fluctuations towards the nozzle lip with differences between the two cases of around $\Delta c_{p,rms} \approx 0.002$. The largest differences occur near the nozzle lip, where for the air plume a local maximum in the pressure fluctuations occurs that is related to the reattachment process (cf. 4.3.5). For the hot plume no reattachment occurs and hence the pressure fluctuations continue to increase, with a particularly strong increase right before the lip due to the highly unstable flow field in this region. This is caused by flow separation of the backflow around the nozzle lip.

In comparison to the cold wall cases, the case with increased wall temperatures deviates significantly with pressure fluctuations being reduced by about 40%. As for the case with hot

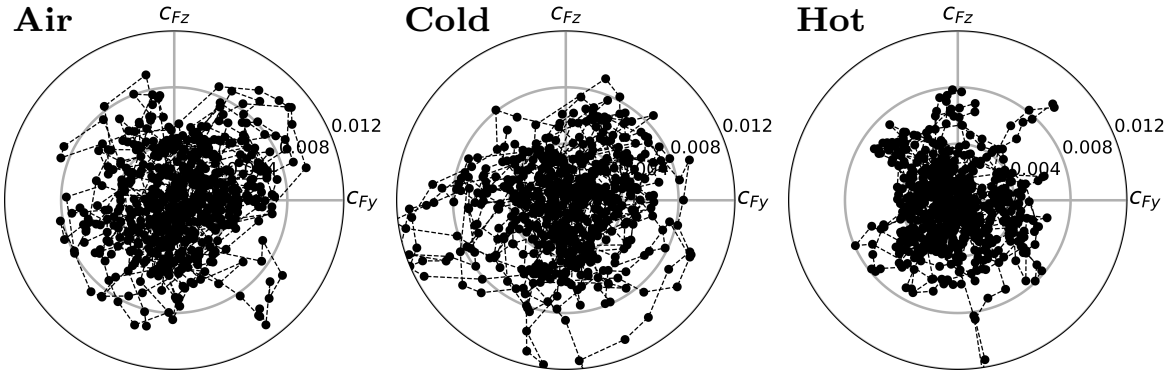

Figure 5.12: Non-dimensional buffeting loads for the long nozzle configuration.

plume and cold walls, a sudden increase in fluctuations can be observed just before the nozzle lip that is also due the missing mean reattachment location and associated unstable flow field around the lip.

Related to the pressure fluctuations are the mechanical loads acting on the nozzle surface. The forces in both radial directions - non-dimensionalized by the free stream dynamic pressure and the main body cross-sectional area - are displayed in a polar style in Fig. 5.12. For the cases with cold walls the force amplitudes are very similar, with slightly larger mean amplitudes observed for the hot plume case by about 5%. For the hot wall case the force amplitudes are visibly reduced, with a mean force amplitude that is about 20% lower than for the cold wall case.

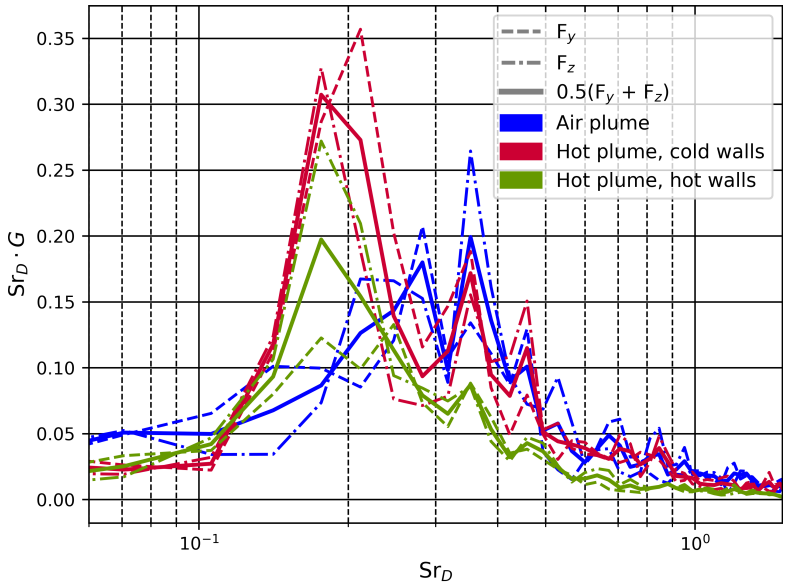

Figure 5.13: Premultiplied PSD of the buffet loads for the long nozzle configuration.

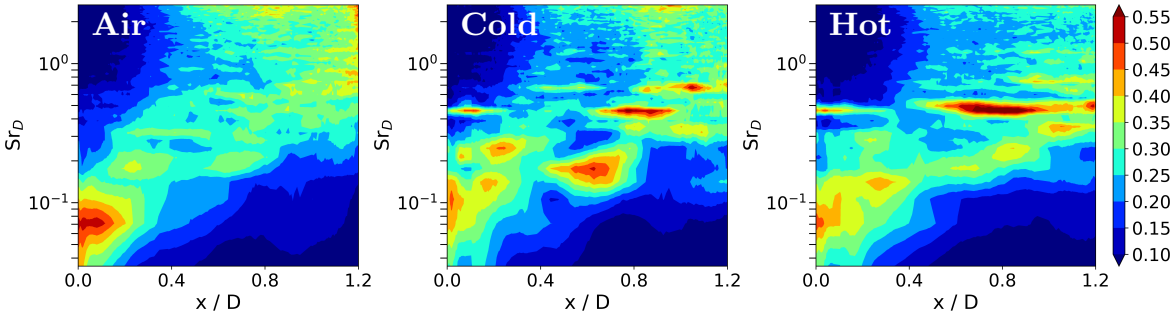

Figure 5.14: Scaled premultiplied PSD of the pressure on the external nozzle surface.

A spectral analysis of the forces is shown in Fig. 5.13 in both directions individually as well as averaged. A very dominant peak in the buffeting loads around $\mathrm{Sr}_D \approx 0.18$ is clearly visible for both hot plume cases, whereas for the air plume case a peak near this frequency only appears in one direction and on average the peak appears around $\mathrm{Sr}_D \approx 0.27$ instead. A second peak around $\mathrm{Sr}_D \approx 0.35$ is visible for all cases, however. This second peak was also observed by Statnikov et al. [61] as well as in the investigations in Chapter 4. However, both of these investigations showed the dominant peak around $\mathrm{Sr}_D \approx 0.18..0.2$. The likeliest explanation for this difference is connected to the different plume exit conditions. In the previous investigations ([61], Chapter 4) the plume is underexpanded or only slightly overexpanded with a full flowing nozzle whereas in the current configuration the strong overexpansion leads to flow separation in the nozzle, which might affect amplification of different frequencies. The shift could also be related to grid resolution, as a similar observation was made in the grid study in Chapter 4 for the coarsest grid. This seems unlikely, however, as the used grids feature a similar or finer grid resolution than those used in the grid study. Neither of these arguments explains why this shift only appears for the air plume case, but not for the hot plume cases, and hence further investigations should be conducted in the future.

Note that no scaling of the PSD is applied and hence the peak height correlates with the force amplitudes for the respective frequency range. Taking this into account, it is visible that the reduction of loads for the hot wall case is visible over all frequencies whereas the relative amplitude of the peaks to each other does not change significantly compared to the cold wall case. A comparison between the cold wall cases shows that the amplitude of the PSD is very comparable for all frequencies, with the exception of the peak at $\mathrm{Sr}_D \approx 0.2$ which is much stronger for the hot plume case.

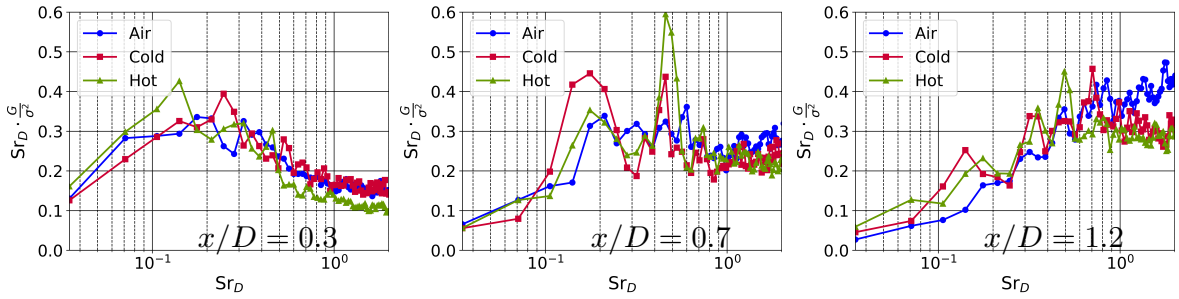

Figure 5.15: Scaled premultiplied PSD of the pressure on the external nozzle surface at $x/D = 0.3, 0.7, 1.2$ (left to right).

Spectral analysis of pressure fluctuations

To gain a better understanding of the features in the buffeting force spectra, the scaled premultiplied PSD of the wall pressure on the external nozzle surface is displayed in Fig. 5.14. In addition to the color contours showing the spectral content over all axial locations and frequencies for each case shown in this figure, the spectra are also displayed as line plots at three distinct axial locations in Fig. 5.15 to allow better quantitative comparison between the cases. The overall qualitative spectra look similar for all cases, with a shift of spectral content to higher frequencies closer to the nozzle lip. All three cases show a peak at $\mathrm{Sr}_D \approx 0.2$ in the region $0.4 < x/D < 0.8$. However, the peak amplitude differs, with the peak much more pronounced for the cold wall case. For the air plume and hot wall case the peak height is fairly similar, most clearly visible in the spectra at $x/D = 0.7$ in Fig. 5.15. The reduced distinctiveness of the peak for the air plume case is mostly due to a large amount of fluctuations at high frequencies $\mathrm{Sr}_D > 1$ as well as a generally more broadband distribution with less distinct peaks. This high frequency content is reduced for the hot plume cases, and even further reduced if the walls are hot as well: For the hot wall case contributions at $\mathrm{Sr}_D > 1$ are essentially non-existent, whereas for the cold wall case they appear for $x/D > 0.8$ and for the air plume case even further upstream for $x/D > 0.4$.

A distinct feature that is visible for all cases are a peak around $\mathrm{Sr}_D \approx 0.1$ for $x/D < 0.2$ as well as an increased broadband spectral content around $\mathrm{Sr}_D \approx 0.6 \ldots 0.7$ towards the nozzle lip. An small peak around $\mathrm{Sr}_D \approx 0.35$ is also visible for all cases, but appears dominantly around $x/D \approx 1$ for the hot plume cases and more widely spread out between $0.2 < x/D < 0.8$ for the air plume case.

One distinct difference between the air and hot plume cases exists as well: For the cases with hot plume a strong peak around $\mathrm{Sr}_D \approx 0.4 \ldots 0.5$ for $x/D < 0.2$ and $x/D > 0.6$ is very pronounced, particularly for the case with hot walls. The increased strength of this peak in the region $0.5 < x/D < 0.8$ is also the main reason for the reduced amplitude of the peak around

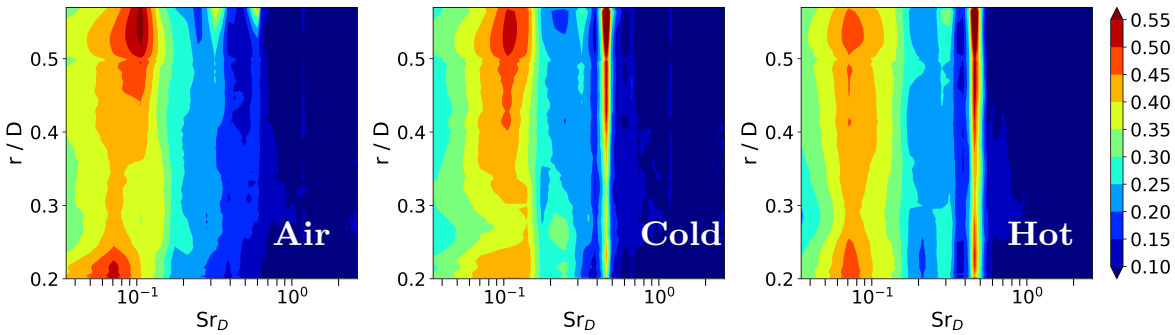

Figure 5.16: Scaled premultiplied PSD of the pressure on the base surface.

$\mathrm{Sr}_D \approx 0.2$ in this region. For the air plume case there is also some content in this frequency range, but of similar amplitude as at slightly higher frequencies and thus very difficult to distinguish from the overall increased broadband content for the air plume case.

Interestingly, the peak around $\mathrm{Sr}_D \approx 0.45$ is also visible as the dominant feature in the spectral analysis of the base pressure for the cases with a hot plume, as shown in Fig. 5.16. The spectra also indicate that the peak amplitude increases towards larger radii. For the air plume case a similar peak above the base surface (i.e. for $r/D > 0.5$ in/ above the boundary layer) is visible, but this peak is located around $\mathrm{Sr}_D \approx 0.6$ rather than $\mathrm{Sr}_D \approx 0.45$ and thus seems to originate from a different phenomenon. A similar peak around $\mathrm{Sr}_D \approx 0.65$ is also faintly visible in the hot plume cases (e.g. $x/D = 0.55$ in Fig. 5.17). Aside from this dominant feature, for all cases some spectral content is visible around $\mathrm{Sr}_D \approx 0.1$ at all radii as well as some contribution around $\mathrm{Sr}_D \approx 0.35$ at larger radii. These two features also agree very well in amplitude between the cases.

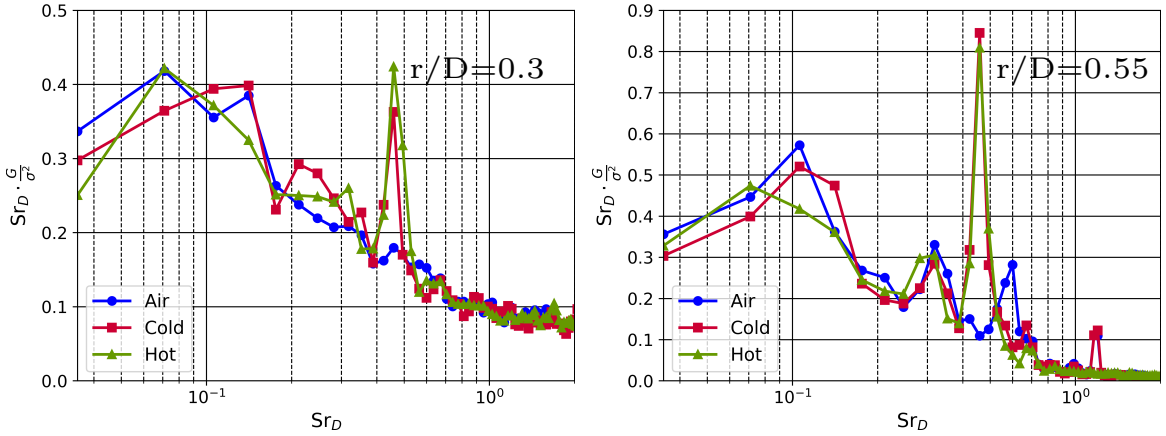

Figure 5.17: Scaled premultiplied PSD of the pressure on the base surface at $r/D = 0.3$ (left) and $r/D = 0.55$ (right).

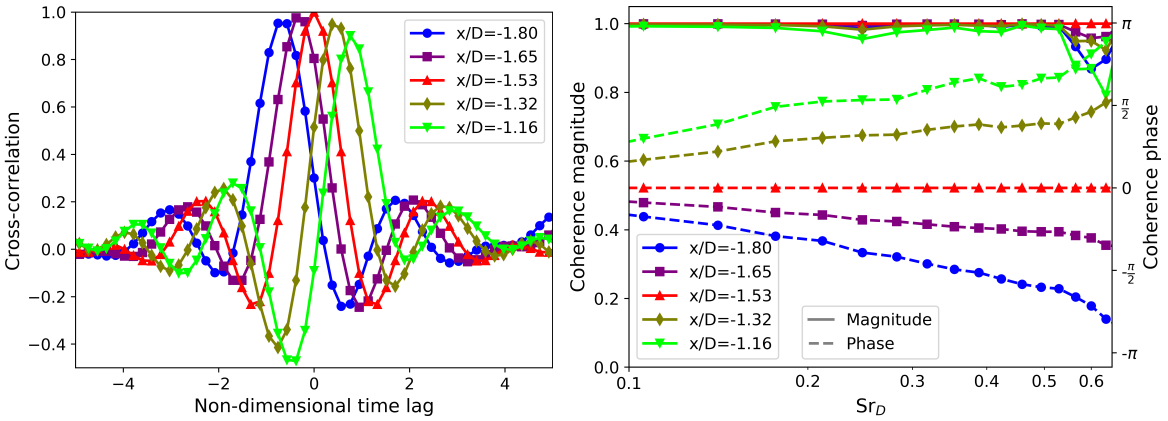

Figure 5.18: Cross correlation (left) and coherence function (right) between pressure signals at different axial locations on the main body.

To ensure the found spectral features are not influenced by the inflow conditions, the cross correlation between pressure histories of points on the wall of the main body are computed and displayed on the left of Fig. 5.18 for the hot wall case. A positive time lag in the figure corresponds to the signal at the reference location (here: $x/D = -1.53$) lagging behind that at the evaluated position.

It is visible that for locations that are further downstream the cross correlation peaks with values close to unity at a positive time lag whereas for positions upstream of the reference position a negative time lag is visible. This is a clear indication that information is traveling upstream and no numerical disturbances are created by the inflow condition.

The coherence function shown on the right of Fig. 5.18 confirms this behaviour as well: A very close to unity amplitude of the coherence magnitude is visible for all positions over all considered frequencies, indicating a mostly undisturbed propagation of the pressure signal. The phase of the coherence function confirms the behaviour observed by the cross correlation function, with negative phase for the positions upstream of the reference location and positive phase downstream of it. This analysis shows that the observed spectral content, including that at frequency $\mathrm{Sr}_D \approx 0.45$, is not propagated from the inflow into the domain, but instead the dominant pressure features originate from interactions within the flow field.

Considering the peak at $\mathrm{Sr}_D \approx 0.45$ in the wall pressure PSD appeared neither in previous investigations (e.g. [42, 52, 61, 73]) nor the investigation with a similar configurations in Chapter 4 allows to narrow down the possible origins of this phenomenon. The major differences in the current investigation are the inclusion of the wind tunnel walls and the plume conditions, whereas relative geometrical dimensions and free stream conditions are similar. Weiss and Deck [71] point out that the wind tunnel walls can have an impact on the observed frequency peaks,

but for a wind tunnel diameter that is much closer to the model diameter ($D_{tunnel} \approx 2.86D$ whereas here $D_{tunnel} = 5.1D$). In their investigation the effect is also not the creation of an additional peak, but an amplification of the existing instability at $\mathrm{Sr}_D \approx 0.2$. Furthermore, this aspect does not explain why the peak is much more pronounced in the hot plume cases since inflow and wind tunnel walls exist for all investigated configurations. Hence, it seems unlikely that the wind tunnel walls are the origin of the phenomenon. Instead, the additional frequency contribution most likely originates from the different plume conditions.

Further insight into the different frequency peaks can be gained by evaluating the contributions of the different frequencies to the pressure fluctuations in the flow field as is shown in Fig. 5.19 for $\mathrm{Sr}_D \in [0.1, 0.18, 0.32, 0.46]$ for the hot wall case. The lowest dominant frequency $\mathrm{Sr}_D \approx 0.1$ contributes to the pressure fluctuations in the recirculation region mainly near the base wall and in the recirculation corner, whereas for $\mathrm{Sr}_D \approx 0.18$ the highest contributions are visible in the center of the external nozzle surface. This matches the observations e.g. by Weiss et al. [73]. The frequencies $\mathrm{Sr}_D \approx 0.35$ and $\mathrm{Sr}_D \approx 0.45$ have peaks located closer to the nozzle lip. For the latter an additional peak can be found near the top of the base wall. The footprint of these contributions on the wall was already visible in Fig. 5.14 and Fig. 5.16. The visualization in Fig. 5.19 shows that the pressure fluctuations in the field with the displayed frequencies exhibit reduced amplitudes in the shear layer itself and increased amplitudes below (in the recirculation region) and above (in the free stream). Since the shear layer is dominated by small scale turbulent structures and/or Kelvin-Helmholtz-like instabilities with higher frequencies [42] this is to be expected. The dominant pressure fluctuations on the wall are instead created by the overall movement of the shear layer that is modulating the pressure field, which explains the impact both on the recirculation region as well as on the free stream flow and is also in agreement with observations by Statnikov et al. [61]. Note that the contributions inside the nozzle are based on a very low amount of overall pressure fluctuations (cf. 5.10) and are due to numerical noise and do not represent significant physical phenomena.

Interestingly, the two higher frequencies show alternating regions of low contributions and slightly larger contributions; e.g. for $\mathrm{Sr}_D \approx 0.32$ there is essentially no contribution for $0 < x/D < 0.8$, but an increase for $0.8 < x/D < 1.2$ followed by another region with lower content. This pattern matches a swinging motion of the shear layer as observed by Statnikov et al. [61], with the node of the swinging located around $x/D \approx 1$, i.e. the low intensity areas are regions where the shear layer moves in the radial direction. Consequently, the maximum contribution for this frequency is also located at the position of the node since at this location the pressure is modulated by both the upstream as well as the downstream shear layer movement. The visualization for $\mathrm{Sr}_D \approx 0.46$ shows a similar pattern, indicating a swinging motion as well, but with a shorter wave length due to the higher frequency. Hence the peak location is shifted

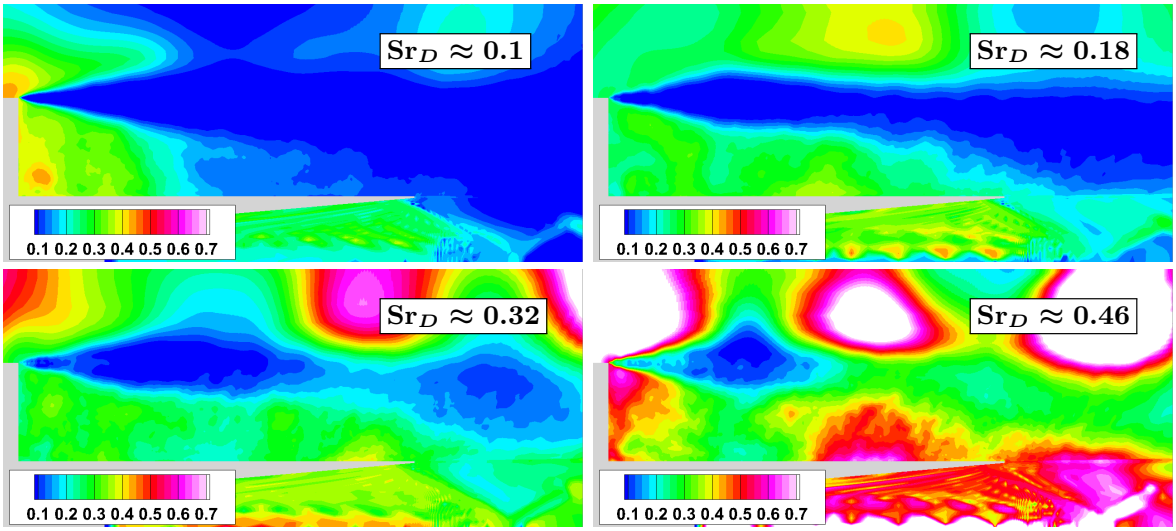

Figure 5.19: Distribution of scaled premultiplied PSD in the field for selected frequencies $\mathrm{Sr}_D \approx 0.1$, $\mathrm{Sr}_D \approx 0.18$, $\mathrm{Sr}_D \approx 0.32$, $\mathrm{Sr}_D \approx 0.46$ (top left to bottom right).

upstream to $x/D \approx 0.75$.

For this frequency there is also a strong contribution in the plume visible, particularly in the region of the nozzle flow separation shock system. This indicates that the shock and separation location oscillate predominantly with this frequency. As a consequence the pressure disturbances associated with this shock movement can interact with and amplify the shear layer movement, leading to the strong frequency peak visible in the recirculation region. There is also an explanation why this phenomenon appears in the frequency range $\mathrm{Sr}_D \approx 0.4 \ldots 0.5$: For the shown frequency the second node of the swinging motion is located just downstream of the nozzle lip, and hence a peak at this frequency is visible at this axial location. This peak in spectral content is optimally located to affect the nozzle separation location and shock system by modulating the pressure at the nozzle lip. For other frequencies, e.g. $\mathrm{Sr}_D \approx 0.32$ the pressure maximum is located too far upstream and thus is blocked by the nozzle structure.

It should be noted that the plume itself is treated in (U)RANS mode and thus the detailed interaction between the (separated) plume boundary layer turbulence and the external flow turbulence is not captured. The observed interaction and amplification is expected to be captured accurately because the ability of (U)RANS to react accurately to outside pressure disturbances has been shown [20]. However, additional flow phenomena that are created by the detailed interaction of turbulent structures from inside the nozzle boundary layer might not be represented.

Insights into the connection between the pressure spectra and the buffeting force spectra can be gained by an analysis of circumferential modes based on the wall pressure coherence function

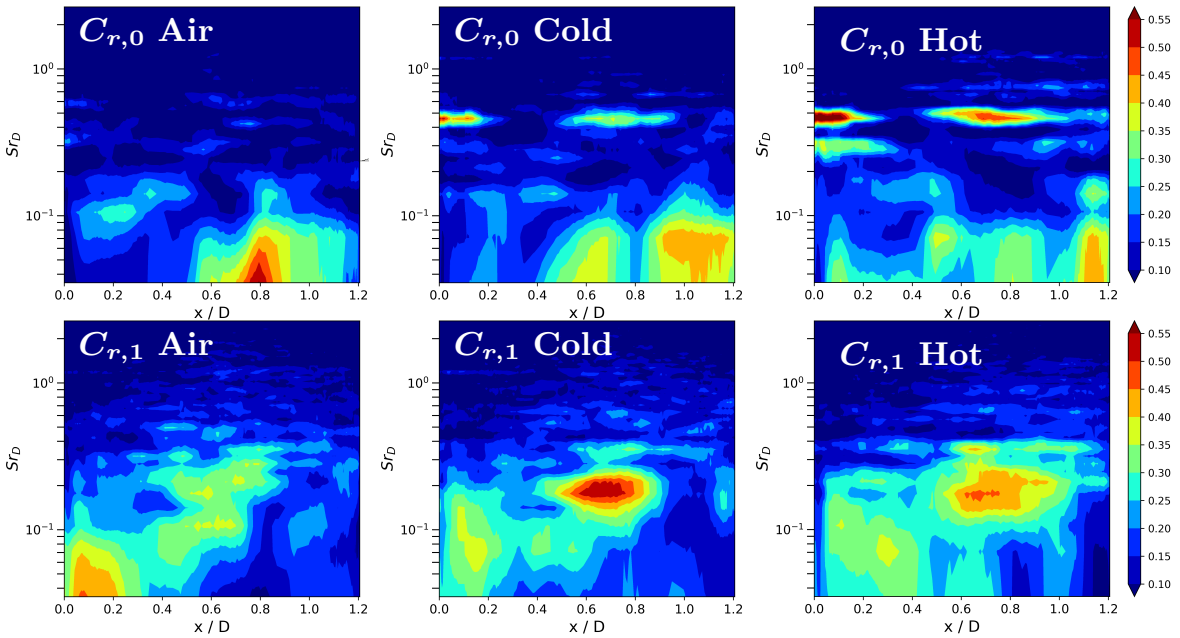

Figure 5.20: Coherence mode $C_{r,0}$ (top) and $C_{r,1}$ (bottom) of external nozzle wall pressure.

(cf. Sec. 3.7) on the external nozzle wall, which is shown in Fig. 5.20 and Fig. 5.21. The antisymmetric mode $C_{r,1}$ shows a clear peak around $\mathrm{Sr}_D \approx 0.2$ in the region $0.4 < x/D < 0.8$ as well as some content around $\mathrm{Sr}_D \approx 0.1$ in the vicinity of the base wall for all cases. This agrees well with the results shown by Pain et al. [42] who investigated a configuration without plume.

However, for the air plume case, the contribution around $\mathrm{Sr}_D \approx 0.2$ is less distinct, but spread out over multiple frequencies $0.2 < \mathrm{Sr}_D < 0.3$. Additionally, a contribution at $\mathrm{Sr}_D \approx 0.35$ can be seen for all cases, most notably for the hot wall case. Since $C_{r,1}$ is responsible for the buffeting loads it is to be expected that the same frequencies are found that were also visible in the force spectra in Fig. 5.13. The reason the contribution at $\mathrm{Sr}_D \approx 0.1$ is not found in Fig. 5.13 is the very low amount of wall pressure fluctuations near the base, as visible in Fig. 5.11.

For $C_{r,0}$ the air plume case only shows some contribution for $\mathrm{Sr}_D < 0.1$, most likely associated with the symmetrical cross pumping observed by Statnikov et al. [61]. This contribution is also visible for the cases with hot plume. However, these also show a significant peak at $\mathrm{Sr}_D \approx 0.4 \ldots 0.5$ at essentially the same positions the peaks at this frequency showed up in the wall pressure PSD in Fig. 5.14. The new feature with hot plumes hence presents itself as a symmetric mode, i.e. the pressure is modulated at all circumferential locations at approximately the same time, and hence does not yield a resulting buffeting force. This also

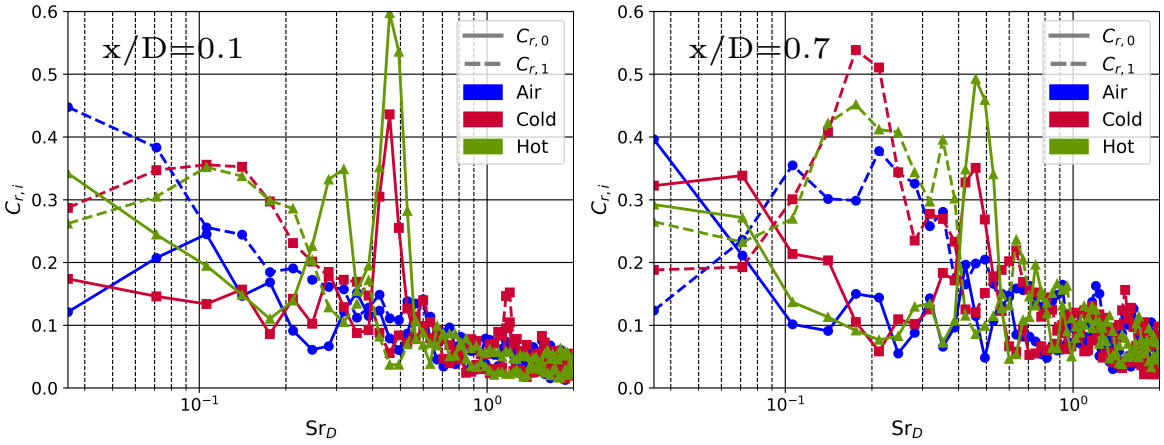

Figure 5.21: Coherence modes at $x/D = 0.1$ (left) and $x/D = 0.7$ (right).

explains why this frequency does not exhibit a dominant peak in the force spectra in Fig. 5.13, even though it is the most dominant feature in the pressure spectra and located in a region of high pressure fluctuations. The small remaining increase in the force spectra at this frequency might either be due to small disturbances in the pressure distributions that would disappear for longer data collection periods or an asymmetric contribution of this frequency with low amplitude.

DMD Analysis

The the time resolved flow field can additionally be analysed using Dynamic Mode Decomposition (DMD) (see Section 3.7). Figure 5.22 shows the obtained modes with their respective frequencies and amplitudes for the three cases in an analysis using a circumferential resolution of 7.5° (cf. Fig. 3.4). Additionally, the difference in the obtained modes when including the plume in the analysis is shown.

For all cases the highest amplitude modes appear at similar frequencies, namely around $\mathrm{Sr}_D \approx 0.1, 0.2, 0.35, 0.45$, which matches the features observed in the wall pressure spectra (cf. Fig. 5.14). For the air plume case two modes are visible at $\mathrm{Sr}_D \approx 0.08, 0.11$, three at $\mathrm{Sr}_D \approx 0.19, 0.22, 0.26$ as well as two around $\mathrm{Sr}_D \approx 0.31, 0.35$ and one around $\mathrm{Sr}_D \approx 0.43$. With the inclusion of the plume in the analysis the modes at $\mathrm{Sr}_D \approx 0.08, 0.22, 0.31$ increase slightly in amplitude, but the general mode distribution and frequencies do not change. A similar mode distribution is also found for the case with a hot plume and cold walls, with a slight increase in frequency of the first mode pair to $\mathrm{Sr}_D \approx 0.09, 0.12$ and the last dominant mode to $\mathrm{Sr}_D \approx 0.48$. For the hot wall case the distribution is similar to the cold wall case, but the modes at $\mathrm{Sr}_D \approx 0.26, 0.31$ are reduced in amplitude. For both hot plume cases the effect of

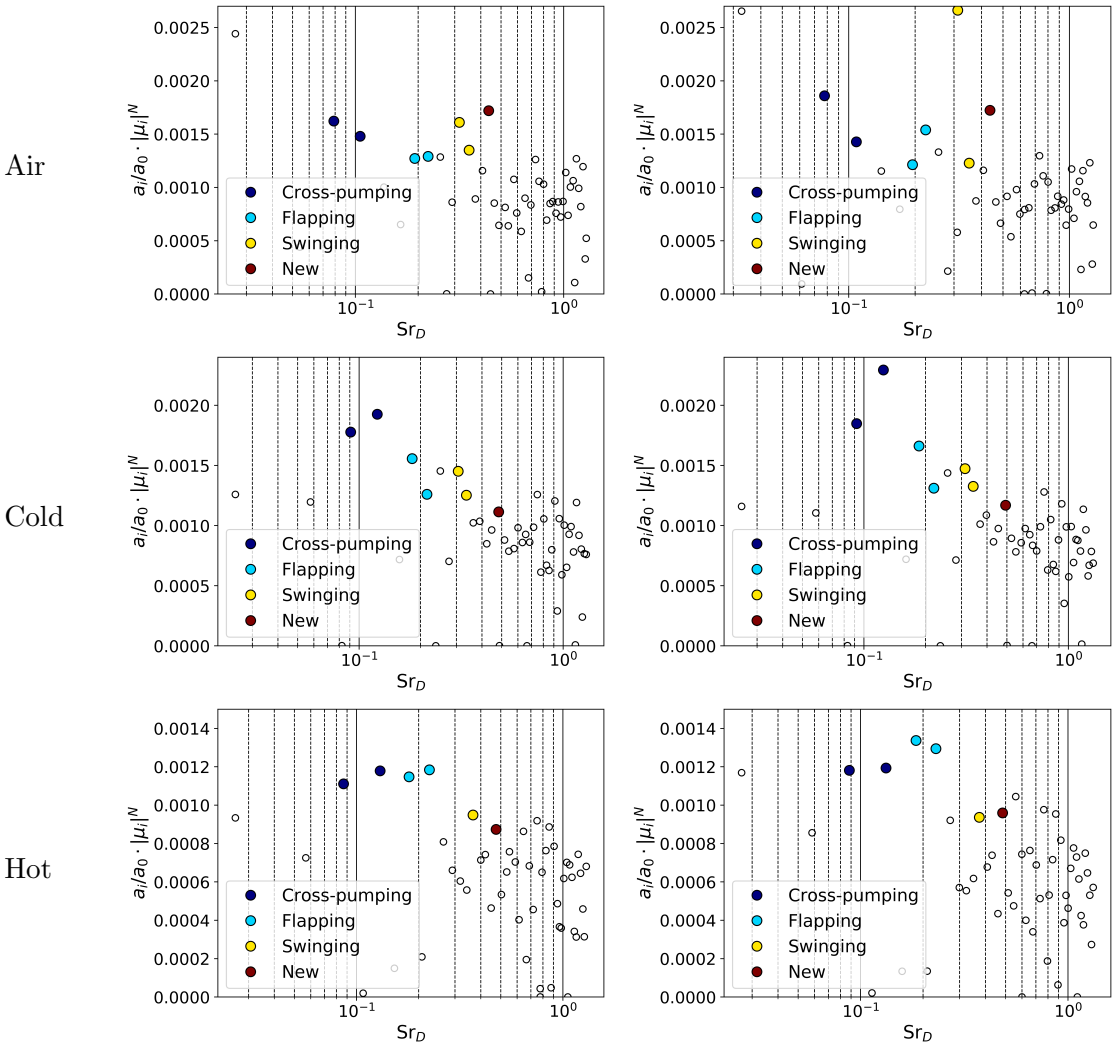

Figure 5.22: Mode amplitudes and frequencies obtained by Dynamic Mode Decomposition (DMD) when not including (left) and including (right) the plume in the analysis.

inclusion or omission of the plume in the analysis is even smaller than for the air plume case, leading only to small differences in the mode amplitudes. All cases also show a mode with medium to high amplitude around $\mathrm{Sr}_D \approx 0.025$. The impact on the spectral content cannot be evaluated, however, since the frequency resolution of $\Delta\mathrm{Sr}_D \approx 0.035$ is insufficient.

In addition to the similar mode distributions, the symmetry of the individual pressure modes is similar between the cases as well. This is shown exemplary for the mode at $\mathrm{Sr}_D \approx 0.2$ in Fig. 5.23. Even though differences between the mode shapes are visible, for all cases this mode shows an antisymmetric pressure distribution. This is most clearly visible for the cold wall

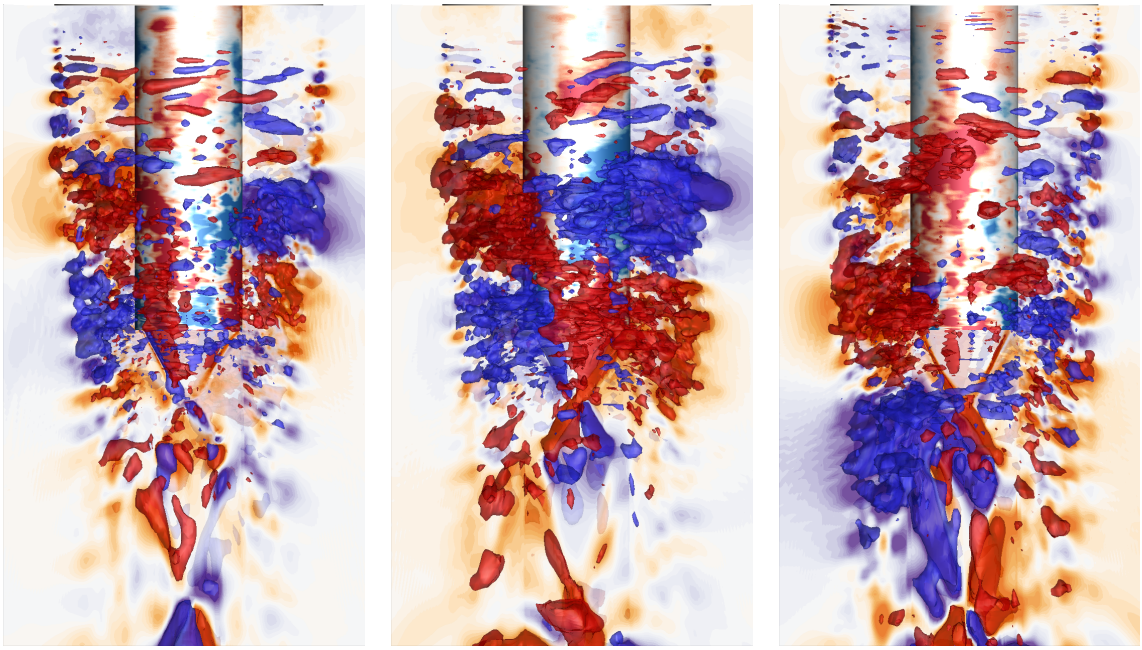

Figure 5.23: DMD pressure modes around $\mathrm{Sr}_D \approx 0.2$ for the difference cases.

case, with positive and negative pressure isosurfaces clearly located on opposite sides of the external nozzle surface. For the hot wall case this behaviour does not appear as strongly and is mainly visible by the presence of isosurfaces on one side and the absence of them on the other. Comparable similarities can be observed for the other obtained mode shapes.

The fact that similar dominant modes and mode shapes are obtained both for different plume characteristics and for different wall temperatures shows that the underlying flow physics appear largely unaffected by these parameters. Furthermore, even the frequencies these phenomena occur at seem nearly unchanged.

The shapes of selected dominant modes for the hot wall case that match the features in the wall pressure spectra are displayed in Fig. 5.24. In addition to a snapshot of the pressure mode, the reconstructed axial velocity and an isosurface of zero axial velocity at two time instances half a period apart is shown to visualize the shear layer movement. The movement is also indicated by yellow arrows.

It is visible that the mode at $\mathrm{Sr}_D \approx 0.1$ creates a symmetric pressure distribution and exhibits a longitudinal growing and shrinking of the recirculation region. At $\mathrm{Sr}_D \approx 0.2$ the mentioned asymmetric pressure distribution is visible that is accompanied by a pronounced asymmetric flapping motion of the shear layer near the nozzle lip. For the mode at $\mathrm{Sr}_D \approx 0.35$ the pressure distribution shows tilted pressure isosurfaces that lead to an asymmetric footprint as well For this mode the shear layer movement occurs further upstream, leading to a swinging-like motion.

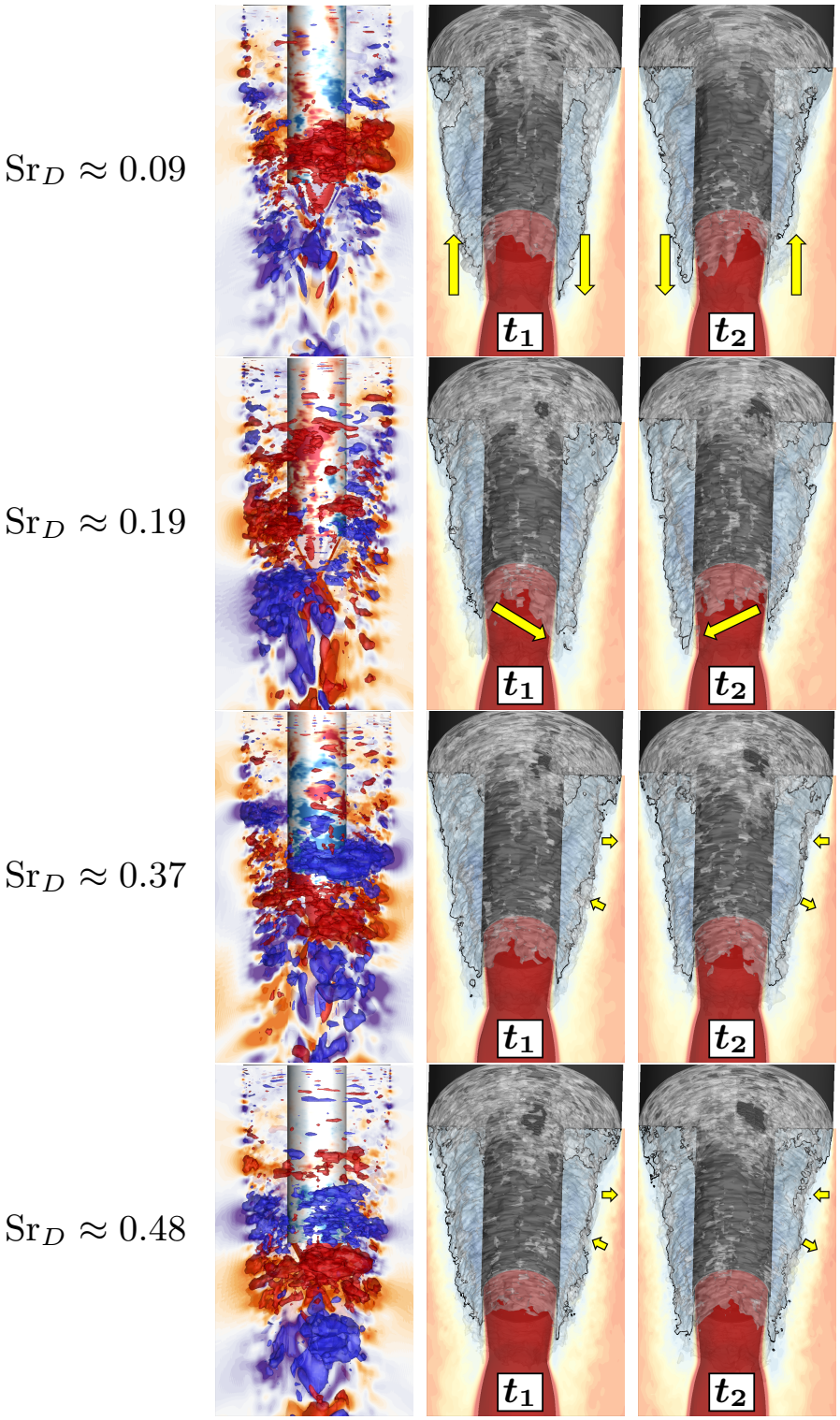

Figure 5.24: DMD modes (left: Pressure, Center & Right: Axial velocity) for the hot wall case.

The last displayed mode at $\mathrm{Sr}_D \approx 0.45$ shows a clear symmetric pressure distribution and the shear layer movement can also best be described as swinging-like, albeit less pronounced than for the mode at $\mathrm{Sr}_D \approx 0.35$.

The extracted pressure distributions closely match the results obtained from the analysis of the circumferential coherence modes (cf. Fig. 5.20). Furthermore, the extracted shear layer movement also matches the distribution of the spectral content at the respective frequency in the pressure field (cf. Fig. 5.19), e.g. alternating regions of high and low amplitude of the PSD indicating a swinging motion of the shear layer for $\mathrm{Sr}_D \approx 0.35$ and $\mathrm{Sr}_D \approx 0.45$. Finally, the extracted shear layer movement also agrees with results from Statnikov et al. [61]. In their investigation of an aft-body flow in the presence of an air plume three dominant modes were found which they designated as "longitudinal cross-pumping" around $\mathrm{Sr}_D \approx 0.1$, "shear layer flapping" around $\mathrm{Sr}_D \approx 0.2$ and "shear layer swinging" around $\mathrm{Sr}_D \approx 0.35$.

The additional mode at $\mathrm{Sr}_D \approx 0.45$ in the current analysis is, as mentioned in the discussion of Fig. 5.19, most likely attributed to the interaction of the recirculation region with the nozzle flow separation. Hence, it does not appear in the analysis of Statnikov et al. [61] since their setup did not feature nozzle flow separation. Interestingly, the current analysis shows the mode not only for the hot wall cases, but even for the air case for which no clear peak in the pressure PSD was visible at this frequency. The missing peak in the wall pressure PSD might be either due to the upstream reattachment location on the nozzle surface, and hence reduced interaction between recirculation region and plume, or due to the plume properties. An argument against the latter is that the pressure fluctuations in the flow separation shock region are actually highest for the air plume case and lowest for the hot case (cf. Fig. 5.10). If the plume properties played a major role in the amplification of this frequency, it seems counter-intuitive that the case with the lowest pressure fluctuations in the plume would lead to the highest amplification. An argument for a dominant impact of the reattachment location is the strong correlation between both quantities, i.e. the case with the furthest downstream reattachment location shows the largest amplification.

5.3 Short nozzle configuration

For the short nozzle configuration different combustion chamber conditions are chosen to allow for higher overall temperatures as well as for plume characteristics that are closer to realistic flight conditions. These conditions are summarized in Table 5.3 together with those for the long nozzle configuration.

The wall temperature distributions obtained from coupled RANS simulations are displayed on the left of Fig. 5.25 showing wall temperatures of up to 1100 K near the nozzle lip. Similarly

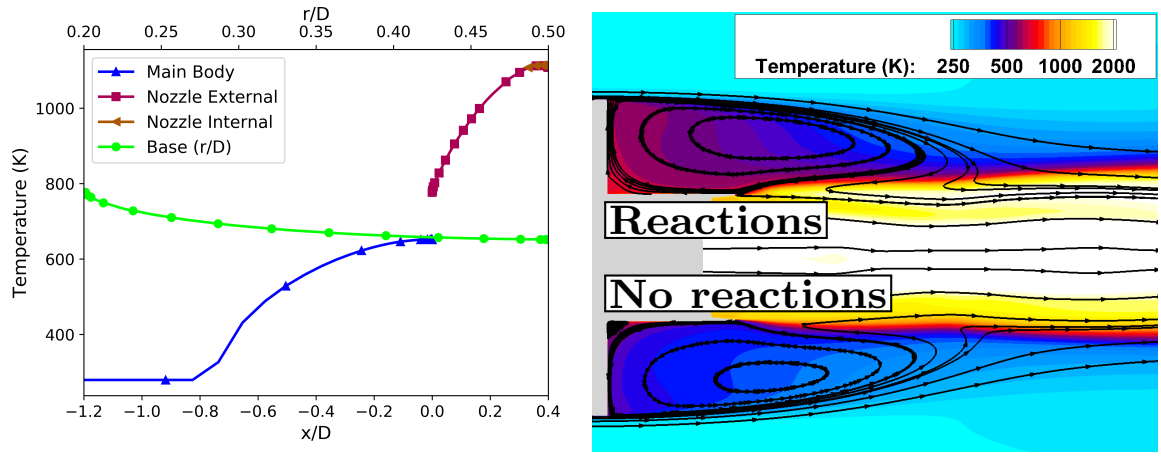

Figure 5.25: Wall temperatures (left) and RANS flow field (right; top: actived chemical reactions, bottom: deactived chemical reactions) for the hot wall case of the short nozzle configuration.

to the long nozzle configuration, the temperature difference between the internal and external nozzle walls is minimal, making the lines in the figure essentially indistinguishable. Since in an experimental setup the combustion chamber walls would need to be cooled for this condition, the main body walls do not heat up except just upstream of the separation location $x/D > -0.8$, leading to a significantly colder incoming boundary layer than for the long nozzle configuration. In addition, this also closer represents the flow around actual launch vehicles. The wall temperature at the separation location is about 650 K and the base corner shows a temperature of approximately 780 K.

The resulting flow field and temperature distribution from precursor RANS simulations are shown on the right of Fig. 5.25 and show the shape of the recirculation region above the plume. Due to the significantly shorter nozzle the shear layer does not reattach on the nozzle wall, but instead the majority of the recirculation region is located above the plume and consequently plume and recirculation region interact significantly. Hence, more hot fluid is transported into the recirculation region and consequently temperatures in the recirculation region are significantly higher than in the long nozzle configuration (cf. Fig. 5.3). A more detailed investigation of the mean temperature distribution in the recirculation region is discussed in subsection 5.3.1.

The figure also shows the field if chemical reactions are deactivated. In this case the temperature increase in the plume shear layer is absent and the temperatures in the recirculation region and in particular above the external nozzle surface are significantly reduced by about 100K to 150K due to less hot fluid being transported in the back flow. The recirculation region size also shrinks slightly. Considering these strong effects on the overall recirculation

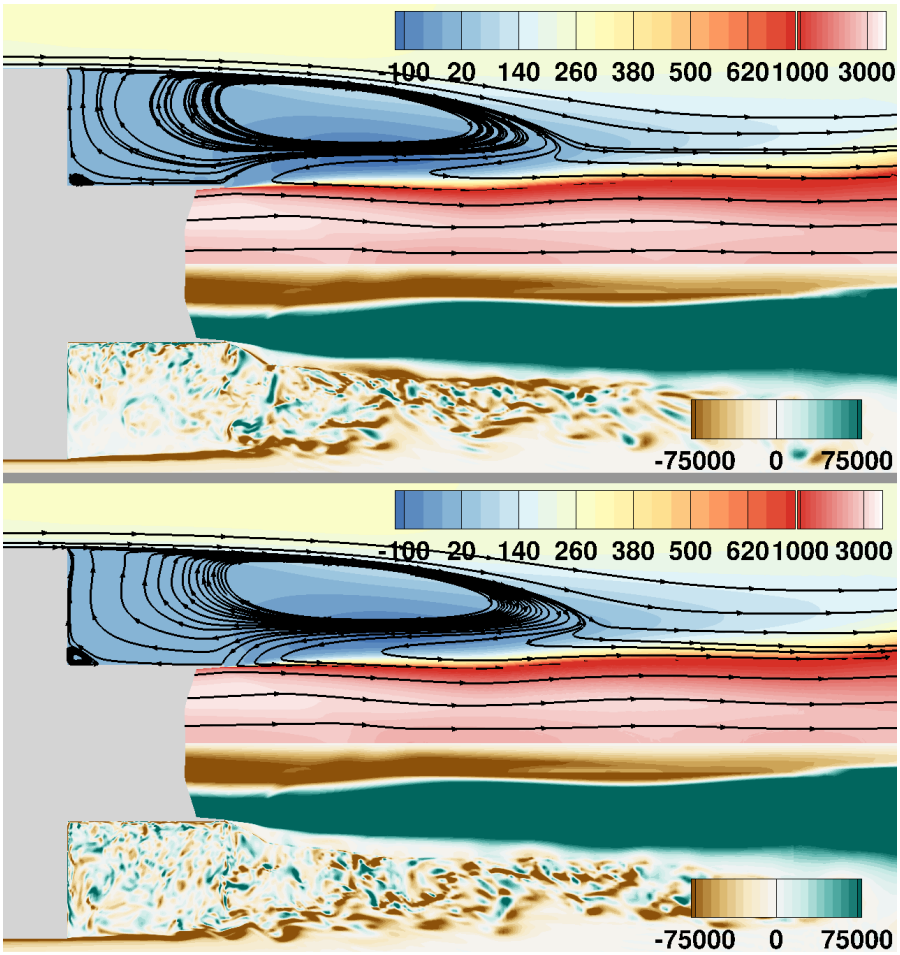

Figure 5.26: Mean and instantaneous flow fields for the cases with with cold walls (top) and hot walls (bottom). Mean axial velocity (top) in m/s and instantaneous circumferential vorticity (bottom) in 1/s.

region characteristics the scale resolving simulations also include 9 components and a full set of reactions as described in appendix C.

In addition to the case with hot walls ("Hot") a simulation with colder walls at an ambient temperature of $T_w = 300$ K ("Cold") is investigated for the short nozzle configuration.

5.3.1 Mean flow fields

In Fig. 5.26 the mean flow field for both cases of this configuration is displayed. It is visible that the flow field is drastically changed compared to that for the long nozzle configuration displayed in Fig. 5.4. The shape of the recirculation region for the short nozzle configuration is more elongated and the end of the recirculation region is shifted to larger radii compared

to the long nozzle configuration. This is caused by the acceleration of the flow in the plume shear layer which prevents backflow at lower radii.

Consequently, a reattachment location is not clearly defined, in particular the previously chosen definition (cf. subsection 5.2.1) is not meaningful for this configuration. Instead, the length of the recirculation region can be analysed by defining it as the furthest downstream axial location with negative axial velocity. The obtained values for the recirculation region size are shown in Table 5.5. It is visible that this definition yields very similar values to the reattachment location definition for the long nozzle configuration cases (cf. Table 5.4). The table shows that for the short nozzle configuration there is a smaller difference in recirculation region size between the hot and cold wall cases of about $0.064D$, or about 5%, compared to the difference of about $0.130D$ for the long nozzle configuration. Additionally, it can be seen that the RANS computations predict a shorter recirculation region size for this configuration than the IDDES whereas for the long nozzle configuration it was the other way around for most cases. The error between the predictions with RANS and IDDES is larger as well, which might point to a larger impact of the resolved turbulent structures on the flow topology that cannot be captured by RANS modeling. Similarly to the long nozzle configuration the qualitative difference between the two cases is captured in RANS, however.

The axial mean wall pressure distributions for both cases are shown in Fig. 5.27. The IDDES results show only a small negative pressure gradient on the external nozzle surface with the pressure for the hot wall case slightly higher than that for the cold wall case. Results from RANS computations show a lower pressure on the external nozzle wall and a pronounced minimum in wall pressure around $x/D = 0.3$ that is not visible in the scale resolving simulation results. Upstream of the separation location a much stronger pressure gradient is visible in both RANS and IDDES results and the quantitative pressure levels differ slightly between RANS and IDDES as well as between different wall temperatures. The upstream pressure drop is comparable to that for the long nozzle configuration (cf. Fig. 5.5); in fact, for the short nozzle IDDES results the overall axial mean pressure distribution between $-0.4 < x/D < 0.4$ is quite similar to that of the long nozzle IDDES results. For the RANS computations the results with different nozzle lengths differ more strongly, however, leading to larger deviations between RANS and IDDES in this region than for the long nozzle configuration.

	Long nozzle cold walls	Long nozzle hot walls	Short nozzle cold walls	Short nozzle hot walls
IDDES	$1.324D$	$1.460D$	$1.267D$	$1.331D$
RANS	$1.366D$	$1.448D$	$1.172D$	$1.183D$

Table 5.5: Recirculation region size for different cases of both configurations.

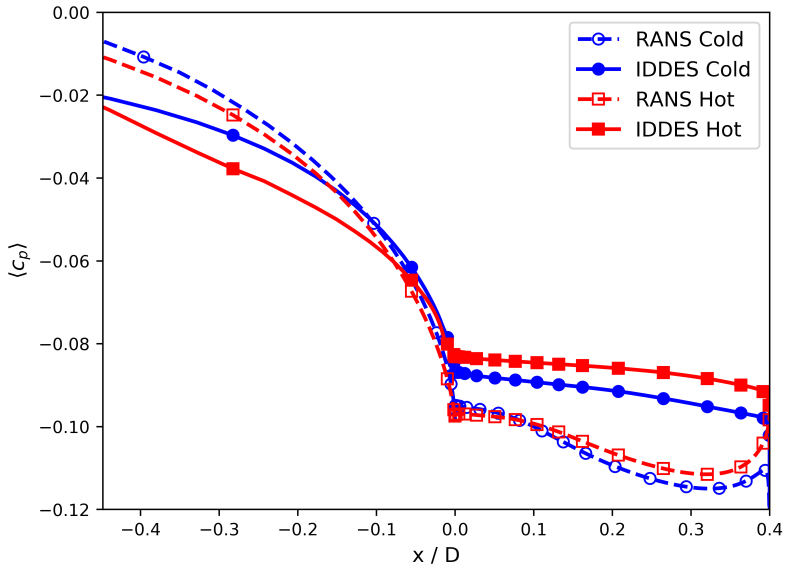

Figure 5.27: Mean pressure coefficient distribution for the short nozzle configuration.

The small differences in the mean pressure distribution and recirculation region size between both cases for this configuration can be explained by the small impact of the wall temperatures on the overall recirculation region temperature. This is due to the fact that the recirculation region is already significantly heated up by the hot plume. Figure 5.28 shows the radial mean temperature distribution at four axial locations for cold and hot wall cases of both configurations. The figure shows that the temperatures in the recirculation region even near the base wall at $x/D = 0.01$ are substantially higher for the cold wall case of the short nozzle configuration than for the hot wall case of the long nozzle configuration. Additionally, the temperature distribution in the region behind the nozzle lip ($x/D > 0.4$), which actually covers the majority of the recirculation region, is very similar for the short nozzle cases. It is also visible that for all cases the temperature is relatively independent of the radial position in the region above the nozzle (i.e. for all locations for the long nozzle configuration and for $x/D = 0.01$ and $x/D = 0.2$ for the short nozzle configuration), but differs significantly between radial positions downstream of the nozzle ($x/D = 0.6$ and $x/D = 1.2$ for the short nozzle configuration).

5.3.2 Mean heat fluxes

In contrast to the long nozzle configuration, for the short nozzle configuration significant wall heat fluxes are observed for both cold and hot wall cases. The mean heat fluxes for both cases are shown in Fig. 5.29 and show predominantly positive heat flux values for the hot wall case and predominantly negative heat flux values for the cold wall case. The former indicates that

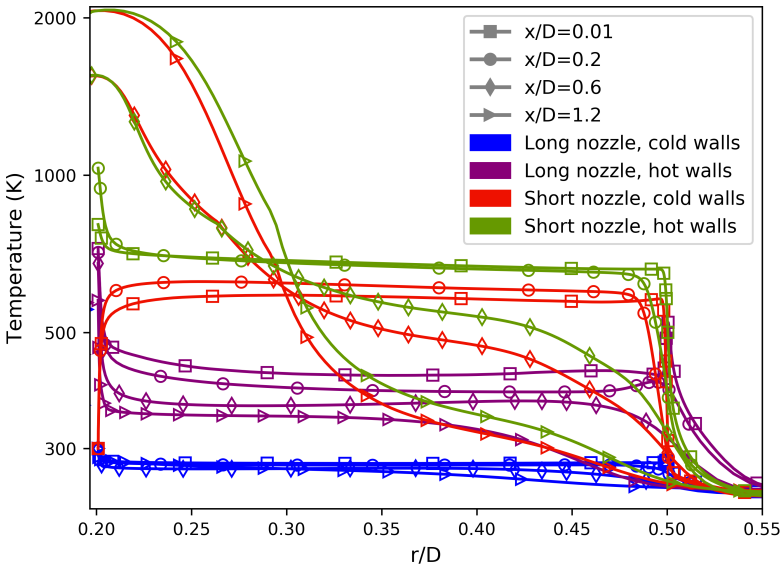

Figure 5.28: Radial temperature distribution at different axial locations.

the flow is heated by the walls as a consequence of the high wall temperatures whereas the latter that the walls are heated by the flow due to the hot plume gases convected towards the base.

For the cold wall case the heat flux on the external nozzle surface increases almost linearly from around -75 kW/m^2 near the base to around -110 kW/m^2 at $x/D = 0.35$ and more strongly towards the nozzle lip with peak values of around -650 kW/m^2. For the hot wall case the heat flux on the external nozzle surface also increases nearly linearly from around 25 kW/m^2 near the base to around 150 kW/m^2 at $x/D = 0.35$ and more strongly towards the

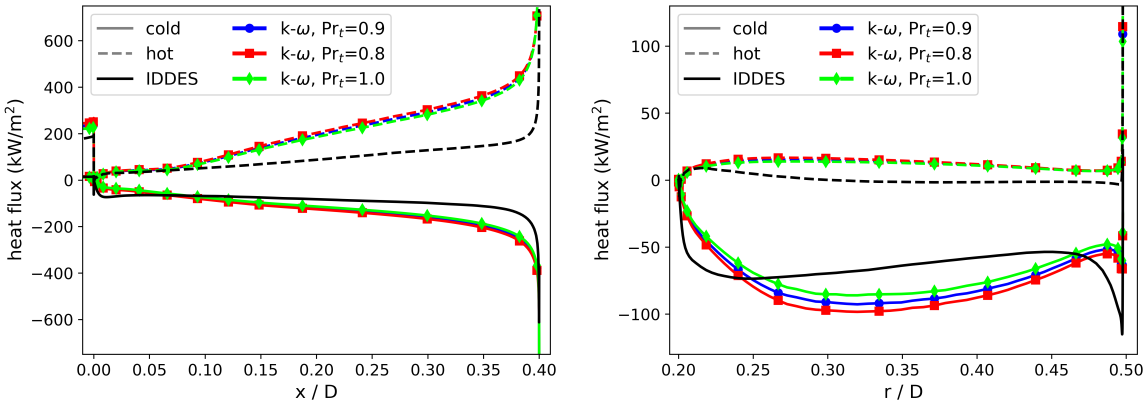

Figure 5.29: Mean heat flux distribution along the external nozzle surface (left) and the base surface (right).

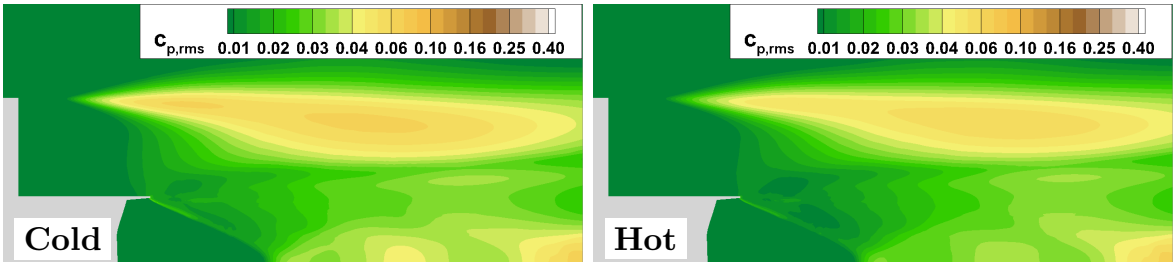

Figure 5.30: Rms pressure coefficient in the field for the short nozzle configuration.

lip with peak values of around 750 kW/m^2. The strong increase towards the nozzle lip can be attributed to the high unsteadiness of the flow field at the nozzle lip, as was already visible for the long nozzle configuration.

On the base surface the heat flux for the cold wall case shows a local maximum of 75 kW/m^2 around $r/D = 0.24$, followed by a slight decrease and a strongly increasing heat flux just below the top of the base that is associated with the larger velocity fluctuations in this region. At the top edge the effect of the (cold) boundary layer is visible that leads to a positive heat flux. For the hot wall case only very small heat fluxes with peak values of around 10 kW/m^2 at $r/D = 0.21$ are observed, except right below the top of the base where the impact of the incoming boundary layer dominates. The low heat fluxes can be explained with the similar temperature of the base walls ($700 - 800$ K, cf. Fig. 5.25) and the recirculation region fluid. In fact, between $0.3 < r/D < 0.5$ the heat flux is slightly negative, indicating the base wall being heated by the fluid.

The heat fluxes obtained from k-ω RANS computations appear qualitatively similar, but differ again strongly in the quantitative predictions. On the external nozzle surface a stronger axial gradient is visible in RANS which leads to heat fluxes at $x/D = 0.35$ that are about twice as high than in the IDDES for both cold and hot walls. On the base surface the local maximum is shifted towards larger radii $r/D \approx 0.3$ for both cold and hot walls with peak values that are about 30% higher than in the IDDES. Other observations are that for the cold wall case the heat flux increases less strongly near the top of the base and for the hot wall case the heat flux stays positive for all radii. A change in turbulent Prandtl number by $\Delta \mathrm{Pr}_t = 0.1$ leads to a heat flux difference of about 7% on the base wall and of about 4% on the external nozzle wall.

5.3.3 Unsteady flow fields

Pressure fluctuations and buffeting loads

The pressure fluctuations in the field indicated by the rms pressure coefficient are shown in Fig. 5.30. Only small differences between the cold and hot wall case are visible, with the cold

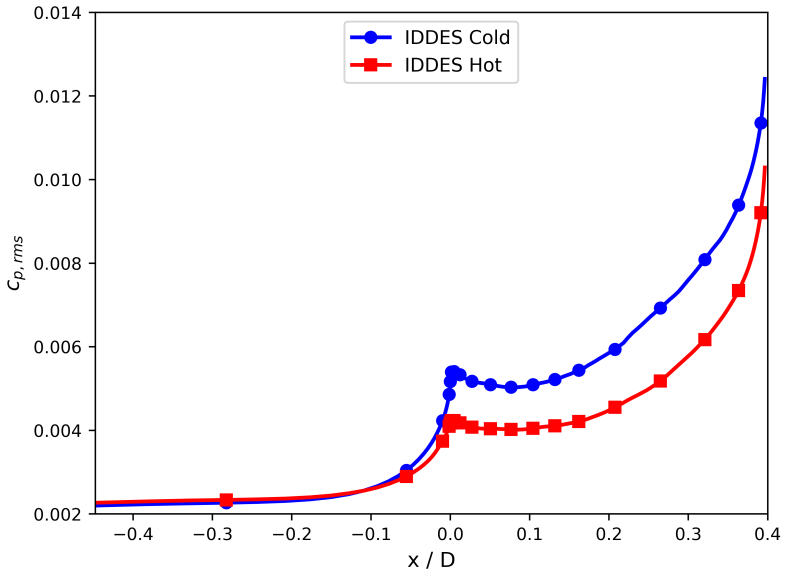

Figure 5.31: Rms wall pressure coefficient distribution for the short nozzle configuration.

wall case showing slightly higher values with maximum $c_{p,rms} \approx 0.066$ as opposed to maximum values for the hot wall case of $c_{p,rms} \approx 0.062$. Compared to the distributions for the long nozzle configuration (cf. Fig. 5.10) the region of high pressure fluctuations has a clearly different shape and remains at larger radii for further upstream locations. This matches the changes observed in the recirculation region shape. The maximum values for the long nozzle configuration with cold walls were slightly higher ($c_{p,rms} \approx 0.069$), but for the case with hot walls were significantly lower ($c_{p,rms} \approx 0.052$). The lower impact of hot walls on the pressure fluctuations for this case might be associated with the shorter region of boundary layer heating and thus a colder initial shear layer as this showed to be the major driving force for the changes observed for the hot wall case of the long nozzle configuration. Additionally, the generally more alike temperature distribution in the recirculation region and flow topology likely also contribute to a more alike distribution of pressure fluctuations.

An additional major difference between the short and long nozzle configuration visible in the figure is the strength of pressure fluctuations in the plume, particularly in the region of the nozzle flow separation shock. For the short nozzle configuration only small levels of fluctuations with $c_{p,rms} < 0.026$ at the axis are visible whereas for the long nozzle configuration values of $c_{p,rms} > 0.75$ can be seen. Slightly higher fluctuation levels are visible in the second shock cell, but these still do not reach levels nearly as high as those for the long nozzle configuration.

The footprint of the pressure fluctuations on the wall is visualized in Fig. 5.31, showing lower values of $c_{p,rms}$ for the hot wall case by about 25%. However, towards the nozzle lip the differences decrease to about 15%. Compared to the long nozzle configuration, the rms wall

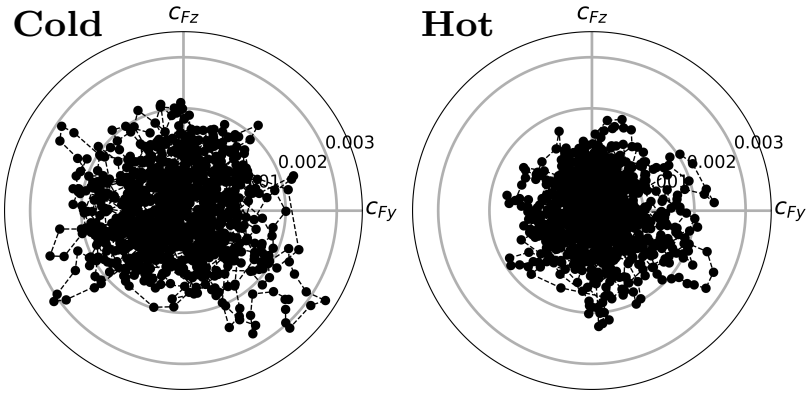

Figure 5.32: Non-dimensional buffeting loads for the short nozzle configuration.

pressure levels are significantly reduced (cf. Fig. 5.11), both on the external nozzle walls by about a factor of 2 for equal axial locations as well as in the boundary layer before separation by about a factor of 4. Additionally, due to the shorter nozzle length the maximum rms wall pressure values are reduced by about a factor of 4 as well.

The effect of this is also visible in the radial nozzle forces that are displayed in a polar style in Fig. 5.32. These show that the lower amount of pressure fluctuations for the short nozzle configuration is also reflected in the observed nozzle forces. For the cold wall case the mean force amplitude is reduced by about a factor of 4 compared to the corresponding long nozzle configuration case (cf. 5.12). In addition, for the hot wall case the mean force amplitude is about an additional 25% lower than for the cold wall case in this configuration.

The premultiplied PSD of the forces for the short nozzle configuration are visible in Fig. 5.33 and show that the lower force amplitude for the hot wall case is also reflected in the spectra. The cold wall case spectra show the highest pPSD amplitude around $\mathrm{Sr}_D \approx 0.13$ with a smaller peaks around $\mathrm{Sr}_D \approx 0.26$ and several minor peaks at higher frequencies. For the hot wall case a similar distribution is visible, but the first peak appears around $\mathrm{Sr}_D \approx 0.11$ and the second one around $\mathrm{Sr}_D \approx 0.22$ instead. Additionally, the first two peaks are less distinct and stronger differences between the two directions are visible for these peaks than for the cold wall case. The doubling of the frequency from first to second peak as well as the regularity of the following minor peaks might indicate that these are harmonics of the main peak around $\mathrm{Sr}_D \approx 0.13$ and $\mathrm{Sr}_D \approx 0.11$, respectively.

Spectral analysis of pressure fluctuations

The two main peaks are also visible in the pressure spectra on the external nozzle surface displayed in Fig. 5.34. For the cold wall case a dominant peak around $\mathrm{Sr}_D \approx 0.13$ is visible

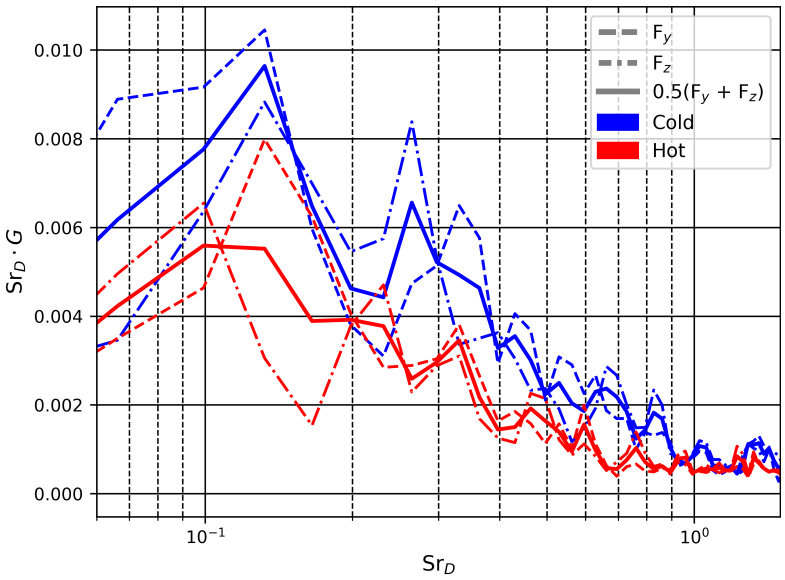

Figure 5.33: Premultiplied PSD of the buffeting loads for the short nozzle configuration.

mainly for $x/D < 0.3$ and a second peak around $\mathrm{Sr}_D \approx 0.26$ for $x/D > 0.2$. A further minor peak is visible for all axial locations around $\mathrm{Sr}_D \approx 0.56$. For the hot wall case the dominant peak is that at $\mathrm{Sr}_D \approx 0.26$ and extends to all axial locations. A smaller peak is visible around $\mathrm{Sr}_D \approx 0.1$ for $x/D < 0.2$. A quantitative comparison between the two cases is visible in the spectra at $x/D = 0.2$ and $x/D = 0.4$ shown in Fig. 5.35. At both locations the spectra appear fairly similar. The main difference between them is the increased strength of the first peak for the cold wall case and of the second peak for the hot wall case. It is also visible that near the nozzle lip at $x/D = 0.4$ the spectra for the hot wall case show a broad peak around

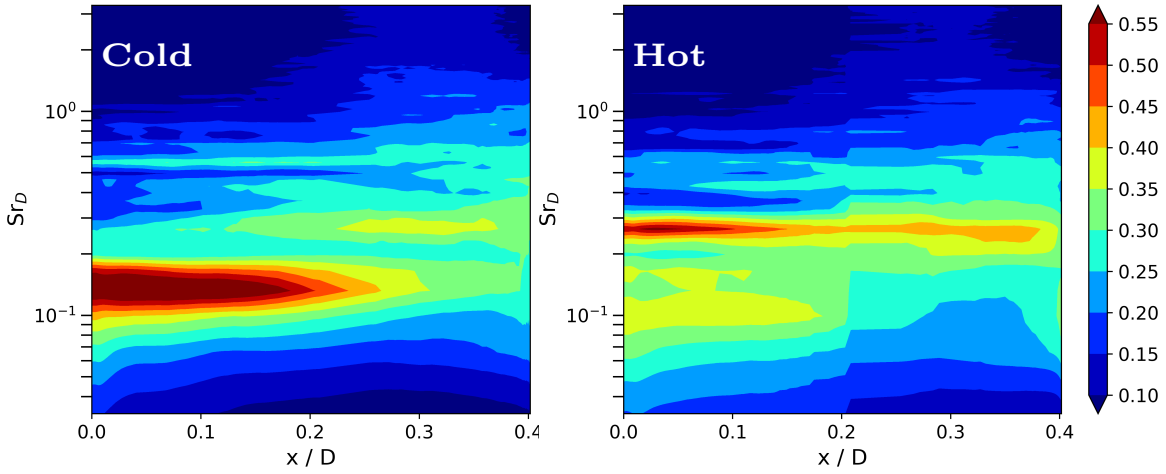

Figure 5.34: Scaled premultiplied PSD of the pressure on the external nozzle surface.

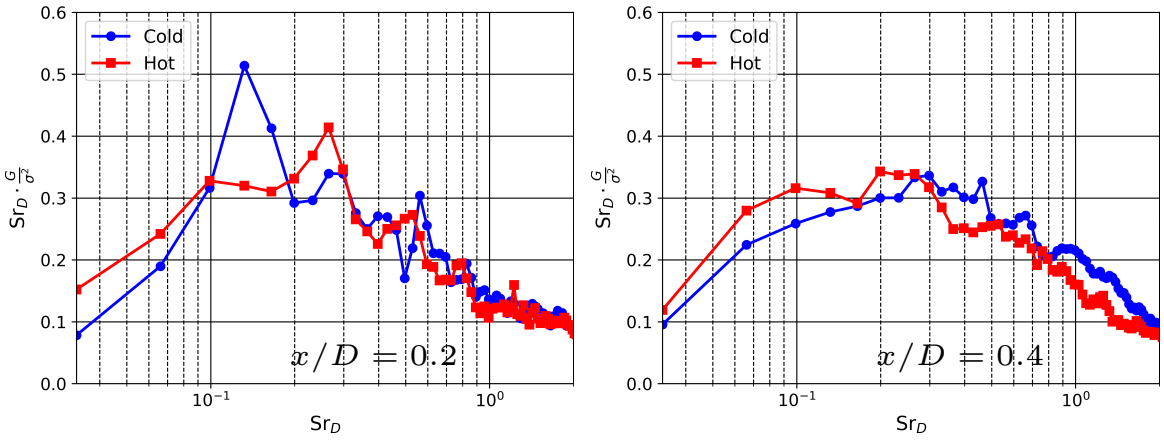

Figure 5.35: Scaled premultiplied PSD of the pressure on the external nozzle surface at $x/D = 0.1$ (left) and $x/D = 0.3$ (right).

$\mathrm{Sr}_D \approx 0.2 \ldots 0.26$. As this region shows the largest pressure fluctuations (cf. Fig. 5.31) this might be part of the explanation why the force spectra for this case show the second peak located around $\mathrm{Sr}_D \approx 0.22$ instead of $\mathrm{Sr}_D \approx 0.26$.

The difference in peak strength between both cases is also visible in the spectra of the base wall pressure shown in Fig. 5.36. For the cold wall case the spectra are dominated by the peak around $\mathrm{Sr}_D \approx 0.13$ whereas for the hot wall case the peak around $\mathrm{Sr}_D \approx 0.26$ is most dominant. The respective other peak appears with a reduced amplitude. Both cases also show a small peak around $\mathrm{Sr}_D \approx 0.56$ that is also visible - more clearly for the cold wall case - in the nozzle surface wall spectra in Fig. 5.34. The observed features are nearly independent of the radial location for both cases.

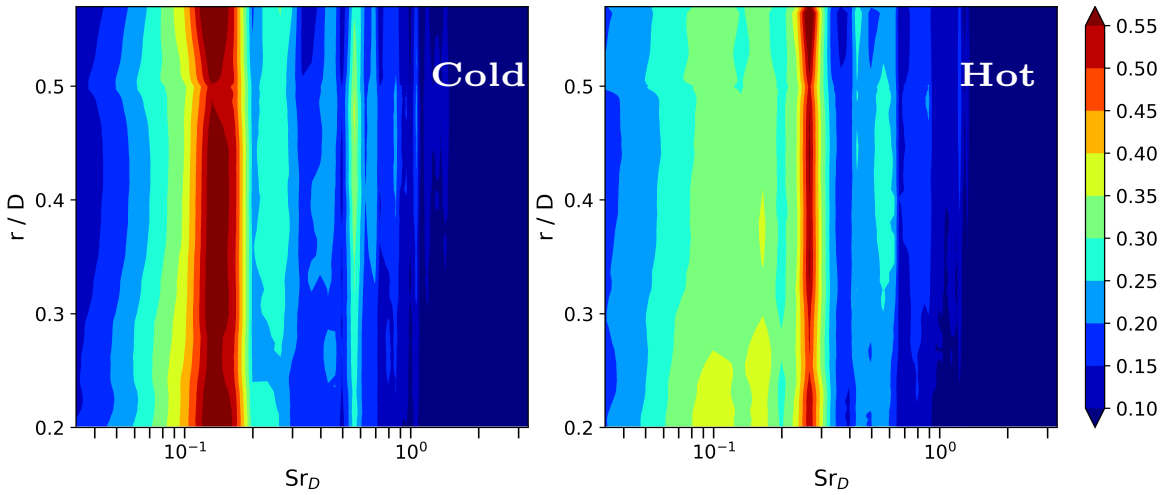

Figure 5.36: Scaled premultiplied PSD of the pressure on the base surface.

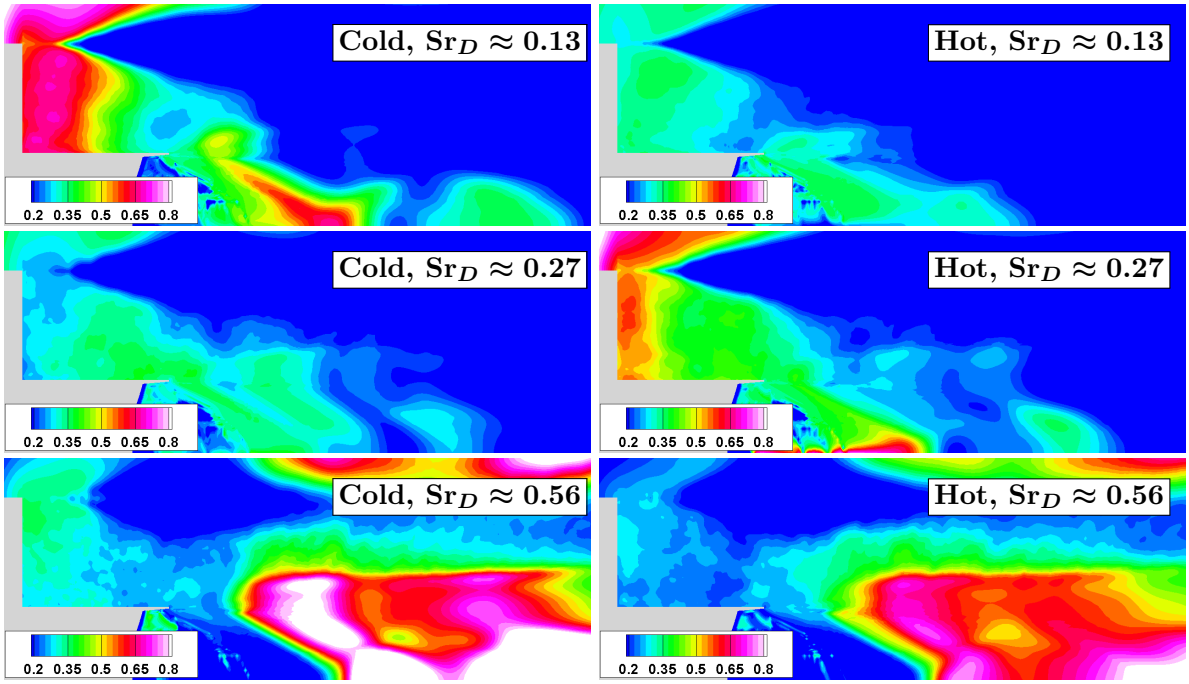

Figure 5.37: Distribution of scaled premultiplied PSD in the field for selected frequencies $\mathrm{Sr}_D = 0.13$, $\mathrm{Sr}_D = 0.27$, $\mathrm{Sr}_D = 0.56$ (left to right) for the cold (top) and hot (bottom) wall case.

The distribution of pressure spectral content in the flow field is shown in Fig. 5.37 for three selected frequencies. These were chosen to display the differences in the main peaks ($\mathrm{Sr}_D \approx 0.13, 0.26$) and the similarity for other frequencies ($\mathrm{Sr}_D \approx 0.56$). For $\mathrm{Sr}_D \approx 0.13$ the strongly increased amplitude for the cold wall case at small axial locations and on the base wall as well as in the plume region behind the nozzle lip is clearly visible. A similar increase for $\mathrm{Sr}_D \approx 0.26$ is visible for the hot wall case.

However, the regions with contribution from each frequency are actually very similar, albeit at different absolute amplitudes. For example, for $\mathrm{Sr}_D \approx 0.13$ a sudden decrease in amplitude for $0.33 < x/D < 0.4$ is visible for both cases as well as an increase in the plume region. The distribution at $\mathrm{Sr}_D \approx 0.56$, which displays very high amplitudes downstream of the nozzle lip, shows this similarity between the cases well. In fact, the similar amplitude distribution can be observed for nearly all frequencies, indicating a generally similar behavior between both cases with only certain quantitative differences.

In Fig. 5.38 the first two circumferential coherence modes $C_{r,0}$ and $C_{r,1}$ are displayed. The symmetric mode $C_{r,0}$ shows high amplitudes mainly for smaller axial locations $x/D < 0.3$ for both cases. For the cold wall case particularly strong peaks are visible around $\mathrm{Sr}_D \approx 0.13$ and $\mathrm{Sr}_D \approx 0.56$ whereas for the hot wall case a peak appears around $\mathrm{Sr}_D \approx 0.27$ and in the entire

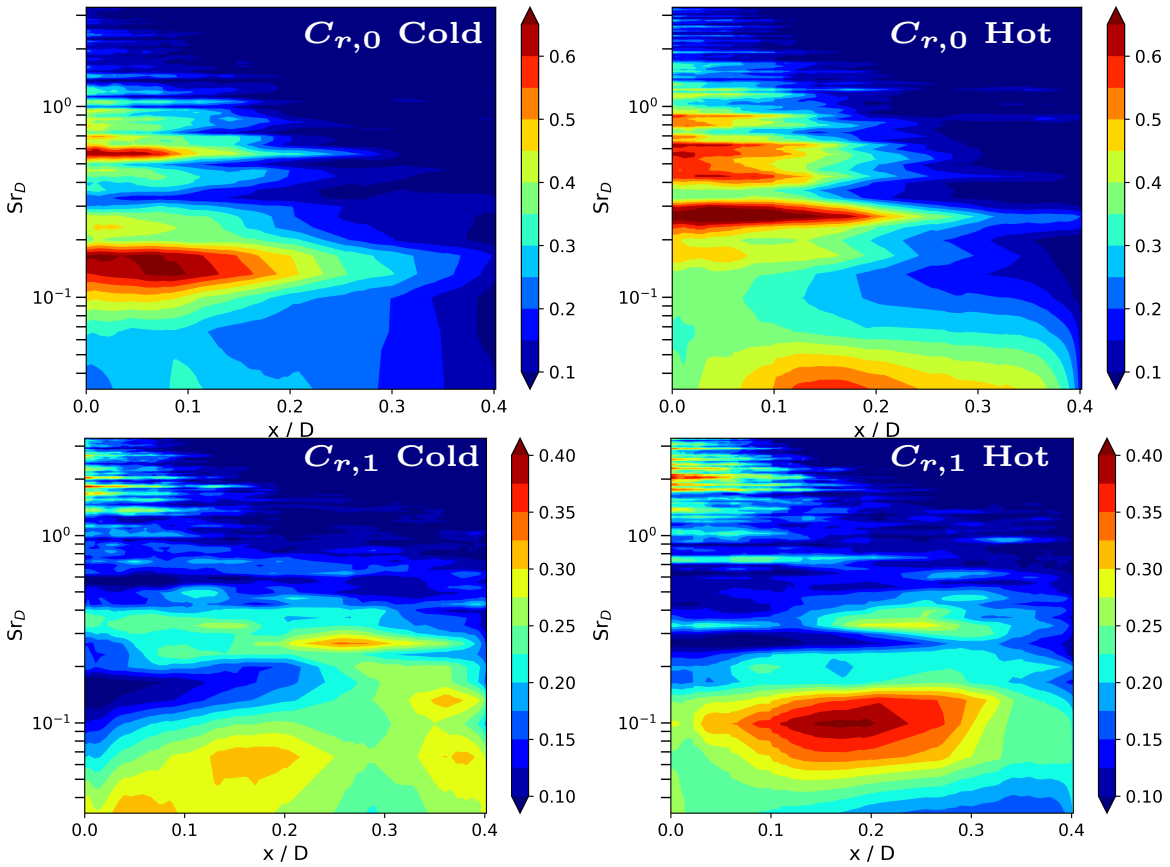

Figure 5.38: Coherence modes $C_{r,0}$ (top) and $C_{r,1}$ (bottom) of external nozzle wall pressure for the short nozzle configuration.

range between $\mathrm{Sr}_D \approx 0.4 \ldots 0.9$.

The asymmetric mode $C_{r,1}$ on the other hand shows contributions around $\mathrm{Sr}_D \approx 0.26$ for $0.2 < x/D < 0.4$ and around $\mathrm{Sr}_D \approx 0.13$ for $0.3 < x/D < 0.4$ for the cold wall case. For the hot wall case higher amplitudes of $C_{r,1}$ are visible around $\mathrm{Sr}_D \approx 0.1$ for $0.1 < x/D < 0.3$ and around $\mathrm{Sr}_D \approx 0.35$ for $0.15 < x/D < 0.3$.

Considering the obtained amplitudes of the asymmetric mode $C_{r,1}$ one at first might expect different peak amplitudes or frequencies in the first spectra than those displayed in Fig. 5.33. For example, for the cold wall case the contribution at $\mathrm{Sr}_D \approx 0.26$ appears with higher amplitude and further axial extension for $C_{r,1}$, but the force spectra show a stronger peak for $\mathrm{Sr}_D \approx 0.13$. Similarly, for the hot wall case the amplitude of $C_{r,1}$ at $\mathrm{Sr}_D \approx 0.2$ is very small, but still appears with considerable strength in the force spectra. The reason for these apparent discrepancies lies in the computation of the coherence modes (cf. equation (3.35)), which only indicate the relative strength of each mode for a given axial location and frequency.

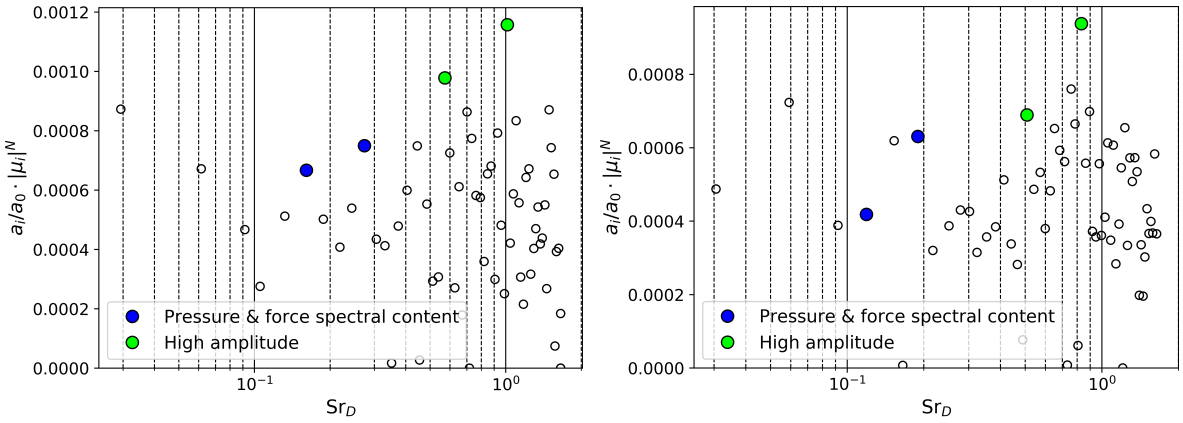

Figure 5.39: DMD mode amplitudes and frequencies for the cold (left) and hot (right) case of the short nozzle configuration.

Hence to evaluate the overall effect on the buffeting loads, the level of pressure fluctuations as well as the scaled amplitude of the respective frequency have to be taken into account. Consequently, considering the strong increase of the pressure fluctuations towards the nozzle lip (cf. Fig. 5.31), the contributions near the nozzle lip have an unproportionally large impact on the buffeting loads. In this region, for the cold wall case $C_{r,1}$ shows a higher amplitude at $\mathrm{Sr}_D \approx 0.13$ than for $\mathrm{Sr}_D \approx 0.26$ and for the hot wall case contributions around $\mathrm{Sr}_D \approx 0.1$ and $\mathrm{Sr}_D \approx 0.2$ show the highest amplitude, which matches the observed peaks in the force spectra. In addition to the effect of the rms pressure distribution, it is also possible for buffeting force contributions caused by $C_{r,1}$ to cancel each other out if the pressure fluctuations between different axial positions have certain phase differences.

Overall, the fact that no clearly dominant feature is visible in PSD, circumferential coherence modes and force spectra - like it was the case e.g. for $\mathrm{Sr}_D \approx 0.2$ for the long nozzle configuration - indicates that there is no single strong phenomenon dominating the unsteady behavior.

DMD analysis

The DMD modes obtained from the flow field of the short nozzle cases are shown in Fig. 5.39. For both cases no dominant modes that match observed features in the spectral analysis are visible, with many modes appearing at high frequencies with similar amplitudes. An exception is the mode around $\mathrm{Sr}_D \approx 0.58$ for the cold wall case which could faintly be seen in the pressure spectra. For completeness, selected modes are shown in Fig. 5.40 for the cold wall case and in Fig. 5.41 for the hot wall case nonetheless. These are modes that match the observed features in the spectral content - but show relatively low amplitudes - and those that exhibit the highest amplitudes - but do not show up as dominant features in the spectral content. The respective

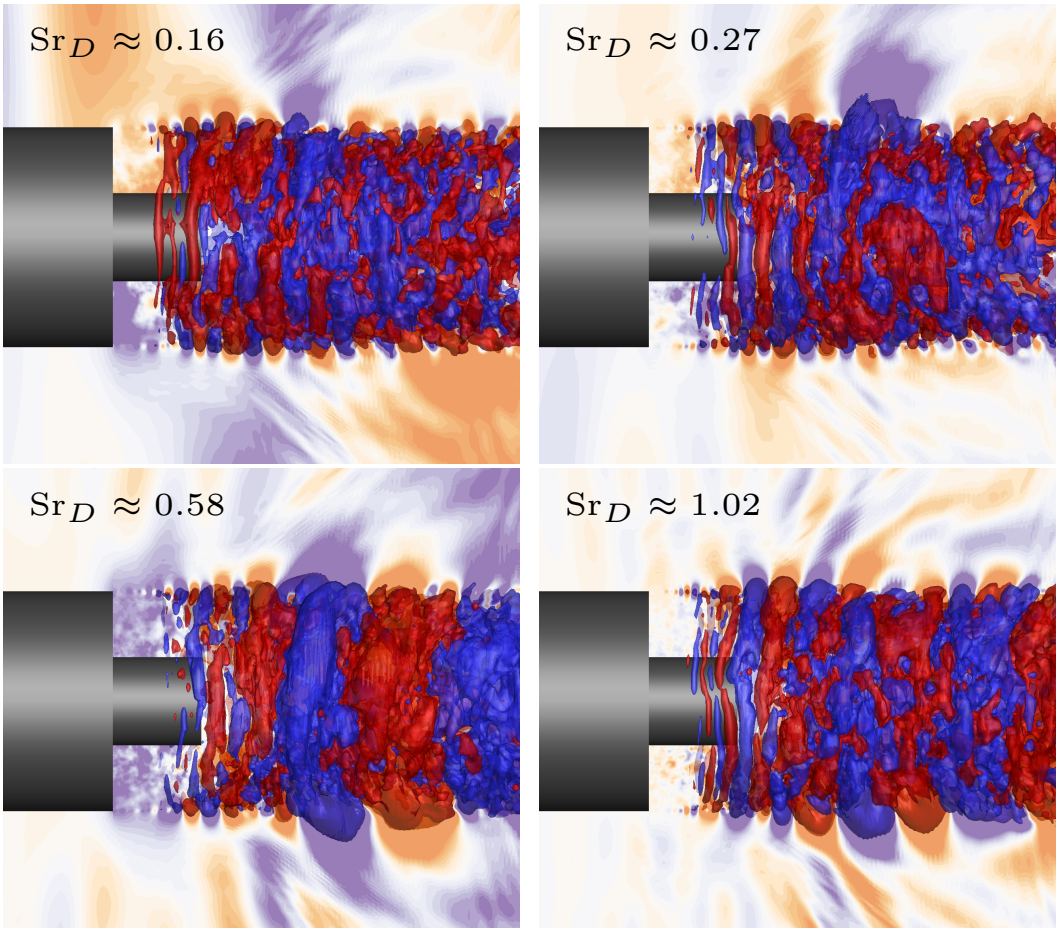

Figure 5.40: DMD pressure modes for the cold wall case of the short nozzle configuration.

selected modes are also marked in Fig. 5.39.

The first displayed mode for the cold wall case is located at $\mathrm{Sr}_D \approx 0.16$ and hence close to the observed peak around $\mathrm{Sr}_D \approx 0.13$ in the buffeting force and wall pressure spectra. The pressure distribution for this mode does not present a clear pattern, exhibiting many small pockets of positive and negative pressure fluctuations. However, it is visible that the majority of strongest fluctuations occurs downstream of the nozzle lip and only small levels of fluctuations appear near the nozzle walls. These appear to be asymmetric, however, which might indicate a possible connection to the observed buffeting loads. The second considered mode is located at $\mathrm{Sr}_D \approx 0.27$, close to the observed second feature in the buffeting and wall pressure spectra. Similarly to the first mode no clear pattern emerges, but in the vicinity of the nozzle walls small amplitude asymmetric pressure fluctuations can be observed.

The two highest amplitude modes are located at $\mathrm{Sr}_D \approx 0.58$ and $\mathrm{Sr}_D \approx 1.02$, which both show a symmetric pressure distribution. For the mode at $\mathrm{Sr}_D \approx 0.58$ this is particularly visible.

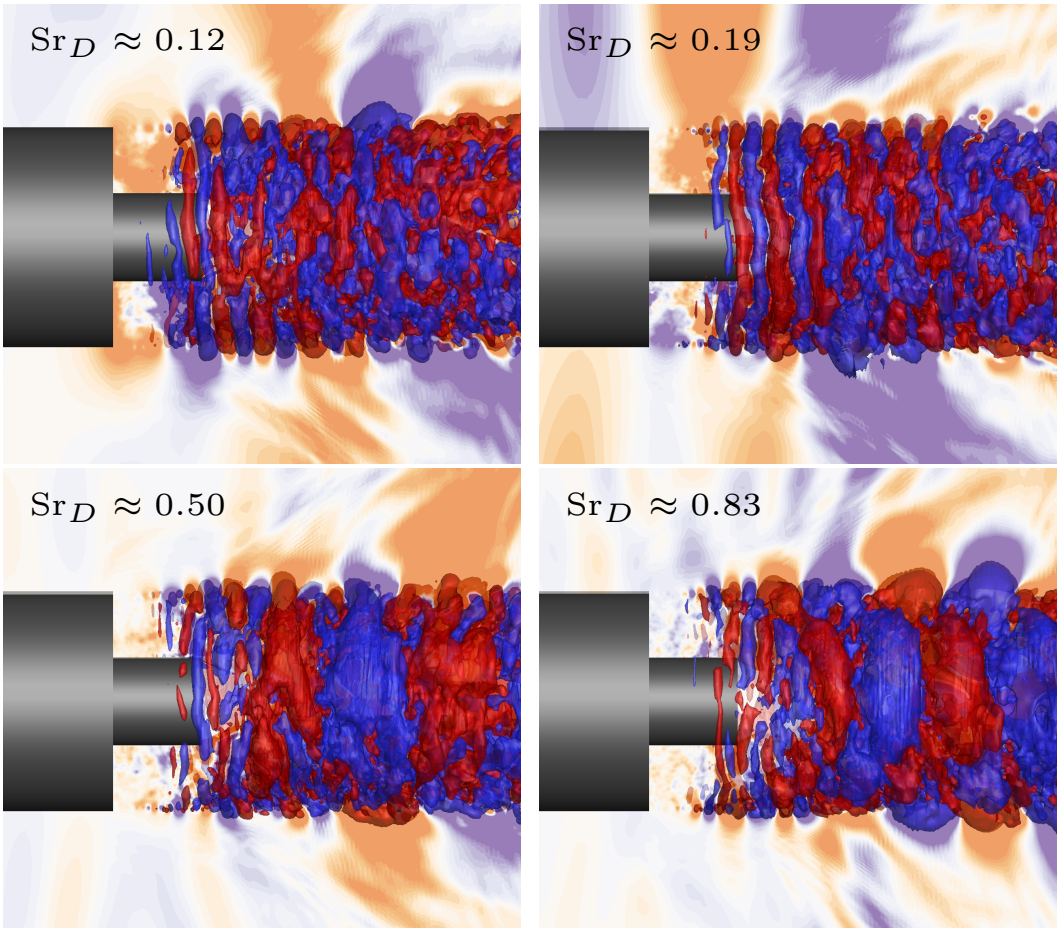

Figure 5.41: DMD pressure modes for the hot wall case of the short nozzle configuration.

Additionally, the pressure distribution for this mode also shows a clear symmetric pressure footprint above the nozzle surface. For the mode at $\mathrm{Sr}_D \approx 1.02$ the symmetric distribution is less distinct and little to no pressure fluctuations are visible in the region near the walls. Particularly for the mode at $\mathrm{Sr}_D \approx 0.58$ the symmetric pressure footprint is also visible in the circumferential coherence mode of the wall pressure distribution $C_{r,0}$ (cf. Fig. 5.38) and hence indicates at least some impact of the global features on the local pressure fluctuations on the wall.

The pressure distribution of the mode at $\mathrm{Sr}_D \approx 0.11$ for the hot wall case appears predominantly symmetric, but like for the cold wall case the pattern exhibits many small pockets of pressure fluctuations. Near the nozzle wall a slightly asymmetric pattern is visible, but the feature is not very strongly pronounced. A similar observation can be made for the mode at $\mathrm{Sr}_D \approx 0.19$.

The pressure distributions for the higher amplitude modes at $\mathrm{Sr}_D \approx 0.50$ and $\mathrm{Sr}_D \approx 0.83$

appear more clearly asymmetric, but show very small levels of fluctuations in the vicinity of the walls. Hence, these contributions do not appear in the buffeting or wall pressure spectra.

Overall, the DMD analysis for the short nozzle configuration allows only little insight into the dominant flow features responsible for the observed buffeting and wall pressure spectra since the strongest features of the modes are located downstream of the nozzle lip and hence the interaction with the model walls is minuscule. Some features, particularly for the cold wall case, appear to be related to the observed wall pressure spectral content, however.

6 Conclusions

The main goal of the present work has been to provide an accurate understanding of the impact of hot plumes and hot walls on the aft-body flow field of generic space launch vehicles. Additionally and in support of this, the sensitivity of scale resolving simulations of launch vehicle aft-body flows to grid and parameter changes was investigated and the accuracy of the employed methods in comparison to numerical and experimental data from literature was shown. In the scope of this thesis the low dissipation numerical schemes necessary for accurate Hybrid RANS-LES, in particular the convective transport scheme and the preconditioning scheme applied to the matrix dissipation, were also extended to allow computing flows with multiple species and chemical reactions.

The grid study showed that the in-plane resolution and the element type used in the LES region have only a minor impact on the mean flow results as well as on the spectral content of the flow. An exception to this is the axial resolution immediately downstream of the separation location, which affected the spectral content and observed buffeting forces significantly. The obtained results were also reflected in the employed grid sensors, showing that these can support the optimization of grid resolution for scale resolving simulations. It was found that the circumferential resolution has a larger impact on the mean flow field, but does not change the results drastically if a plume is present. For the case without a plume, the circumferential resolution affected the mean flow field strongly, which was attributed mostly to the effect on the small scale structures in the second recirculation region behind the investigated geometry. In addition to the reduction of sensitivity to circumferential resolution changes, the presence of a propulsive air plume was also found to introduce an additional peak around $\mathrm{Sr}_D \approx 0.35$ in the spectral content of external nozzle wall pressure and of the buffeting loads.

The parameter study showed that changes in time step size and turbulence model do not significantly affect the obtained results. Changing the fluid model affected the mean flow field by shifting the reattachment location downstream, but does not alter the obtained spectral content of the wall pressure nor the buffeting loads significantly. The sensitivity of the solution to the filter length definition was visible in all quantities, however. It further indicated that similar results as with a fine grid and an improved filter length definition can be achieved with a coarser grid and a non-optimal filter length definition due to error cancellation on the coarse grid. It was also found that the data collection period can significantly affect the obtained results, with only small effects visible for the mean flow field, but strong effects in the spectral

analysis of wall pressure and buffeting loads. The sensitivity study also showed that good agreement with previous experimental and numerical comparison data from literature can be achieved with optimal parameter settings and grid design.

Replacing the cold air plume with a hot plume resulting from an H_2-O_2 combustion was shown to shift the reattachment location of the shear layer significantly downstream and change the mean wall pressure distribution. The effect is about one order of magnitude stronger than the strongest shift in the sensitivity study and was shown to be due to a strong acceleration of the external flow by the plume and the resulting suction effect. A similar shift in reattachment location and change in mean wall pressure was visible if the wall temperatures are increased due to heat transfer through the material from combustion chamber and nozzle. The majority of this change was attributed to heating of the oncoming boundary layer which decelerated the growth of fluctuations in the shear layer and to a lesser extend to an increase of the corner vortex due to high temperatures in the base corner. RANS results differed significantly in the quantitative prediction of reattachment location and pressure distribution, but were able to capture the qualitative changes between the different cases. Significant differences between IDDES and RANS predictions of the wall heat flux were also observed and were attributed to an insufficient capturing of the turbulent heat transport in the employed RANS models. The fundamental mechanisms of the wall temperature impact on turbulent shear layer development and the discrepancies between RANS and IDDES modeling should be further explored in the future to better understand their origin and possible remedies.

The buffeting loads were found to be reduced by about 20% if the wall temperature is increased whereas the plume properties do not affect the force amplitude significantly. However, the force spectra showed a strong similarity between both cases with hot plume whereas the main peak is shifted slightly higher than $\mathrm{Sr}_D \approx 0.2$ for the air plume case. Since in the sensitivity study the peak location was around $\mathrm{Sr}_D \approx 0.2$ the most likely reason for the latter was argued to be a combination of nozzle flow separation and reattachment location. Furthermore, an analysis employing Dynamic Mode Decomposition showed that the underlying flow phenomena are very similar independent of plume properties and wall temperatures. Further research is required to better understand the shift of the dominant peak for the air plume case and to confirm the found hypothesis relating it to nozzle flow separation.

The spectral analysis of the pressure fluctuations indicated that the hot plume introduces an additional frequency contribution around $\mathrm{Sr}_D \approx 0.45$ that was shown to be related to a modulation of the nozzle flow separation location and shock system by the swinging shear layer if the shear layer reattachment location is downstream of the nozzle lip. However, it was shown that the pressure fluctuations introduced by this phenomenon are symmetric and hence do not significantly affect the observed buffeting loads. Nonetheless, it might be of

interest for future work to compare those results to ones without flow separation in the nozzle to confirm the phenomenon is indeed dependent on nozzle flow separation. Additionally, this would allow to ensure that no other unforeseen interactions between shear layer movement and plume without flow separation appear and to gain a generally better understanding of the exact interaction between nozzle flow separation and shear layer reattachment position. In this context, treatment of the plume boundary layer in LES instead of RANS mode could also be explored.

In a final configuration it was shown that the reduction of the nozzle length from $L/D = 1.2$ to $L/D = 0.4$ changes the shape of the recirculation region significantly due to the stronger acceleration of the backflow by the plume. Additionally, a post combustion region in the vicinity of the recirculation region is present and hence hot gases are transported towards the base. Consequently, only a small impact of the wall temperature on the mean flow field was observed for this configuration. However, the increased wall temperatures still decrease the pressure fluctuations and the observed buffeting loads by about 25%, indicating this effect is influenced by the local wall temperatures instead of the overall recirculation region temperatures. In comparison to the long nozzle configuration, the buffeting loads were found to be reduced by about a factor 4 due to the lower amount of pressure fluctuations on the nozzle surface as well as due to the smaller external nozzle surface area. The force spectra showed peaks around $\mathrm{Sr}_D \approx 0.11 \ldots 0.13$ and $\mathrm{Sr}_D \approx 0.22 \ldots 0.26$ as well as several minor peaks at higher frequencies. Considering these strong differences between largely similar configurations it should be assessed which other geometrical parameters aside from the nozzle length might have an impact on the flow field. Furthermore, the general portability of the obtained results to less generic configurations such as vehicles with contoured nozzle surfaces or with multiple nozzles might be an interesting avenue of research to pursue.

A spectral analysis of the pressure fluctuations for the short nozzle configuration showed the general distribution of spectral energy is mostly independent of wall temperature, but whereas with cold walls content at $\mathrm{Sr}_D \approx 0.13$ is increased, with hot walls content at $\mathrm{Sr}_D \approx 0.26$ is increased. An analysis of the circumferential coherence and DMD modes did not yield clearly dominant features that could be directly connected to the observed buffeting loads or features in the pressure spectra, indicating that no globally dominating phenomenon is responsible for these loads.

The research shows that hot plumes have a strong impact on the aft-body flow field, even in cases where no strong immediate interaction between recirculation region and plume is present. It also shows that a consideration of the wall temperatures is necessary to accurately predict the buffeting loads on the nozzle structure. On the other hand, the fundamental flow features in the recirculation region appear to be unaffected by plume properties and wall temperatures

and hence the understanding and manipulation of these might possibly be investigated without the additional complexity of hot plumes and increased wall temperatures. However, changing the nozzle length has a large impact on the flow field, underlying phenomena and loads.

Bibliography

[1] Nikolaus A Adams, Wolfgang Schröder, Rolf Radespiel, Oskar J Haidn, Thomas Sattelmayer, Christian Stemmer, and Bernhard Weigand. *Future Space-transport-system Components Under High Thermal and Mechanical Loads: Results from the DFG Collaborative Research Center TRR40*. Springer Nature, 2021.

[2] Steven R Allmaras and Forrester T Johnson. Modifications and clarifications for the implementation of the Spalart-Allmaras turbulence model. In *Seventh international conference on computational fluid dynamics (ICCFD7)*, pages 1–11, 2012.

[3] Mario Capitelli, Gianpiero Colonna, and Lionel Marraffa. *Tables of internal partition functions and thermodynamic properties of high-temperature Mars-atmosphere species from 50K to 50000K*. European Space Agency, 2005.

[4] Nicolas Chauvet, Sebastien Deck, and Laurent Jacquin. Zonal detached eddy simulation of a controlled propulsive jet. *AIAA journal*, 45(10):2458–2473, 2007.

[5] Haecheon Choi and Parviz Moin. Grid-point requirements for large eddy simulation: Chapman's estimates revisited. *Physics of fluids*, 24(1):011702, 2012.

[6] Y-H Choi and Charles L Merkle. The application of preconditioning in viscous flows. *Journal of computational physics*, 105(2):207–223, 1993.

[7] Sébastien Deck. Recent improvements in the zonal detached eddy simulation (ZDES) formulation. *Theoretical and Computational Fluid Dynamics*, 26(6):523–550, 2012.

[8] Sébastien Deck and Pascal Thorigny. Unsteadiness of an axisymmetric separating-reattaching flow: Numerical investigation. *Physics of fluids*, 19(6):065103, 2007.

[9] D Deprés, P Reijasse, and JP Dussauge. Analysis of unsteadiness in afterbody transonic flows. *AIAA journal*, 42(12):2541–2550, 2004.

[10] Richard Dwight. *Efficiency improvements of RANS-based analysis and optimization using implicit and adjoint methods on unstructured grids*. PhD thesis, University of Manchester, 2006.

[11] European Space Association. Arianespace flight 157 - inquiry board submits findings, 2003. URL `https://www.esa.int/Enabling_Support/Space_Transportation/Arianespace_Flight_157_-_Inquiry_Board_submits_findings2`.

[12] P. Gerlinger, H. Möbus, and D. Brüggemann. An implicit multigrid method for turbulent combustion. *Journal of Computational Physics*, 167:247–276, 2001.

[13] Peter Gerlinger. *Numerische Verbrennungssimulation: Effiziente numerische Simulation turbulenter Verbrennung*. Springer-Verlag, 2005.

[14] LV Gurvich, IV Veyts, Ch B Alcock, and DL Hildenbrand. Thermodynamic properties of individual substances. Volume 3, Parts 1 and 2. *Journal of Chemical Thermodynamics*, 27(3):335, 1995.

[15] Klaus Hannemann, Jan M Schramm, Alexander Wagner, Sebastian Karl, and Volker Hannemann. A closely coupled experimental and numerical approach for hypersonic and high enthalpy flow investigations utilising the HEG shock tunnel and the DLR TAU code. Technical report, German Aerospace Center, Institute of Aerodynamics and Flow Technology, 2010.

[16] Klaus Hannemann, H Ludeke, J-F Pallegoix, Arnaud Ollivier, Hadrien Lambare, JEJ Maseland, EGM Geurts, Manuel Frey, Sebastien Deck, and FFJ Schrijer. Launch vehicle base buffeting-recent experimental and numerical investigations. In *7th European symposium on aerothermodynamics*, volume 692, page 102, 2011.

[17] F Herning and L Zipperer. Calculation of the viscosity of technical gas mixtures from the viscosity of the individual gases. *Gas u. Wasserfach*, 79:69, 1936.

[18] Joseph O Hirschfelder. Generalization of the eucken approximation for the heat conductivity of polyatomic or chemically reacting gas mixtures. Technical report, Wisconsin Univ-Madison Theroretical Chemistry Inst, 1957.

[19] Joseph O Hirschfelder, Charles F Curtiss, Robert Byron Bird, and Maria Goeppert Mayer. *Molecular theory of gases and liquids*, volume 165. Wiley New York, 1964.

[20] Tim Horchler, Wolfgang Armbruster, Justin Hardi, Sebastian Karl, Klaus Hannemann, Andreas Gernoth, and Marco De Rosa. Modeling combustion chamber acoustics using the dlr tau code. *Space Propulsion*, 2018, 2018.

[21] CR Illingworth. The effect of heat transfer on the separation of a compressible laminar boundary layer. *The Quarterly Journal of Mechanics and Applied Mathematics*, 7(1):8–34, 1954.

[22] Antony Jameson, Wolfgang Schmidt, and Eli Turkel. Numerical solutions of the Euler equations by finite volume methods using Runge-Kutta time-stepping schemes. *AIAA paper*, 1259:1981, 1981.

[23] Mihailo R Jovanović, Peter J Schmid, and Joseph W Nichols. Sparsity-promoting dynamic mode decomposition. *Physics of Fluids*, 26(2):024103, 2014.

[24] Sebastian Karl. *Numerical investigation of a generic scramjet configuration*. PhD thesis, Saechsische Landesbibliothek-Staats-und Universitaetsbibliothek Dresden, 2011.

[25] D. Kirchheck and A. Gülhan. Characterization of a GH2/GO2 combustor for hot plume

wind tunnel testing. In C. Stemmer, N. A. Adams, O. J. Haidn, R. Radespiel, T. Sattelmayer, W. Schröder, and B. Weigand, editors, *SFB/TRR 40 Annual Report 2018*, pages 85–97. Lehrstuhl für Aerodynamik und Strömungstechnik, Technische Universität München, 2018.

[26] JC Kok. A high-order low-dispersion symmetry-preserving finite-volume method for compressible flow on curvilinear grids. *Journal of Computational Physics*, 228(18):6811–6832, 2009.

[27] Norbert Kroll and Romesh Kumar Jain. Solution of two-dimensional Euler equations: Experience with a finite volume code. *NASA STI/Recon Technical Report N*, 88:20572, 1987.

[28] Yen Liu and Marcel Vinokur. Upwind algorithms for general thermo-chemical nonequilibrium flows. In *27th Aerospace Sciences Meeting*, page 201, 1989.

[29] Johannes Löwe, Axel Probst, Tobias Knopp, and Roland Kessler. A low-dissipation low-dispersion second-order scheme for unstructured finite-volume flow solvers. In *53rd AIAA Aerospace Sciences Meeting*, page 0815, 2015.

[30] Heinrich Lüdeke, Jean Daniel Mulot, and Klaus Hannemann. Launch vehicle base flow analysis using improved delayed detached-eddy simulation. *AIAA Journal*, 53(9):2454–2471, 2015.

[31] Dimitri J Mavriplis and Antony Jameson. Multigrid solution of the Navier-Stokes equations on triangular meshes. *AIAA journal*, 28(8):1415–1425, 1990.

[32] Bonnie J McBride. *NASA Glenn coefficients for calculating thermodynamic properties of individual species*. National Aeronautics and Space Administration, John H. Glenn Research Center, 2002.

[33] Philippe Meliga and Philippe Reijasse. Unsteady transonic flow behind an axisymmetric afterbody equipped with two boosters. In *25th AIAA Applied Aerodynamics Conference*, page 4564, 2007.

[34] Florian Menter. Zonal two equation kw turbulence models for aerodynamic flows. In *23rd fluid dynamics, plasmadynamics, and lasers conference*, page 2906, 1993.

[35] Florian Menter. Two-equation eddy-viscosity turbulence models for engineering applications. *AIAA journal*, 32(8):1598–1605, 1994.

[36] Florian Menter and M Kuntz. Adaptation of eddy-viscosity turbulence models to unsteady separated flow behind vehicles. In *The aerodynamics of heavy vehicles: trucks, buses, and trains*, pages 339–352. Springer, 2004.

[37] Florian Menter and Christopher Rumsey. Assessment of two-equation turbulence models for transonic flows. In *Fluid Dynamics Conference*, page 2343, 1994.

[38] RA Merz. Subsonic base pressure fluctuations. *AIAA Journal*, 17(4):436–438, 1979.

[39] RA Merz, RH Page, and CEG Przirembel. Subsonic axisymmetric near-wake studies. *AIAA journal*, 16(7):656–662, 1978.

[40] Charles Mockett, Marian Fuchs, Andrey Garbaruk, Michael Shur, Philippe Spalart, Michael Strelets, Frank Thiele, and Andrey Travin. Two non-zonal approaches to accelerate RANS to LES transition of free shear layers in DES. In *Progress in Hybrid RANS-LES modelling*, pages 187–201. Springer, 2015.

[41] R Pain, P-E Weiss, and S Deck. Zonal detached eddy simulation of the flow around a simplified launcher afterbody. *AIAA journal*, 52(9):1967–1979, 2014.

[42] R Pain, P-E Weiss, Sébastien Deck, and J-C Robinet. Large scale dynamics of a high reynolds number axisymmetric separating/reattaching flow. *Physics of Fluids*, 31(12): 125119, 2019.

[43] Stephen B Pope. *Turbulent flows*. Cambridge university press, 2000.

[44] Axel Probst, Johannes Löwe, Silvia Reuß, Tobias Knopp, and Roland Kessler. Scale-resolving simulations with a low-dissipation low-dispersion second-order scheme for unstructured flow solvers. *AIAA Journal*, 2016.

[45] R Radespiel and N Kroll. An improved flux vector split discretization scheme for viscous flows. *Forschungsbericht DLR-FB*, pages 93–53, 1993.

[46] Silvia Reuß. *A grid-adaptive algebraic hybrid RANS/LES method*. Deutsches Zentrum für Luft-und Raumfahrt, Bibliotheks-und Informationswesen, 2016.

[47] Silvia Reuß, T Knopp, A Probst, and M Orlt. Assessment of local LES-resolution sensors for hybrid RANS/LES simulations. In *Progress in Hybrid RANS-LES Modelling*, pages 93–103. Springer, 2015.

[48] Philip L Roe. Approximate riemann solvers, parameter vectors, and difference schemes. *Journal of computational physics*, 43(2):357–372, 1981.

[49] Axel Rohde. Eigenvalues and eigenvectors of the euler equations in general geometries. In *15th AIAA Computational Fluid Dynamics Conference*, page 2609, 2001.

[50] Rumsey, C. Nasa turbulence modeling resource. URL `https://www.turbmodels.larc.nasa.gov`.

[51] Peter J Schmid. Dynamic mode decomposition of numerical and experimental data. *Journal of fluid mechanics*, 656:5–28, 2010.

[52] Jan-Erik Schumann, Volker Hannemann, and Klaus Hannemann. Investigation of structured and unstructured grid topology and resolution dependence for scale-resolving simulations of axisymmetric detaching-reattaching shear layers. In *Progress in Hybrid RANS-LES Modelling*, pages 169–179. Springer, 2020.

[53] Jan-Erik Schumann, Siavash Toosi, and Johan Larsson. Assessment of grid anisotropy effects on large-eddy-simulation models with different length scales. *AIAA Journal*, pages 1–12, 2020.

[54] Jan-Erik Schumann, Markus Fertig, Volker Hannemann, Thino Eggers, and Klaus Hannemann. Numerical characterization of hot plume impact. In *Future Space-Transport-System Components under High Thermal and Mechanical Loads*, page ?? Springer, 2021.

[55] Jan-Erik Schumann, Volker Hannemann, and Klaus Hannemann. Sensitivity of scale resolving aft-body flow simulations to numerical model parameter variations. *CEAS Space Journal*, pages 1–14, 2021.

[56] Mikhail L Shur, Philippe R Spalart, Mikhail Kh Strelets, and Andrey K Travin. A hybrid RANS-LES approach with delayed-DES and wall-modelled LES capabilities. *International Journal of Heat and Fluid Flow*, 29(6):1638–1649, 2008.

[57] Philipe R Spalart and Stephen R Allmaras. A one equation turbulence model for aerodynamic flows. *AIAA journal*, 94, 1992.

[58] Philippe R Spalart. Comments on the feasibility of LES for wings, and on a hybrid RANS/LES approach. In C. Liu and Z. Liu, editors, *Advances in DNS/LES*, pages 137–147. Greyden Press, 1997.

[59] Philippe R. Spalart. Young-person's guide to detached-eddy simulation grids. 2001.

[60] Philippe R Spalart, Shur Deck, Michael L Shur, Kyle D Squires, M Kh Strelets, and Andrei Travin. A new version of detached-eddy simulation, resistant to ambiguous grid densities. *Theoretical and computational fluid dynamics*, 20(3):181, 2006.

[61] Vladimir Statnikov, Matthias Meinke, and Wolfgang Schröder. Reduced-order analysis of buffet flow of space launchers. *Journal of Fluid Mechanics*, 815:1–25, 2017.

[62] Sören Stephan and Rolf Radespiel. Propulsive jet simulation with air and helium in launcher wake flows. *CEAS Space Journal*, 9(2):195–209, 2017.

[63] Petre Stoica and Randolph L Moses. Spectral analysis of signals. 2005.

[64] M Strelets. Detached eddy simulation of massively separated flows. In *39th Aerospace sciences meeting and exhibit*, page 879, 2001.

[65] William Sutherland. LII. the viscosity of gases and molecular force. *The London, Edinburgh, and Dublin Philosophical Magazine and Journal of Science*, 36(223):507–531, 1893.

[66] Siavash Toosi and Johan Larsson. Anisotropic grid-adaptation in large eddy simulations. *Computers & Fluids*, 156:146–161, 2017.

[67] Andrey K Travin, Mikhail L Shur, Philippe R Spalart, and Mikhail Kh Strelets. Improvement of delayed detached-eddy simulation for LES with wall modelling. 2006.

[68] E Turkel. Preconditioning-squared methods for multidimensional aerodynamics. In *13th Computational Fluid Dynamics Conference*, page 2025, 1997.

[69] Y. Wada and M.S. Liou. A flux splitting scheme with high-resolution and robustness for discontinuities. *AIAA paper*, (94-0083), 1994.

[70] Jonathan Weiss and Jayathi Murthy. Computation of reacting flowfields using unstructured adaptive meshes. In *33rd Aerospace Sciences Meeting and Exhibit*, page 870, 1995.

[71] PE Weiss and S Deck. Numerical investigation of the robustness of an axisymmetric separating/reattaching flow to an external perturbation using ZDES. *Flow, turbulence and combustion*, 91(3):697–715, 2013.

[72] Pierre-Élie Weiss and Sébastien Deck. Control of the antisymmetric mode (m= 1) for high Reynolds axisymmetric turbulent separating/reattaching flows. *Physics of Fluids*, 23(9): 095102, 2011.

[73] Pierre-Élie Weiss, Sébastien Deck, Jean-Christophe Robinet, and Pierre Sagaut. On the dynamics of axisymmetric turbulent separating/reattaching flows. *Physics of Fluids*, 21 (7):075103, 2009.

[74] CR Wilke. A viscosity equation for gas mixtures. *The journal of chemical physics*, 18(4): 517–519, 1950.

[75] Yifei Wu, Weihao Zhang, Zhengping Zou, and Jiang Chen. Effects of heat transfer on separated boundary layer behavior under adverse pressure gradients. *International Journal of Heat and Mass Transfer*, 142:118348, 2019.

[76] Nan Zong and Vigor Yang. An efficient preconditioning scheme for real-fluid mixtures using primitive pressure–temperature variables. *International Journal of Computational Fluid Dynamics*, 21(5-6):217–230, 2007.

Appendix

A Averaging and Filtering the governing equations

The terms necessary to derive the RANS and filtered system of equations with the help of equations (2.27) and (2.29) will be shown in the following.

The Favre-averaged total enthalpy can be written as

$$\overline{\rho}\widetilde{H} = \overline{\rho}\widetilde{h} + \frac{1}{2}\widetilde{\rho u_i u_i} = \overline{\rho}\widetilde{h} + \frac{1}{2}\overline{\rho u_i u_i} = \overline{\rho}\widetilde{h} + \frac{1}{2}\left(\overline{\rho}\widetilde{u_i}\widetilde{u_i} + 2\widetilde{u_i}\underbrace{\overline{\rho u_i''}}_{=0} + \underbrace{\overline{\rho u_i'' u_i''}}_{\tau_{ii}^{RANS}}\right) \tag{A.1}$$

For the Favre-filtered total enthalpy this is

$$\overline{\rho}\widetilde{H} = \overline{\rho}\widetilde{h} + \frac{1}{2}\widetilde{\rho u_i u_i} = \overline{\rho}\widetilde{h} + \frac{1}{2}\overline{\rho u_i u_i} = \overline{\rho}\widetilde{h} + \frac{1}{2}\left(\overline{\rho}\widetilde{u_i}\widetilde{u_i} + \underbrace{\overline{\rho u_i u_i} - \overline{\rho}\widetilde{u_i}\widetilde{u_i}}_{\tau_{ii}^{LES}}\right) \tag{A.2}$$

Using this and defining $\widetilde{k} = \frac{1}{2}\tau_{ii}$ the averaged/ filtered enthalpy flux in equation (2.4) can be written as

$$\begin{aligned}\overline{\rho H u_j} &= \overline{\rho(h + \frac{1}{2}u_i u_i)u_j} = \overline{\rho h u_j} + \overline{\rho}\widetilde{h}\widetilde{u}_j - \overline{\rho}\widetilde{h}\widetilde{u}_j + \frac{1}{2}(\overline{\rho u_i u_i u_j} + \overline{\rho}\widetilde{u_i u_i}\widetilde{u}_j - \overline{\rho}\widetilde{u_i u_i}\widetilde{u}_j) \\ &= \overline{\rho}\widetilde{H}\widetilde{u}_j + \overline{\rho h u_j} - \overline{\rho}\widetilde{h}\widetilde{u}_j + \frac{1}{2}(\overline{\rho u_i u_i u_j} - \overline{\rho}\widetilde{u}_i\widetilde{u}_i\widetilde{u}_j) - \widetilde{u}_j\widetilde{k}\end{aligned} \tag{A.3}$$

The turbulent heat flux can be defined as

$$\text{LES:} \qquad q_t = \overline{\rho h u_j} - \overline{\rho}\widetilde{h}\widetilde{u}_j \tag{A.4}$$

$$\text{RANS:} \qquad q_t = \overline{\rho h u_j} - \overline{\rho}\widetilde{h}\widetilde{u}_j = \overline{\rho h'' u_j''} \tag{A.5}$$

The term originating from the kinetic energy can be written as

$$\begin{aligned}&(\overline{\rho u_i u_i u_j} - \overline{\rho}\widetilde{u}_i\widetilde{u}_i\widetilde{u}_j) - \widetilde{u}_j\widetilde{k} = \\ &\overline{\rho}\widetilde{u}_i\widetilde{u}_i\widetilde{u}_j + \overline{\rho u_i'' u_i'' u_j''} + \overline{\rho}\widetilde{u}_i\widetilde{u}_i u_j'' + \overline{\rho}\widetilde{u}_i\widetilde{u}_i u_j'' + \overline{\rho u_i'' u_i'' \widetilde{u}_j} + 2(\overline{\rho}\widetilde{u}_i u_i''\widetilde{u}_j + \overline{\rho}\widetilde{u}_i u_i'' u_j'') - \overline{\rho}\widetilde{u}_i\widetilde{u}_i\widetilde{u}_j - \overline{\rho u_i'' u_i''}\widetilde{u}_j\end{aligned} \tag{A.6}$$

In case of LES (i.e the term represents Favre-filtered expressions) this cannot be further simplified. However, in RANS (i.e. the term represents Favre-averaged expressions)

$$\begin{aligned}&\underbrace{\overline{\rho}\widetilde{u}_i\widetilde{u}_i\widetilde{u}_j}_{1} + \overline{\rho u_i'' u_i'' u_j''} + \underbrace{\overline{\rho}\widetilde{u}_i\widetilde{u}_i u_j''}_{\widetilde{u}_i\widetilde{u}_i\overline{\rho u_j''}} + \underbrace{\overline{\rho u_i'' u_i'' \widetilde{u}_j}}_{2} + 2(\underbrace{\overline{\rho}\widetilde{u}_i u_i''\widetilde{u}_j}_{\widetilde{u}_i\widetilde{u}_j\overline{\rho u_i''}} + \overline{\rho}\widetilde{u}_i u_i'' u_j'') - \underbrace{\overline{\rho}\widetilde{u}_i\widetilde{u}_i\widetilde{u}_j}_{1} - \underbrace{\overline{\rho u_i'' u_i''}\widetilde{u}_j}_{2} \\ &= \overline{\rho u_i'' u_i'' u_j''} + 2\overline{\rho}\widetilde{u}_i\overline{u_i'' u_j''}\end{aligned} \tag{A.7}$$

since $\overline{\rho\Phi''} = 0$ (cf. equation (2.29)) and terms 1 and 2 cancel out.

B Turbulence model description

The used turbulence model is described in the following.

SST RANS model

This two equation model was derived by Menter [34, 37] and defines the source terms in equations (3.20) and (3.21) as follows:

$$P^{(k)} = 2\frac{\mu_t}{\rho} S_{ij} S_{ij} - \frac{2}{3} k \frac{\partial u_i}{\partial x_i} \tag{B.1}$$

$$\varepsilon^{(k)} = \beta^{(k)} k\omega = \frac{k^{3/2}}{l_{k-\omega}} \qquad \text{with} \quad l_{k-\omega} = \frac{\sqrt{k}}{\beta^{(k)}\omega} \tag{B.2}$$

$$D^{(k)} = \frac{1}{\rho}\frac{\partial}{\partial x_i}\left[\left(\mu + \sigma^{(k)}\mu_t\right)\frac{\partial k}{\partial x_i}\right] \tag{B.3}$$

$$P^{(\omega)} = \gamma^{(\omega)} S_c^{(\omega)} P^{(k)} \tag{B.4}$$

$$\Phi^{(\omega)} = \beta^{(\omega)}\omega^2 \tag{B.5}$$

$$C^{(\omega)} = \sigma^{(d)}\frac{1}{\omega}\frac{\partial k}{\partial x_i}\frac{\partial \omega}{\partial x_i} \tag{B.6}$$

$$D^{(\omega)} = \frac{1}{\rho}\frac{\partial}{\partial x_i}\left[\left(\mu + \sigma^{(\omega)}\mu_t\right)\frac{\partial k}{\partial x_i}\right] \tag{B.7}$$

The turbulent viscosity is (see equation (3.22))

$$\mu_t = \frac{\rho k}{\omega}\frac{1}{\max\left(1, \frac{\Omega F_2}{\omega a_1}\right)} \tag{B.8}$$

and the model version specific constants are

$$\Omega = \sqrt{2 S_{ij} S_{ij}} \qquad S_c^{(\omega)} = \frac{\rho}{\mu_t} \qquad a_1 = 0.31 \tag{B.9}$$

The remaining constants are blended between a near wall value and a free stream value using the blending function

$$F = \tanh(G^2) \quad \text{with} \quad G = \max(2\Gamma_1, \Gamma_2) \quad \text{and} \quad \Gamma_1 = \frac{\sqrt{k}}{0.09\omega d_w} \quad \Gamma_2 = \frac{500\mu}{\rho\omega d_w^2} \tag{B.10}$$

where d_w is the wall distance and F blends a constant ϕ as

$$\phi = F\phi_i + (1 - F)\phi_o \tag{B.11}$$

The values of the constants are

$$\beta_i^{(k)} = 0.09 \qquad \sigma_i^{(k)} = 0.85 \qquad \sigma_i^{(\omega)} = 0.5 \qquad \gamma_i^{(\omega)} = 0.555556 \qquad \sigma_i^{(d)} = 0$$
$$\beta_o^{(k)} = 0.09 \qquad \sigma_o^{(k)} = 1.0 \qquad \sigma_o^{(\omega)} = 0.857 \qquad \gamma_o^{(\omega)} = 0.44 \qquad \sigma_o^{(d)} = 2\sigma_o^{(\omega)}$$
$$\beta_i^{(\omega)} = \beta_i^{(k)} \left(\gamma_i^{(\omega)} + \frac{\sigma_i^{(\omega)} \kappa^2}{\sqrt{\beta_i^{(k)}}} \right) \qquad \beta_o^{(\omega)} = \beta_o^{(k)} \left(\gamma_o^{(\omega)} + \frac{\sigma_o^{(\omega)} \kappa^2}{\sqrt{\beta_o^{(k)}}} \right) \qquad \kappa = 0.41$$

IDDES model

In the IDDES model the shielding functions in equation (3.27) are defined as

$$\widetilde{f}_d = \max(1 - f_{dt}, f_B) \qquad f_{dt} = 1 - \tanh((8r_{dt})^3) \qquad f_B = \min(2e^{-9\alpha^2}, 1)$$
$$r_{dt} = \frac{\nu_t}{\kappa^2 d_w^2 \max\left(\sqrt{\frac{\partial u_i}{\partial x_j}\frac{\partial u_i}{\partial x_j}}, 10^{-10}\right)} \qquad \alpha = 0.25 - \frac{d_w}{h_{max}} \qquad \kappa = 0.41$$
$$f_e = \max(f_{e1} - 1, 0) \qquad f_{e1} = \begin{cases} 2e^{-11.09\alpha^2}, & \text{if } \alpha \geq 0 \\ 2e^{-9.0\alpha^2}, & \text{if } \alpha < 0 \end{cases}$$

C Details on species modelling and reaction mechanisms

The species data is taken from Capitelli et al. [3] for the species contained in air (N, N_2, O, O_2, NO) and from McBride [32] for all others (H, H_2, H_2O, HO_2, H_2O_2). The molecular weight for selected species is displayed in Table C.1, with the molecular weight for the remaining species derivable from these. The formation enthalpies for the investigations with active chemical reactions are displayed in Table C.2 and the reaction mechanism displayed in Table C.3 is taken from Gerlinger et al. [12].

The resulting species sensible enthalpy, specific heat capacity, viscosity and thermal conductivity computed from the literature data for each species are displayed as a function of temperature in Fig. C.1, Fig. C.2 and Fig. C.3, respectively.

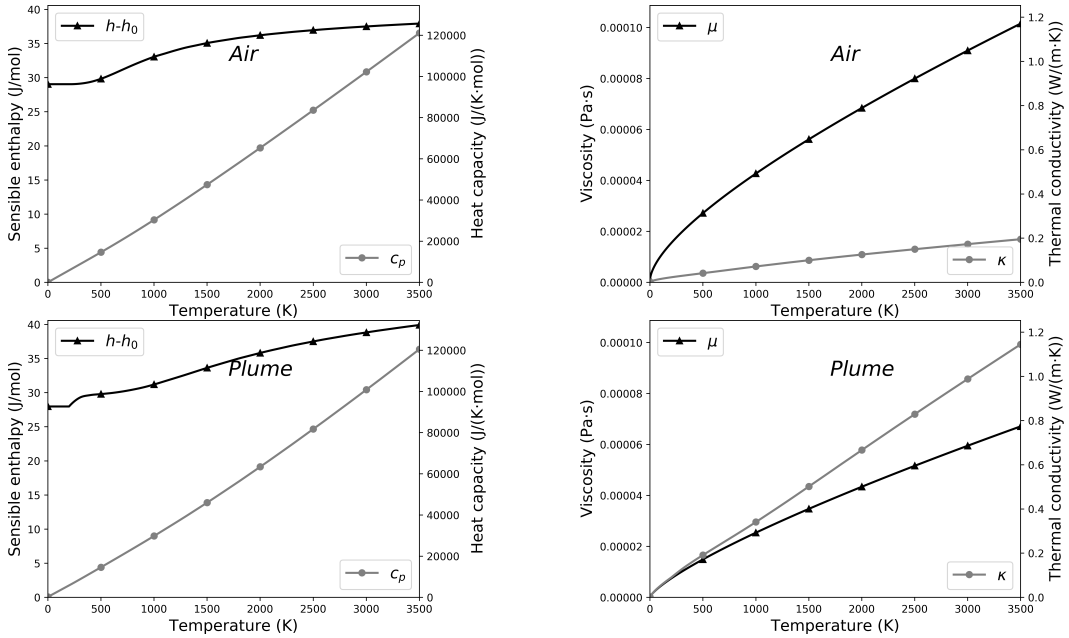

Figure C.1: Species properties for investigations with 2 species.

Species	H	O	N	Air	Plume
$\mathcal{M}$	0.001008	0.015999	0.014007	0.028963	0.003427

Table C.1: Molecular weight of species.

Species	H	O	N_2	O_2	H_2	OH	HO_2	H_2O	H_2O_2
θ^0	40351.0	29682.0	0	0	28736.0	18818.0	15883.2	0	13113.3

Table C.2: Characteristic temperature of formation enthalpy of species.

	Reaction	a^r	b_r	c_r
1	$H_2 + O_2 \longleftrightarrow HO_2 + H$	$1.0 \cdot 10^8$	0.0	18000
2	$H + O_2 \longleftrightarrow OH + O$	$2.6 \cdot 10^8$	0.0	8400
3	$O + H_2 \longleftrightarrow OH + H$	$1.8 \cdot 10^4$	0.0	4450
4	$OH + H_2 \longleftrightarrow H_2O + H$	$2.2 \cdot 10^7$	0.0	2580
5	$OH + OH \longleftrightarrow H_2O + O$	$6.3 \cdot 10^6$	0.0	545
6	$H + OH + M \longleftrightarrow H_2O + M$	$2.2 \cdot 10^{10}$	-2.0	0
7	$H + H + M \longleftrightarrow H_2 + M$	$1.3 \cdot 10^6$	-1.0	0
8	$H + O + M \longleftrightarrow OH + M$	$6.0 \cdot 10^4$	-0.6	0
9	$H + O_2 + M \longleftrightarrow HO_2 + M$	$4.2 \cdot 10^3$	0.0	-500
10	$HO_2 + H \longleftrightarrow OH + OH$	$1.4 \cdot 10^8$	0.0	540
11	$HO_2 + H \longleftrightarrow H_2O + O$	$1.0 \cdot 10^7$	0.0	540
12	$HO_2 + O \longleftrightarrow O_2 + OH$	$1.5 \cdot 10^7$	0.0	475
13	$HO_2 + OH \longleftrightarrow H_2O + O_2$	$8.0 \cdot 10^6$	0.0	0
14	$HO_2 + HO_2 \longleftrightarrow H_2O_2 + O_2$	$2.0 \cdot 10^6$	0.0	0
15	$H + H_2O_2 \longleftrightarrow H_2 + HO_2$	$1.4 \cdot 10^6$	0.0	1800
16	$O + H_2O_2 \longleftrightarrow OH + HO_2$	$1.4 \cdot 10^7$	0.0	3200
17	$OH + H_2O_2 \longleftrightarrow H_2O + HO_2$	$6.1 \cdot 10^6$	0.0	715
18	$H_2O_2 + M \longleftrightarrow OH + OH + M$	$1.2 \cdot 10^{11}$	0.0	22800
19	$O + O + M \longleftrightarrow O_2 + M$	$6.0 \cdot 10^1$	0.0	-900

Third body efficiencies for reactions 6, 7, 8, 9, 18 and 19 are:

r	H	O	N_2	O_2	H_2	OH	HO_2	H_2O	H_2O_2
6	1	1	1	1	1	1	1	6	1
7	1	1	1	1	2	1	1	6	1
8	1	1	1	1	1	1	1	5	1
9	1	1	1	1	2	1	1	16	1
18	1	1	1	1	1	1	1	15	1
19	1	1	1	1	1	1	1	1	1

Table C.3: Used reaction mechanism.

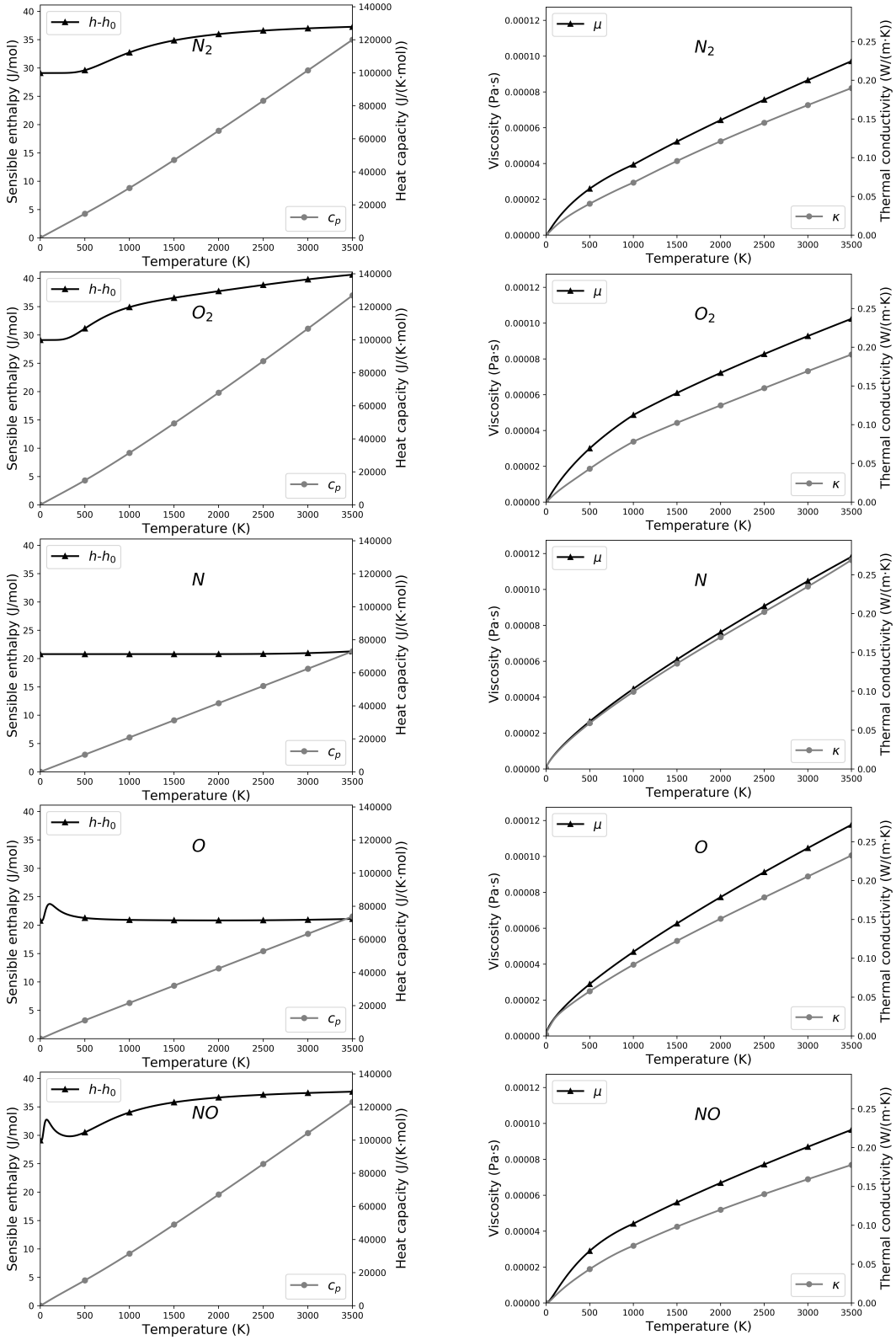

Figure C.2: Species properties for investigations with 5 species.

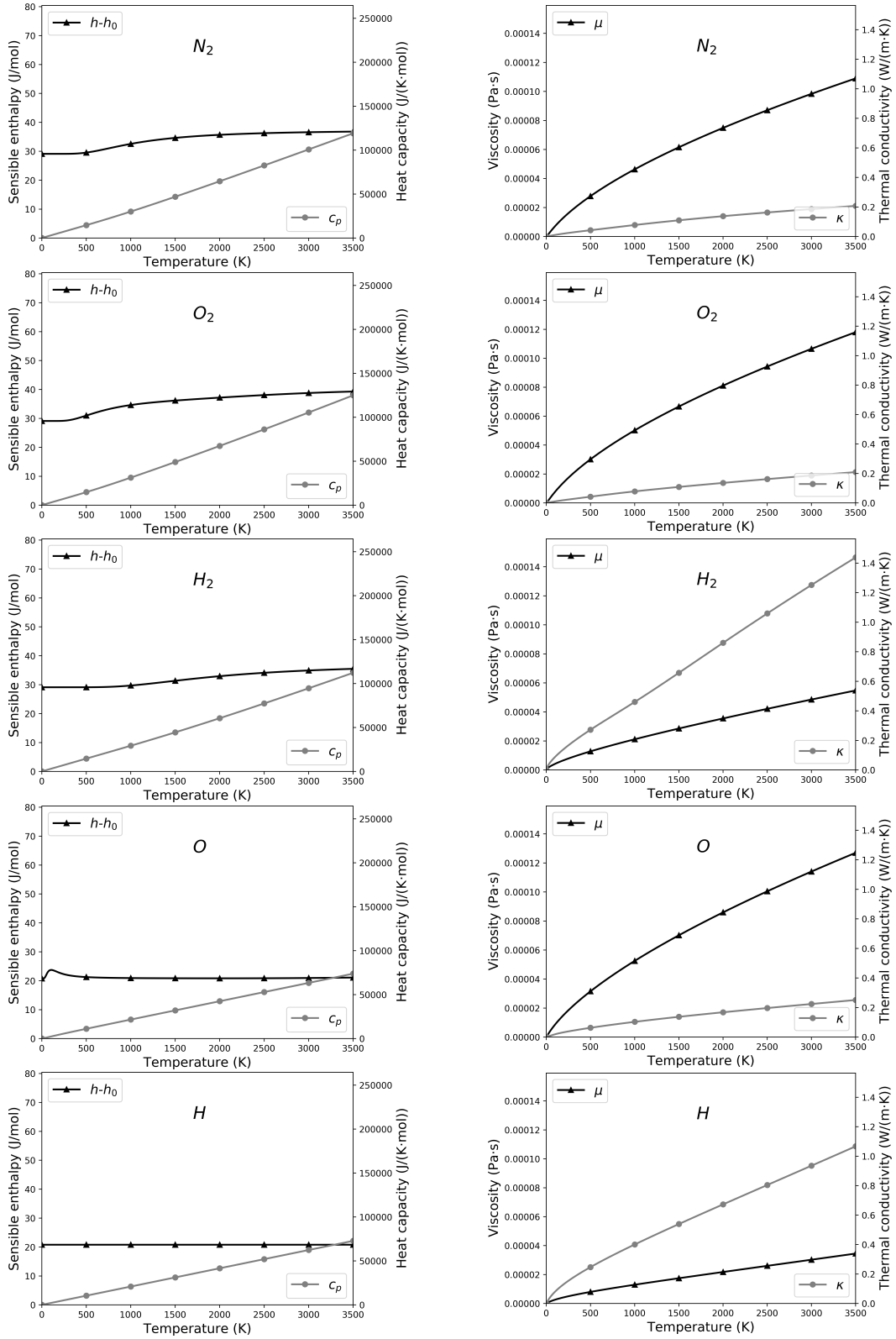

Figure C.3: Species properties for investigations with 9 species.

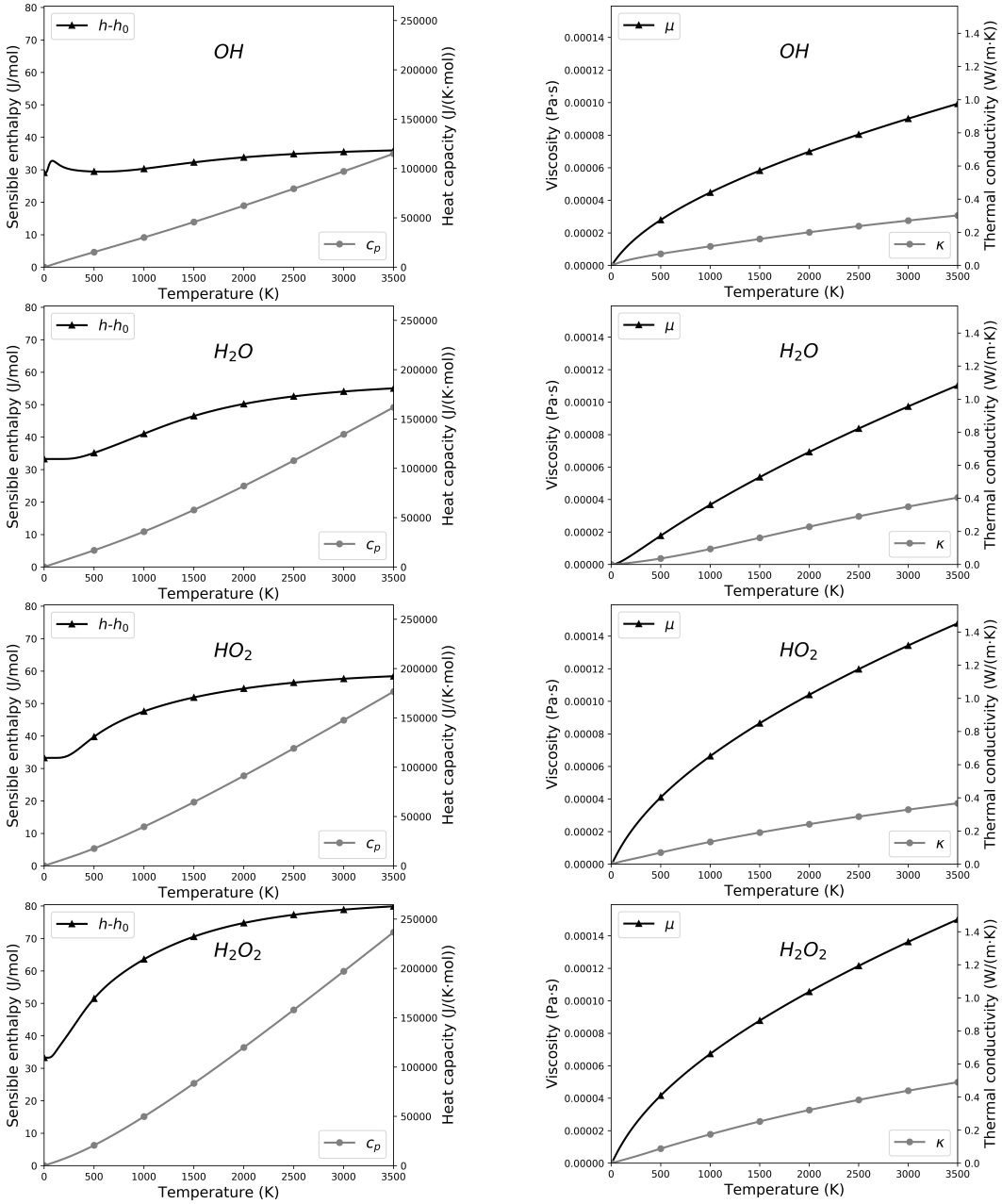

Figure C.3: Species properties for investigations with 9 species (ctd).

D Preconditioning of the equations

Recalling the definition of the residual $R(U)$ the conservation equations take the form

$$\frac{\partial U}{\partial t} = -R(U) \tag{D.1}$$

with conservative variables $U = (\rho Y_1, ..., \rho Y_{N_s}, \rho u, \rho v, \rho w, \rho E)^T$. With the matrix dissipation term D this can be written as

$$\frac{\partial U}{\partial t} + (f + D) = 0 \tag{D.2}$$

with f being the remaining terms of $R(U)$. In order to accelerate convergence at the cost of time accuracy this equation can be preconditioned using a preconditioning matrix[1] P as

$$\frac{\partial U}{\partial t} + \frac{\partial U}{\partial W_P} P(W_P) \frac{\partial W_P}{\partial U} (f + \frac{\partial U}{\partial W_P} P(W_P)^{-1} \frac{\partial W_P}{\partial W_D} D) = 0. \tag{D.3}$$

The loss of time-accuracy here is inconsequential since the preconditioning is only applied to the inner iterations which convergence to a steady state. The two additional sets of variables introduced are the set W_P for which the preconditioner is derived and the set W_D with which the dissipation term is computed. The dissipation term is

$$D = |P_2(W_D) A(W_D)| N_D(W_D) \tag{D.4}$$

with N_D a function that evaluates second and fourth order terms and $A(W_D)$ is the matrix dissipation operator (convective flux jacobian) $\frac{\partial F^{Eu}(W_D)}{\partial W_D}$ with Roe-averaged values on the face (compare to equation (3.13)). The subscript 2 indicates the preconditioner used for the matrix dissipation which can differ from the one used for the time derivative [68]. To evaluate the preconditioned matrix dissipation operator one can compute

$$|P_2(W_D) A(W_D)| = \frac{\partial W_D}{\partial U} \left| \frac{\partial U}{\partial W_P} P_2(W_P) \frac{\partial W_P}{\partial U} A(U) \right| \frac{\partial U}{\partial W_D} = \frac{\partial W_D}{\partial U} G |\Lambda| G^{-1} \frac{\partial U}{\partial W_D} \tag{D.5}$$

with eigendecomposition

$$G|\Lambda|G^{-1} = P_2(U) A(U). \tag{D.6}$$

The full equation then reads

$$\frac{\partial U}{\partial t} + \frac{\partial U}{\partial W_P} P_1(W_P) \frac{\partial W_P}{\partial U} (f + \frac{\partial U}{\partial W_P} P_2^{-1}(W_P) \frac{\partial W_P}{\partial U} G |\Lambda| G^{-1} \frac{\partial U}{\partial W_D} N_D) = 0. \tag{D.7}$$

[1] The definitions of preconditioner and inverse preconditioner differ throughout literature. We choose the notation as in Radespiel and Kroll [45] which defines a preconditioning matrix P. The definition in e.g. Choi and Merkle [6] can be obtained as $\Gamma = \frac{\partial U}{\partial W_\Gamma} \frac{\partial W_\Gamma}{\partial W_P} P^{-1} \frac{\partial W_P}{\partial W_\Gamma}$. Thus if $W_P = W_\Gamma$ then $\Gamma = \frac{\partial U}{\partial W_P} P^{-1}$.

Note that in contrast to Turkel [68] the inverse preconditioning matrix in the matrix dissipation term is based on the same settings as the preconditioning matrix used for the matrix dissipation operator. This allows to adjust the preconditioning for convergence acceleration (P_1) without affecting the converged solution whereas the notation by Turkel changes the amount of artificial dissipation and thus the final solution if the preconditioning for convergence acceleration is changed. On the other hand, the notation proposed by Turkel allows for larger discrepancies between the two preconditioning matrices without losing stability.

In the following the preconditioning variables are chosen as $W_P = W_\Gamma = (p, u, v, w, T, Y_1, ..., Y_{N_s-1})^T$ and the dissipation term is computed in conservative variables (i.e. $W_D = U$). For multi-species systems the preconditioning matrix is given in Zong and Yang [76] or Weiss and Murthy [70]. Both use the notation employing Γ and thus $P^{-1} = \frac{\partial W_P}{\partial U}\Gamma$. Consequently the jacobians $\frac{\partial W_P}{\partial U}$ and $\frac{\partial U}{\partial W_P}$ are required.

Used matrices

In the following the used matrices are presented for $N_s = 3$, from which the matrices for different values of N_s easily follow.
First

$$\Gamma = \begin{bmatrix} \Theta & 0 & 0 & 0 & \frac{\partial \rho}{\partial T}(1-\delta) & \frac{\partial \rho}{\partial Y_1}(1-\delta) & \frac{\partial \rho}{\partial Y_2}(1-\delta) \\ u\Theta & \rho & 0 & 0 & \frac{\partial \rho}{\partial T}u(1-\delta) & \frac{\partial \rho}{\partial Y_1}u(1-\delta) & \frac{\partial \rho}{\partial Y_2}u(1-\delta) \\ v\Theta & 0 & \rho & 0 & \frac{\partial \rho}{\partial T}v(1-\delta) & \frac{\partial \rho}{\partial Y_1}v(1-\delta) & \frac{\partial \rho}{\partial Y_2}v(1-\delta) \\ w\Theta & 0 & 0 & \rho & \frac{\partial \rho}{\partial T}w(1-\delta) & \frac{\partial \rho}{\partial Y_1}w(1-\delta) & \frac{\partial \rho}{\partial Y_2}w(1-\delta) \\ H\Theta + \frac{\partial h}{\partial p}\rho - 1 & \rho u & \rho v & \rho w & H\frac{\partial \rho}{\partial T}(1-\delta) + \frac{\partial h}{\partial T}\rho & H\frac{\partial \rho}{\partial Y_1}(1-\delta) + \frac{\partial H}{\partial Y_1}\rho & H\frac{\partial \rho}{\partial Y_2}(1-\delta) + \frac{\partial H}{\partial Y_2}\rho \\ Y_1\Theta & 0 & 0 & 0 & Y_1\frac{\partial \rho}{\partial T}(1-\delta) & Y_1\frac{\partial \rho}{\partial Y_1}(1-\delta) + \rho & Y_1\frac{\partial \rho}{\partial Y_2}(1-\delta) \\ Y_2\Theta & 0 & 0 & 0 & Y_2\frac{\partial \rho}{\partial T}(1-\delta) & Y_2\frac{\partial \rho}{\partial Y_1}(1-\delta) & Y_2\frac{\partial \rho}{\partial Y_2}(1-\delta) + \rho \end{bmatrix}$$

with $\Theta = \frac{1}{c^2}(1-\delta)(\gamma-1) + \frac{1}{M_r c^2}$. This is in line with the definition by Radespiel [45] for one species and a perfect gas and thus leads to a Turkel-type preconditioning if $\delta = 0$ and a Choi-and-Merkle-type for $\delta = 1$. For general derivatives the Turkel-type ($\delta = 0$) can also be found in Zong and Wang [76]. Further

$$\frac{\partial U}{\partial W_P} = \begin{bmatrix} \frac{Y_1\gamma}{c^2} & 0 & 0 & 0 & Y_1\frac{\partial \rho}{\partial T} & Y_1\frac{\partial \rho}{\partial Y_1} + \rho & Y_1\frac{\partial \rho}{\partial Y_2} \\ \frac{Y_2\gamma}{c^2} & 0 & 0 & 0 & Y_2\frac{\partial \rho}{\partial T} & Y_2\frac{\partial \rho}{\partial Y_1} & Y_2\frac{\partial \rho}{\partial Y_2} + \rho \\ \frac{\gamma}{c^2}Y_3 & 0 & 0 & 0 & \frac{\partial \rho}{\partial T}Y_3 & Y_3\frac{\partial \rho}{\partial Y_1} - \rho & Y_3\frac{\partial \rho}{\partial Y_2} - \rho \\ \frac{\gamma u}{c^2} & \rho & 0 & 0 & \frac{\partial \rho}{\partial T}u & \frac{\partial \rho}{\partial Y_1}u & \frac{\partial \rho}{\partial Y_2}u \\ \frac{\gamma v}{c^2} & 0 & \rho & 0 & \frac{\partial \rho}{\partial T}v & \frac{\partial \rho}{\partial Y_1}v & \frac{\partial \rho}{\partial Y_2}v \\ \frac{\gamma w}{c^2} & 0 & 0 & \rho & \frac{\partial \rho}{\partial T}w & \frac{\partial \rho}{\partial Y_1}w & \frac{\partial \rho}{\partial Y_2}w \\ \frac{H\gamma}{c^2} + \frac{\partial h}{\partial p}\rho - 1 & \rho u & \rho v & \rho w & H\frac{\partial \rho}{\partial T} + \frac{\partial h}{\partial T}\rho & H\frac{\partial \rho}{\partial Y_1} + \frac{\partial H}{\partial Y_1}\rho & H\frac{\partial \rho}{\partial Y_2} + \frac{\partial H}{\partial Y_2}\rho \end{bmatrix}$$

and

$$\frac{\partial W_P}{\partial U} = \begin{bmatrix} \frac{\partial p}{\partial \rho_1} & \frac{\partial p}{\partial \rho_2} & \frac{\partial p}{\partial \rho_3} & -\frac{\partial p}{\partial \rho E}u & -\frac{\partial p}{\partial \rho E}v & -\frac{\partial p}{\partial \rho E}w & \frac{\partial p}{\partial \rho E} \\ -\frac{u}{\rho} & -\frac{u}{\rho} & -\frac{u}{\rho} & \frac{1}{\rho} & 0 & 0 & 0 \\ -\frac{v}{\rho} & -\frac{v}{\rho} & -\frac{v}{\rho} & 0 & \frac{1}{\rho} & 0 & 0 \\ -\frac{w}{\rho} & -\frac{w}{\rho} & -\frac{w}{\rho} & 0 & 0 & \frac{1}{\rho} & 0 \\ \frac{\varphi - \frac{\partial H}{\partial Y_1} - \frac{\partial p}{\partial \rho_1}\left(\frac{\partial h}{\partial p}\rho - 1\right)}{\frac{\partial h}{\partial T}\rho} & \frac{\varphi - \frac{\partial H}{\partial Y_2} - \frac{\partial p}{\partial \rho_2}\left(\frac{\partial h}{\partial p}\rho - 1\right)}{\frac{\partial h}{\partial T}\rho} & \frac{\varphi - \frac{\partial p}{\partial \rho_3}\left(\frac{\partial h}{\partial p}\rho - 1\right)}{\frac{\partial h}{\partial T}\rho} & -\frac{\gamma u}{\frac{\partial h}{\partial T}\rho} & -\frac{\gamma v}{\frac{\partial h}{\partial T}\rho} & -\frac{\gamma w}{\frac{\partial h}{\partial T}\rho} & \frac{\gamma}{\frac{\partial h}{\partial T}\rho} \\ -\frac{Y_1}{\rho} + \frac{1}{\rho} & -\frac{Y_1}{\rho} & -\frac{Y_1}{\rho} & 0 & 0 & 0 & 0 \\ -\frac{Y_2}{\rho} & -\frac{Y_2}{\rho} + \frac{1}{\rho} & -\frac{Y_2}{\rho} & 0 & 0 & 0 & 0 \end{bmatrix}$$

with $\varphi = -H + U^2 + Y_1 \frac{\partial H}{\partial Y_1} + Y_2 \frac{\partial H}{\partial Y_2}$. Thus

$$P(W_P)^{-1} = \begin{bmatrix} -\delta(\gamma-1) + \frac{1}{M_r} & 0 & 0 & 0 & -\frac{\delta \frac{\partial h}{\partial T}\rho(\gamma-1)}{\frac{\partial h}{\partial p}\rho - 1} & -c^2\delta\frac{\partial \rho}{\partial Y_1} & -c^2\delta\frac{\partial \rho}{\partial Y_2} \\ 0 & 1 & 0 & 0 & 0 & 0 & 0 \\ 0 & 0 & 1 & 0 & 0 & 0 & 0 \\ 0 & 0 & 0 & 1 & 0 & 0 & 0 \\ \frac{\left(\frac{\partial h}{\partial p}\rho - 1\right)\left(\delta(\gamma-1)+1-\frac{1}{M_r}\right)}{\frac{\partial h}{\partial T}\rho} & 0 & 0 & 0 & \delta(\gamma-1)+1 & -\frac{c^2\delta\frac{\partial \rho}{\partial Y_1}\left(-\frac{\partial h}{\partial p}\rho+1\right)}{\frac{\partial h}{\partial T}\rho} & -\frac{c^2\delta\frac{\partial \rho}{\partial Y_2}\left(-\frac{\partial h}{\partial p}\rho+1\right)}{\frac{\partial h}{\partial T}\rho} \\ 0 & 0 & 0 & 0 & 0 & 1 & 0 \\ 0 & 0 & 0 & 0 & 0 & 0 & 1 \end{bmatrix}$$

and

$$P(W_P) = \begin{bmatrix} M_r(\delta(\gamma-1)+1) & 0 & 0 & 0 & \frac{M_r\delta\frac{\partial h}{\partial T}\rho(\gamma-1)}{\frac{\partial h}{\partial p}\rho - 1} & M_r c^2\delta\frac{\partial \rho}{\partial Y_1} & M_r c^2\delta\frac{\partial \rho}{\partial Y_2} \\ 0 & 1 & 0 & 0 & 0 & 0 & 0 \\ 0 & 0 & 1 & 0 & 0 & 0 & 0 \\ 0 & 0 & 0 & 1 & 0 & 0 & 0 \\ \frac{(M_r(\delta(\gamma-1)+1)-1)\left(-\frac{\partial h}{\partial p}\rho+1\right)}{\frac{\partial h}{\partial T}\rho} & 0 & 0 & 0 & -M_r\delta(\gamma-1)+1 & -\frac{M_r c^2\delta\frac{\partial \rho}{\partial Y_1}\left(\frac{\partial h}{\partial p}\rho-1\right)}{\frac{\partial h}{\partial T}\rho} & -\frac{M_r c^2\delta\frac{\partial \rho}{\partial Y_2}\left(\frac{\partial h}{\partial p}\rho-1\right)}{\frac{\partial h}{\partial T}\rho} \\ 0 & 0 & 0 & 0 & 0 & 1 & 0 \\ 0 & 0 & 0 & 0 & 0 & 0 & 1 \end{bmatrix}$$

and consequently

$$P(U) = \frac{\partial U}{\partial W_P} P(W_P) \frac{\partial W_P}{\partial U} = \begin{bmatrix} 1 - Y_1\xi_{3,1} & \dots & -Y_1\xi_{3,N_s} & -Y_1 u\xi_2 & -Y_1 v\xi_2 & -Y_1 w\xi_2 & Y_1\xi_2 \\ \vdots & \ddots & \vdots & \vdots & \vdots & \vdots & \vdots \\ -Y_{N_s}\xi_{3,1} & \dots & 1 - Y_{N_s}\xi_{3,N_s} & -Y_3 u\xi_2 & -Y_3 v\xi_2 & -Y_3 w\xi_2 & Y_3\xi_2 \\ -u\xi_{3,1} & \dots & -u\xi_{3,3} & 1 - u^2\xi_2 & -uv\xi_2 & -uw\xi_2 & u\xi_2 \\ -v\xi_{3,1} & \dots & -v\xi_{3,3} & -uv\xi_2 & 1 - v^2\xi_2 & -vw\xi_2 & v\xi_2 \\ -w\xi_{3,1} & \dots & -w\xi_{3,3} & -uw\xi_2 & -vw\xi_2 & 1 - w^2\xi_2 & w\xi_2 \\ -H\xi_{3,1} & \dots & -H\xi_{3,3} & -Hu\xi_2 & -Hv\xi_2 & -Hw\xi_2 & 1 + H\xi_2 \end{bmatrix}$$

with $\xi_1 = \frac{M_r(\delta-1)+1}{c^2}$, $\xi_2 = \frac{\frac{\partial p}{\partial \rho E}(M_r(\delta-1)+1)}{c^2}$ and $\xi_{3,s} = \xi_1 \frac{\partial p}{\partial \rho_s} - M_r\delta$.
Further, the (none-preconditioned) matrix dissipation operator is

$$A(U) = \begin{bmatrix} V - VY_1 & -VY_1 & -VY_1 & Y_1 n_1 & Y_1 n_2 & Y_1 n_3 & 0 \\ -VY_2 & V - VY_2 & -VY_2 & Y_2 n_1 & Y_2 n_2 & Y_2 n_3 & 0 \\ -VY_3 & -VY_3 & V - VY_3 & Y_3 n_1 & Y_3 n_2 & Y_3 n_3 & 0 \\ \frac{\partial p}{\partial \rho_1} n_1 - Vu & \frac{\partial p}{\partial \rho_2} n_1 - Vu & \frac{\partial p}{\partial \rho_3} n_1 - Vu & V + n_1 u - \frac{\partial p}{\partial \rho E} n_1 u & n_2 u - \frac{\partial p}{\partial \rho E} n_1 v & n_3 u - \frac{\partial p}{\partial \rho E} n_1 w & \frac{\partial p}{\partial \rho E} n_1 \\ \frac{\partial p}{\partial \rho_1} n_2 - Vv & \frac{\partial p}{\partial \rho_2} n_2 - Vv & \frac{\partial p}{\partial \rho_3} n_2 - Vv & n_1 v - \frac{\partial p}{\partial \rho E} n_2 u & V + n_2 v - \frac{\partial p}{\partial \rho E} n_2 v & n_3 v - \frac{\partial p}{\partial \rho E} n_2 w & \frac{\partial p}{\partial \rho E} n_2 \\ \frac{\partial p}{\partial \rho_1} n_3 - Vw & \frac{\partial p}{\partial \rho_2} n_3 - Vw & \frac{\partial p}{\partial \rho_3} n_3 - Vw & n_1 w - \frac{\partial p}{\partial \rho E} n_3 u & n_2 w - \frac{\partial p}{\partial \rho E} n_3 v & V + n_3 w - \frac{\partial p}{\partial \rho E} n_3 w & \frac{\partial p}{\partial \rho E} n_3 \\ V\frac{\partial p}{\partial \rho_1} - HV & V\frac{\partial p}{\partial \rho_2} - HV & V\frac{\partial p}{\partial \rho_3} - HV & Hn_1 - V\frac{\partial p}{\partial \rho E} u & Hn_2 - V\frac{\partial p}{\partial \rho E} v & Hn_3 - V\frac{\partial p}{\partial \rho E} w & V + V\frac{\partial p}{\partial \rho E} \end{bmatrix}$$

The eigenvalues of the preconditioned matrix dissipation operator $P(U)A(U)$ are

$$\lambda_1 = V \qquad \lambda_2 = \frac{M_r V + V}{2} + c_m \qquad \lambda_3 = \frac{M_r V + V}{2} - c_m$$
$$\text{with} \qquad c_m = 0.5\sqrt{(M_r - 1)^2 V^2 + 4M_r c^2}$$

where λ_1 has multiplicity $N_s + 2$ and λ_2 and λ_3 each have multiplicity one. The used right and left

eigenvectors (with column (row) N_s+3 corresponding to λ_2 and column (row) N_s+4 to λ_3) are

$$G = \begin{bmatrix} 1 & \dots & 0 & 0 & 0 & Y_1 & Y_1 \\ \vdots & \ddots & \vdots & \vdots & \vdots & \vdots & \vdots \\ 0 & \dots & 1 & 0 & 0 & Y_{N_s} & Y_{N_s} \\ u\,(1-\delta) & \dots & u\,(1-\delta) & b_{1,x}c & b_{2,x}c & u+n_1\psi_5 & u+n_1\psi_6 \\ v\,(1-\delta) & \dots & v\,(1-\delta) & b_{1,y}c & b_{2,y}c & v+n_2\psi_5 & v+n_2\psi_6 \\ w\,(1-\delta) & \dots & w\,(1-\delta) & b_{1,z}c & b_{2,z}c & w+n_3\psi_5 & w+n_3\psi_6 \\ U^2(1-\delta)-\frac{\frac{\partial p}{\partial \rho_1}}{\frac{\partial p}{\partial \rho E}} & \dots & U^2(1-\delta)-\frac{\frac{\partial p}{\partial \rho_{N_s}}}{\frac{\partial p}{\partial \rho E}} & cV_{1,t} & cV_{2,t} & H+V\psi_5 & H+V\psi_6 \end{bmatrix}$$

and

$$G^{-1} = \begin{bmatrix} -\frac{Y_1\frac{\partial p}{\partial \rho_1}}{c^2}+1 & -\frac{Y_1\frac{\partial p}{\partial \rho_2}}{c^2} & -\frac{Y_1\frac{\partial p}{\partial \rho_3}}{c^2} \\ -\frac{Y_2\frac{\partial p}{\partial \rho_1}}{c^2} & -\frac{Y_2\frac{\partial p}{\partial \rho_2}}{c^2}+1 & -\frac{Y_2\frac{\partial p}{\partial \rho_3}}{c^2} \\ -\frac{Y_3\frac{\partial p}{\partial \rho_1}}{c^2} & -\frac{Y_3\frac{\partial p}{\partial \rho_2}}{c^2} & -\frac{Y_3\frac{\partial p}{\partial \rho_3}}{c^2}+1 \\ \left(-\delta+1+\frac{\delta}{c^2}\frac{\partial p}{\partial \rho_1}\right)\frac{-V^{1,t}}{c} & \left(-\delta+1+\frac{\delta}{c^2}\frac{\partial p}{\partial \rho_2}\right)\frac{-V^{1,t}}{c} & \left(-\delta+1+\frac{\delta}{c^2}\frac{\partial p}{\partial \rho_3}\right)\frac{-V^{1,t}}{c} \\ \left(-\delta+1+\frac{\delta}{c^2}\frac{\partial p}{\partial \rho_1}\right)\frac{-V^{2,t}}{c} & \left(-\delta+1+\frac{\delta}{c^2}\frac{\partial p}{\partial \rho_2}\right)\frac{-V^{2,t}}{c} & \left(-\delta+1+\frac{\delta}{c^2}\frac{\partial p}{\partial \rho_3}\right)\frac{-V^{2,t}}{c} \\ -\frac{M_rV(1-\delta)}{2c_m}+\frac{\partial p}{\partial \rho_1}\psi_1 & -\frac{M_rV(1-\delta)}{2c_m}+\frac{\partial p}{\partial \rho_2}\psi_1 & -\frac{M_rV(1-\delta)}{2c_m}+\frac{\partial p}{\partial \rho_3}\psi_1 \\ \frac{M_rV(1-\delta)}{2c_m}+\frac{\partial p}{\partial \rho_1}\psi_2 & \frac{M_rV(1-\delta)}{2c_m}+\frac{\partial p}{\partial \rho_2}\psi_2 & \frac{M_rV(1-\delta)}{2c_m}+\frac{\partial p}{\partial \rho_3}\psi_2 \end{bmatrix}$$

$$\begin{bmatrix} \frac{Y_1\frac{\partial p}{\partial \rho E}u}{c^2} & \frac{Y_1\frac{\partial p}{\partial \rho E}v}{c^2} & \frac{Y_1\frac{\partial p}{\partial \rho E}w}{c^2} & -\frac{Y_1\frac{\partial p}{\partial \rho E}}{c^2} \\ \frac{Y_2\frac{\partial p}{\partial \rho E}u}{c^2} & \frac{Y_2\frac{\partial p}{\partial \rho E}v}{c^2} & \frac{Y_2\frac{\partial p}{\partial \rho E}w}{c^2} & -\frac{Y_2\frac{\partial p}{\partial \rho E}}{c^2} \\ \frac{Y_3\frac{\partial p}{\partial \rho E}u}{c^2} & \frac{Y_3\frac{\partial p}{\partial \rho E}v}{c^2} & \frac{Y_3\frac{\partial p}{\partial \rho E}w}{c^2} & -\frac{Y_3\frac{\partial p}{\partial \rho E}}{c^2} \\ \frac{b^{1,x}}{c}+\frac{\delta\frac{\partial p}{\partial \rho E}u(V^{1,t})}{c^3} & \frac{b^{1,y}}{c}+\frac{\delta\frac{\partial p}{\partial \rho E}v(V^{1,t})}{c^3} & \frac{b^{1,z}}{c}+\frac{\delta\frac{\partial p}{\partial \rho E}w(V^{1,t})}{c^3} & -\frac{\delta\frac{\partial p}{\partial \rho E}(V^{1,t})}{c^3} \\ \frac{b^{2,x}}{c}+\frac{\delta\frac{\partial p}{\partial \rho E}u(V^{2,t})}{c^3} & \frac{b^{2,y}}{c}+\frac{\delta\frac{\partial p}{\partial \rho E}v(V^{2,t})}{c^3} & \frac{b^{2,z}}{c}+\frac{\delta\frac{\partial p}{\partial \rho E}w(V^{2,t})}{c^3} & -\frac{\delta\frac{\partial p}{\partial \rho E}(V^{2,t})}{c^3} \\ \frac{M_rn_1}{2c_m}-u\psi_3 & \frac{M_rn_2}{2c_m}-v\psi_3 & \frac{M_rn_3}{2c_m}-w\psi_3 & \psi_3 \\ -\frac{M_rn_1}{2c_m}-u\psi_4 & -\frac{M_rn_2}{2c_m}-v\psi_4 & -\frac{M_rn_3}{2c_m}-w\psi_4 & \psi_4 \end{bmatrix}$$

where

$$\begin{aligned} V_{1,t} &= V_{1,t} & V_{2,t} &= V_{2,t} \\ V^{1,t} &= \left(b^{1,x}u+b^{1,y}v+b^{1,z}w\right) & V^{2,t} &= \left(b^{2,x}u+b^{2,y}v+b^{2,z}w\right) \\ \psi_1 &= \frac{\left(\frac{V(M_r(1-2\delta)-1)}{2c_m}+1\right)}{2c^2} & \psi_2 &= \frac{\left(-\frac{V(M_r(1-2\delta)-1)}{2c_m}+1\right)}{2c^2} \\ \psi_3 &= \frac{\partial p}{\partial \rho E}\psi_1 & \psi_4 &= \frac{\partial p}{\partial \rho E}\psi_2 \\ \psi_5 &= -\frac{V\,(M_r-1)}{2M_r}+\frac{c_m}{M_r} & \psi_6 &= -\frac{V\,(M_r-1)}{2M_r}-\frac{c_m}{M_r} \end{aligned}$$

The tangential vectors are chosen such that $b_in = b^jn = 0$ and $b_ib^j = \delta_{ij}$ with the Kronecker delta δ_{ij}. Further details can be found in Liu and Vinokur [28] and Rohde [49]. From this $P(U)^{-1}G$ can be

computed as

$$P(U)^{-1}G =$$

$$\begin{bmatrix}
1-Y_1\delta_2 & -Y_1\delta_2 & -Y_1\delta_2 & 0 & 0 & \frac{Y_1}{M_{r,2}} & \frac{Y_1}{M_{r,2}} \\
-Y_2\delta_2 & 1-Y_2\delta_2 & -Y_2\delta_2 & 0 & 0 & \frac{Y_2}{M_{r,2}} & \frac{Y_2}{M_{r,2}} \\
-Y_3\delta_2 & -Y_3\delta_2 & 1-Y_3\delta_2 & 0 & 0 & \frac{Y_3}{M_{r,2}} & \frac{Y_3}{M_{r,2}} \\
u\,(1-\delta-\delta_2) & u\,(1-\delta-\delta_2) & u\,(1-\delta-\delta_2) & b_{1,x}c & b_{2,x}c & \frac{u}{M_{r,2}}+n_1\psi_5 & \frac{u}{M_{r,2}}+n_1\psi_6 \\
v\,(1-\delta-\delta_2) & v\,(1-\delta-\delta_2) & v\,(1-\delta-\delta_2) & b_{1,y}c & b_{2,y}c & \frac{v}{M_{r,2}}+n_2\psi_5 & \frac{v}{M_{r,2}}+n_2\psi_6 \\
w\,(1-\delta-\delta_2) & w\,(1-\delta-\delta_2) & w\,(1-\delta-\delta_2) & b_{1,z}c & b_{2,z}c & \frac{w}{M_{r,2}}+n_3\psi_5 & \frac{w}{M_{r,2}}+n_3\psi_6 \\
U^2\,(1-\delta)-H\delta_2-\frac{\frac{\partial p}{\partial \rho_1}}{\frac{\partial p}{\partial \rho E}} & U^2\,(1-\delta)-H\delta_2-\frac{\frac{\partial p}{\partial \rho_2}}{\frac{\partial p}{\partial \rho E}} & U^2\,(1-\delta)-H\delta_2-\frac{\frac{\partial p}{\partial \rho_3}}{\frac{\partial p}{\partial \rho E}} & cV_{1,t} & cV_{2,t} & \frac{H}{M_{r,2}}+V\psi_5 & \frac{H}{M_{r,2}}+V\psi_6
\end{bmatrix}$$

where the index 2 is added if the variable is based on the preconditioning of the time-derivative instead of the matrix operator (for more details see [68]). Technically, further multiplication of right eigenvectors, eigenvalues and left eigenvectors would be possible, i.e. $M = P(U)^{-1}G|\Lambda|G^{-1}$. However, the eigenvalues might have to be modified to ensure non-decreasing entropy and thus need to be kept in the final matrix as a variable. This leads to a final matrix with huge entries that dramatically reduce readability of the code. Hence the last multiplication is done in the code and the small additional computational effort is accepted in order to improve readability. The none-preconditioned case is recovered for $\delta = 0$ and $M_r = 1$.

For an ideal gas the following relations apply to compute the derivatives from know quantities:

$$\frac{\partial p}{\partial \rho E} = \gamma - 1 \qquad \frac{\partial p}{\partial \rho_s} = \frac{\gamma-1}{2}\left(u^2+v^2+w^2\right) + R_s T - (\gamma-1)e_s$$

In the derivation the following additional derivatives are used (that cancel out in the final matrices):

$$\frac{\partial h}{\partial p} = 0 \qquad \frac{\partial h}{\partial T} = c_p$$

$$\frac{\partial \rho}{\partial Y_s} = \rho M \frac{M_s - M_{N_s}}{M_s M_{N_s}} \qquad \frac{\partial H}{\partial Y_s} = h_s - h_{N_s}$$

Eidesstattliche Versicherung

Ich erkläre: Ich habe die vorgelegte Dissertation selbstständig und ohne unerlaubte fremde Hilfe und nur mit den Hilfen angefertigt, die ich in der Dissertation angegeben habe. Alle Textstellen, die wörtlich oder sinngemäß aus veröffentlichten Schriften entnommen sind, und alle Angaben, die auf mündlichen Auskünften beruhen, sind als solche kenntlich gemacht. Ich stimme einer evtl. Überprüfung meiner Dissertation durch eine Antiplagiat-Software zu. Bei den von mir durchgeführten und in der Dissertation erwähnten Untersuchungen habe ich die Grundsätze guter wissenschaftlicher Praxis, wie sie in der entsprechenden Satzung der federführenden Hochschule niedergelegt sind und die mir ausgehändigt wurde, eingehalten.

Gießen, 26.10.2022.

Statutory Declaration

I declare that I have completed this dissertation single-handedly without the unauthorized help of a second party and only with the assistance acknowledged therein. I have appropriately acknowledged and cited all text passages that are derived verbatim from or are based on the content of published work of others, and all information relating to verbal communications. I consent to the use of an anti- plagiarism software to check my thesis. I have abided by the principles of good scientific conduct laid down in the regulations of the leading University which were delivered to me in carrying out the investigations described in the dissertation.

Gießen, 26/10/2022.